

Title	固体電解質界面(SEI)の形成制御を指向したリチウムイオン二次電池負極を高度安定化するBIAN型機能性高分子バインダーの戦略的設計
Author(s)	GUPTA, Agman
Citation	
Issue Date	2021-09
Type	Thesis or Dissertation
Text version	ETD
URL	<a href="http://hdl.handle.net/10119/17530">http://hdl.handle.net/10119/17530</a>
Rights	
Description	Supervisor:松見 紀佳, 先端科学技術研究科, 博士

Doctoral Dissertation

Stabilizing High-Performance Li-Ion Battery  
Anodes by Strategic BIAN-based Functional  
Polymer Binders Design for Controlled Solid-  
Electrolyte Interphase (SEI) Formation

AGMAN GUPTA

Supervisor: Professor Noriyoshi Matsumi

Graduate School of Advanced Science and Technology

Japan Advanced Institute of Science and Technology

Materials Science

September 2021

# Stabilizing High-Performance Li-Ion Battery Anodes by Strategic BIAN-based Functional Polymer Binders Design for Controlled Solid-Electrolyte Interphase (SEI) Formation

## Chapter-1: Introduction

The development of high energy density lithium-ion batteries (LIBs) for future applications in electric vehicles (EVs), hybrid electric vehicles (HEVs), portable electronic devices, etc. is one of the prime areas of research across the globe. In this regard, various suitable high-capacity alternatives like Sn, Ge, and Si have been explored to replace commercial graphite anode in a LIB. Among various alternatives, Si has been recognized as the next generation anode active material because of its high theoretical capacity ( $\sim 4200 \text{ mAhg}^{-1}$ ) and natural abundance. However, commercial graphite anode and its potential next generation alternative Si have their own sets of drawbacks. But the quality of solid-electrolyte interphase (SEI) is one common drawback associated with both that destabilizes their long-term cycling performance with poor reversible capacity. As a remedy to mitigate all the drawbacks, especially those associated with the interphase formation on these anodes, the utilization of polymers as binders has been recognized as a good strategy. Compounds of the family bis(aryl)acenaphthene (Ar-BIAN) are famous for their ability to act as ligand for transition metal complexes in catalysis as they can act as electron reservoir and offer rich redox chemistry (Figure 1). Also, they have exhibited impressive synthetic versatility as they are potent with structural modification, functionalization, and have tunable electronic properties because of the availability of suitable precursors. Most importantly, their low-lying lowest unoccupied molecular orbital (LUMO) empowers them with the possibility

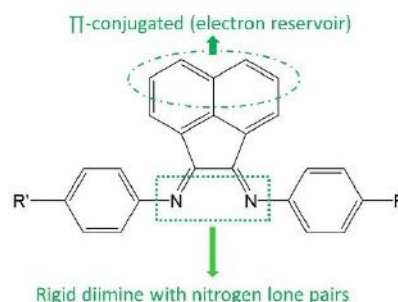


Figure 1: Bis(aryl)acenaphthenequinonediimine

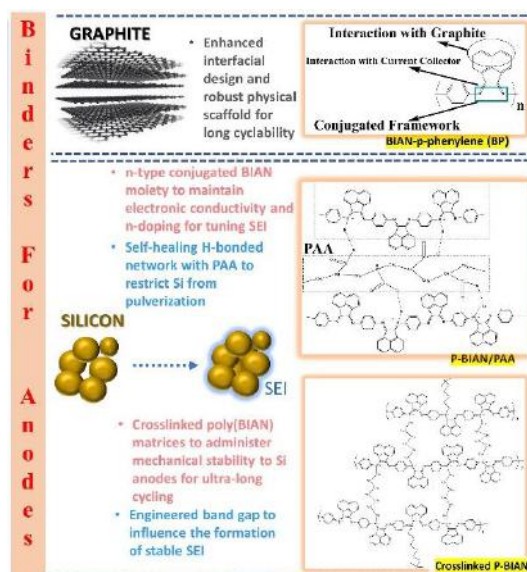


Figure 2: Graphical abstract of this dissertation

of undergoing n-doping in the reducing cathodic environment to restrict the electrolyte decomposition and control the SEI formation if utilized as binders for anodes in LIBs. Therefore, this dissertation work is focused on design, synthesis, and application of novel polymers belonging to the family of compounds bis(aryl)acenaphthenequinone (Ar-BIAN) as binders (Figure 2) to stabilize Li-ion battery (LIB) anodes by the controlled SEI formation, administering mechanical robustness, and maintaining electrical conductivity within the electrode laminate.

## Chapter-2: BIAN-based functional polymer binder to stabilize graphite anode for ultra-long cycling performance.

PVDF has been the conventional polymer binder to stabilize graphite anodes in a LIB. However, because of its non-conducting nature, inability to undergo doping in the cathodic environment to influence the SEI formation, and poor mechanical robustness disqualify it from being a go-to binder choice for ultra-long cycling of graphite anode at a high current rate for future applications. Therefore, this chapter details the design, synthesis, and application of a novel BIAN-p-phenylene (BP) copolymer as binder for graphite in a LIB. The salient features of BP-copolymer that prove it to be superior to PVDF are (Figure 3): (i) better mechanical robustness (higher Young's modulus), (ii) latching of the electrode laminate on to the

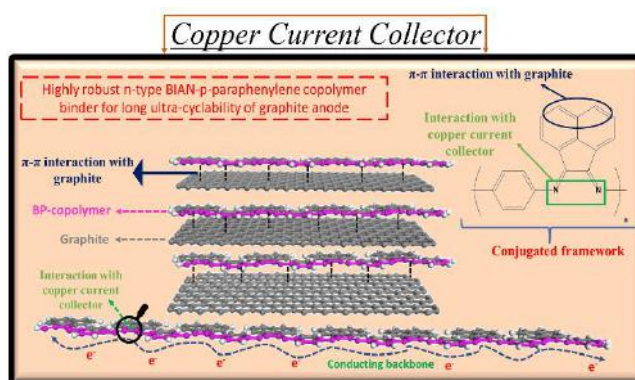


Figure 3: Structural significance of BP-copolymer

current collector through electron rich diimine nitrogen atoms of BP-copolymer, (iii) conjugated framework provides inherent electrical conductivity within the electrode laminate, (iv) its ability to establish tentative  $\pi$ - $\pi$  interaction with graphite framework to administer mechanical robustness, and (v) most importantly, its low-lying LUMO enables it to undergo n-doping in the cathodic environment to restrict the excessive electrolyte decomposition on the anode surface to control the optimal SEI formation. The synergy between all the above-mentioned salient features stabilized the graphite anode in a LIB for over 1700 cycles at a high current rate of 1C with reversible capacity of  $260 \text{ mAhg}^{-1}$  and 95% capacity retention. The anodic half-cells were electrochemically characterized by cyclic voltammetry (CV) studies and dynamic electrochemical impedance spectroscopy (DEIS) studies to understand the interphase formation and its effect on the performance of graphite anode. Further, the postmortem characterization of anodes after electrochemical evaluation was carried out by XPS and FESEM techniques to understand the SEI thickness and surface morphology of the anode.<sup>1</sup>

### Chapter-3: BIAN-based functional n-type conducting self-healing composite binder to stabilize silicon anode in a LIB.

Silicon is potent with 10 times higher gravimetric capacity ( $4200 \text{ mAhg}^{-1}$ ) than the commercial graphite ( $372 \text{ mAhg}^{-1}$ ). Therefore, it is regarded as the next generation anode active materials that can lead to development of LIBs with higher energy density. Also, it can be more economical than graphite because of its natural abundance. However, it has several drawbacks that have hindered its full-scale commercialization in the past decade. The drawbacks are as follows (Figure 4):



Figure 4: Drawbacks associated with Si anodes

(i) rapid volume expansion ( $\sim 300\%$ ) on repeated charge-discharge that pulverizes Si particles into smaller fragments, (ii) the pulverization causes loss of interparticle electrical contact and particle to current collector electrical contact, and (iii) continuous decomposition of electrolyte components on the newly pulverized Si surfaces causes thick SEI formation on the anode surface. These drawbacks together destabilize the Si anodes and cause rapid capacity fade with poor cyclability. Therefore, various functional polymer binders that can mitigate these drawbacks have been explored. However, the synthesis of a versatile binder that can collectively mitigate all the drawbacks of silicon anodes is an important area of research. In this regard, this chapter reports the strategic design, synthesis, and application of a novel electrostatically hydrogen bonded P-BIAN/PAA composite binder (Figure 5) that is potent with excellent mechanical robustness, self-healing property, can maintain electrical conductivity within the electrode laminate, and can undergo n-doping by virtue of its low-lying LUMO to restrict the excessive electrolyte decomposition to form a thin SEI. Thus, the silicon anode was stabilized for over 600 cycles of charge-discharge with a high reversible capacity of  $2100 \text{ mAhg}^{-1}$  and 95% capacity retention. The fabricated anodic half-cells were electrochemically characterized by CV and DEIS studies, respectively to understand the interfacial impedance and properties. Also, the electrochemically characterized anodes were subjected to XPS and FESEM techniques to understand the SEI thickness and anode's surface morphology after cycling for over 600 cycles.

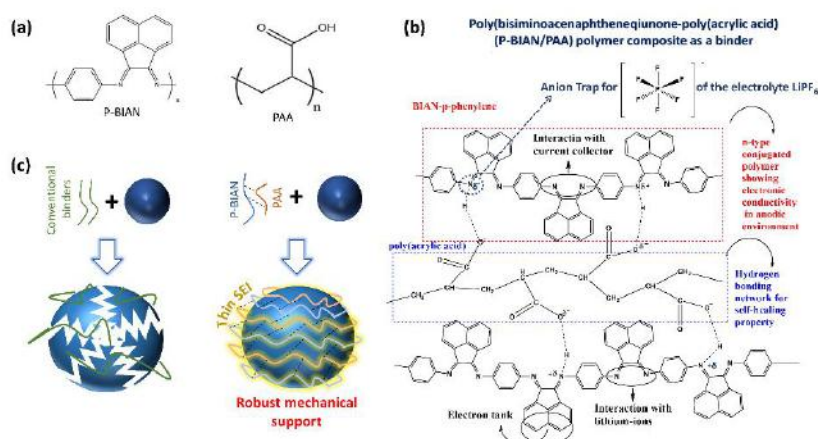
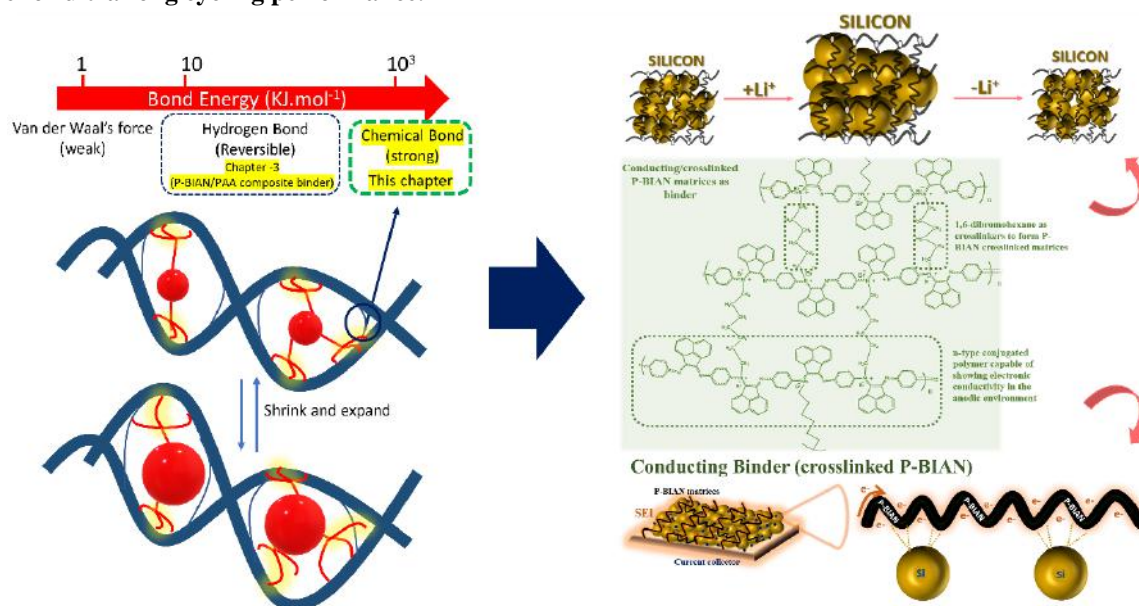


Figure 5: Structural significance of P-BIAN/PAA polymer composite

Therefore, various functional polymer binders that can mitigate these drawbacks have been explored. However, the synthesis of a versatile binder that can collectively mitigate all the drawbacks of silicon anodes is an important area of research. In this regard, this chapter reports the strategic design, synthesis, and application of a novel electrostatically hydrogen bonded P-BIAN/PAA composite binder (Figure 5) that is potent with excellent mechanical robustness, self-healing property, can maintain electrical conductivity within the electrode laminate, and can undergo n-doping by virtue of its low-lying LUMO to restrict the excessive electrolyte decomposition to form a thin SEI. Thus, the silicon anode was stabilized for over 600 cycles of charge-discharge with a high reversible capacity of  $2100 \text{ mAhg}^{-1}$  and 95% capacity retention. The fabricated anodic half-cells were electrochemically characterized by CV and DEIS studies, respectively to understand the interfacial impedance and properties. Also, the electrochemically characterized anodes were subjected to XPS and FESEM techniques to understand the SEI thickness and anode's surface morphology after cycling for over 600 cycles.

**Chapter-4: BIAN-based functional n-type conducting covalently crosslinked composite binder to stabilize silicon anode for ultra-long cycling performance.**



**Figure 6:** Structural significance of BP-copolymer

In chapter 3, the electrostatic hydrogen bonding between the P-BIAN and PAA polymeric chains could empower the P-BIAN/PAA composite binder with an ability to stabilize Si anodes. However, for future applications, the demand of LIB with robust and durable cyclability is imminent. Therefore, in Chapter 4, a novel covalently crosslinked P-BIAN polymer matrices were designed, synthesized, and utilized as binder to improve the cyclic stability of Si anodes with higher reversible capacity. The covalently crosslinked P-BIAN binder matrices can restrict drastic volume expansion of Si particles for longtime because of the improved mechanical robustness in comparison to its hydrogen bonded counterpart in chapter 3 as shown in Figure 6. Also, the covalent crosslinking via diimine nitrogen backbone in the P-BIAN would tentatively lower its band energy of LUMO furthermore in comparison to the hydrogen bonded counter in chapter 3. Therefore, by the synergistic effect of its ability to render improved mechanical robustness and n-doping driven SEI formation, Si anodes were stabilized for over 1000 cycles with higher reversible capacity of  $2500 \text{ mAhg}^{-1}$  and 99.1% capacity retention. The fabricated anodic half-cells were electrochemically characterized by CV and DEIS studies, respectively to understand the interfacial impedance and properties. Also, the electrochemically characterized anodes were subjected to XPS and FESEM techniques to understand the SEI thickness and anode's surface morphology after cycling for over 1000 cycles.

**Keywords:** Bisiminoacenaphthene (BIAN), conducting binders, self-healing binders, solid-electrolyte interphase (SEI), silicon anodes, Li-ion batteries.

**Reference:**

1. Gupta, A.; Badam, R.; Nag, A.; Kaneko, T.; Matsumi, N., Bis-imino-acenaphthenequinone-Paraphenylene-Type Condensation Copolymer Binder for Ultralong Cyclable Lithium-Ion Rechargeable Batteries. *ACS Applied Energy Materials* **2021**, *4* (3), 2231-2240.

# Preface

This thesis is the compilation of the results obtained during the course of my doctoral research work titled “Stabilizing High-Performance Li-Ion Battery Anodes by Strategic BIAN-based Functional Polymer Binders Design for Controlled Solid-Electrolyte Interphase (SEI) Formation.” This research work was carried out under the supervision of *Prof. Noriyoshi Matsumi* at the Graduate School of Advanced Science and Technology, Japan Advanced Institute of Science and Technology during the period 2018-2021.

Electrochemical energy storage devices and conversion systems like batteries and fuel cells have emerged as potential full-scale environment friendly replacement alternatives to traditionally used non-renewable energy resources like fossil fuels. The widespread application of lithium-ion battery (LIB) technology has been remarkable. Out of many governing factors that determine the performance of LIBs, the formation of a passivation layer termed as solid-electrolyte interface (SEI) is one critical factor. The thickness, composition, and integrity of the SEI influence the performance of a battery to a large extent. Therefore, to tune the formation of an optimal SEI, a variety of polymer binders, electrolyte additives, and surface modified electrode materials, etc. have been investigated. The compounds belonging to bisiminoacenaphthene (BIAN) family have been recognized for their rich redox properties, low-lying LUMO (lowest unoccupied molecular orbitals) that can lead to their n-doping in the anodic environment, and electron rich diimine backbone for electronic conductivity. This thesis is based on the design, synthesis, and application of various BIAN-based novel composite binders to stabilize graphite and silicon anodes by tuning the formation of an effective SEI as well as providing required electronic conductivity and mechanical robustness within the electrode laminate. The thesis culminates with a concluding chapter summarizing all the studies and providing insights on future applications of BIAN-based materials in LIBs.

Agman Gupta

Graduate School of Advanced Science and Technology

Japan Advanced Institute of Science and Technology

September 2021.

# Acknowledgements

This research work has been performed under the supervision of *Prof. Noriyoshi Matsumi* at Graduate School of Advanced Science and Technology, Japan Advanced Institute of Science and Technology in the period 2018-2021. The author is thankful, grateful, and expresses deepest gratitude to his supervisor *Prof. Noriyoshi Matsumi* for his constant support, encouragement, and guidance during the course of this work.

The author also takes this opportunity to sincerely thank the members of the review committee, *Prof. Yuki Yamada*, *Assoc. Prof. Yuki Nagao*, *Prof. Toshiaki Taniike* and *Prof. Tatsuo Kaneko* for their valuable time, suggestions, and guidance during the process of thesis evaluation.

The author expresses his gratitude to *Prof. Vito DiNoto* for allowing him to work in his laboratory at the University of Padova, Italy for the completion of minor research work. The author is also thankful to *Prof. Toshiaki Taniike* for his valuable support and guidance for the minor research project.

During the course of this work at JAIST, the author is thankful to *Sr. Lecturer Rajashekar Badam* for his motivation, encouragement, suggestions, and contributions to this thesis. Also, the author is grateful to all the past and current lab members of *Matsumi laboratory* for their constant encouragement, help, cooperation, and having brainstorming scientific discussions during this work.

The author is indebted to his parents, family, and close friends for being an able support both emotionally and intellectually, providing unconditional love, and mental strength to keep working hard and serve science with great fervor.

Last but not least, the author expresses his gratitude with deep reverence and surrender to the almighty for blessing him with this wonderful opportunity in life.

Agman Gupta

Graduate School of Advanced Science and Technology

Japan Advanced Institute of Science and Technology

September 2021.

# Table of Contents

<b>Preface</b> .....	<b>I</b>
<b>Acknowledgement</b> .....	<b>II</b>
<b>Chapter 1 Introduction</b> .....	<b>1</b>
1.1 Abstract .....	1
1.2 A journey from conventional non-renewable power sources to electrochemical power sources .....	2
1.2.1 Capacitors and Supercapacitors.....	4
1.2.2 Fuel Cells (FCs).....	5
1.2.3 Batteries.....	7
1.2.3.1 Nickle Cadmium (NiCds) Batteries .....	9
1.2.3.2 Lead Acid Batteries (LABs) .....	10
1.2.3.3 Lithium-Ion Batteries (LIBs) .....	11
1.3 BIAN-based materials to stabilize LIB electrodes.....	21
1.4 Objective and Scope of the Thesis .....	25
<b>Chapter 2 BIAN-paraphenylene Type Condensation Type Copolymer Binder for Ultra-long Cyclable Lithium-Ion Rechargeable Battery</b> .....	<b>33</b>
2.1 Abstract .....	33
2.2 Introduction .....	34
2.3 Experimental Section .....	36
2.3.1 Materials .....	36
2.3.2 Synthesis.....	36
2.3.3 Characterization of the polymer .....	37
2.3.4 Electrode preparation.....	38
2.3.5 Electrochemical measurements .....	38
2.4 Results and Discussion.....	39
2.4.1 Theoretical Studies .....	39
2.4.2 Mechanical properties evaluation of BP-copolymer .....	40
2.4.3 Electrochemical characterization.....	41
2.4.4 Post-mortem characterization of anodes .....	56
2.5 Conclusion.....	63
<b>Chapter 3 Poly(BIAN)/Poly(acrylic acid) Based Self-Healing Composite Binder for High Capacity Silicon Anodes in Lithium-Ion Secondary Batteries</b> .....	<b>69</b>
3.1 Abstract .....	69
3.2 Introduction .....	70
3.3 Experimental Section .....	72
3.3.1 Materials .....	72



3.3.2 Electrode preparation.....	73
3.3.3 Characterization of electrodes .....	73
3.3.4 Coin-cell fabrication and electrochemical characterization .....	74
3.4 Results and Discussion.....	74
3.4.1 Theoretical studies.....	74
3.4.2 Pristine electrode characterization.....	76
3.4.3 Electrochemical characterization.....	80
3.4.4 Post-mortem characterization of anodes .....	92
3.5 Conclusion.....	98
<b>Chapter 4 Crosslinked Polymer BIAN Matrices to Stabilize Silicon Anode in Lithium - Ion Secondary Battery .....</b>	<b>104</b>
4.1 Abstract .....	104
4.2 Introduction .....	105
4.3 Experimental Section .....	108
4.3.1 Materials .....	108
4.3.2 Instrumentation.....	109
4.3.3 P-BIAN crosslinked polymer synthesis.....	109
4.3.4 Electrode preparation.....	113
4.3.5 Electrochemical measurements .....	114
4.4 Results and Discussion.....	114
4.4.1 Theoretical studies.....	114
4.4.2 Electrochemical characterization.....	117
4.4.3 Post-mortem characterization of anodes .....	128
4.5 Conclusion.....	130
<b>Chapter 5 General Conclusions.....</b>	<b>136</b>
5.1 Conclusions .....	136
5.2 Future Prospects .....	138
<b>Publication and Conferences .....</b>	<b>140</b>
<b>Curriculum Vitae .....</b>	<b>143</b>

# Chapter 1

## Introduction

### 1.1 Abstract

Electrochemical energy systems have become an indispensable part of our everyday life as they provide a sustainable environment friendly outlook to the future over combustible fossil fuels. This chapter briefs on the hierarchical convention of primary sources of energy, their harvesting, drawbacks, and detrimental impact on the environment along with insights on their potential sustainable alternatives. Carrying it forward, the evolutionary research and development in lithium-ion battery (LIB) technology has been detailed with focus on critical components that determine the performance of a LIB. The chapter details on the importance of solid-electrolyte interface (SEI) in the determining the battery performance by studying its composition, thickness, and integrity. Successively, importance of factors like binders and electrolyte additives that play a key role in tuning the SEI formation has been detailed. Finally, the chapter introduces BIAN-based compounds by highlighting their versatile mechanical and electrochemical properties that can help in stabilizing next generation LIBs based on high energy density electrodes by tuning the SEI as well as providing mechanical robustness.

## 1.2 A journey from conventional non-renewable power sources to electrochemical power sources

Energy has become the backbone of economic growth in the modern world. In the late 18<sup>th</sup> century, the inception and progress of rapid industrialization was majorly dependent on readily available fossil fuels like oil, natural gas, and coal as energy sources. Fossil fuels are the slow degradative conversion products of the remains of plethora of flora and fauna after undergoing the natural transformative processes within the Earth after many geological ages.

The past 300 years of global civilization has witnessed a makeshift turn around in the way man perceived life. Energy has been the primary requirement to suffice the demands of an ever-improving lifestyle of man. We leaped from being dependent on windmills and watermills to obtain energy to non-renewable fossil fuels. The significance of fossil fuels comes from their ability to get oxidized to carbon dioxide and resultant water. This burning of fossil fuels produces substantial amounts of energy that could be utilized to aid the human labor for the expansion of erstwhile small-scale businesses. Coal is one such vital fuel that was recognized centuries ago to light furnaces for the smelting of ores, burning of household stoves, and other mechanical operatives. Progressive advancements led to its developed application at thermal power stations to produce electricity at a global forum. Unquestionably, the human inquisitiveness and intellect pulled off remarkable technological strides by availing other forms of fossil fuels like natural gas, petroleum, etc. for their apt applications. Petroleum, commonly known as crude oil, can be refined into various supplementary fuels like gasoline, kerosene, diesel, petroleum jelly, etc. which have been utilized extensively from transportation needs to synthetic materials (chemicals and pharmaceuticals) to asphalt. Similarly, natural gas (non-renewable hydrocarbon) is also used for mundane but indispensable activities like cooking, manufacturing of plastic, electricity generation, etc. The easy availability of fossil fuels sparked a wildfire of technological development that has spanned for over 2 centuries now.

Unfortunately, the non-judicious utilization of these non-renewable sources of energy has triggered many alarming concerns like environment pollution, global warming, greenhouse gas emission, acid rain, deforestation, shift in season cycle affecting the topographical habitation, the worry of their exhaustion as their reserves in the nature are limited, etc. The data and analysis by the Asia/World Energy Outlook 2016 of the IEEJ estimated that the primary energy demand will increase by 1.2% per year from 13.7 billion TOE (tonne of oil equivalent) in 2014 to 18.9 billion TOE in 2040, globally. Further, they detailed the energy share

distribution of various sources of energy by 2040 with oil leading by contributing 29% of the share, followed by natural gas with 25%, coal 24%, and renewable energy sources 22%. Fossil fuels will still be the leading stake holders in energy contribution by an overwhelming 78% share by 2040<sup>1</sup>. This predictive survey and estimate raise a great concern as to how the society is going to find a balance between the ever-growing demand for development and healthy ecosystem for the survival of living species. Therefore, the need of sustainable sources of energy with affordable prices is paramount today that are ecofriendly and meet the energy requirement of the future generation. In this regard, the electrochemical energy production has emerged as one game changer alternative to make the future sustainable with stellar technological progress.

The mechanism of Electrochemical Energy Storage (EES) technologies follows the conversion and storage of electrical energy into materials and devices in a form to transform it again back to electrical energy when in need<sup>2</sup>. Figure 1 shows the deductive classification of EES technologies based on function, time of response, and storing periods<sup>2</sup>.

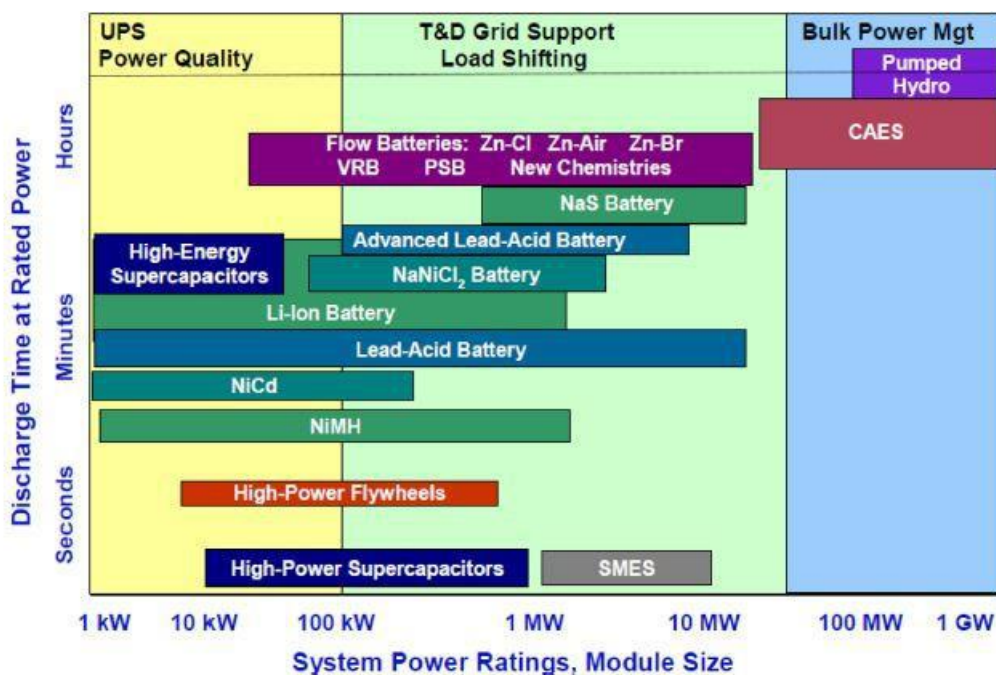


**Figure 1:** Classification of Energy Storage Technologies (EES)<sup>2</sup>

In EES technologies, the forms and modes of energy storage are of various types (Figure 2) as mentioned below:

1. Mechanical (pumped hydroelectric storage, compressed air energy storage, and flywheels)
2. Thermal (sensible heat storage and latent heat storage)

3. Thermochemical (solar fuels)
4. Chemical (hydrogen storage with fuel cells)
5. Electrochemical (conventional rechargeable batteries and flow batteries)
6. Electrical (capacitors and super capacitors)<sup>2-3</sup>

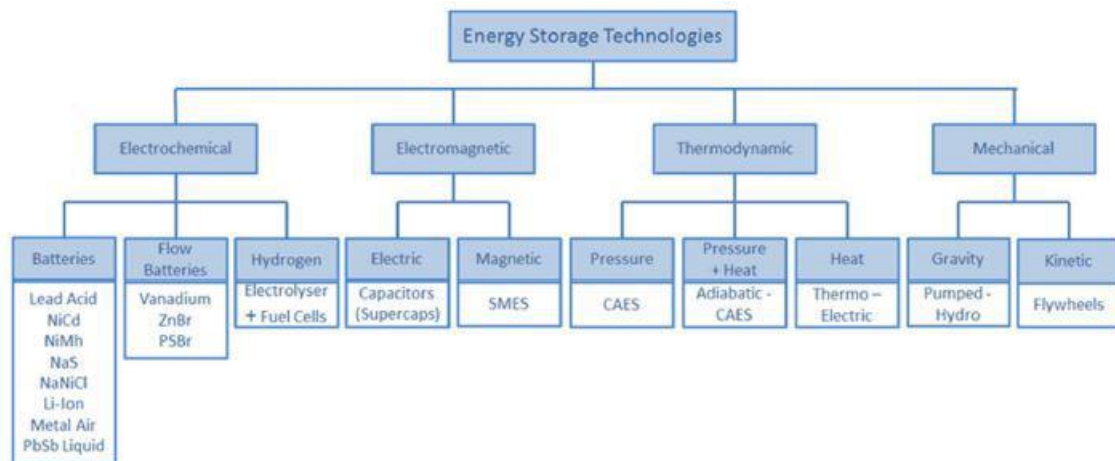


**Figure 2:** Various forms and modes of energy storage in EES devices<sup>2</sup>

Within the scope of this work, out of all the aforementioned EES technology modes, the undermentioned modes of application have been further detailed:

- (a) Capacitors and Supercapacitors
- (b) Hydrogen storage with fuel cells
- (c) Batteries

In all the three systems listed above, the energy providing mechanism is similar as it takes place at the dual phase boundary commonly known as electrode-electrolyte interface. Also, the electron transfer and ion transport pathways are well differentiated in these three systems<sup>4</sup>.

### 1.2.1 Capacitors and supercapacitors

Though supercapacitors can operate at high power rates compared to batteries, they are incapable of storing the equivalent charge in the same volume as batteries<sup>5</sup>. Therefore, the current utility of supercapacitors is limited to applications needing rapid power bursts but not high energy storage<sup>5</sup>. Additionally, they have long cycle life (can withstand millions of cycle)

based on the charge storage mechanism that is devoid of irreversible chemical reactions (storing charges in an electric double layer on the electrode surface)<sup>5-6</sup>. However, the charge storage mechanism in supercapacitors demands the operation at low potentials to avoid the electrolyte from suffering an irreversible decomposition<sup>7</sup>. The general schematic of charge storage mechanism in a general supercapacitor is shown in Figure 3.

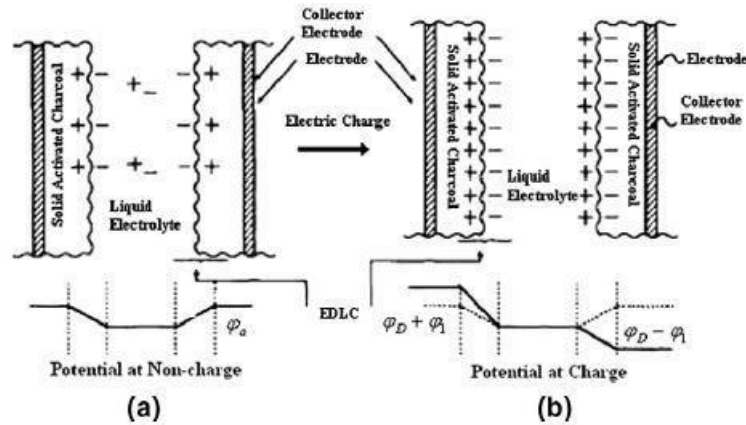


**Figure 3:** The charge storage mechanism in a general EDLC<sup>7</sup>

Based on the storage mechanism and cell configuration, electrochemical capacitors (supercapacitors/ultra-capacitors) have been categorized into three types: electric double layer capacitors (EDLCs), pseudo-capacitors (PCs), and hybrid capacitors (HCs). EDLCs store energy by separation of electric charge by the formation of electric double layer at an interface (electrode-electrolyte) upon polarization. In the EDLCs, the charge separation (few Ångstroms) and high surface areas results in their high capacitance in comparison to electrostatic capacitors. On the other hand, pseudo-capacitors exhibit the capacitor-like properties by electrochemical over physical charge storage in ECs. However, hybrid capacitors comprise of both physical and chemical charge storage processes<sup>8-9</sup>.

## 1.2.2 Fuel cells (FCs)

Fuel cells have gained popularity for their ecofriendly operating mechanism, cost-effectiveness, and good efficiency. On practical operation-based observation, fuel cells due to their static nature create low noise decibels with capability for a wide range application in power generation (portable and stationary)<sup>10-11</sup>. In a fuel cell, the energy conversion takes place by conversion of chemical energy during a reaction directly into electricity giving water and heat as byproducts. The schematic structure of a basic fuel cell is shown in Figure 4<sup>12-13</sup>.

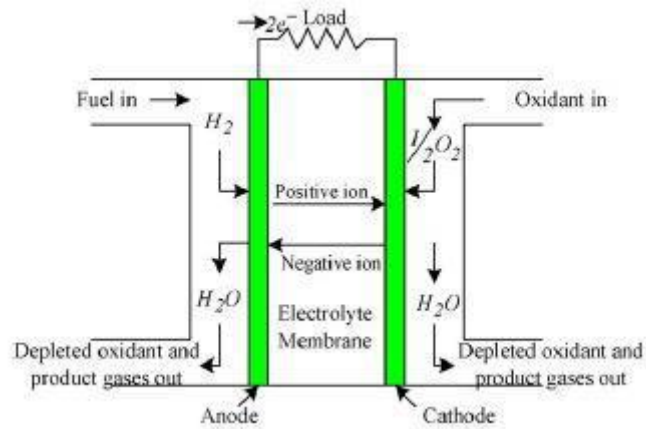


**Figure 4:** Schematic showing fuel cell operation<sup>12</sup>.

The basic engineering in a fuel cell has two electrodes separated by an electrolyte on the either side with hydrogen fuel being fed to anode and the oxidant (oxygen) of the air fed to the cathode. At the anode, the hydrogen fuel gets decomposed continuously to protons. The electrolyte membrane that acts as an intermediary is selective towards permeation of only positive ions to flow towards cathode while acting as an insulator for electrons. For the charge balance in the system, these electrons move through an external circuit to the cathode to recombine. As a result, at the cathode, the positive and negative ions recombine with oxidant to regenerate depleted oxidant (pure water)<sup>12</sup>.

Based on the choice of electrolyte and fuel, fuel cells have been available in 6 different types as listed below:

(i) Proton exchange membrane fuel cell (PEMFC):

- Direct formic acid fuel cell (DFAFC)
- Direct ethanol fuel cell (DEFC)

(ii) Alkaline fuel cell (AFC)

- Proton ceramic fuel cell (PCFC)
- Direct borohydride fuel cell (DBFC)

(iii) Phosphoric acid fuel cell (PAFC)

(iv) Molten carbonate fuel cell (MCFC)

(v) Solid oxide fuel cell (SOFC)

(vi) Direct methanol fuel cell (DMFC)<sup>12</sup>

The industry is evolving its approach towards fuel cell technology by making comprehensive attempts to understand the current drawbacks and obstacles that hinder its application in all walks of life<sup>13</sup>. Figure 5 shows the conjunctions/relations between operative principles, feature-based merits, and potential areas of application of fuel cells<sup>11</sup>.

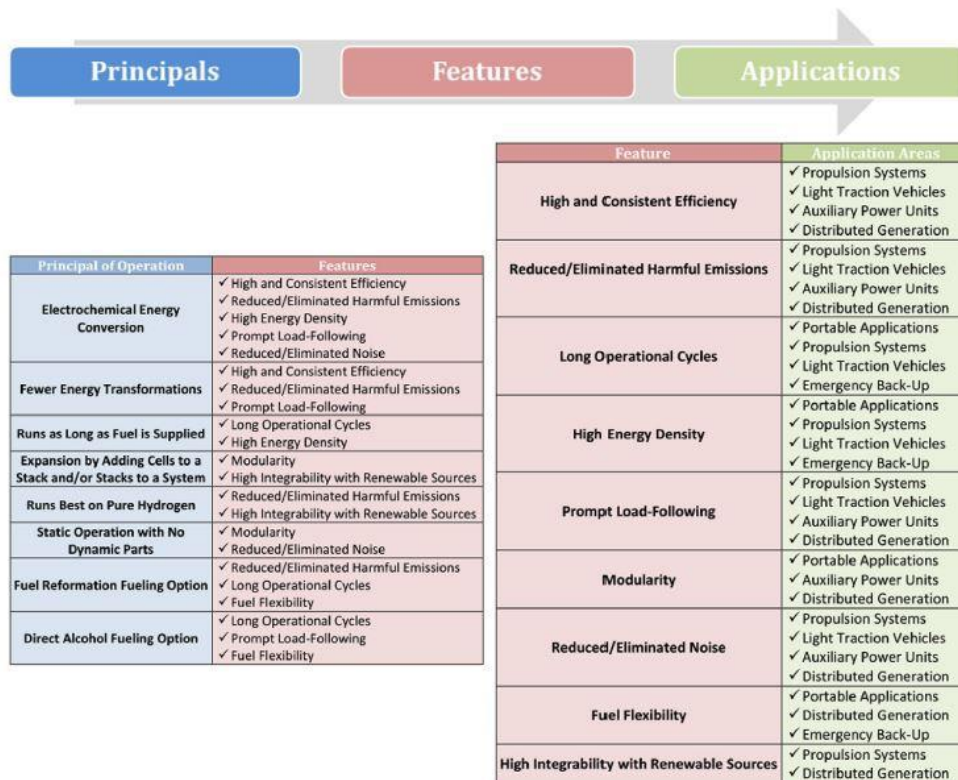
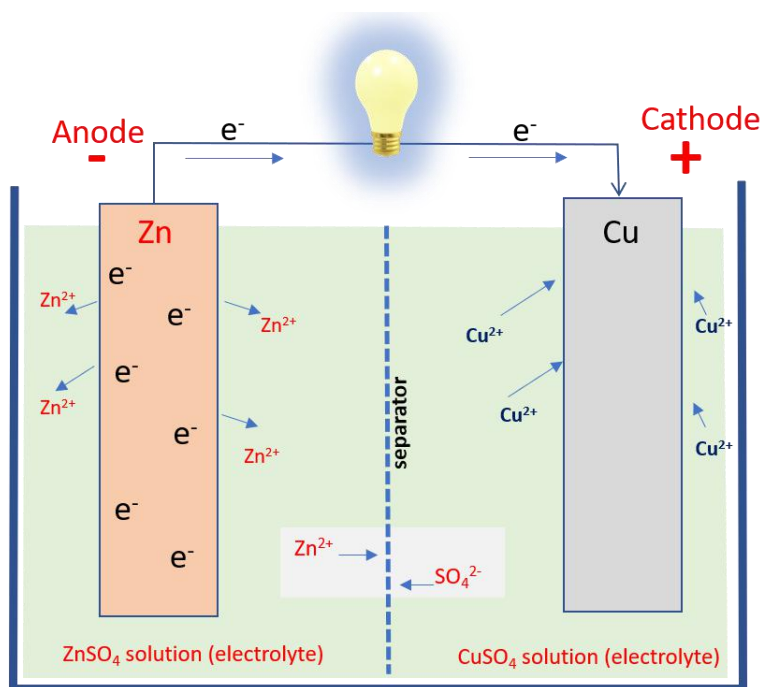


Figure 5: Principles, features, and applications of fuel cell<sup>11</sup>

### 1.2.3 Batteries

A battery is a chemical power source that is built by the external combination of one or more electrochemical cells<sup>4</sup>. There are two terminals, namely electrodes: cathode (positive) and anode (negative). The negative terminal (anode) acts as the source of electrons that flow via an external circuit to the positive terminal (cathode). When connected to a load, within a battery, a redox reaction gets triggered based on the ability of the reactants to undergo chemical transformation to form low energy products<sup>14</sup>. This chemical energy is converted to electrical energy and gets delivered to the load via an external circuit (Figure 6)<sup>4</sup>.





**Figure 6:** Schematic explaining the working principle of the battery (ionic and electronic flow)

In addition to anode and cathode, electrolyte is an important component of the battery. An electrolyte is an ion-conducting (and electron insulating) medium with another utility of being a separator between the electrodes. While the electrolyte serves as the channel for ion-conduction, the external circuit acts a pathway for electron transport. This makes a complete electrochemical circuit. Fundamentally, batteries are classified into two types: (a) Primary batteries and (b) secondary batteries (Table 1). This classification is based on their ability to be recharged. Primary batteries are non-rechargeable batteries. They are commonly known as single-use or disposable batteries because during the discharge of the battery the chemical species undergo irreversible reaction. Hence the ever-growing demand of energy cannot be sufficed by primary battery as they have limited life and no refilling scope. This led to the development of secondary batteries. Secondary batteries are termed as rechargeable batteries. In a secondary battery, the charging half-cycle dictates that the cathode gets oxidized by releasing electrons whereas the anode gets reduced by consuming the electrons and vice-versa during the discharge half-cycle. However, the electrolyte remains unaffected (neither oxidized nor reduced) during the operation other than maintaining the ions' flow. Therefore, such rechargeable batteries have the potential to undergo hundreds of charge-discharge cycles before the battery components (electrodes and electrolyte) are completely worn out. This makes them a sustainable, eco-friendly, and relatively cheaper alternative to the conventional power sources.

Few of the most famous types of secondary batteries are discussed below (Table 1):

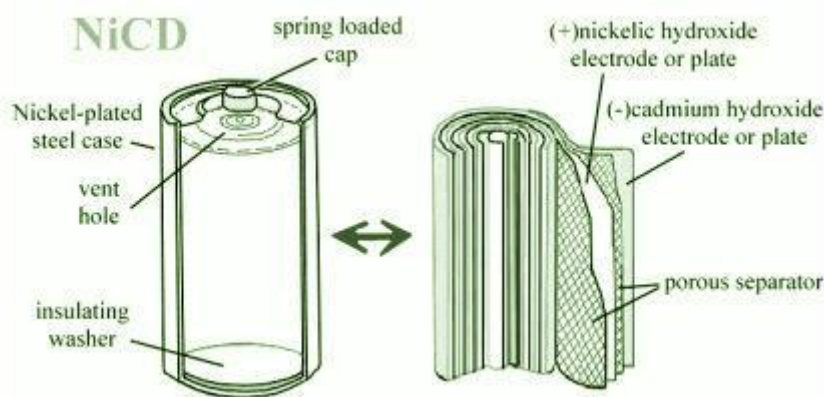
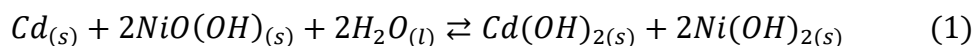
Types of Primary Batteries	Types of Secondary Batteries
<ul style="list-style-type: none"> <li>▪ Alkaline batteries</li> <li>▪ Aluminium air batteries</li> <li>▪ Bunsen batteries</li> <li>▪ Chromic acid cell</li> <li>▪ Clark cell based on Zn/Hg</li> <li>▪ Daniel cell based on Zn/Cu</li> <li>▪ Galvanic cell</li> <li>▪ Mercury battery</li> <li>▪ Grove cell</li> <li>▪ Magnesium battery</li> <li>▪ Silicon-air battery</li> <li>▪ Zinc-air battery</li> <li>▪ Zamboni cell</li> </ul>	<ul style="list-style-type: none"> <li>▪ Carbon battery</li> <li>▪ Lead-acid battery</li> <li>▪ Lithium-air battery</li> <li>▪ Lithium-ion battery</li> <li>▪ Lithium polymer battery</li> <li>▪ Lithium ion phosphate battery</li> <li>▪ Lithium titanate battery</li> <li>▪ Lithium-sulfur battery</li> <li>▪ Lithium ceramic battery</li> <li>▪ Nickle-cadmium battery</li> <li>▪ Nickle-hydrogen battery</li> <li>▪ Nickle-iron battery</li> <li>▪ Nickle-lihtium battery</li> <li>▪ Nickle-metal hydride battery</li> <li>▪ Nickle-Zinc battery</li> <li>▪ Magnesium ion battery</li> <li>▪ Pottasium ion battery</li> <li>▪ Sodium battery</li> <li>▪ Silver Zinc battery</li> <li>▪ Sodium-sulfur battery</li> <li>▪ Zinc-bromide battery</li> </ul>

**Table 1:** Classification of batteries (primary and secondary) with different examples (*source Wikipedia*)

**1.2.3.1 Nickle cadmium (NiCds) batteries**

The NiCd battery are best suited for operating at a constant potential and low temperature with an appreciably longer shelf life. The components of a general NiCd battery are shown in Figure 7. The regular cathode is nickle hydroxide and anode cadmium hydroxide. Aqueous KOH is used as a general electrolyte. The overall chemical reaction happening during the charge-discharge is shown in equation (1). During the charging half-cycle, at cathode, the nickle hydroxide (Ni(OH)<sub>2</sub>) gets converted to nickle oxide hydroxide (NiOOH). And at anode, the cadmium hydroxide (Cd(OH)<sub>2</sub>) gets oxidized to Cd. While discharging, Cd combines with

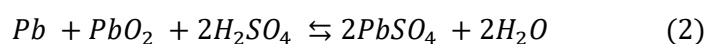
NiOOH to give Ni(OH)<sub>2</sub> and Cd(OH)<sub>2</sub>. Unfortunately, NiCd batteries are expensive as well as their energy density is not as high as other alternatives like nickel-zinc (NiZn). Also, they suffer substantial capacity loss if charged without complete discharge<sup>15</sup>.



**Figure 7:** Schematic representing the components of a NiCd battery.

### 1.2.3.2 Lead acid batteries (LABs)

The most famous secondary batteries are lead-acid batteries to have known to be invented in the 19<sup>th</sup> century. These have been widely used across the market for over a century now. Few of the applications where these are extensively used are: UPS, for storage in backup power supplies in towers, automobiles ignition, lighting, off-grid household electric power systems, and other high current burst demanding situations. Figure 8 shows the schematic with various components and working principle of a general LAB. The discharge state of a LAB has both positive and negative electrodes as lead sulfate (PbSO<sub>4</sub>) while the electrolyte is majorly water by the dissolution of sulfuric acid. Whereas, in a fully charged state, the negative electrode is lead and positive electrode is lead dioxide with electrolyte having a high concentration of aqueous sulfuric acid as shown in equation (2). The application of these secondary batteries has raised serious environment and health hazards. Lead compounds can be extremely toxic, and lack of full-scale recycling possibility is increasing the extent of lead content in landfills more with time. Therefore, “Getting the lead out” has been the slogan for many environment activists and industries which has driven the research and development to more sustainable and eco-friendly alternatives<sup>16</sup>.



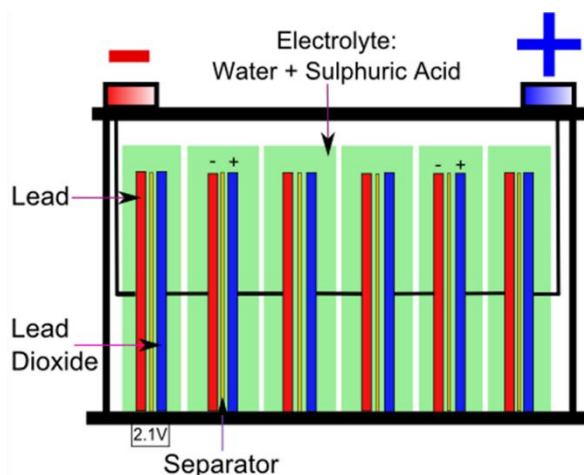


**Figure 8:** Schematic showing the components and working principle of lead-acid battery.

### 1.2.3.3 Lithium-ion batteries (LIBs)

In comparison to other secondary batteries like nickel-cadmium, lead-acid, nickel-zinc, and nickel-iron, lithium-ion batteries (LIBs) have been perceived as the most promising secondary battery alternative for electrochemical energy storage. This notion of LIBs being better alternative originates from a few facts like their low reduction potential, fast diffusion, easy host-guest compatibility of Li ions in various solid matrices, and high volumetric energy/power density<sup>17-18</sup>. A conventional LIB comprises of an anode capable of lithium intercalation/alloying like graphite/ silicon, cathode being transition metal oxides-based lithium rich materials like lithium cobalt oxide, a porous polymer separator, and lithium salt based organic electrolyte<sup>17</sup> as depicted in Figure 9.

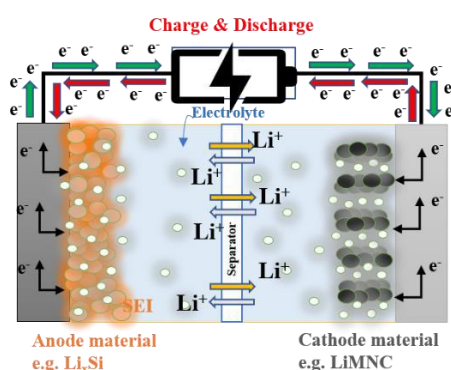


**Figure 9:** Schematic showing the components and working principle of LIB

The working mechanism of a conventional LIB is based on “intercalation” chemistry unlike other secondary batteries where the energy production takes place by the reversible dissolution and deposition of electrode components. In a LIB, during charge half-cycle, the

lithium in cathode matrices gets oxidized to  $\text{Li}^+$  and migrates via electrolyte towards the anode to get intercalated by receiving the electron transferred from cathode to anode via an external circuit. Whereas, during the discharge half-cycle, the intercalated lithium in the anode host matrices migrates back to the cathode via the electrolyte. This is a reversible phenomenon. Therefore, the intercalation and deintercalation of  $\text{Li}^+$  ions between the electrodes balanced by the flow of electrons in the external circuit provides the desirable electrical energy<sup>18</sup>. Figure 10 shows the schematic roadmap of the developments that have taken place in LIB technology till date. With remarkable efforts for over 25 years, LIBs were successfully commercialized and ever since the daily life has been dependent on energy storage devices<sup>19-20</sup>.

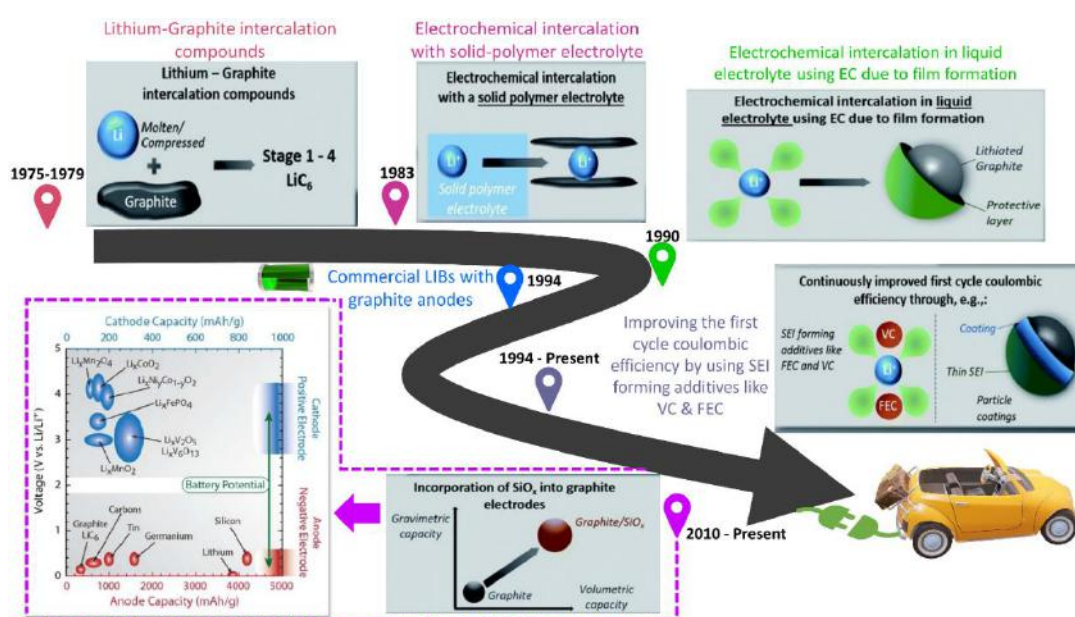


**Figure 10:** Roadmap showing the development in LIB technology in the past 3 decades and future ahead.

The comparison between other secondary batteries and LIBs based on various parameters that determine their performances has been listed in Table 2<sup>21</sup>. In terms of specific energy, internal resistance, cycle life, charging time, overcharge tolerance, cell voltage (charge and discharge cut-off), etc., LIBs have an edge over other technologies. Hence, LIB technology holds a promising future towards developing sustainable and ecofriendly energy storage devices. However, the ever-growing demand of high energy density LIBs requires active materials with higher specific capacity, low processing cost, easy availability, wide operating potential window, and good electrochemical life<sup>22</sup>. Therefore, an understanding on the types of anode and cathode materials available (both commercial and potent with the scope of commercialization in the future) is mandatory because they determine the energy/power

## CHAPTER 1

density of a LIB. The next section details the status of research and development in LIB electrodes. It highlights salient features as well as scope of future improvement of electrode materials (both cathodes and anodes).

**Table 2:** A comprehensive comparison list of various types of secondary batteries.

Specifications	Lead Acid	NiCd	NiMH	Li-ion <sup>1</sup>		
				Cobalt	Manganese	Phosphate
Specific energy (Wh/kg)	30–50	45–80	60–120	150–250	100–150	90–120
Internal resistance	Very Low	Very low	Low	Moderate	Low	Very low
Cycle life <sup>2</sup> (80% DoD)	200–300	1,000 <sup>3</sup>	300–500 <sup>3</sup>	500–1,000	500–1,000	1,000–2,000
Charge time <sup>4</sup>	8–16h	1–2h	2–4h	2–4h	1–2h	1–2h
Overcharge tolerance	High	Moderate	Low	Low. No trickle charge		
Self-discharge/month (room temp)	5%	20% <sup>5</sup>	30% <sup>5</sup>	<5% Protection circuit consumes 3%/month		
Cell voltage (nominal)	2V	1.2V <sup>6</sup>	1.2V <sup>6</sup>	3.6V <sup>7</sup>	3.7V <sup>7</sup>	3.2–3.3V
Charge cutoff voltage (V/cell)	2.40 Float 2.25	Full charge detection by voltage signature		4.20 typical Some go to higher V		3.60
Discharge cutoff voltage (V/cell, 1C)	1.75V	1.00V		2.50–3.00V		2.50V
Peak load current Best result	5C <sup>8</sup> 0.2C	20C 1C	5C 0.5C	2C <1C	>30C <10C	>30C <10C
Charge temperature	–20 to 50°C (–4 to 122°F)	0 to 45°C (32 to 113°F)		0 to 45°C <sup>9</sup> (32 to 113°F)		
Discharge temperature	–20 to 50°C (–4 to 122°F)	–20 to 65°C (–4 to 149°F)		–20 to 60°C (–4 to 140°F)		
Maintenance requirement	3–6 months <sup>10</sup> (topping chg.)	Full discharge every 90 days when in full use		Maintenance-free		
Safety requirements	Thermally stable	Thermally stable, fuse protection		Protection circuit mandatory <sup>11</sup>		
In use since	Late 1800s	1950	1990	1991	1996	1999
Toxicity	Very high	Very high	Low	Low		
Coulombic efficiency <sup>12</sup>	~90%	~70% slow charge ~90% fast charge		99%		
Cost	Low	Moderate		High <sup>13</sup>		

### A brief overview of anode materials in LIBs

High specific capacities, easy processibility, and wide operating potential window of active materials (electrodes) majorly determine the energy density of LIBs. This has led to

## CHAPTER 1

significant research, advancement, and funding in LIBs towards developing alternate electrode materials to the conventionally used ones. Table 3 and 4 list the typical anode and cathode materials that are being explored across the globe<sup>20</sup>.

**Table 3:** List of chosen anode materials for LIBs<sup>20</sup>

Active materials	Specific capacity mA h g <sup>-1</sup> /mA h cm <sup>-3</sup>	Potential (V vs. Li <sup>+</sup> /Li)	Advantages	Disadvantages
Graphite	372/735	0.17	Commercialization, long cycle stability High specific capacity, low working potential, high energy density	Low specific capacity, low energy density Infinite volume change, Li dendrite formation, short circuit, high reactivity, consuming electrolytes
Li	3861/2062	0		
Si	3579/2190	0.4	High specific capacity, low working potential, high energy density, low cost	Large volume change, unstable interface, low first CE
P (red)	2596/2270	0.8	High specific capacity, high energy density, low cost	Large volume change, unstable interface, low first CE
Al	993/1386	0.38		
Sn	994/1991	0.38	High specific capacity, high energy density	Large volume change, unstable interface, low first CE, high cost
Ge	1384/2179	0.4	No volume change, long cycle stability, high rate capability High specific capacity	Low specific capacity, low energy density, high working potential, high cost High working potential, high cost, low first CE, large volume change
Li <sub>4</sub> Ti <sub>5</sub> O <sub>12</sub> (LTO)	175/607	1.55		
Fe <sub>2</sub> O <sub>3</sub>	1007/2741	1.2	High specific capacity	High working potential, high cost, low first CE, large volume change
NiS	591/1571	1.3		
TiF <sub>3</sub>	767/2002	1.4		

**Table 4:** List of chosen cathode materials for LIBs<sup>20</sup>

Active materials	Specific capacity mA h g <sup>-1</sup> /mA h cm <sup>-3</sup>	Potential (V vs. Li <sup>+</sup> /Li)	Advantages	Disadvantages		
LiFePO <sub>4</sub>	170/612	3.4	Low cost, stable long cycle, commercialization	Low electronic conductivity, low specific capacity, low energy density		
LiCoO <sub>2</sub>	140/714	3.8	Long cycle, mature technology, high voltage, high energy density	High cost, low specific capacity, high toxicity, low thermal stability, irreversible phase change		
High-voltage LiCoO <sub>2</sub>	185/944	3.95				
LiNi <sub>0.8</sub> Co <sub>0.1</sub> Mn <sub>0.1</sub> O <sub>2</sub>	200/930	3.8	Super high voltage, high energy density	Low specific capacity, low thermal stability, irreversible phase change, electrolyte decomposition, poor cycle stability		
LiNi <sub>0.8</sub> Co <sub>0.15</sub> Al <sub>0.05</sub> O <sub>2</sub>	220/979	3.6				
LiNi <sub>0.5</sub> Mn <sub>1.5</sub> O <sub>4</sub> (LNMO)	147/625	4.7				
LiNiPO <sub>4</sub> (LNP)	169/657	5.1				
LiCoPO <sub>4</sub> (LCP)	167/618	4.8	High specific capacity, low cost, high energy density	Large voltage hysteresis, poor cycle stability, low reversibility, poor rate capability, material dissolution, volume change		
CuF <sub>2</sub>	528/2002	3.55				
FeF <sub>3</sub>	712/2196	2.74				
CoF <sub>2</sub>	553/2038	2.80				
NiF <sub>2</sub>	554/2040	2.96				
CuCl <sub>2</sub>	399/1115	3.17				
FeCl <sub>3</sub>	496/1172	2.83				
S	1675/1937	2.28			Abundant, low toxicity, rather low cost, high specific capacity, high energy density	Dissolution and shuttle, low working potential, low electronic conductivity, large volume change Rather poor reaction kinetics
Li <sub>2</sub> S	1166/1937	2.28				
O <sub>2</sub>	1675/2698	2.96			High specific capacity, high electronic conductivity	High cost/high toxicity, dissolution and shuttle, low working potential
Li <sub>2</sub> O <sub>2</sub>	1168/2698	2.96				
Se	679/1659	2.07				
Li <sub>2</sub> Se	578/1659	2.07				

Commonly known anode materials with their theoretical gravimetric capacities, working potential limits, and volumetric capacities as mentioned in the literature are shown in Figure 11a and b. Well known to all, out of all these anode materials, graphite (C) and lithium titanate (Li<sub>4</sub>Ti<sub>5</sub>O<sub>12</sub> : LTO) are being already used in commercial LIBs<sup>23-24</sup>. The highlighting features of graphite and LTO as anode active materials comes from their low delithiation potential (vs Li/Li<sup>+</sup>), high Li<sup>+</sup> diffusion, low cost, natural abundance, good electrical conductivity, and reasonable cycle life for commercial applications. Even now, graphite is the

commercial choice of anode-active material. Graphite is electrochemically active because it can intercalate Li ions between graphene planes with guest-host ratio of 1 Li atom for very 6C as shown in Figure 11c<sup>23</sup>. It has a theoretical capacity of 372 mAhg<sup>-1</sup>. Though it is a commercial choice in the present LIB technology, 372 mAhg<sup>-1</sup> is insufficient to increase the energy density of next generation LIBs<sup>25</sup>. Spinel LTO (Figure 11d) is one interesting material that can exhibit rapid charge-discharge with high energy density and good cyclability because of its zero-strain intercalation and good rate capability. But they lack their merit as they have low reversible capacity of 175 mAhg<sup>-1</sup><sup>25-26</sup>. Therefore, a variety of conversion-type and alloy-type materials have been explored to meet market demands (comprehensive Figure 11). High-capacity conversion-type anode active materials (including transition metal sulfides, oxides, and fluorides) have been reported to show higher theoretical capacities than the conventional graphite anode. A few reported conversion-type anode active materials are: NiS – 591 mAhg<sup>-1</sup>, TiF<sub>3</sub> – 767 mAhg<sup>-1</sup>, and Fe<sub>2</sub>O<sub>3</sub> – 1007 mAhg<sup>-1</sup>. But they suffer multiple drawbacks like large voltage hysteresis, high irreversible capacity loss, and higher working potential (1.0 – 1.8 V vs. Li/Li<sup>+</sup>)<sup>20</sup>. Therefore, as an alternate to conversion-type anode materials, alloy-type materials were explored as they have the potential to achieve higher energy densities because they possess high theoretical gravimetric capacities with low operating potentials<sup>20, 27</sup>. Figure 11a and 12b show that alloy-type anode materials generally belong to group IV (Si, Ge, Sn, Pb) or group V (P, As, Sb, Bi) or light metals like Li, Mg, and Al in the periodic table of elements<sup>20</sup>. A few interesting elements belonging to alloy-type materials are Si with working potential of 0.4 V (vs Li/Li<sup>+</sup>) and theoretical capacity - 3579 mAhg<sup>-1</sup> when fully lithiated (Li<sub>15/4</sub>Si) (Figure 11e)<sup>20, 28</sup> and Ge with working potential 0.4 V (vs Li/Li<sup>+</sup>) and theoretical capacity – 1384 mAhg<sup>-1</sup> when fully lithiated (Li<sub>15/4</sub>Ge)<sup>20</sup>. Also, some candidates like metal phosphides, tin oxide, and tin sulfide cannot be ignored as they show conversion-alloy-type behavior during lithiation. Figure 11f differentiates some of the most interesting anode active materials (graphite, LTO, MnO, and Si) based on their characteristic charge-discharge profiles. This also differentiates them based on their operating potential, voltage hysteresis, and specific capacity<sup>20</sup>.



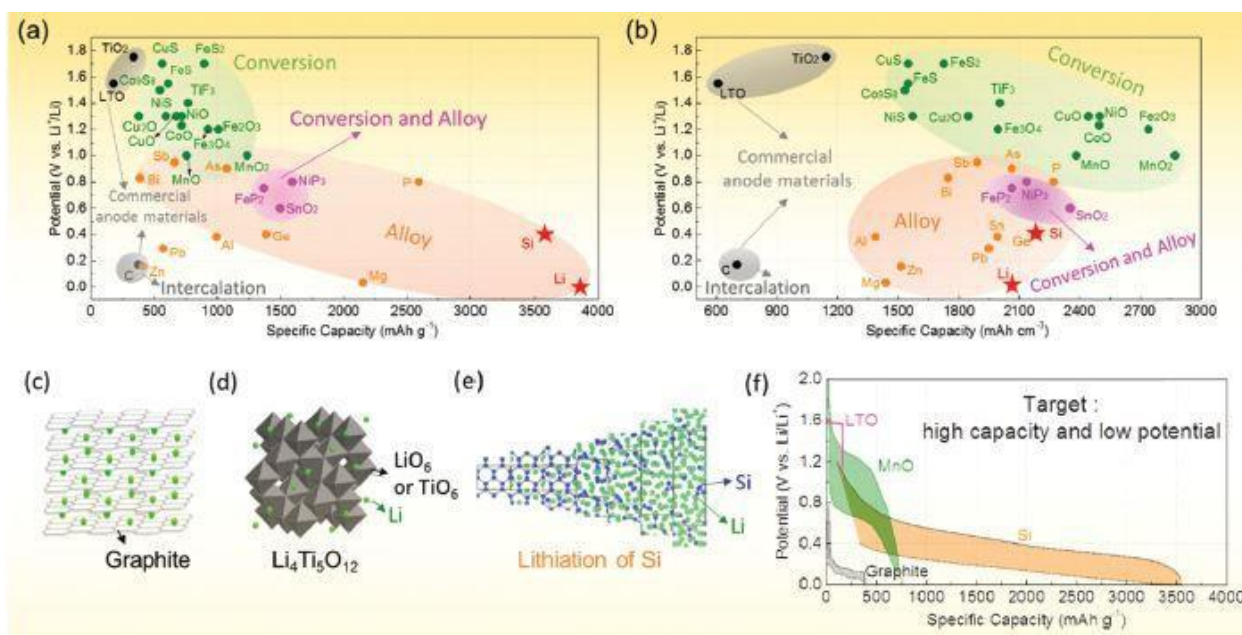


**Figure 11:** (a) & (b) Theoretical and volumetric capacities of various conversion and alloy-type materials, (c), (d), and (e) schematics of lithiated graphite, LTO, and Si. (f) de-/lithiation profiles of graphite, LTO, MnO, and Si-based anodes<sup>20</sup>.

Figure 12 shows a few classes of intercalation-type cathode materials (high-voltage and commercially used cathodes based on their specific gravimetric/volumetric capacities and operating potentials). Also, it shows the crystal structures of LiMO<sub>2</sub> (M = Ni, Co or Mn) with its lithium and manganese rich derivatives xLi<sub>2</sub>MnO<sub>2</sub>-(1-x)LiMO<sub>2</sub> (M = Ni, Co or Mn)<sup>20, 22, 29</sup>. Major drawbacks like low specific gravimetric capacities (<180 mAhg<sup>-1</sup>) and low operating potentials (<3.8 V vs Li/Li<sup>+</sup>) that are associated with commercial cathodes like lithium-iron phosphate (LiFePO<sub>4</sub>), lithium manganese oxide (LiMnO<sub>2</sub>), and lithium cobalt oxide (LiCoO<sub>2</sub>) are well known<sup>20</sup>. Therefore, to increase the energy density, tremendous efforts are being made to obtain novel cathode materials with comparatively higher theoretical capacities (>200 mAhg<sup>-1</sup> target value) and optimally high working potentials (>4.0 V vs Li/Li<sup>+</sup>)<sup>20</sup>. In latest reports, immediate solutions like nickle-rich, lithium-rich, and manganese rich layered oxides have been promising<sup>30-31</sup>. In this regard, the class of Ni-rich layered oxides (LiNi<sub>1-x</sub>M<sub>x</sub>O<sub>2</sub>, M = Co, Mn, and Al) include LiNi<sub>0.8</sub>Co<sub>0.1</sub>Mn<sub>0.1</sub>O<sub>2</sub> (NCM811, ~200 mAhg<sup>-1</sup>) and LiNi<sub>0.8</sub>Co<sub>0.15</sub>Al<sub>0.05</sub>O<sub>2</sub> (NCA, ~220 mAhg<sup>-1</sup>) show higher specific gravimetric capacities when compared with other intercalation-type materials<sup>20</sup>. Also, LiNi<sub>0.6</sub>Co<sub>0.2</sub>Mn<sub>0.2</sub>O<sub>2</sub> (NCM622, ~170 mAhg<sup>-1</sup>) and LiNi<sub>1/3</sub>Co<sub>1/3</sub>Mn<sub>1/3</sub>O<sub>2</sub> (NCM333, ~150 mAhg<sup>-1</sup>) have also attracted significant attraction. As an alternative to Ni-rich layered oxides, Li-rich layered oxides (Li<sub>1+x</sub>M<sub>1-x</sub>O<sub>2</sub> or xLi<sub>2</sub>MnO<sub>3</sub>-(1-x)LiMO<sub>2</sub>, M = Mn, Ni, Co, etc.) have the potential to provide a higher

gravimetric capacity ( $250 \text{ mAhg}^{-1}$ ) with cost effectiveness. Further, high-voltage spinel oxide  $\text{LiNi}_{0.5}\text{Mn}_{1.5}\text{O}_4$  (LNMO) comes with higher working potential  $\sim 4.7 \text{ V}$  (vs  $\text{Li/Li}^+$ ) and gravimetric capacity  $\sim 147 \text{ mAhg}^{-1}$ <sup>20</sup>.

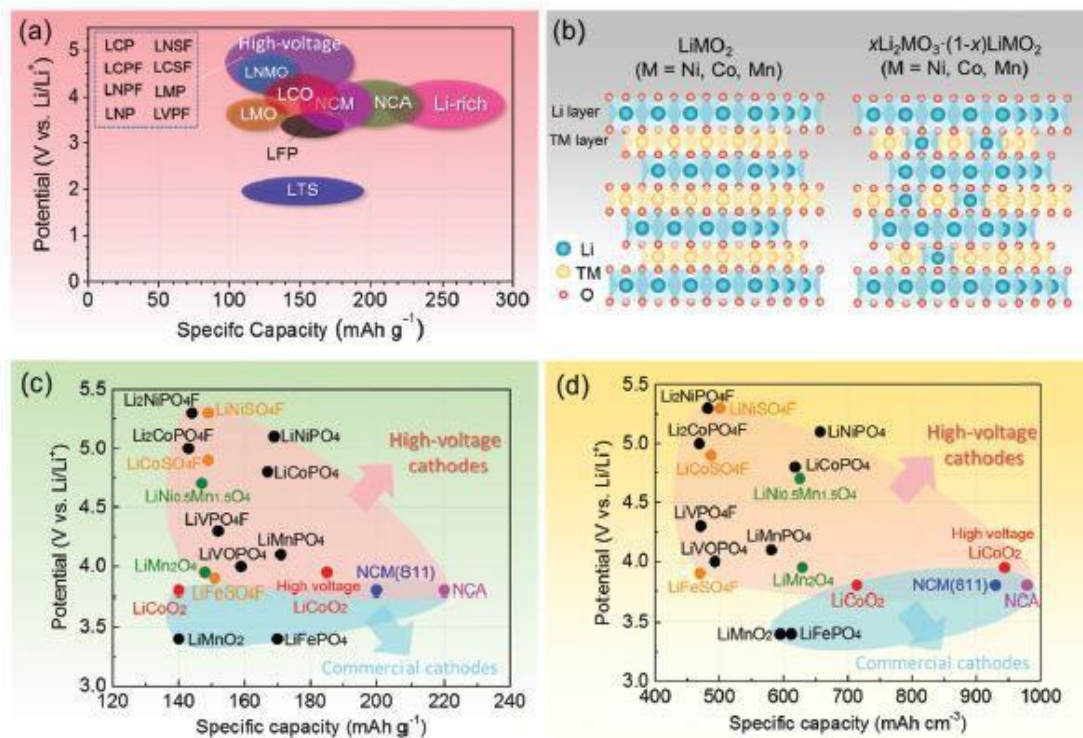


**Figure 12:** (a) comparison of high voltage cathode materials in comparison to commercially available cathodes, (b) crystal structures of  $\text{LiMO}_2$  and its lithium and manganese-rich derivative, (c) gravimetric, and (d) volumetric capacities of some chosen cathode materials<sup>20</sup>.

Till now, the discussion was based primarily on the literature reports with elaborated mention of different types commercial and under-development electrode materials (cathodes and anodes). The research and development towards exploring high-capacity anode materials and high potential cathode materials is the current trend to increase the energy/power density of LIBs. Especially, dedicated efforts are being made towards developing high-capacity anodes as they determine the derivable capacity of a LIB. In this regard, this work is focused on stabilizing high-performance anode materials - graphite and silicon to empower LIBs with higher capacity for future applications.

Some major problems associated with graphite anodes are: (a) low reversible capacity to meet the energy requirements of next generation LIBs, (b) fracture of graphitic framework over extended cycling at a high current-rate, (c) high irreversible capacity loss due to excessive electrolytic decomposition, and (d) thick SEI formation with high interfacial impedance<sup>19, 32</sup>.

Therefore, as a substitute of graphite, Si has been the primary choice for the reasons which have already been discussed earlier. However, Si suffers major drawbacks like (a) rapid volume expansion on repeated de-/alloying (~300%) which leads to their pulverization within a few cycles of charge-discharge, (b) upon pulverization, Si particles lose electrical contact with the current collector, (c) natural insulating property of Si, and (d) thick SEI formation led by repeated exposure of new Si surfaces upon pulverization. These drawbacks cause drastic capacity fade, low rate-capability, and poor cyclability of Si anodes. Figure 13 shows the schematic of problems associated with Si anodes<sup>33</sup>.

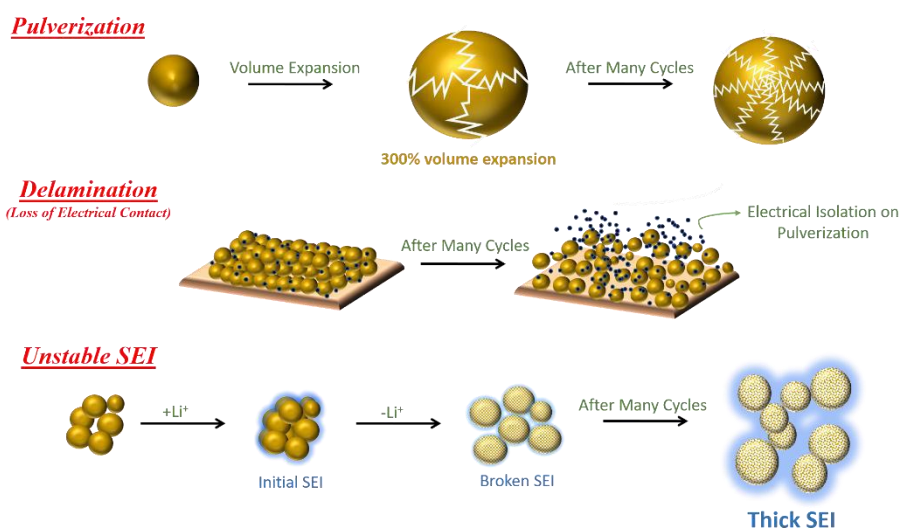


**Figure 13:** Schematic of failure mechanism of Si anodes in LIBs

Anode materials (graphite and silicon) as mentioned above have their own set of drawbacks that need to be answered to stabilize their performance. Apart from their discrete drawbacks, there is one common drawback associated with them. The common drawback is the quality of interface formed between respective electrodes: solid-electrolyte interface (SEI). The formation of SEI on these materials has mightily affected their performance as this interfacial aspect is a conjunction between active materials and electrolyte. Therefore, in this journey towards finding most apt solutions to mitigate the drawbacks with these electrode materials, the understanding of the SEI is especially important.

### Solid-electrolyte interface (SEI)

Ubiquitous terminology used for SEI well known in layman's terms is "protecting layer". It is formed on electrodes of LIBs by the decomposition of electrolytic species in the very first cycle. It determines the performance of a battery by directly/indirectly influencing

certain factors like irreversible capacity loss, cyclability, internal impedance of the battery, rate capability, Li-ion diffusion, exfoliation of graphite, pulverization of Si particles, and corrosion of transition metals-based cathode materials.

For the better performance of LIB anode materials, a comprehensive understanding of the state-of-art of the SEI's composition and morphology on anode surface is crucial. It would help to tune SEI formation that can restrict the continuous excessive decomposition of the electrolyte on the anode surface. Generally, the anode SEI layer comprises of resultant precipitates obtained from reduced decomposition of solvents, salts, lithium, ions, and impurities within the electrolyte as they are unstable in the operating potential window of the anode<sup>34-35</sup>. The formation of SEI majorly takes place in the first charge cycle which further continues to grow gradually until maturity. An ideal SEI must be electrically insulating exhibiting high lithium-ion selectivity and permeability with lowered interfacial impedance. After the complete formation of SEI at maturity, the further decomposition of electrolyte species (salts and solvents) does not occur as electrons do not transfer through the layer. Therefore, the layer pertains increased electronic resistance which in turn increases the potential on the anode. As a result, the surface potential shifts within the stability window of the chosen electrolyte. Practically, the scenario is a little different. The SEI layer gets thicker upon repeated cycling because of electron exposure to electrolyte components or seeping of bulk electrolyte to the electrode surface. In quantitative terms, this increase is not as significant as it happens during the first charge cycle decomposition. But this slow thickening consumes active Li-ions, solvent species, and dissolved salts. Hence the cell resistance increases over a period. The result of this process is capacity fade and compromised coulombic efficiency<sup>36</sup>.

Most used organic electrolyte choices in a LIB involve carbonates (ethylene carbonate, dimethyl carbonate, ethyl methyl carbonate, propylene carbonate, etc.)<sup>35, 37</sup>. Basically, these are aprotic salt solution with low molecular weight organic solvents. These carbonates have the oxidation potential at  $\sim 4.7$  V vs Li/Li<sup>+</sup> corresponding to their highest occupied molecular orbital (HOMO) and reduction potential at  $\sim 1.0$  V vs Li/Li<sup>+</sup> corresponding to lowest unoccupied molecular orbital (LUMO), respectively<sup>38</sup>. This means that they undergo reductive decomposition at the surface of anode below 1 V and oxidative decomposition at the surface of cathode above 4.7 V during the charging cycle or their storage. Figure 14<sup>36</sup> compares the electron energies of anode, electrolyte, and cathode of a thermodynamically redox pair in a battery. Here,  $\mu_A$  and  $\mu_C$  correspond to the electrochemical potentials of the anode and cathode. The stability window (shown as  $E_g$ ) of the selected electrolyte is determined by the difference

between the respective energy of the LUMO and HOMO. Therefore, deductively it means that, when  $\mu_A$  is above the LUMO energy level, the reduction of electrolyte will happen. Similarly, if  $\mu_C$  is below the HOMO energy level, the oxidation of electrolyte will happen. To enhance the energy density of the redox pair, the energy separation between the chosen set of cathode and anode must be as high as possible. Graphite anode can be considered as an example. The intercalation potential of lithium ion into the graphite framework is known to be between 0V and 0.25 V vs Li/Li<sup>+</sup>. This intercalation potential is well below the reduction potential of general carbonate-based electrolytes. This means that the potential of graphite as anode falls below the stability window of the electrolyte during lithiation. That is why it decomposes at the surface of graphite leading to SEI formation<sup>35-36</sup>.

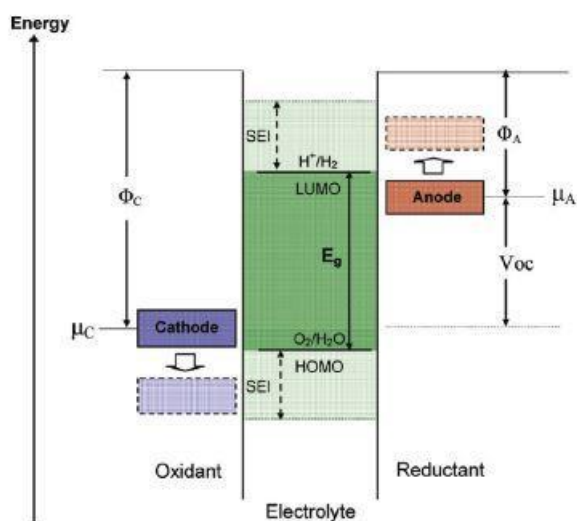


**Figure 14:** Schematic showing the energetics of the formation of anode and cathode SEI protection layer<sup>35-36</sup>

In view of the scope of this study, to stabilize LIB anodes based on graphite and silicon, the strategic design of SEI is crucial. However, the electronic energy levels of graphite and silicon are not subject to change. Therefore, the need an external interpreter with suitable electronic energy level that can help in tailoring the desired SEI to stabilize these anodes is indispensable. This external interpreter is usually categorized as an inactive component of LIBs because it cannot determine the specific capacity/energy density of LIB anodes. But its presence is valuable as it is used to patch the intrinsic drawbacks and failure mechanisms of anodes and electrode-electrolyte interface.

Broadly, these inactive components (interpreter) have been classified as: (a) Polymer binders (part of the electrode composition in a low gravimetric weight) and (b) electrolyte

additive (part of electrolyte composition in low concentration). To stabilize LIB electrodes, these inactive components are used in various proportions and concentrations based on their mechanical and electrochemical properties. Polymeric binders and electrolyte additives can directly influence the formation of SEI on the electrode surface as they are present on either side of the SEI junction (Polymer binder as a part of electrode laminate and additive within the electrolyte).

Hence, the focus of this work has been the design, synthesis, theoretical and electrochemical evaluation of novel class of polymer binders to stabilize graphite and Si anodes by providing mechanical robustness as well tailoring the SEI formation on them.

### **1.3 BIAN-based materials to stabilize LIB electrodes**

For many years now, compounds of the family bisiminoacenaphthene (BIAN) have been recognized as ligand materials for transition metals in catalysis as they have been reported to form stable complexes with almost all d-block metals<sup>39</sup>. As shown in Figure 15, their affinity to host such metal centers alongside other versatile characteristics originate from their structural importance. They possess conformational rigidity because of diimine bonds, possibility to achieve a variety of synthetic products based on R (spacer) substituents, and electron source-sink (reservoir) significance. In addition, it has been reported in the literature that naphthalene is capable to undergo reduction to form radical anions with alkali metals<sup>40</sup>. Also, the diimine framework has the potential to delocalize electron cloud through their antibonding orbitals to form stable complexes with a variety of metals<sup>41</sup>. This unique combination of naphthalene ring with diimine unit makes a 14 e<sup>-</sup>  $\pi$ -system known as Hückel system. Therefore, BIAN moiety can delocalize diimine electron lone pairs and offer intrinsic electronic conductivity.

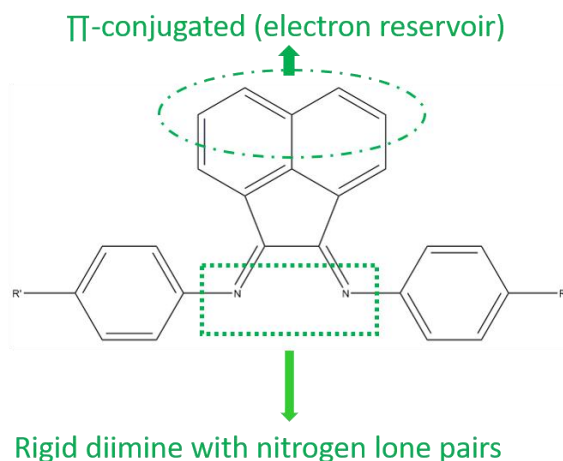


**Figure 15:** Structural significance of BIAN-based ligands

BIAN-based transition metal ligands have been notably ascribed as active redox materials that can undergo several disproportionate reactions<sup>42</sup>. To list a few BIAN-based complexes out of many available in literature, Table 5 has been generated.

**Table 5:** Structure and application of some relevant BIAN-based complexes.

	BIAN complex with titanium. Acting as redox equivalents having enhanced activity <sup>42</sup>
	The inception of coordination to main group elements by BIAN ligands <sup>43</sup>
	Reversible reduction of BIAN-based mono, di, tri, and tetra anion form by Na <sup>44</sup>
	Reversible redox active complexes of BIAN-based anion with Mg <sup>45</sup>

However, the electronic diversity that can be explored by BIAN-based complexes is not only limited to d-block metals but also spans across the periodic table to s and p block elements<sup>39</sup>. Feduskin and coworkers have reported several types of BIAN-based ligands with group 1 and group 2 elements along with their applications<sup>46</sup>. As these materials can act as electron reservoir, they react with metallic Na, Li, and Mg very spontaneously. The authors

formed Na complexes with mono, di, tri, and tetra anions of the BIAN ligand. Within five hours of observation, the tetra anion-based Na complex was isolated as it was sensitive to moisture content and air within the reaction setup. After X-ray-based structure deduction, it was concluded that two electrons are located at the diimine moiety and other two electrons at the naphthalene moiety<sup>44</sup>. This could be attributed to the low-lying LUMO in BIAN-based ligands having major contribution from diimine nitrogen atoms. Hence, they can easily interact with electron deficient species. To confirm the above-described conclusion on the electron distribution in BIAN-based ligands, similar experiments were conducted with stable complexes of BIAN with Li and Mg. And upon systematic studies and analysis by characterization techniques like UV-vis, ESR measurements, and single crystal XRD, the conclusion was same as that of Na-based BIAN complexes (2 electrons located on diimine nitrogen atoms and 2 on the naphthalene moiety)<sup>44,46</sup>. This interesting characteristic of BIAN-based complexes to undergo redox reactions led to their first successful application as reported by Armand et al<sup>47</sup>. They synthesize polymeric Schiff bases by easy condensation reactions and utilized them as redox centers to reversibly store Na<sup>+</sup> ions. A two-step reaction corresponding to two different processes between the polymer and sodium ion was established while working in the potential window 0.005 V to 1.6 V vs Na/Na<sup>+</sup> as shown in Figure 16. The most interesting aspect of the study was the tunability of redox voltage for each step by varying the type of substituents in the phenyl rings without affecting the planarity and conjugated framework. Though the capacity reported was not high, but this work created an avenue to explore such redox active compounds for energy storage applications.

Tapping on the hidden potency the BIAN-based compounds, recently, Gourang et al. reported the design, synthesis, and application of bisiminoacenaphthenequinone(BIAN)-fluorene as a functional polymer binder for graphite anode in LIBs<sup>48</sup>. They exploited the 3-fold characteristics (Figure 17) of BIAN-fluorene copolymer namely: (a) low-lying LUMO driven n-doping to tune the SEI formed on the graphite anode, (b) intrinsic electronic conductivity provided by the extended conjugation in the polymer network, and (c) stable  $\pi$ - $\pi$  interaction with graphite to administer mechanical stability. Therefore, BIAN-fluorene binder stabilized the graphite anode by not only providing the mechanical support to the graphite framework but also influence the tailoring of a desired SEI with low interfacial impedance.



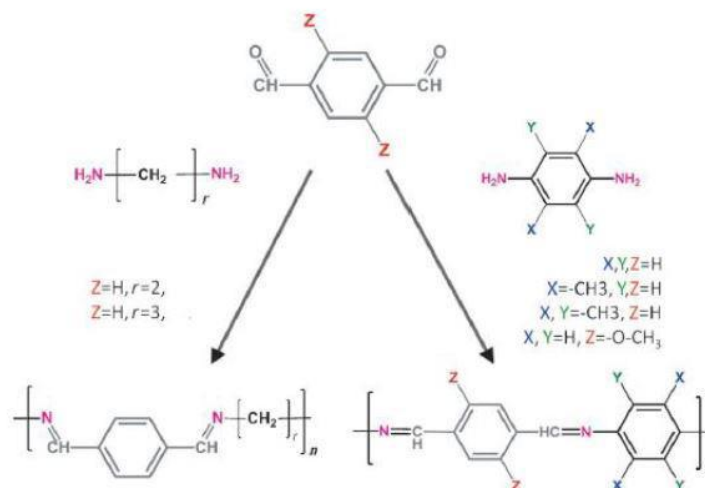


**Figure 16:** Schiff base polymer used for Na-ion storage application<sup>47</sup>

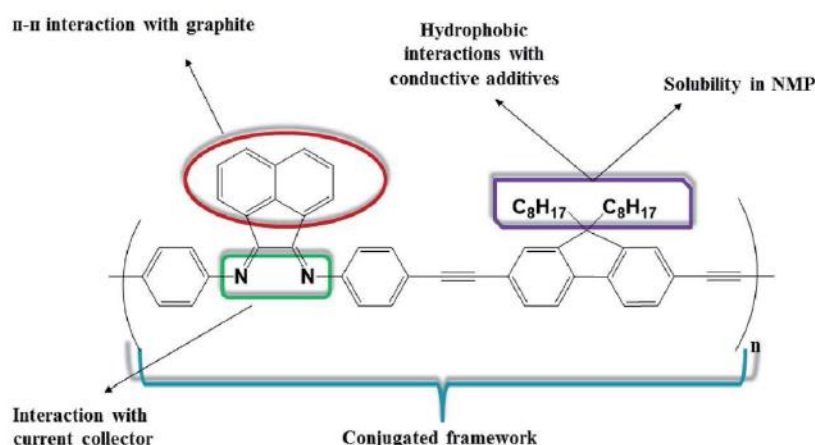


**Figure 17:** Structural and functional significance of BIAN-fluorene binder<sup>48</sup>

Further they (Gourang et al.) utilized BIAN-p-phenylene copolymer as polymeric electrocatalyst for oxygen reduction reaction (ORR) (Figure 18a)<sup>49</sup> as well as BIAN-based diamine (BIANODA) as electrolyte additive to tune the interface formed to stabilize MNC cathodes in LIBs (Figure 18b)<sup>50</sup>.

Therefore, BIAN-based materials have shown that they are potent with possibility of structural modification by the availability of suitable precursors to design novel compounds with excellent redox properties and tunable band energies for their future application in LIBs.

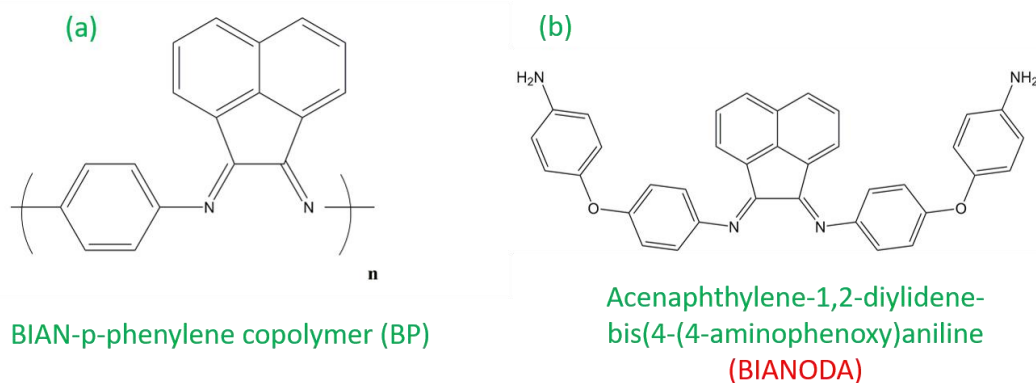


**Figure 18:** As reported by Gourang et al., (a) BP-copolymer utilized as ORR catalyst in Li-air batteries and (b) BIANODA utilized as electrolyte additive to stabilize MNC cathodes in LIBs<sup>49-50</sup>

## 1.4 Objective and Scope of the Thesis

The objective of the thesis is to explore excellent structural and chemical properties of the compounds of the family bis(imino)acenaphthenes (BIAN) to strategically design, synthesize, and utilize novel BIAN-based functional polymers as binders to stabilize high-performance anode active materials. The compounds of BIAN family possess conformational rigidity because of diimine bonds, possibility to achieve a variety of synthetic products based on spacer groups (substituents) as well as having the potential to be able to undergo crosslinking to design a plethora of composite polymer matrices via an external dopant to electron rich nitrogen atoms in the BIAN backbone, and electron source-sink (reservoir) significance. Also, the diimine framework has the potential to delocalize electron cloud through their antibonding orbitals to enrich it with extended conjugation. This unique combination of naphthalene ring with diimine unit makes a  $14 e^- \pi$ -system known as Hückel system. Therefore, BIAN moiety can delocalize diimine electron lone pairs and offer intrinsic electronic conductivity. Also, they can provide robust mechanical support, enhance the ionic conductivity, and increase electrochemical stability by virtue of their excellent redox properties. This makes the compounds belonging to BIAN family suitable to be utilized in battery chemistry because of their synergistically versatile structure-property relationship that accounts for their mechanical and electrochemical properties. In addition, their low lying lowest unoccupied molecular orbital (LUMO) makes them capable of undergoing n-doping in anodic environment thereby limiting the electrolytic reduction on the electrode surface and influencing the formation of a thin and mechanically robust SEI. Therefore, this class of compounds are a

wholesome package that can be used and engineered based on the application to achieve required stability of anode materials in LIBs. In this work, BIAN-based functional, composite, and crosslinked polymers have been utilized to stabilize graphite and silicon anodes in a progressive approach by modulating the mechanical robustness necessary as well as tuning the SEI by engineering the band gap of respective polymers. A comprehensive graphical abstract to provide an overview of the studies conducted as a part of this work is shown in Figure 19.

Chapter 2 details the ultra-long cycling performance of graphite anode in LIB by utilizing BIAN-p-phenylene (BP) copolymer as binder because graphite is a commercially used anode material and enhancing its stability further has a wide scope of immediate application. Robust mechanical properties, structural aspects, and n-doping of the binder influenced well-tuned SEI formation were instrumental in administering the cyclic stability. The BP-copolymer has outperformed the BIAN-fluorene binder reported by Gourang et al.<sup>48</sup> for reasons as follows: (i) Unlike BIAN-fluorene polymer wherein the spacer group between two BIAN moieties is the lengthy fluorene group, the BP-copolymer has a shorter phenylene group as a spacer. This increases the density of BIAN moieties in per mole of the binder used in case of BP-copolymer when compared with that in BIAN-fluorene. Therefore, the adherence of the electrode laminate on the copper current collector was improved because of the availability of more electron rich diimine nitrogen atoms in BP-copolymer in comparison to the BIAN-fluorene binder. In addition, because of higher BIAN structural density in BP-copolymer, a greater number of naphthalene moieties were available to establish  $\pi$ - $\pi$  interaction with graphite framework to administer better mechanical robustness in comparison to BIAN-fluorene binder. (ii) The synthesis of BP-copolymer follows single step procedure with acetic acid as a reaction catalyst. While the BIAN-fluorene polymer follows 3-step reaction procedure with low yield and use of expensive Pd catalyst which makes it industrially unviable for large-scale production. The BP-copolymer could stabilize graphite anode for over 1700 long cycles. Whereas the conventional graphite anode exhibits cyclic durability to a maximum of 600 cycles. As the ultra-long stability is most needed for next generation Li-ion batteries, the utilization of BP-copolymer administered ultra-long cyclic stability to graphite anode in comparison to the commercial PVDF and earlier reported BIAN-fluorene binders.

Chapter 3 elaborates the deductive approach to stabilize high-capacity silicon anodes as they are deemed to be superior alternative to graphite anodes in terms of their cost-effectiveness and higher specific capacity. The success of BP-copolymer in chapter-2 to stabilize graphite anode inspired us to strategically design a versatile conducting and self-

healing composite binder by utilizing BP-copolymer and an external dopant to its diimine framework to stabilize silicon anodes. The structural property of BP-copolymer was utilized by establishing electrostatic hydrogen bonding between poly(acrylic acid) (PAA)'s carboxyl moiety and electron rich diimine of the BP-copolymer. This design could provide required mechanical support due to its self-healing property. Also, it led to a formation of a thin SEI with reduced impedance as the LUMO of the composite polymer was further lowered due to the presence of PAA as a dopant to its diimine framework that enabled it to undergo n-doping in the anodic environment.

Chapter 4 is inspired by the success of binder design from the previous chapter (chapter 3) wherein hydrogen bonding was instrumental in providing mechanical robustness to stabilize Si anodes. However, the hydrogen bonding cannot deliver the required mechanical robustness to Si anodes for ultra-long durability. Therefore, taking a step ahead, this chapter elucidates the design, synthesis, and application of a robust covalently crosslinked poly(BIAN) matrices (via 1,6-dromohexane linker) that provided mechanical support to the Si anodes for ultra-long cycling while maintaining the electronic conductivity in the electrode laminate and also forming an interface with reduced impedance. Here, the performance of Si anodes was further enhanced by the excellent design of crosslinked poly(BIAN).

Finally, chapter 5 concludes this study by highlighting the systematic approach by which the structure-property relationship and electrochemical significance of BIAN-based novel functional polymers were studied and utilized to stabilize high-performance LIB anodes. Also, the scope of this thesis has been elaborated in this chapter wherein it has been discussed that the potential impact of BIAN-family of compounds can be even more widespread. It can not only be limited to silicon anodes in a LIB but also to other high-capacity anode materials that suffer extreme volume expansion/shrinking on repeated charge-discharge like phosphorous, boron, MoS<sub>2</sub>, etc. and to other alkali metal-ion batteries like Na and K-ion batteries. Therefore, compounds of the family can be recognized with widespread applications in various forms of future energy storage technologies.

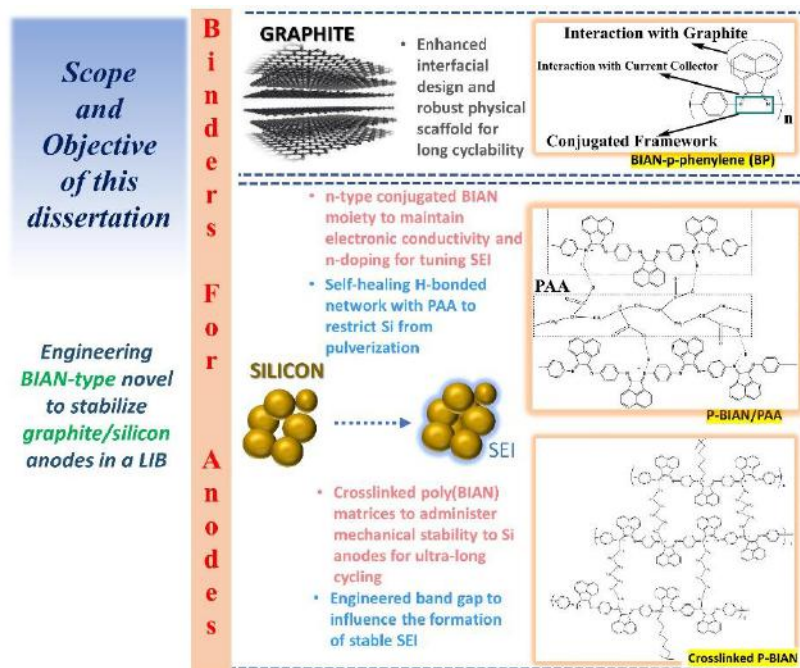


**Figure 19:** Schematic abstract of the thesis

## References

1. Koyama, K., The Role and Future of Fossil Fuel. *IEEJ* **2017**, (Special Issue)
2. Al Shaqsi, A. Z.; Sopian, K.; Al-Hinai, A., Review of energy storage services, applications, limitations, and benefits. *Energy Reports* **2020**, *6*, 288-306.
3. Luo, X.; Wang, J.; Dooner, M.; Clarke, J., Overview of current development in electrical energy storage technologies and the application potential in power system operation. *Applied Energy* **2015**, *137*, 511-536.
4. Winter, M.; Brodd, R. J., What are batteries, fuel cells, and supercapacitors? *Chemical Reviews* **2004**, *104* (10), 4245-4270.
5. González, A.; Goikolea, E.; Barrena, J. A.; Mysyk, R., Review on supercapacitors: Technologies and materials. *Renewable and Sustainable Energy Reviews* **2016**, *58*, 1189-1206.
6. Ding, J.; Hu, W.; Paek, E.; Mitlin, D., Review of hybrid ion capacitors: from aqueous to lithium to sodium. *Chemical Reviews* **2018**, *118* (14), 6457-6498.
7. Sharma, P.; Bhatti, T. S., A review on electrochemical double-layer capacitors. *Energy Conversion and Management* **2010**, *51* (12), 2901-2912.
8. Abbas, Q.; Mirzaeian, M.; Hunt, M. R. C.; Hall, P.; Raza, R., Current state and future prospects for electrochemical energy storage and conversion systems. *Energies* **2020**, *13* (21).

9. Panda, P. K.; Grigoriev, A.; Mishra, Y. K.; Ahuja, R., Progress in supercapacitors: roles of two dimensional nanotubular materials. *Nanoscale Advances* **2020**, 2 (1), 70-108.
10. Staffell, I.; Scamman, D.; Velazquez Abad, A.; Balcombe, P.; Dodds, P. E.; Ekins, P.; Shah, N.; Ward, K. R., The role of hydrogen and fuel cells in the global energy system. *Energy & Environmental Science* **2019**, 12 (2), 463-491.
11. Sharaf, O. Z.; Orhan, M. F., An overview of fuel cell technology: Fundamentals and applications. *Renewable and Sustainable Energy Reviews* **2014**, 32, 810-853.
12. Kirubakaran, A.; Jain, S.; Nema, R. K., A review on fuel cell technologies and power electronic interface. *Renewable and Sustainable Energy Reviews* **2009**, 13 (9), 2430-2440.
13. Aki, H.; Yamamoto, S.; Kondoh, J.; Maeda, T.; Yamaguchi, H.; Murata, A.; Ishii, I., Fuel cells and energy networks of electricity, heat, and hydrogen in residential areas. *International Journal of Hydrogen Energy* **2006**, 31 (8), 967-980.
14. Whittingham, M. S., History, evolution, and future status of energy storage. *Proceedings of the IEEE* **2012**, 100 (Special Centennial Issue), 1518-1534.
15. Omar, N.; Firouz, Y.; Monem, M. A.; Samba, A.; Gualous, H.; Coosemans, T.; Van den Bossche, P.; Van Mierlo, J., Analysis of nickel-based battery technologies for hybrid and electric vehicles. In *Reference Module in Chemistry, Molecular Sciences and Chemical Engineering*, Elsevier: 2014.
16. May, G. J.; Davidson, A.; Monahov, B., Lead batteries for utility energy storage: A review. *Journal of Energy Storage* **2018**, 15, 145-157.
17. Kim, T.; Song, W.; Son, D.-Y.; Ono, L. K.; Qi, Y., Lithium-ion batteries: outlook on present, future, and hybridized technologies. *Journal of Materials Chemistry A* **2019**, 7 (7), 2942-2964.
18. Nitta, N.; Wu, F.; Lee, J. T.; Yushin, G., Li-ion battery materials: present and future. *Materials Today* **2015**, 18 (5), 252-264.
19. Asenbauer, J.; Eisenmann, T.; Kuenzel, M.; Kazzazi, A.; Chen, Z.; Bresser, D., The success story of graphite as a lithium-ion anode material – fundamentals, remaining challenges, and recent developments including silicon (oxide) composites. *Sustainable Energy & Fuels* **2020**, 4 (11), 5387-5416.
20. Wu, F.; Maier, J.; Yu, Y., Guidelines and trends for next-generation rechargeable lithium and lithium-ion batteries. *Chemical Society Reviews* **2020**, 49 (5), 1569-1614.
21. Secondary (rechargeable) batteries – Battery university  
[http://batteryuniversity.com/learn/article/secondary\\_batteries](http://batteryuniversity.com/learn/article/secondary_batteries) (accessed Apr 11, 2018)

22. Tarascon, J. M.; Armand, M., Issues and challenges facing rechargeable lithium batteries. *Nature* **2001**, *414* (6861), 359-367.
23. Yamada, Y.; Usui, K.; Chiang, C. H.; Kikuchi, K.; Furukawa, K.; Yamada, A., General observation of lithium intercalation into graphite in ethylene-carbonate-free superconcentrated electrolytes. *ACS Applied Materials & Interfaces* **2014**, *6* (14), 10892-10899.
24. Teshima, K.; Inagaki, H.; Tanaka, S.; Yubuta, K.; Hozumi, M.; Kohama, K.; Shishido, T.; Oishi, S., Growth of well-developed  $\text{Li}_4\text{Ti}_5\text{O}_{12}$  crystals by the cooling of a sodium chloride flux. *Crystal Growth & Design* **2011**, *11* (10), 4401-4405.
25. Wu, F.; Borodin, O.; Yushin, G., In situ surface protection for enhancing stability and performance of conversion-type cathodes. *MRS Energy & Sustainability* **2017**, *4*, E9.
26. Scharner, S.; Weppner, W.; Schmid-Beurmann, P., Evidence of two-phase formation upon lithium insertion into the  $\text{Li}_{1.33}\text{Ti}_{1.67}\text{O}_4$  spinel. *Journal of The Electrochemical Society* **1999**, *146* (3), 857-861.
27. Nitta, N.; Yushin, G., High-capacity anode materials for lithium-ion batteries: choice of elements and structures for active particles. *Particle & Particle Systems Characterization* **2014**, *31* (3), 317-336.
28. Chan, M. K. Y.; Wolverton, C.; Greeley, J. P., First principles simulations of the electrochemical lithiation and delithiation of faceted crystalline silicon. *Journal of the American Chemical Society* **2012**, *134* (35), 14362-14374.
29. Choi, J. W.; Aurbach, D., Promise and reality of post-lithium-ion batteries with high energy densities. *Nature Reviews Materials* **2016**, *1* (4), 16013.
30. Rossen, E.; Jones, C. D. W.; Dahn, J. R., Structure and electrochemistry of  $\text{Li}_x\text{Mn}_y\text{Ni}_{1-y}\text{O}_2$ . *Solid State Ionics* **1992**, *57* (3), 311-318.
31. Rossouw, M. H.; Liles, D. C.; Thackeray, M. M., Synthesis and structural characterization of a novel layered lithium manganese oxide,  $\text{Li}_{0.36}\text{Mn}_{0.91}\text{O}_2$ , and its lithiated derivative,  $\text{Li}_{1.09}\text{Mn}_{0.91}\text{O}_2$ . *Journal of Solid State Chemistry* **1993**, *104* (2), 464-466.
32. Qi, W.; Shapter, J. G.; Wu, Q.; Yin, T.; Gao, G.; Cui, D., Nanostructured anode materials for lithium-ion batteries: principle, recent progress and future perspectives. *Journal of Materials Chemistry A* **2017**, *5* (37), 19521-19540.
33. Su, X.; Wu, Q.; Li, J.; Xiao, X.; Lott, A.; Lu, W.; Sheldon, B. W.; Wu, J., Silicon-based nanomaterials for lithium-ion batteries: A Review. *Advanced Energy Materials* **2014**, *4* (1), 1300882.

34. Goodenough, J. B.; Park, K.-S., The Li-Ion Rechargeable Battery: A Perspective. *Journal of the American Chemical Society* **2013**, *135* (4), 1167-1176.
35. Goodenough, J. B.; Kim, Y., Challenges for rechargeable Li batteries. *Chemistry of Materials* **2010**, *22* (3), 587-603.
36. An, S. J.; Li, J.; Daniel, C.; Mohanty, D.; Nagpure, S.; Wood, D. L., The state of understanding of the lithium-ion-battery graphite solid electrolyte interphase (SEI) and its relationship to formation cycling. *Carbon* **2016**, *105*, 52-76.
37. Wohlfahrt-Mehrens, M.; Vogler, C.; Garche, J., Aging mechanisms of lithium cathode materials. *J Power Sources* **2004**, *127* (1), 58-64.
38. Wood, D. L.; Li, J.; Daniel, C., Prospects for reducing the processing cost of lithium ion batteries. *J Power Sources* **2015**, *275*, 234-242.
39. Hill, N. J.; Vargas-Baca, I.; Cowley, A. H., Recent developments in the coordination chemistry of bis(imino)acenaphthene (BIAN) ligands with s- and p-block elements. *Dalton Transactions* **2009**, (2), 240-253.
40. Aricò, A. S.; Bruce, P.; Scrosati, B.; Tarascon, J.-M.; van Schalkwijk, W., Nanostructured materials for advanced energy conversion and storage devices. *Nature Materials* **2005**, *4* (5), 366-377.
41. Blanco Rodríguez, A. M.; Gabrielsson, A.; Motevalli, M.; Matousek, P.; Towrie, M.; Šebera, J.; Zális, S.; Vlček, A., Ligand-to-diimine/metal-to-diimine charge-transfer excited states of  $[\text{Re}(\text{NCS})(\text{CO})_3(\alpha\text{-diimine})]$  ( $\alpha\text{-diimine}$  = 2,2'-bipyridine, di-*i*Pr-N,N-1,4-diazabutadiene). A Spectroscopic and computational study. *The Journal of Physical Chemistry A* **2005**, *109* (23), 5016-5025.
42. Clark, K. M., Synthesis and reactivity of low-coordinate titanium synthons supported by a reduced redox-active ligand. *Inorganic Chemistry* **2016**, *55* (13), 6443-6448.
43. Wang, J.; Ganguly, R.; Yongxin, L.; Díaz, J.; Soo, H. S.; García, F., Synthesis and the optical and electrochemical properties of indium(III) bis(arylimino)acenaphthene complexes. *Inorganic Chemistry* **2017**, *56* (14), 7811-7820.
44. Fedushkin, I. L.; Skatova, A. A.; Chudakova, V. A.; Fukin, G. K., Four-step reduction of dpp-bian with sodium metal: crystal structures of the sodium salts of the mono-, di-, tri- and tetraanions of dpp-bian. *Angewandte Chemie International Edition* **2003**, *42* (28), 3294-3298.
45. Fedushkin, I. L.; Morozov, A. G.; Chudakova, V. A.; Fukin, G. K.; Cherkasov, V. K., Magnesium(II) complexes of the dpp-BIAN radical-anion: synthesis, molecular structure, and



catalytic activity in lactide polymerization. *European Journal of Inorganic Chemistry* **2009**, 2009 (33), 4995-5003.

46. Fedushkin, I. L.; Chudakova, V. A.; Skatova, A. A.; Fukin, G. K., Solvent-free alkali and alkaline earth metal complexes of di-imine ligands. *Heteroatom Chemistry* **2005**, 16 (7), 663-670.

47. Castillo-Martínez, E.; Carretero-González, J.; Armand, M., Polymeric schiff bases as low-voltage redox centers for sodium-ion batteries. *Angewandte Chemie International Edition* **2014**, 53 (21), 5341-5345.

48. Patnaik, S. G.; Vedarajan, R.; Matsumi, N., BIAN based functional diimine polymer binder for high performance Li ion batteries. *Journal of Materials Chemistry A* **2017**, 5 (34), 17909-17919.

49. Patnaik, S. G.; Vedarajan, R.; Matsumi, N., BIAN based electroactive polymer with defined active centers as metal-free electrocatalysts for oxygen reduction reaction (ORR) in aqueous and nonaqueous media. *ACS Applied Energy Materials* **2018**, 1 (3), 1183-1190.

50. Patnaik, S. G.; Vedarajan, R.; Matsumi, N., Rational design of a BIAN-based multi-functional additive for higher durability and performance of  $\text{LiMn}_{1/3}\text{Ni}_{1/3}\text{Co}_{1/3}\text{O}_2$  cathodes. *Molecular Systems Design & Engineering* **2019**, 4 (4), 939-950.

## Chapter 2

# BIAN-paraphenylene Type Condensation Copolymer Binder for Ultra-long Cyclable Lithium-Ion Rechargeable Battery

### 2.1 Abstract

Graphite has been the conventional lithium-ion anode for the negative electrode for the past three decades. One of the major challenges for graphite anodes is the exfoliation of graphite framework on deep cycling at a fast current-rate leading to a gradual capacity fade. In this regard, PVDF has been the conventional binder widely used for stabilizing the graphite framework. Unfortunately, its non-conducting nature, slow dissolution in the electrolyte, and poor adherence to the current collector limit its utility as a robust binder for LIBs with long cycle life. Here, we report an n-type conjugated copolymer, bis-imino-acenaphthenequinone(BIAN)-paraphenylene (BP) as an alternate binder material for graphite anode. The BP binder-based anodic half-cells outperformed the PVDF-based counterpart showing an excellent performance with a reversible capacity of  $260 \text{ mAhg}^{-1}$ , cyclability up to 1735 long cycles at 1C-rate, and 95% capacity retention. The superior performance of the BP binder was attributed to its ability to provide mechanical robustness to the electrode laminate, maintain the electronic conductivity within the electrode, and undergo n-doping in the anodic environment influencing the formation of a thin solid-electrolyte interface (SEI) with low interfacial impedance.

## 2.2 Introduction

Nowadays, rechargeable lithium-ion batteries with high energy density and long cyclability are in demand to suffice the flourishing energy storage requirements for their applications in hybrid and electric vehicles, portable electronic devices, and grid-scale energy storage systems<sup>1-2</sup>. Graphite has been the conventional choice as an active anode material for the commercial Li-ion battery<sup>3-4</sup>. Major drawbacks associated with graphite-based anodes are exfoliation of graphite sheets on deep cycling at a high current rate, its irregular distribution in the electrode matrix, and subdued mechanical binding ability of the conductive additive<sup>5-6</sup>. These drawbacks result in the fracture of the graphite framework over long cycling causing the capacity to fade gradually and poor adherence of the electrode laminate to the copper current collector<sup>6</sup>. To overcome these drawbacks, compatible binders that can provide good mechanical support were studied to prolong the battery life and performance<sup>7-10</sup>. Poly(vinylidene fluoride) (PVDF) has been a conventional binder for graphite anodes in LIBs by its satisfactory electrochemical, thermal, and chemical stability, reasonable adherence to the current collector, and electrolyte absorption<sup>11-13</sup>. Over the years, many drawbacks associated with PVDF binder have been reported like its dissolution in the electrolyte over long cycling, the inability of maintaining the conducting linkage between the active material and conductive additives, environmental concerns due to its fluorinated framework, and incapability to provide the required mechanical support to the active material<sup>5, 11-13</sup>. These drawbacks result in capacity fading, average cyclability, and increased cell resistance. In recent times, polymers with conjugated frameworks that can be cathodically doped (n-type) by the electrons because of their low lying lowest unoccupied molecular orbitals (LUMOs) in the reducing anodic environment have exhibited the potential as alternatives to PVDF<sup>14-19</sup>. Owing to their structural significance, conjugated polymers can 1) offer robust mechanical support to the active material and 2) adhere electrode laminate to the copper current collector. And owing to their ability to undergo n-doping, conjugated polymers can 1) facilitate the formation of a thin SEI by curbing the extent of electrolytic decomposition on the anode surface, 2) boost the electronic conductivity within the electrode laminate, and 3) enhance the lithium-ion diffusion through polymer matrices<sup>20-23</sup>. Therefore, the design, synthesis, and application of novel binder systems with these characteristics is paramount for the next-generation high energy density LIBs<sup>24</sup>.

In this regard, the compounds of the family bis(aryl)acenaphthenequinonediimine (ARBIAN) have been explored for electrochemical applications because of their affluent redox properties, availability of suitable precursors, and utility as ligands for transition metals<sup>7, 25</sup>.

Recently, our group reported bis-imino-acenaphthenequinone (BIAN)-fluorene based  $\pi$ -conjugated polymer as an alternate binder material to graphite anode which showed substantially improved discharge capacity with lowered interfacial impedance<sup>7</sup>. Also, we reported bis-imino-acenaphthenequinone (BIAN)-paraphenylene-based copolymer (BP), as an electroactive substrate for metal-free electrocatalysis for oxygen reduction reaction (ORR) in aqueous and non-aqueous media<sup>26</sup>. In this chapter, the remarkable utility of BP as a binder for graphite anode is reported and discussed. Figure 1 shows the structural highlights of the BP copolymer (design concepts). The fused-planar naphthalene moiety can establish  $\pi$ - $\pi$  stacking interaction with the graphite skeleton. The diimine component can potentially adhere to the copper current collector, hence making it viable for the binder to hold the electrode laminate on the current collector. The phenylene moiety as part of the polymeric backbone can provide the conjugated network thus ensuring efficient electronic conductivity throughout the electrode laminate.

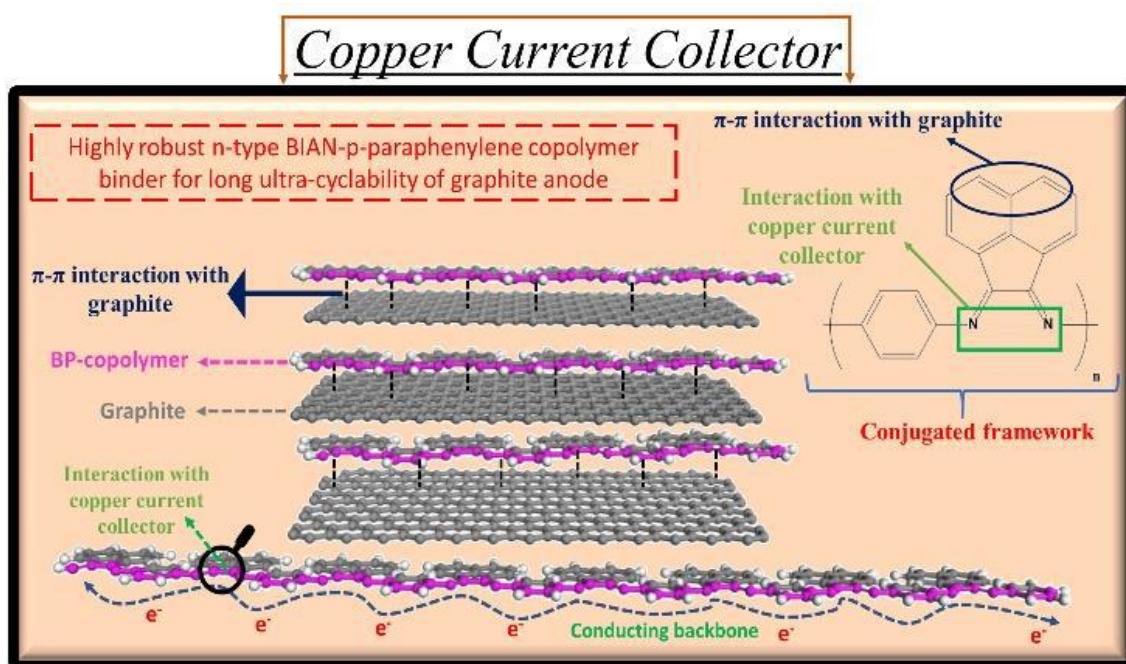


**Figure 1:** Design concepts of BP binder

## 2.3 Experimental Section

### 2.3.1 Materials

Acenaphthenequinone, 1,4-phenylenediamine, *N*-methylpyrrolidone (NMP), and acetic acid were purchased from Tokyo Chemical Industry Co., Ltd. Super dehydrated acetonitrile was purchased from Wako Pure Chemical Industries, Ltd. Poly(vinylidene fluoride) was purchased from Sigma-Aldrich. 1.0 M LiPF<sub>6</sub> (50/50) EC/DEC electrolyte was purchased from Sigma-Aldrich. Graphite superfine powder (<50 μm) was procured from Merck to be used as an active material. Battery-grade acetylene black was purchased from Denka Japan Private Co., Ltd., to be used as a conductive additive. Copper foil of a thickness of 20 μm was purchased from the Nilaco corporation. All the chemicals were used without any further purification.

### 2.3.2 Synthesis

The BIAN-p-phenylene-based copolymer was synthesized by following the procedure reported by our group<sup>26</sup>. The synthetic scheme is shown in Figure 2. The synthesized polymer was characterized by <sup>1</sup>H-NMR and FT-IR as shown in Figure 3 and 4. The chemicals (acenaphthenequinone and 1,4-phenylenediamine) have strict safety and regulations during their handling as they are hazardous and dangerous that can lead to serious eye irritation, skin irritation, allergic reactions, and to an extent carcinogenic on prolonged exposure. Therefore, adequate precautions must be taken while handling these chemicals.

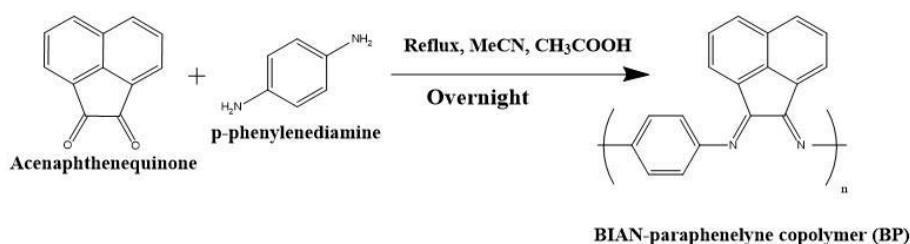


**Figure 2:** Synthetic scheme of the BP-copolymer

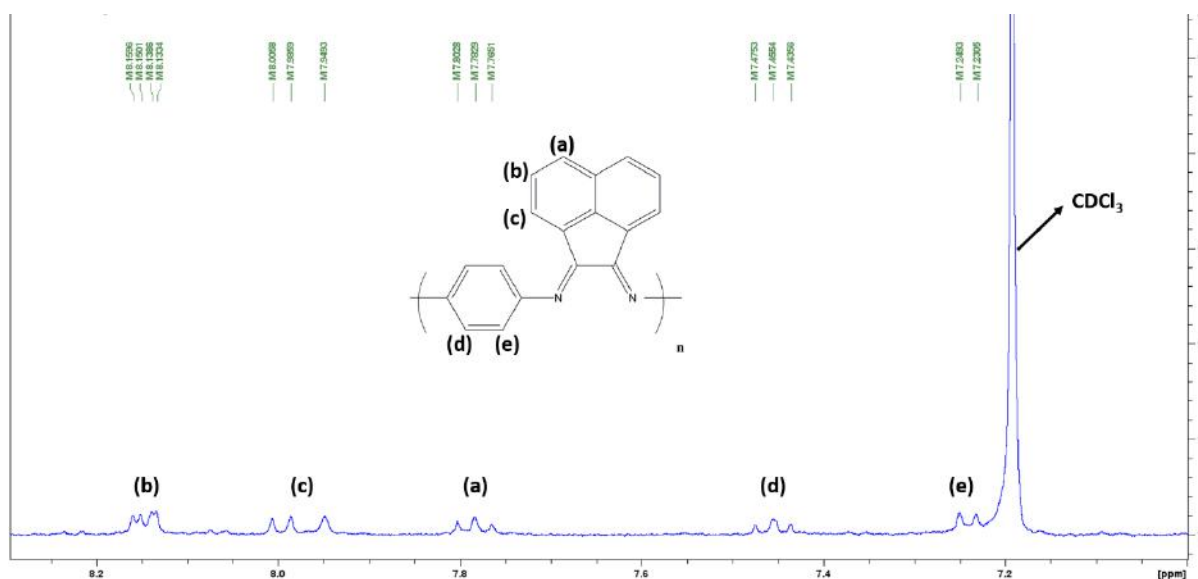


**Figure 3:**  $^1\text{H}$ -NMR spectrum of BP-copolymer

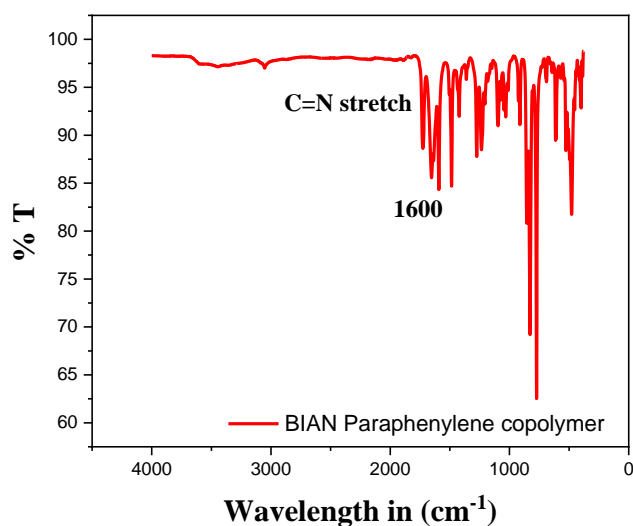


**Figure 4:** FT-IR spectrum of the BP-copolymer

### 2.3.3 Characterization of the polymer

$^1\text{H}$  NMR spectrum was recorded with Bruker Avance II 400 Mhz spectrometer. In the spectrum, the respective chemical shifts are depicted in ppm according to the protons of the deuterated solvent used as an internal standard. The FT-IR spectrum was recorded using Perkin Elmer 100 FT-IR spectrometer. The spectrum was averaged over 100 scans with a resolution of  $2\text{ cm}^{-1}$  in the ATR mode. Hitachi S-4500 FESEM instrument was used to obtain SEM images of respective anodes before and after fabrication at 1.0 kV voltage. X-ray photoelectron

spectroscopy (XPS) measurements were conducted on Fisons instruments S-probe TM 2803. Stress-strain analysis of the polymer films prepared over a 10-mm length was performed in the elongation mode with a crosshead speed of 3 mm/min at room temperature using a tensile testing machine (3365-L5, INSTRON) with a load cell (5 kN). The stress-strain curves of the five specimens were averaged to obtain the mean values for Young's moduli ( $E$ ), tensile strength ( $\sigma$ ), and elongation at break ( $\varepsilon$ ).

### 2.3.4 Electrode Preparation

For the electrode fabrication, the slurry was prepared in *N*-methylpyrrolidone (NMP) solvent with 10 wt % of BP binder, 10 wt % of acetylene black, and 80 wt % of graphite. The slurry was coated on the copper foil using the conventional doctor blade method with a coating thickness of 0.100 mm. After drying the electrode under vacuum at 80 °C for 8 hours, the electrode was calendered at 0.07 mm thickness at 80 °C. The obtained electrode was used for half-cell fabrication for electrochemical studies. The electrode with the PVDF binder was also prepared similarly for control study.

### 2.3.5 Electrochemical measurements

2025-type coin cells were fabricated configuring graphite anode, polypropylene separator (25  $\mu\text{m}$ , Celgard 2500), 1.0M  $\text{LiPF}_6$  in (50/50) EC/DEC electrolyte, and Li metal as the counter as well as the reference electrode. The fabrication of anodic half-cells was performed in an argon-filled glovebox (UNICO UN-650,  $\text{H}_2\text{O}$ , and  $\text{O}_2$  level  $<0.1$  ppm). The charge and discharge tests were carried out using a battery cycler (Electrofield-EFT-001) at 25 °C. A BioLogic VSP electrochemical workstation equipped with a frequency response analyzer (FRA) was used for electrochemical characterizations. Cyclic voltammetry (CV) for the anodic half-cells was performed between 0.01 V – 2.1 V vs  $\text{Li}/\text{Li}^+$  at 25 °C with a scan rate of 0.1  $\text{mVs}^{-1}$ . Electrochemical impedance spectroscopy (EIS) and dynamic electrochemical impedance spectroscopy (DEIS) studies were conducted within a frequency range of 10 MHz to 0.1 Hz with a sinus amplitude of 10 mV. The ionic conductivity measurements were conducted on a Solartron 1260 impedance analyzer using AC amplitude of 100 mV and the frequency range of 1MHz – 0.1 Hz within the temperature range of 30-60 °C.

## 2.4 Results and Discussion

### 2.4.1 Theoretical studies

The electrolyte decomposition on the surface of the electrode (laminate comprising of active material, conductive additive, and binder) leads to the formation of SEI. Since the binder present in the electrode laminate is always exposed to the electrolyte, the design of a suitable binder must involve the basic understanding of the energy levels of its highest occupied molecular orbital (HOMO) and lowest unoccupied molecular orbital (LUMO). Compounds with high lying HOMO are prone to undergo oxidation and those having a low lying LUMO are susceptible to reduction in the cathodic and anodic environments, respectively<sup>27-29</sup>. Therefore, for better performance, n-type conjugated binders like BP must have a low lying LUMO to undergo n-doping in the anodic environment. In this regard, the BP-copolymer was subjected to DFT calculations on Materials Studio using Dmol 3 software with optimization parameters like DND basis set, gga (pW91)-density functional, and unrestricted spin polarization by maintaining the charge neutrality. The DFT optimized structure of the BP binder is shown in Figure 5. The HOMO-LUMO energy level comparison of BP and PVDF with electrolyte components ethylene carbonate (EC) and diethyl carbonate (DEC) is shown in Figure 6. In the case of PVDF, the high lying LUMO suggested the possibility of excessive decomposition of the electrolyte on the anode surface. This will lead to a formation of a thick SEI which would restrict lithium-ion diffusion and result in high interfacial impedance. Unlike the PVDF binder, the low lying LUMO ( $E_{\text{LUMO}} = -3.17 \text{ eV}$ ) of the BP binder suggested that the n-type doping of BP in the anodic environment would prevent the decomposition of the electrolyte and lead to a thinner SEI with lower interfacial impedance.



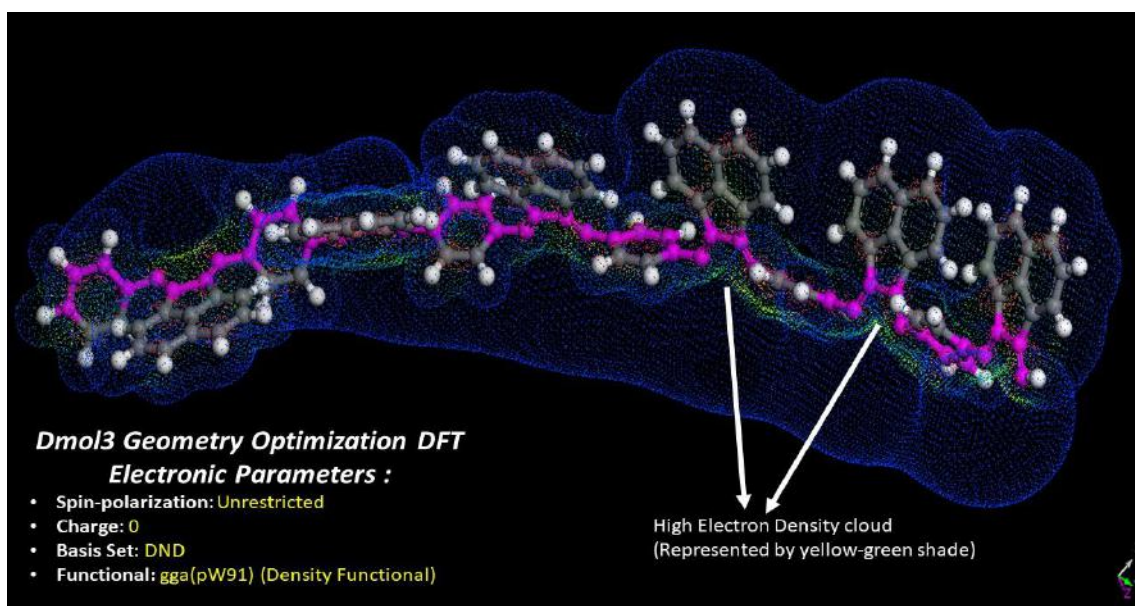


**Figure 5:** Optimized Structure of the BP-copolymer obtained after DFT calculations.

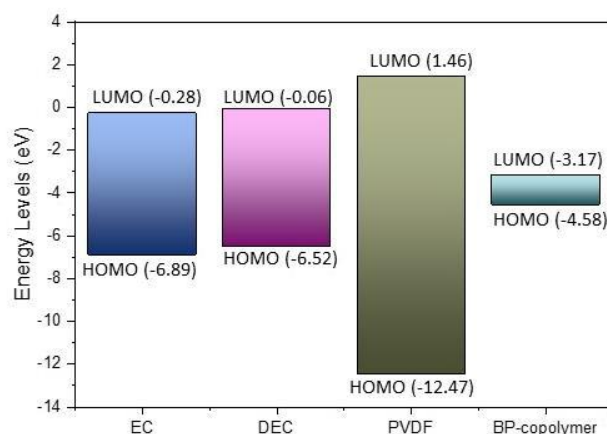


**Figure 6:** HOMO and LUMO energy levels of BP binder, PVDF, and EC/DEC based electrolyte.

## 2.4.2 Mechanical properties evaluation of BP-copolymer

The mechanical properties of a binder considerably influence the electrode's durability on cycling. Therefore, the BP-copolymer film of length 14.5 mm, width 4.3 mm, and thickness 0.11 mm was subjected to stress-strain analysis to understand its tensile strength and Young's modulus. Figure 7 shows the tensile curve of BP-copolymer film recorded at 25 °C with a draw ratio of 3 mm/min. The obtained numerical data is presented in Table 1. The BP-copolymer

showed a tensile strength of 34 MPa against the PVDF with 22 MPa, Young's modulus 1.1 GPa against the PVDF with 0.35 GPa, and 4.4% strain against the PVDF with 2.4%. Therefore, mechanically, the BP-copolymer was evaluated to be more robust than the conventional PVDF binder.

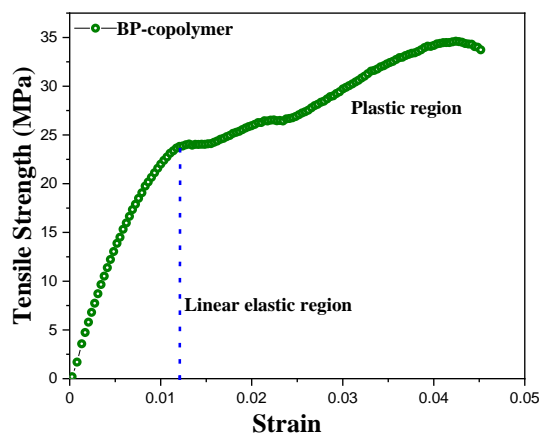


**Figure 7:** Tensile curve for BP-copolymer binder at 25 °C with a draw ratio of 3 mm/min

**Table 1:** Tensile properties of BP-copolymer and PVDF

Samples	Tensile Strength (MPa)	Young's Modulus (GPa)	Strain (%)
BP-copolymer	34 ± (1.2)	1.1 ± (0.7)	4.4 ± (0.6)
PVDF	22 ± (2.9)	0.35 ± (0.04)	2.4 ± (1.0)

### 2.4.3 Electrochemical characterization

To evaluate the performance of the BP binder against the commercial PVDF binder, two anodic half-cells were fabricated. (i) with BP binder-based anode (Graphite/acetylene black/BP-copolymer anode = 80/10/10 by wt %) and (ii) PVDF binder-based anode (Graphite/acetylene black/BP-copolymer anode = 80/10/10 by wt %). The electrode parameters are provided in Table 2.

**Table 2:** Electrode parameters for BP and PVDF-based anodes.

Parameters	BP-copolymer based anode	PVDF-based anode
Electrode Thickness	$60 \pm (0.5) \mu\text{m}$	$56 \pm (0.5) \mu\text{m}$
Total electrode loading	$2.2 \text{ mg/cm}^2$	$1.92 \text{ mg/cm}^2$
Active material loading	$1.76 \text{ mg/cm}^2$ (80 wt % graphite)	$1.53 \text{ mg/cm}^2$ (80 wt % graphite)

### Cyclic voltammetry studies

For the electrochemical characterization of BP and PVDF-based anodic half-cells, cyclic voltammetry (CV) studies were conducted. To evaluate the doping potential of the BP binder, as shown in Figure 8, the CV profile of the half-cell with a copper electrode coated with a pure BP binder was recorded. Characteristic peaks in the potential window 1.25 V-1.9 V vs Li/Li<sup>+</sup> corresponding to the BP binder doping were observed. This suggested that the binder doping would influence the SEI formation on the BP binder-based anode. Therefore, a cyclic voltammogram of BP binder-based anodic half-cell was recorded as shown in Figure 9a. The first reverse scan showed two types of characteristic reduction peaks. The first peak was observed in the potential window 1.4 V – 1.9 V vs Li/Li<sup>+</sup> corresponding to the binder doping and the second peak at about 0.65 V vs Li/Li<sup>+</sup> corresponding to regular electrolyte decomposition<sup>30-31</sup>. On the contrary, as shown in Figure 9b, PVDF being a non-conducting binder showed only one peak in the first reverse scan at about 0.65 V vs Li/Li<sup>+</sup> corresponding to the electrolyte reduction at the electrode surface<sup>30-31</sup>. Also, the deintercalation potential in the case of BP binder-based anode was found to be 0.10 V lower than the PVDF-based anode as shown in Figure 10.

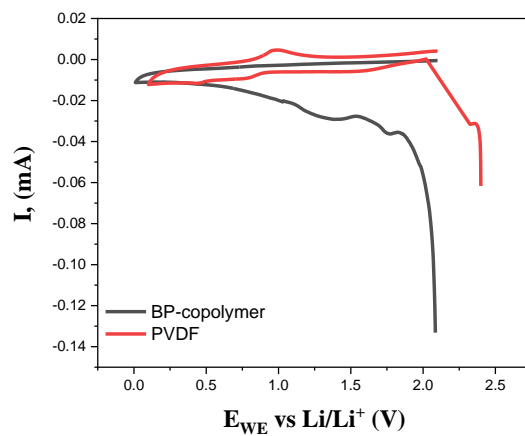


**Figure 8:** The first cycle CV of pure BP-copolymer and PVDF polymer films on the current collector with respect to lithium electrode in 1M LiPF<sub>6</sub> in (1:1) v/v EC:DEC electrolyte.

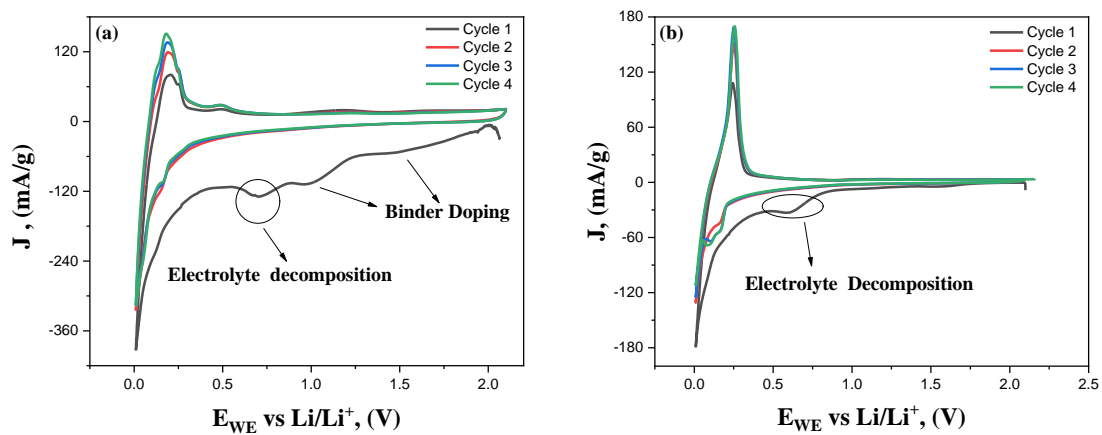


**Figure 9:** Cyclic Voltammograms of (a) BP, (b) PVDF as binders for graphite anode in 1.0M LiPF<sub>6</sub> in 1:1 EC/DEC (v/v).

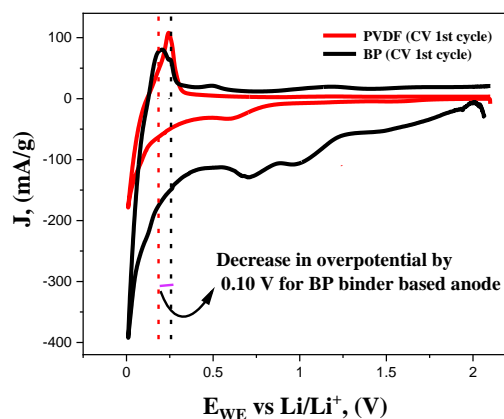


**Figure 10:** Comparison between the 1<sup>st</sup> cycle of CV profiles of BP and PVDF based binder anodes in 1.0M LiPF<sub>6</sub> in 1:1 EC/DEC (v/v).

### Electrochemical impedance spectroscopy studies

To understand the effect of doping and its influence on interfacial properties as suggested by CV studies, the anodic half-cells with respective binders were subjected to electrochemical impedance spectroscopy (EIS) measurements at OCP. The Nyquist comparison plots of anodic half-cells with respective binders are shown in Figure 11a and 11b. In BP binder-based anodic half-cell, the initial charge-transfer resistance after fabrication was higher than the cell with the PVDF binder. This could be due to the undoped state of the BP binder. But after CV studies, the interfacial impedance of the anode with BP binder was observed to be lower than that of the PVDF binder-based anode. This significant decrease in the impedance after CV studies indicate that owing to the binder doping before the reductive decomposition of the electrolyte, interface formed on the BP binder-based anode had lower impedance against the PVDF-based anode. Also, as shown in Figure 12, the conductivity calculations were carried out by recording the Nyquist spectrum of anodic half-cells having electrodes with respective binder coatings (without graphite and conductive additive). Table 3 compares the parameters illustrating the results as the conductivity of the BP binder was calculated to be one order magnitude higher ( $3.80 \times 10^{-3} \Omega^{-1} \text{ m}^{-1}$ ) than the counterpart PVDF binder ( $9.01 \times 10^{-4} \Omega^{-1} \text{ m}^{-1}$ ).

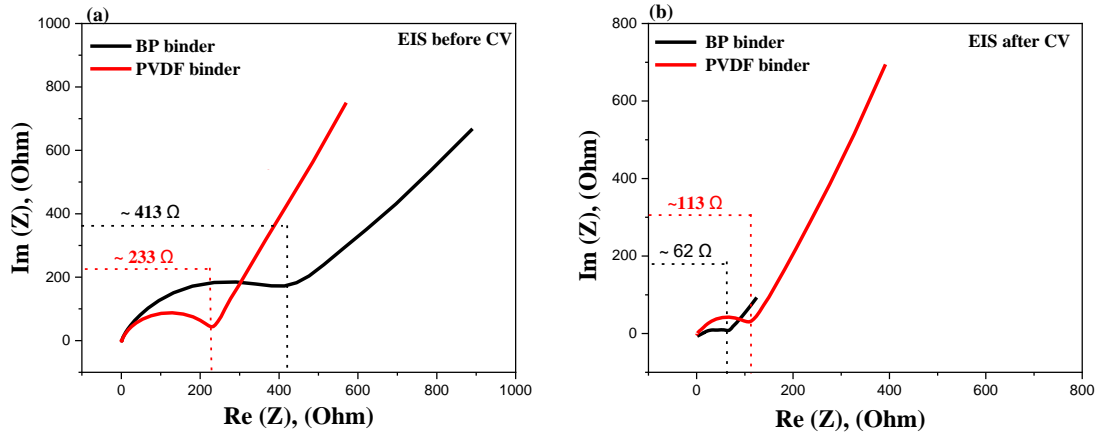


**Figure 11:** Nyquist impedance plots of anodic half-cells with BP and PVDF as binders (a) before and (b) after CV.

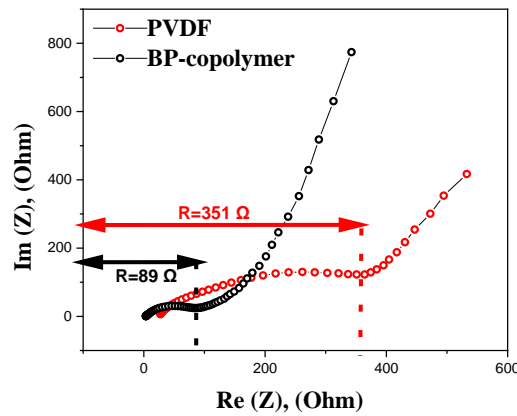


**Figure 12:** Nyquist spectra of anodic half-cells having electrodes with pure binder coating (without graphite and acetylene black)

$$R = \rho \frac{l}{A} \quad (1)$$

In equation 1, R is the resistance in ohm ( $\Omega$ ), l is the length in meter (m) of the specimen, A is the cross-sectional area ( $m^2$ ) of the specimen, and  $\rho$  the resistivity ( $\Omega m$ ). The conductivity  $\sigma$  ( $\Omega^{-1} m^{-1}$ ) of a material is the inverse of its resistivity as shown in equation 2.

$$\sigma = \frac{1}{\rho} \quad (2)$$

**Table 3:** Parameters associated with the conductivity measurement of BP and PVDF binders.

Material	Area of the electrode (A)	Thickness of the electrode (L)	Resistance	Conductivity
BP-copolymer	$1.77 \times 10^{-4} \text{ m}^2$	60 $\mu\text{m}$	89 $\Omega$	$3.80 \times 10^{-3} \Omega^{-1} \text{ m}^{-1}$
PVDF	$1.77 \times 10^{-4} \text{ m}^2$	56 $\mu\text{m}$	351 $\Omega$	$9.01 \times 10^{-4} \Omega^{-1} \text{ m}^{-1}$

### Diffusion studies and ionic conductivity measurements

To evaluate the merit of lithium-ion diffusion coefficient, cyclic voltammograms of the anodic half-cells with BP and PVDF binders were recorded with varying scan rates<sup>32-35</sup>. Usually, the diffusion coefficient is expressed by the Randles-Sevcik equation (3)<sup>33-36</sup>:

$$i_p = 0.4463F \left(\frac{F}{RT}\right)^{1/2} C v^{1/2} A D^{1/2} \quad (3)$$

where  $i_p$ ,  $F$ ,  $R$ ,  $T$ ,  $C$ ,  $v$ ,  $A$  and  $D$  are the peak current in amperes (A), the Faraday constant (96485 C mol<sup>-1</sup>), the universal gas constant (8.314 J mol<sup>-1</sup> K<sup>-1</sup>), temperature (K), the electrolyte concentration in mol cm<sup>-3</sup>, the scan rate in mV s<sup>-1</sup>, the electrode area in cm<sup>2</sup>, and the diffusion constant of in cm<sup>2</sup> s<sup>-1</sup>, respectively. Since all the electrochemical measurements were carried out at 25 °C consistently, the equation (3) can be edited as

$$\frac{i_p}{m} = 2.69 \times 10^5 C v^{1/2} A D^{1/2} \quad (4)$$

Where  $m$  is the mass of the respective electrode in g,  $C$  is the concentration of Li in LiPF<sub>6</sub> in mol cm<sup>-3</sup>,  $A$  is the electrode area per unit mass in cm<sup>2</sup> g<sup>-1</sup>, and  $D$  corresponds to the diffusion constant of Li-ion in cm<sup>2</sup> s<sup>-1</sup>. Figures 13 (a) and 13 (b) show the cyclic voltammograms of the half-cells with the respective binders in the increasing order of scan rate from 0.01 mVs<sup>-1</sup> to 1 mVs<sup>-1</sup>. To determine the lithium diffusion coefficient, normalized peak currents were plotted against the square root of scan rates ( $v^{1/2}$ ) as shown in Figure 14 (a) and 14 (b). The linear fit indicated that the peak current was proportional to the square root of the scan rate. Therefore, this confirmed that the electron transfer at the working electrode (graphite anode) was fast and the current was limited by the diffusion of the electrolyte species to the electrode surface. The lithium-ion diffusion coefficient was calculated to be 15% higher in the case of the cell with the BP binder than the PVDF. Lithium-ion diffusion coefficients for both systems were  $8.845 \times 10^{-9} \text{ cm}^2 \text{ s}^{-1}$  and  $7.519 \times 10^{-9} \text{ cm}^2 \text{ s}^{-1}$ , respectively.

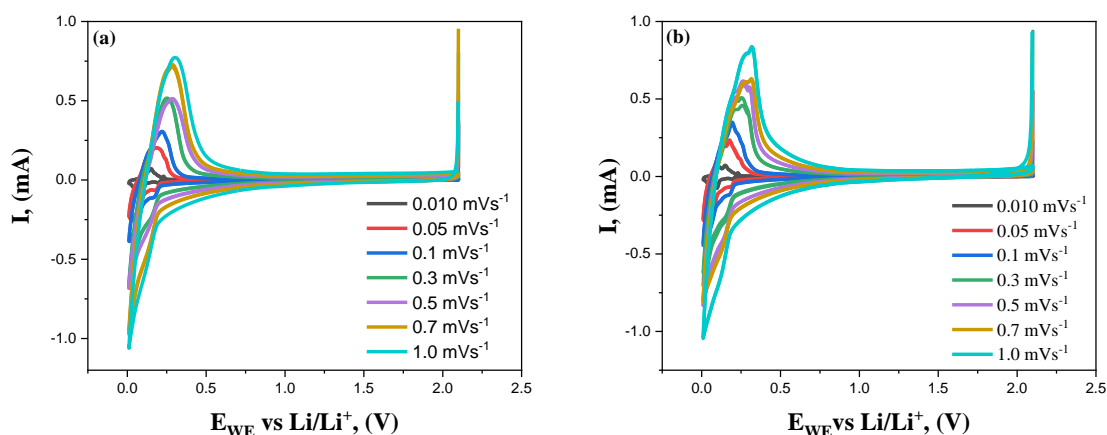


**Figure 13:** CV at varying scan rates for the graphite electrode with (a) BP-copolymer, and (b) PVDF binders in 1.0 M LiPF<sub>6</sub> in (1:1) (v/v) EC:DEC

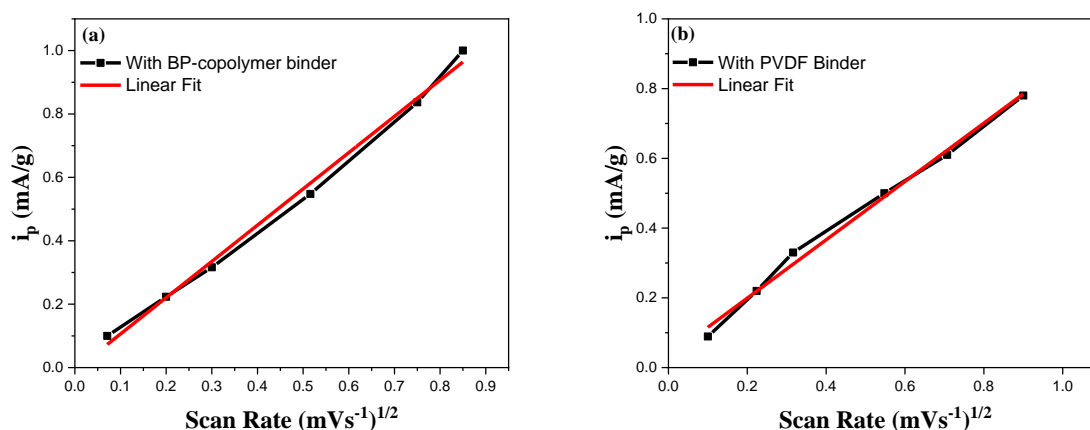


**Figure 14:** Plot of peak current vs the square root of scan rates (a) BP-copolymer, (b) PVDF

For further electrochemical evaluation of the BP binder, ionic conductivity measurements were carried out. BP-copolymer was added with LiTFSI by mixing the lithium salt into the BP binder by solubilizing in NMP solvent. Figure 15a shows the Arrhenius plot of the BP binder with LiTFSI. There was a linear increase in the ionic conductivity shown by the BP binder with increasing temperature from 30 °C – 42 °C. Under higher temperature, the plot deviated from Arrhenius behaviour towards non-Arrhenius. The maximum ionic conductivity was observed to be  $1.2 \times 10^{-5} \text{ S cm}^{-1}$  at 42 °C. The VFT (Vogel-Fulcher-Tammann) plot was also fitted following the linear regression equation (5) to obtain the carrier ion number and activation energy for ion transport, respectively<sup>37</sup>.



$$\sigma_{i(T)} = \frac{A}{\sqrt{T}} e\left(\frac{-B}{\kappa(T-T_0)}\right) \quad (5)$$

In VFT equation 3,  $\sigma_{i(T)}$  correspond to the ionic conductivity at a temperature T,  $T_0$  is ideal glass transition temperature optimized to provide linear VFT plot. A is the carrier ion number and B the activation energy for ion transport, respectively. Figure 15b shows the VFT plot of the BP-copolymer with LiTFSI. The VFT parameters, carrier ion number (A) was calculated to be  $3.06 SK^{1/2} cm^{-2}$  and activation energy (B) to be 0.89 eV.

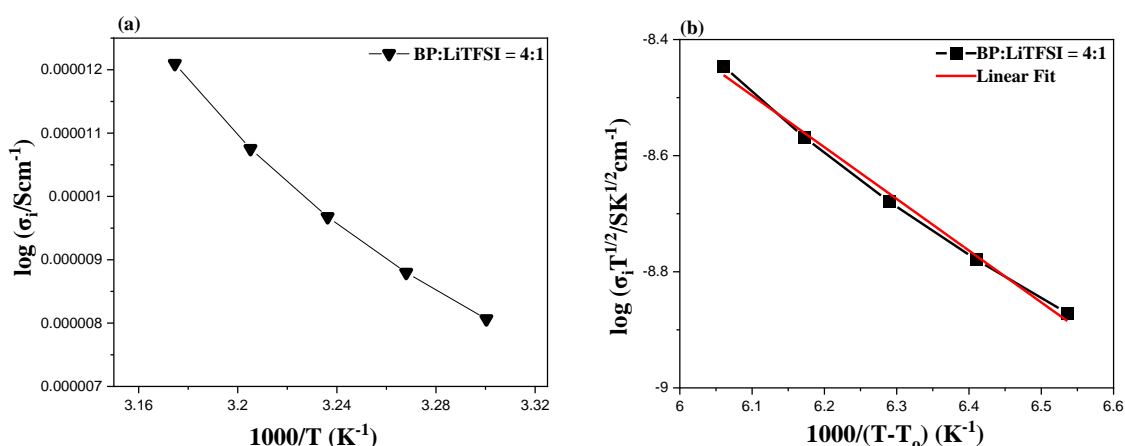


**Figure 15:** (a) Arrhenius plot of BP-copolymer with LiTFSI (Temperature dependence of the ionic conductivity) and (b) VFT plots of the BP-copolymer with LiTFSI

### Charge-discharge measurements

After theoretical and electrochemical evaluation of the fabricated anodic half-cells, charge & discharge studies were conducted to compare the cyclability and discharge capacity of the BP binder-based anode with the PVDF-based anode. Figure 16a shows the cycling profiles of the anodic half-cells with BP and PVDF binders at various current rates in the potential window 0.01 V – 2.1 V vs Li/Li<sup>+</sup>. The cell with BP binder showed substantially higher discharge capacity at all current-rates with 98% coulombic efficiency (CE) against the PVDF binder-based cell with 95%. Long cycling charge & discharge studies were conducted at 1C-rate to monitor the cyclability and specific discharge capacity of the cells with both binders. Figure 16b shows the comparison of long cycle discharge profiles between both systems in the potential window 0.01 V – 2.1 V vs Li/Li<sup>+</sup>. The BP binder based anodic half-cell was cycled for 1735 long cycles at a 1C rate with ~95% capacity retention having a maximum discharge capacity of ~260 mAhg<sup>-1</sup>. Whereas the PVDF binder-based anode was cycled for 525 cycles with reversible capacity fading to ~132 mAhg<sup>-1</sup> with a poor capacity retention of ~65% due to

its inability to provide mechanical robustness, maintain conductivity within the electrode laminate, to influence the formation of a good SEI, and slow dissolution in the electrolyte. CE is a measure of quantitative evaluation of the ratio of discharge capacity to charge capacity of a system. In the very first cycle of lithiation, reductive electrolytic decomposition takes place that leads to the SEI formation. So, to understand the extent of irreversible capacity loss due to the electrolyte decomposition, the first cycle discharge CEs of the PVDF and BP binder-based were compared. The PVDF-based anode showed an initial coulombic efficiency (ICE) of ~89% in the first cycle whereas the BP binder-based anode showed an ICE of ~86% indicating a more irreversible capacity loss. However, the coulombic efficiency (CE) for the BP binder-based anodic half-cell stabilized to ~99% within 7 cycles of charge & discharge. Contrarily, the PVDF-based anodic half-cell achieved ~97% coulombic efficiency after 27 cycles. To further understand this phenomenon, galvanostatic cycling profiles for both the systems were studied. Figure 16c shows the galvanostatic de-/lithiation profiles of anodic half-cell with PVDF binder at 1C-rate in the potential window 0.01 V – 2.1 V vs Li/Li<sup>+</sup> for the 1<sup>st</sup>, 100<sup>th</sup>, 300<sup>th</sup>, and 525<sup>th</sup> cycles, respectively. The first lithiation half-cycle showed a plateau in the potential window 1.1 V – 0.5 V attributed to the irreversible capacity loss due to the electrolytic decomposition on the surface of the anode. Figure 16d shows the galvanostatic de-/lithiation profiles of anodic half-cell with BP binder at 1C-rate in the potential window 0.01 V – 2.1 V vs Li/Li<sup>+</sup> for the 1<sup>st</sup>, 100<sup>th</sup>, 500<sup>th</sup>, 1000<sup>th</sup>, 1500<sup>th</sup>, and 1735<sup>th</sup> cycles, respectively. The plateau in the first lithiation half-cycle in the potential window 1.25 V – 0.48 V was characteristically different from that of the PVDF binder-based anode. Figure 17 compares the 1<sup>st</sup> lithiation half-cycles of the PVDF and BP binder-based anodic half-cells. The extent of overall electrolyte decomposition is almost similar for both the systems. However, as the structural composition of the BP-copolymer has naphthalene moieties as well as comprises of diimine backbone, the irreversible capacity loss due to the BP binder framework cannot be neglected. The plateau in the first lithiation half-cycle of the BP binder-based anode comprises of irreversible capacity loss due to the lithium uptake of the binder as well as the electrolyte decomposition. To determine the irreversible capacity loss in the first cycle of charge-discharge due to C=C and C=N functional groups of BP-copolymer, the galvanostatic cycling performance of the electrode with only BP binder coating (without graphite and conductive additive) was recorded as shown in Figure 18a and 18b. With a binder loading of 2.54 mg cm<sup>-2</sup>, the irreversible first cycle lithiation of BP-copolymer coated electrode was ~20 mAhg<sup>-1</sup>. This suggested that extent of electrolyte decomposition because of the presence of BP binder was significantly lowered. The interface

formed on the anode with the BP binder influenced by the cathodic doping (n-type) of the BP-copolymer as well as the lithium-ion insertion into its C=N and C=C framework led to better cyclic stability, coulombic efficiency, and reversible capacity than the PVDF counterpart.

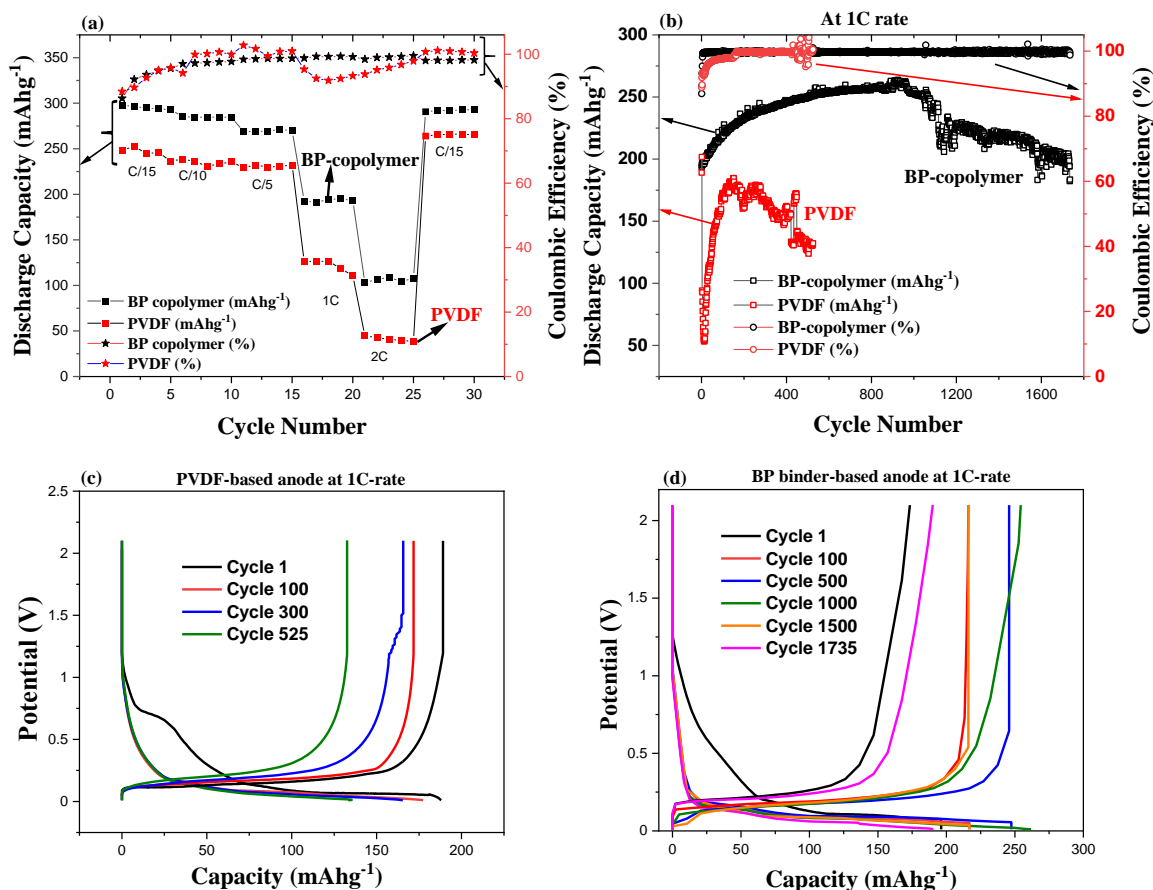


**Figure 16:** (a) Charge and discharge comparison profiles between BP and PVDF binder-based anodic half-cells at varying current rates, (b) Long cycling performance of the anodic half-cells with respective binders with 1.0 M LiPF<sub>6</sub> in (1:1) (v/v) EC:DEC electrolyte at 1C rate in the potential window 2.1 V – 0.01 V vs Li/Li<sup>+</sup>, (c) Galvanostatic de-/lithiation profiles of the PVDF-based anodic half-cell at 1C-rate, and (d) Galvanostatic de-/lithiation profiles of the BP binder-based anodic half-cell at 1C-rate.

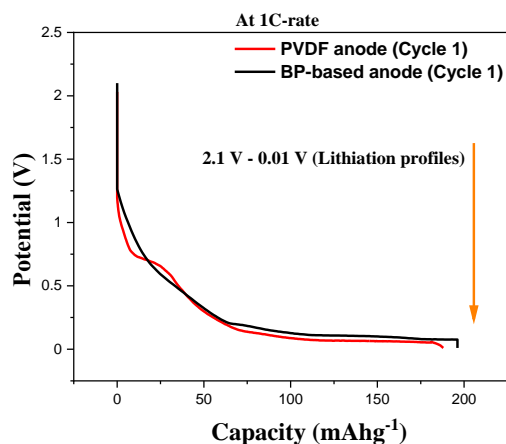


**Figure 17:** Comparison between the 1<sup>st</sup> galvanostatic lithiation cycles of PVDF and BP binder-based anodic half-cells in the potential window 0.01 V – 2.1 V vs Li/Li<sup>+</sup>

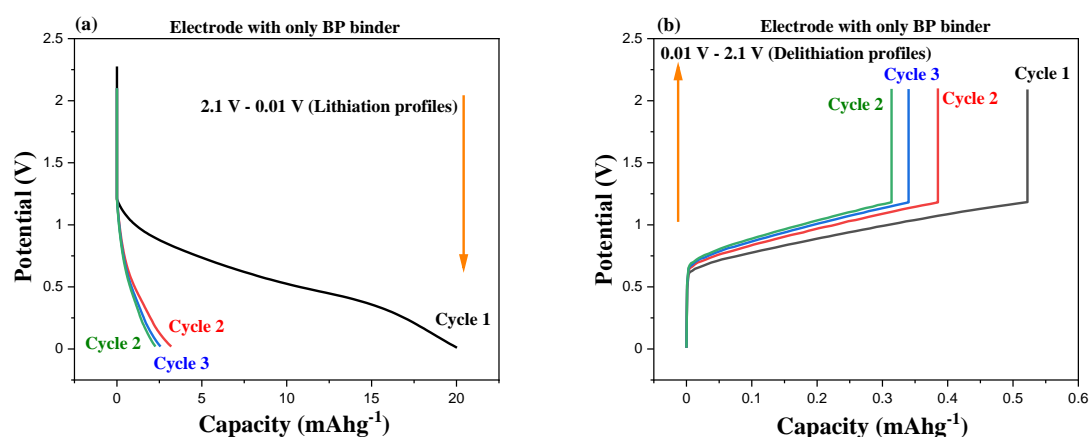


**Figure 18:** Galvanostatic cycling profiles of the electrode with only BP binder (without graphite and conductive additive) in the potential window 0.01 V – 2.1 V vs Li/Li<sup>+</sup> (a) lithiation half-cycle profiles for cycle 1, cycle 2, and cycle, and (b) delithiation half-cycle profiles for cycle 1, cycle 2 and cycle 3, respectively.

### Dynamic electrochemical impedance spectroscopy (DEIS) studies

In the conventional EIS, the impedance spectra of a battery are recorded at a steady state with no direct current (DC). Though this information is important, it does not reflect all the interfacial processes happening during real-time charge and discharge of the anodic half-cell. As an improvement to EIS, dynamic electrochemical impedance spectroscopy (DEIS) was allowed to record the impedance measurements during the charge and discharge cycles wherein the variable frequency response against the potential could be recorded corresponding to an

AC signal<sup>7,29,38-39</sup>. For the detailed investigation on the impedance of different interfaces, DEIS studies were conducted on the anodic half-cells with BP and PVDF binders from 0.01V to 2.1V<sup>38</sup>. Figure 19a and 19b, show the recorded DEIS spectra as 3D-Nyquist plots during lithiation for half-cycle of the BP and PVDF binder-based anodes. Figure 20a and 20b, show the DEIS profiles during the delithiation process of the half-cells with respective binders. To extract the quantitative impedance components, these DEIS profiles were fitted to suitable equivalent electric circuit models (EECMs). The EECM shown in Figure 19c was the best fit for the data obtained from DEIS studies. Each element of the EECM was classified in the following sequence: Ohmic resistance of the electrolyte, an intrinsic impedance of the graphite anode, SEI, charge transfer (CT) processes, and lithium-ion diffusion element known as Warburg diffusion. Table 4 and Table 5 list the respective ohmic resistance values corresponding to each of the interfaces as indicated by the EECM. The representative EECM fit of one of the Bode profiles is shown in Figure 21. The comparison plot of the SEI resistance values ( $R_{SEI}$ ) vs potential (V) for the PVDF and BP binder-based anodic half-cells is shown in Figure 19d. The  $R_{SEI}$  values in the case of the BP binder-based anode were half of that for the PVDF-based anode. Hence the DEIS studies showed that the formation of a better solid electrolyte interface (SEI) with lower impedance was one of the important factors behind the durable performance and improved specific capacity of the anodic half-cell with BP binder.

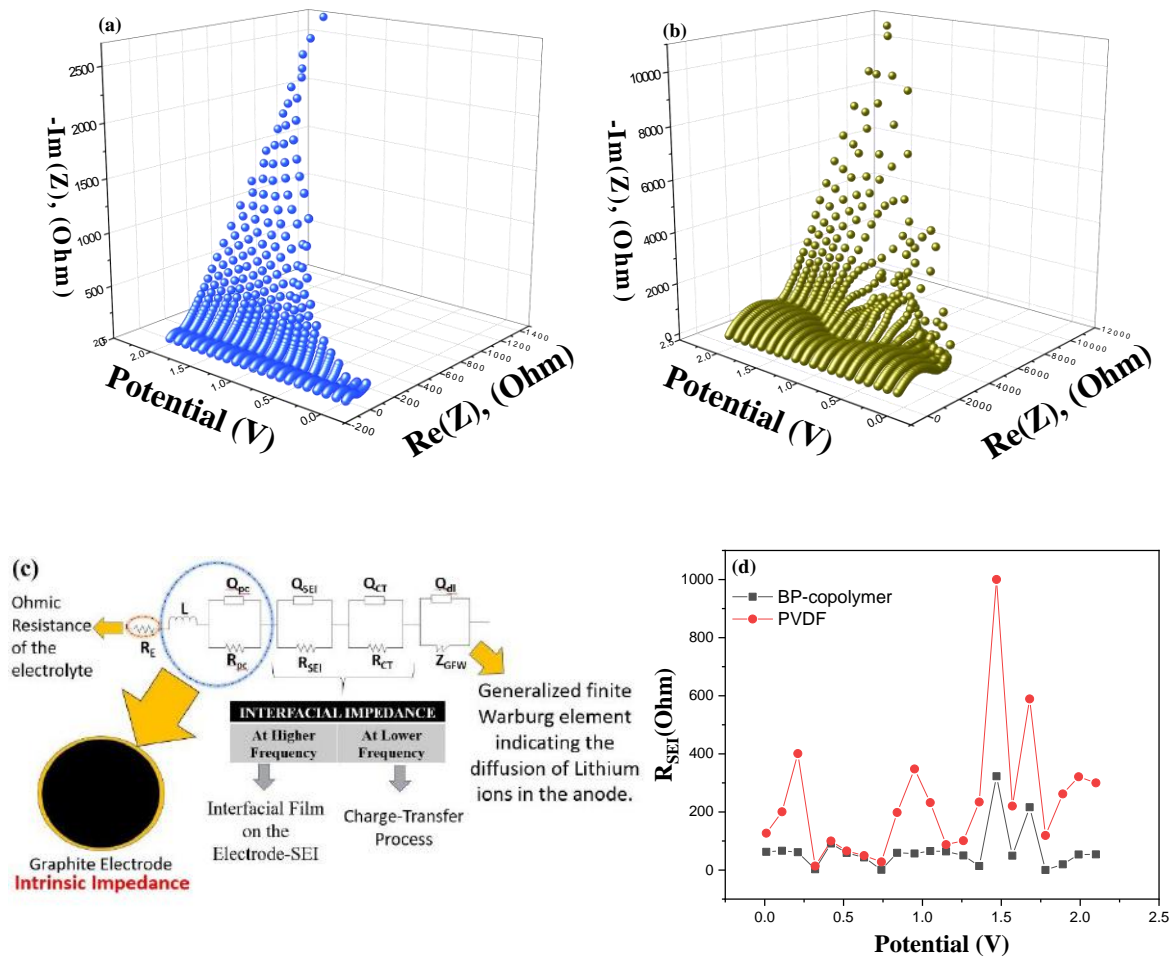


**Figure 19:** DEIS profiles during the lithiation of the anodic half-cells with (a) BP binder (after 1735 cycles at 1C), (b) PVDF (after 525 cycles at 1C), (c) Equivalent circuit model used to fit the obtained DEIS data, and (d) a plot of SEI impedance versus potential during lithiation for BP and PVDF binder-based anodes.

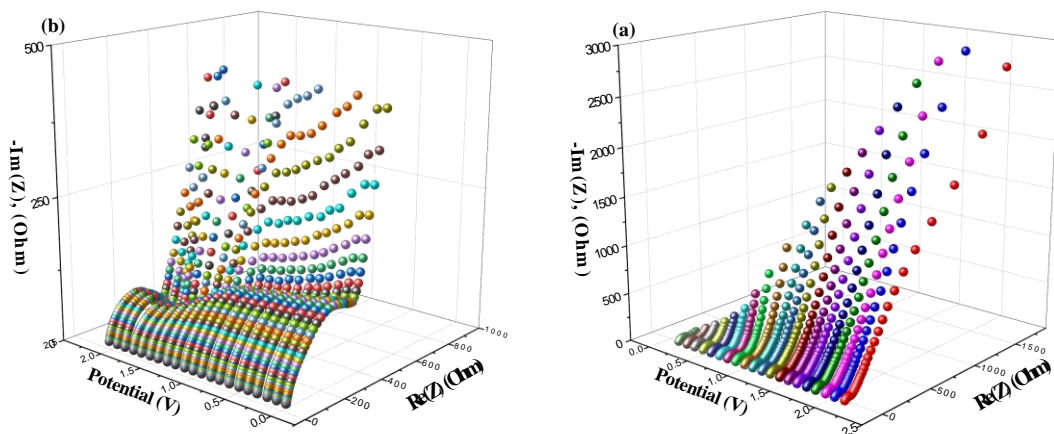


**Figure 20:** DEIS profiles during the delithiation of the anodic half-cells with (a) BP-copolymer (after 1735 cycles at 1C), (b) PVDF (after 525 cycles at 1C)

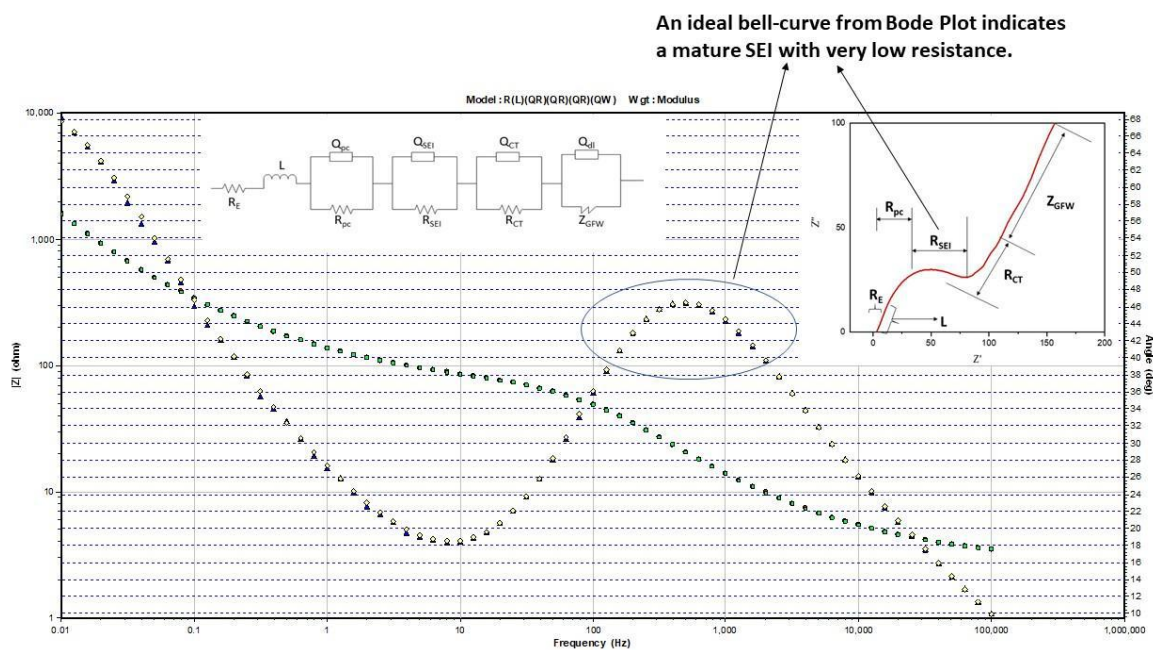


**Figure 21:** An EECM fit representative Bode's plot during lithiation in case of the BP-copolymer showing various interfaces.

**Table 4:** - DEIS circuit fitting parameters during charging with BP-copolymer as a binder

<b>R<sub>E</sub></b>	<b>R<sub>PC</sub></b>	<b>R<sub>SEI</sub></b>	<b>R<sub>CT</sub></b>	<b>χ<sup>2</sup></b>	<b>Circuit</b>	<b>Potential (V)</b>
0.029	1.822	62.53	5.18E+01	5.00E-04	R(L)(QR)(QR)(QR)(QW)	0.01
2.391	15.54	66.48	5.98E-05	4.73E-05	R(L)(QR)(QR)(QR)(QW)	0.11
2.566	49.31	61.19	3.99E+01	1.18E-05	R(L)(QR)(QR)(QR)(QW)	0.21
2.852	704.2	2.529	7.36E+01	2.07E-05	R(L)(QR)(QR)(QR)(QW)	0.32
2.55	61.02	91.19	5.51E+01	1.73E-05	R(L)(QR)(QR)(QR)(QW)	0.42
2.87	63.15	58.77	4.74E+01	4.18E-05	R(L)(QR)(QR)(QR)(QW)	0.52
2.42	540.9	43.19	2.91E+01	1.89E-05	R(L)(QR)(QR)(QR)(QW)	0.63
1.505	173.9	0.9606	6.09E+01	4.12E-05	R(L)(QR)(QR)(QR)(QW)	0.74
0.7	1.75	59.18	496	2.91E-05	R(L)(QR)(QR)(QR)(QW)	0.84
2.44	5.94	56.97	1.57E+04	3.24E-05	R(L)(QR)(QR)(QR)(QW)	0.95
3.04	2.256	65.33	4.28E+02	3.85E-05	R(L)(QR)(QR)(QR)(QW)	1.05
2.97	2.222	63.9	4.32E+02	4.52E-05	R(L)(QR)(QR)(QR)(QW)	1.15
0.3068	2.18	49.99	1.12E+07	9.24E-05	R(L)(QR)(QR)(QR)(QW)	1.26
2.201	8.731	1390	34.36	1.90E-04	R(L)(CR)(QR)(CR)(QW)	1.36
2.423	2.55E+02	322.8	53.21	3.20E-05	R(L)(QR)(QR)(QR)(QW)	1.47
2.54	344.1	49.35	127.5	3.05E-05	R(L)(QR)(QR)(QR)(QW)	1.57
2.544	2096	216.1	49.93	3.51E-05	R(L)(QR)(QR)(QR)(QW)	1.68
2.75	3.13E+11	0.03	45.48	6.79E-05	R(L)(QR)(QR)(QR)(QW)	1.78
2.57	2.79E+04	19.67	42.71	3.00E-05	R(L)(QR)(QR)(QR)(QW)	1.89
2.847	25.81	5338	659.2	5.8×10 <sup>-4</sup>	R(QR)(CR)(QR)(RW)	1.99
2.957	2.162	53.75	3628	0.0007	R(QR)(CR)(QR)(RW)	2.10

**Table 5:** - DEIS circuit fitting parameters during charging with PVDF as a binder

<b>R<sub>E</sub></b>	<b>R<sub>PC</sub></b>	<b>R<sub>SEI</sub></b>	<b>R<sub>CT</sub></b>	<b>χ<sup>2</sup></b>	<b>Circuit</b>	<b>Potential (V)</b>
2.4	3.62	2.57E+04	126.73	1.00E-04	R(L)(QR)(QR)(QR)(QW)	0.01
2.7	81.38	1.19E+13	200.65	9.00E-05	R(L)(QR)(QR)(QR)(QW)	0.11
1.31	131.7	66.42	400.8	3.00E-04	R(L)(QR)(QR)(QR)(QW)	0.21
2.12	3.46E+04	72.34	13.78	2.69E-05	R(L)(QR)(QR)(QR)(QW)	0.32
2.26	73.25	137.9	100.1	2.23E-05	R(L)(QR)(QR)(QR)(QW)	0.42
2.4	0.87	101	65.86	2.12E-05	R(L)(QR)(QR)(QR)(QW)	0.52



2.65	72.19	91.2	49.68	1.90E-05	R(L)(QR)(QR)(QR)(QW)	0.63
1.8	17.93	57.94	27.89	2.38E-05	R(L)(QR)(QR)(QR)(QW)	0.74
0.12	1.89	68.11	198.24	3.20E-05	R(L)(QR)(QR)(QR)(QW)	0.84
2.15	188.9	66.43	347.87	3.52E-05	R(L)(QR)(QR)(QR)(QW)	0.95
2.53	6.79	76.56	231.97	4.60E-05	R(L)(QR)(QR)(QR)(QW)	1.05
2.51	1.065	69.89	87.31	4.70E-05	R(L)(QR)(QR)(QR)(QW)	1.15
2.15	66.3	9307	100.96	1.00E-04	R(L)(QR)(QR)(QR)(QW)	1.26
0.82	1.36	6527	234.21	1.00E-04	R(L)(QR)(QR)(QR)(QW)	1.36
2.92	4.22E+00	278.3	1000.24	9.50E-05	R(L)(QR)(QR)(QR)(QW)	1.47
2.19	6.41E+01	1.01E+04	220.1	6.03E-05	R(L)(QR)(CR)(QR)(CW)	1.57
2.81	1.80E+02	3.73E+01	589	1.00E-04	R(L)(QR)(CR)(QR)(QW)	1.68
2.23	1.06E+03	31.01	119	1.00E-04	R(L)(QR)(CR)(QR)(CW)	1.78
2.47	6.00E+01	253.7	261.9	9.58E-05	R(L)(QR)(QR)(QR)(QW)	1.89
2.17	60.97	7976	320.89	0.0001	R(L)(QR)(QR)(QR)(CW)	1.99
2.81	5865	95.29	300.1	0.0002	R(L)(QR)(QR)(CR)(QW)	2.10

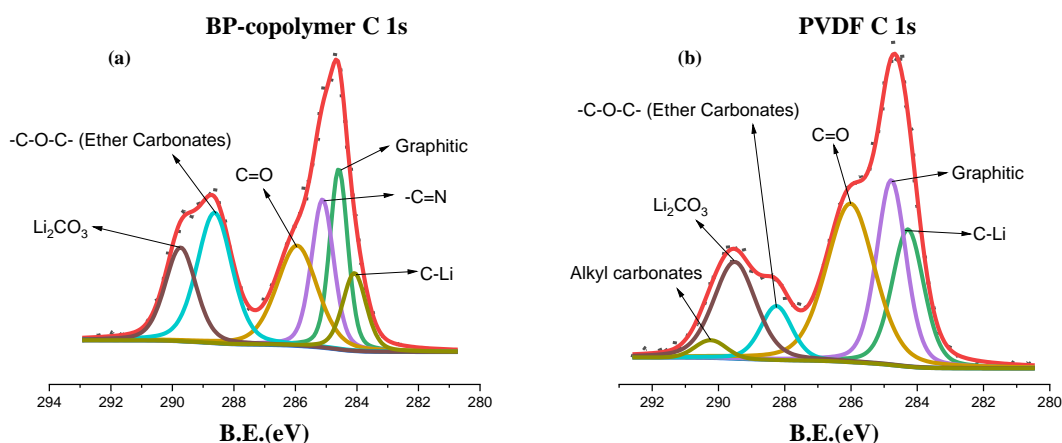
## 2.4.4 Post-mortem characterization of anodes

### X-ray photoelectron spectroscopy (XPS) measurements

To understand the SEI composition and binder doping for the electrode with BP binder, X-ray photoelectron spectroscopy studies were carried out. In the case of the electrode with BP binder, the cells were disassembled after cycling for 1735 cycles at OCP in an Argon filled glove box. The electrode was separated from the redundant cell components and washed with the dehydrated EC:DEC solvent multiple times before left for drying under a high vacuum for 16 hours. A similar procedure was repeated in the case of the electrode with the PVDF binder cycled for 525 cycles. The obtained XPS spectra were calibrated to the graphite carbon (C=C) character set to 284.6 eV<sup>40</sup>. The deconvolution and curves fit were performed keeping 70% Gaussian 30% Voigt peak shape. Figure 22a and 22b show the C 1s spectra for BP and PVDF binder-based anodes, respectively. All the standard peaks like lithium intercalation peak C-Li at (284.08 eV), C=C at (284.60 eV) corresponding to the graphite framework, C=O at (285.94 eV), -C-O-C- (288.63 eV) (ether carbons, corresponding to ethylene carbonate and diethyl carbonate), and lithium carbonates (Li<sub>2</sub>CO<sub>3</sub>) at (289.73 eV) were common in both the electrodes<sup>41-42</sup>. Additionally, in the case of the electrode with BP binder, the peak at 285.11 eV

was ascribed to the characteristic (-C=N) peak recognizing the diimine framework of the BP binder<sup>40</sup>. Figure 23 shows the N1s spectrum of the anode with the BP binder. The peak at 398.59 eV was attributed to the  $sp^2$  - a pyridinic type of (-C-N=C-) nitrogen atom<sup>43</sup> and the peak at 399.75 eV was attributed to the quaternary nitrogen due to lithium doping<sup>41, 44</sup>. The detection of lithium doped quaternary nitrogen is reflective of the irreversible capacity loss during the first lithiation half-cycle. Table 6d shows the percentage area under the curve for each type of nitrogen peak. After 1735 cycles of charge and discharge at 1C-rate, 25% of the diimine nitrogen have been found doped with lithium-ions in a quaternary state. Figure 22c and 22d show the O 1s spectrum with binding energies corresponding to C=O (530.88 eV) carbonates, C-O (531.61 eV), and ether (532.72 eV) are common in both the anodes with the BP and PVDF binders<sup>45</sup>. Figure 22e and 22f show the F 1s spectra of the BP and PVDF binder-based anodes. The F 1s peaks at 684.32 eV and 687.85 eV correspond to LiF and  $Li_xPF_y$  components in the PVDF-based anode<sup>46</sup>. The F 1s peaks at 687.98 eV and 691.13 eV correspond to  $Li_xPF_y$  and CF components in the BP binder-based anode. Table 6 shows the data with the binding energy values and the percentage area under the peak for each element in the case of BP and PVDF binder-based anodes.

XPS is a surface technique with the detection depth limited to ~5-10 nm. Therefore, detection of the species is signature of their presence within the detection depth of XPS. Hence the detection of (i) nitrogen (N 1s) peaks of BP binder and (ii) (-C=N) in C 1s spectrum of BP binder-based anode means that the SEI formed on the surface of the BP binder-based anode was thin. Whereas, in the case of PVDF-based anode, the carbon-fluoride peak in F 1s spectrum attributing to the PVDF molecular framework was absent which indicated that the SEI on PVDF-based anode was thick.



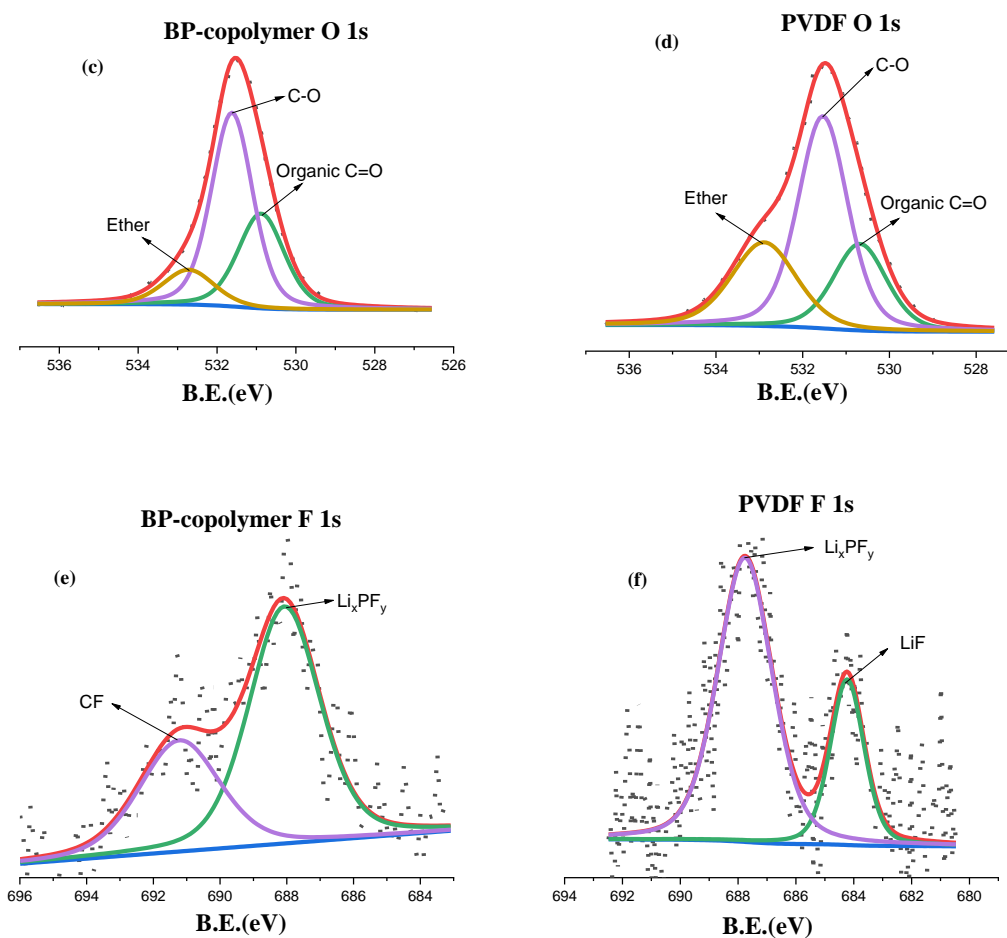


**Figure 22:** The XPS spectra (a), (c), and (e) for the BP-copolymer binder based anode for C 1s, O 1s, and F 1s respectively, and (b), (d), and (f) for the PVDF binder based anode for C 1s, O 1s and F 1s, respectively, with the respective SEI components.

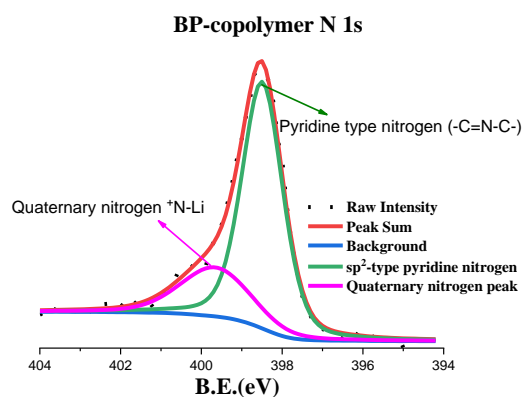


**Figure 23:** The XPS spectrum of N 1s component of diimine framework of the BP binder-based anode cycled for 1735 cycles.

(a) C 1s (BP-copolymer and PVDF)

Component	BP-copolymer (eV)	% area under the curve	PVDF (eV)	% area under the curve
C-Li	284.08	9.26	284.03	18.35
Graphite	284.6	16.35	284.62	23.37
-C=N	285.11	16.58	-	-
C=O	285.94	20.38	285.82	30.92
C-O-C (ether carbonates)	288.63	22.79	288.03	8.16
Lithium carbonates (Li <sub>2</sub> CO <sub>3</sub> )	289.73	14.61	289.28	15.34
Alkyl carbonates (R-OCO <sub>2</sub> -Li)	-	-	289.93	3.85

(b) O 1s (BP-copolymer and PVDF)

Component	BP-copolymer (eV)	% area under the curve	PVDF (eV)	% area under the curve
C=O (organic species)	530.88	30.82	530.68	22.39
C-O	531.61	56.67	531.52	51.34
Ether	532.72	12.49	532.89	26.25

(c) F 1s (BP-copolymer and PVDF)

Component	BP-copolymer (eV)	% area under the curve	PVDF (eV)	% area under the curve
CF	691.13	34.71		
LiF	-	-	684.32	26.59
Li <sub>x</sub> PF <sub>y</sub>	687.98	65.28	687.85	73.4

(d) N 1s (BP-copolymer)

Component	BP-copolymer (eV)	% area under the curve
Pyridinic Type	398.59	74.5
Li doped N	399.75	25.49

**Table 6 (a), (b), and (c):** The binding energy values and corresponding % area under the curve corresponding to C 1s, O 1s, and F 1s for BP-copolymer and PVDF based electrodes. **(d)** corresponding to N 1s for BP-copolymer.

### Scanning electron microscope (SEM) measurements (Morphology studies)

After the XPS studies, surface morphologies of the respective anodes were studied using the FESEM technique. Figure 24a and 24b show the SEM micrographs of the pristine BP-based anode and the anode after 1735 cycles of charge and discharge, respectively. Apart from a few small cracks at a few places, the electrode laminate maintained good adherence to the copper foil even after 1735 cycles. Figure 24c and 24d show the SEM micrographs of the pristine PVDF-based anode and the anode after 525 cycles of charge and discharge, respectively. After 525 cycles of charge and discharge, irregular large cracks were observed in the PVDF-based anode. Also, the electrode laminate was peeling off from the copper current collector due to poor adherence. PVDF could not administer the mechanical stability to the graphite during lithium-ion intercalation & deintercalation at a high current rate for more than 525 cycles. Whereas the BP binder-based anode retained the morphology to a large extent.

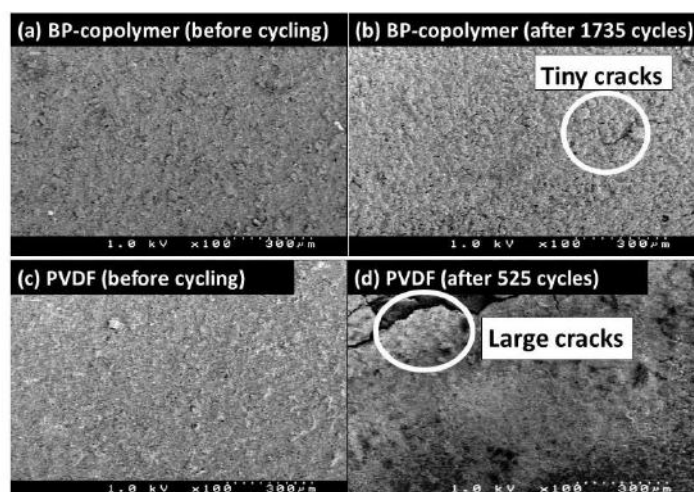


**Figure 24:** The FESEM micrographs of (a) BP-based pristine electrode, (b) BP-based electrode after 1735 cycles, (c) PVDF-based pristine electrode, and (d) PVDF-based electrode after 525 cycles.

### Electrolyte interaction

It has been reported that the PVDF reacts with the electrolyte on storage<sup>13,47</sup>. Therefore, to compare the change in the physical state of the BP and PVDF binders on storage in the electrolyte (1.0 M LiPF<sub>6</sub> in (1:1) v/v EC:DEC), 2 mg of each type of binder was stored in 2 ml of electrolyte for 15 days in dark. Figure 25 and Figure 26 show the pictures of the vials with respective binders stored in the electrolyte on 1<sup>st</sup> day after 15<sup>th</sup> day, respectively. It was observed that the solution in the vial with the BP binder did not show any change after storage.

But in the case of the PVDF binder, it turned turbid after 15 days. This indicated that the PVDF binder on long term exposure to the electrolyte would lose its merit as a good binder. This justifies the inability of the PVDF binder to provide robust mechanical support to graphite over deep cycling and the poor adhesion of the electrode laminate to the copper current collector.

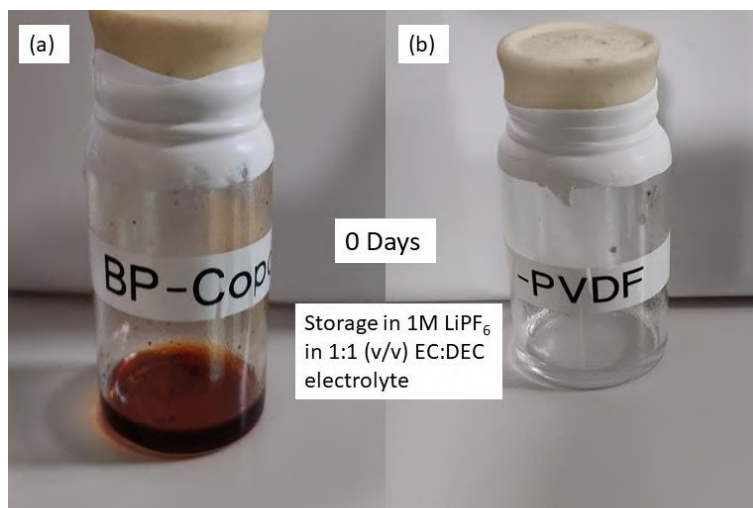


**Figure 25:** The observation on storage (0 days) in 1M LiPF<sub>6</sub> in (1:1) v/v EC:DEC electrolyte (a) BP-copolymer, and (b) PVDF

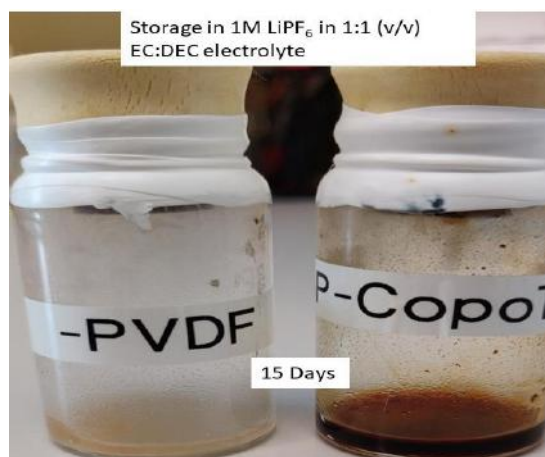


**Figure 26:** The observation on storage (15 days) in 1M LiPF<sub>6</sub> in (1:1) v/v EC:DEC electrolyte of both the binders.

### Comparison of BP-copolymer as binder with reported binders in the literature

Table 7 compares the BP binder with other binders reported in the literature like PVDF, CMC-Na, Acryl S020, poly(acrylamide-co-diallyldimethylammonium chloride)

**Table 7:** Comparison of BP-copolymer binder with other reported binders for graphite anode

Binder	Peak discharge capacity at 1C rate	Capacity Retention	References
PVDF <sup>7-9, 48</sup>	~200 mAhg <sup>-1</sup> (1C rate)	~50 % (100 cycles)	7, 8, 9, 42
CMC-Na <sup>8, 49</sup>	~200 mAhg <sup>-1</sup> (1C rate)	~80 % (100 cycles)	8, 43
Acryl S020 <sup>50</sup>	166 mAhg <sup>-1</sup> (1C rate)	~92% (100 cycles)	44
AMAC (poly(acrylamide-co-diallyldimethylammonium chloride) <sup>9</sup>	~210 mAhg <sup>-1</sup> (1C rate)	~90 % (65 cycles)	9
Xanthan Gum (XG) <sup>49</sup>	~350 mAhg <sup>-1</sup> (C/12 rate)	~90% (100 cycles)	43
SBR <sup>51</sup>	~340 mAhg <sup>-1</sup> (C/10 rate)	~95% (100 cycles)	45
SBR-PVDF <sup>52</sup>	~260 mAhg <sup>-1</sup> (C/5 rate)	~60% (100 cycles)	46
BIAN-Fluorene polymer <sup>7</sup>	270 mAhg <sup>-1</sup> (1C rate)	~93% (100 cycles)	7
Allylimidazolium-Based Poly(ionic liquid) <sup>48</sup>	210 mAhg <sup>-1</sup> (1C rate)	~87% (500 cycles)	42
BIAN-paraphenylene copolymer	260 mAhg <sup>-1</sup> (1C rate)	~95 % (1735 cycles)	This Work

## 2.5 Conclusion

BP-copolymer as a binder for graphite anode exhibited better interfacial properties, reversible capacity, capacity retention, lithium-ion diffusion, and morphology retention in comparison to the conventional PVDF binder. The structural benefits like  $\pi$ - $\pi$  stacking with graphite, n-type characteristics with intrinsic electronic conductivity, and diimine nitrogen atoms to interact with copper current collector empowered the BP binder to provide robust mechanical support to the active material. The CV studies indicated that the low lying LUMO inspired the binder doping which prevented the electrolyte decomposition. This suppressed the excess electrolyte decomposition that led to the formation of a thinner solid-electrolyte interface (SEI). CV-based scan rate studies showed that the lithium-ion diffusion coefficient for the BP binder-based anode was 15% higher than the PVDF based anode. The impedance spectroscopy studies showed a reduced interfacial impedance ( $R_{SEI}$ ) for BP binder-based anode. As a result, the BP based anodic half-cell showed improved charge and discharge performance at a high current rate of 1C with maximum reversible capacity of about  $260 \text{ mAhg}^{-1}$ , cyclability up to 1735 cycles, and capacity retention of about 95%. The XPS and SEM analysis of the respective anodes after cycling confirmed that the SEI formed in the case of BP-binder anode was thinner and the morphology retention was better than the PVDF based anode. Therefore, the superior performance of the BP-copolymer makes it a promising candidate as an alternate binder material for graphite anodes in LIBs.

## References

1. Armand, M.; Tarascon, J. M., Building better batteries. *Nature* **2008**, *451* (7179), 652-657.
2. Tarascon, J. M.; Armand, M., Issues and challenges facing rechargeable lithium batteries. *Nature* **2001**, *414* (6861), 359-367.
3. Zhu, G.-N.; Wang, Y.-G.; Xia, Y.-Y., Ti-based compounds as anode materials for Li-ion batteries. *Energy & Environmental Science* **2012**, *5* (5), 6652-6667.
4. Nitta, N.; Wu, F.; Lee, J. T.; Yushin, G., Li-ion battery materials: present and future. *Materials Today* **2015**, *18* (5), 252-264.
5. Dudney, N. J.; Li, J., Using all energy in a battery. *Science* **2015**, *347* (6218), 131.



6. Taberna, P. L.; Mitra, S.; Poizot, P.; Simon, P.; Tarascon, J. M., High rate capabilities Fe<sub>3</sub>O<sub>4</sub>-based Cu nano-architected electrodes for lithium-ion battery applications. *Nature Materials* **2006**, *5* (7), 567-573.
7. Patnaik, S. G.; Vedarajan, R.; Matsumi, N., BIAN based functional diimine polymer binder for high performance Li ion batteries. *Journal of Materials Chemistry A* **2017**, *5* (34), 17909-17919.
8. Versaci, D.; Nasi, R.; Zubair, U.; Amici, J.; Sgroi, M.; Dumitrescu, M. A.; Francia, C.; Bodoardo, S.; Penazzi, N., New eco-friendly low-cost binders for Li-ion anodes. *Journal of Solid State Electrochemistry* **2017**, *21* (12), 3429-3435.
9. Zhang, S. S.; Xu, K.; Jow, T. R., Evaluation on a water-based binder for the graphite anode of Li-ion batteries. *J Power Sources* **2004**, *138* (1), 226-231.
10. Bresser, D.; Buchholz, D.; Moretti, A.; Varzi, A.; Passerini, S., Alternative binders for sustainable electrochemical energy storage – the transition to aqueous electrode processing and bio-derived polymers. *Energy & Environmental Science* **2018**, *11* (11), 3096-3127.
11. Fransson, L.; Eriksson, T.; Edstrom, K.; Gustafsson, T.; Thomas, J. O., Influence of carbon black and binder on Li-ion batteries. *J Power Sources* **2001**, *101* (1), 1-9.
12. Yoo, M.; Frank, C. W.; Mori, S.; Yamaguchi, S., Interaction of poly(vinylidene fluoride) with graphite particles. 2. Effect of solvent evaporation kinetics and chemical properties of pvdf on the surface morphology of a composite film and its relation to electrochemical performance. *Chemistry of Materials* **2004**, *16* (10), 1945-1953.
13. Wang, Y.; Zheng, H.; Qu, Q.; Zhang, L.; Battaglia, V. S.; Zheng, H., Enhancing electrochemical properties of graphite anode by using poly(methylmethacrylate)-poly(vinylidene fluoride) composite binder. *Carbon* **2015**, *92*, 318-326.
14. Li, Z.-F.; Zhang, H.; Liu, Q.; Liu, Y.; Stanciu, L.; Xie, J., Novel pyrolyzed polyaniline-grafted silicon nanoparticles encapsulated in graphene sheets as li-ion battery anodes. *ACS Applied Materials & Interfaces* **2014**, *6* (8), 5996-6002.
15. Zhao, H.; Wei, Y.; Qiao, R.; Zhu, C.; Zheng, Z.; Ling, M.; Jia, Z.; Bai, Y.; Fu, Y.; Lei, J.; Song, X.; Battaglia, V. S.; Yang, W.; Messersmith, P. B.; Liu, G., Conductive polymer binder for high-tap-density nanosilicon material for lithium-ion battery negative electrode application. *Nano Letters* **2015**, *15* (12), 7927-7932.
16. Choi, J.; Kim, K.; Jeong, J.; Cho, K. Y.; Ryou, M.-H.; Lee, Y. M., Highly adhesive and soluble copolyimide binder: improving the long-term cycle life of silicon anodes in lithium-ion batteries. *ACS Applied Materials & Interfaces* **2015**, *7* (27), 14851-14858.

17. Liu, G.; Xun, S.; Vukmirovic, N.; Song, X.; Olalde-Velasco, P.; Zheng, H.; Battaglia, V. S.; Wang, L.; Yang, W., Polymers with tailored electronic structure for high capacity lithium battery electrodes. *Advanced Materials* **2011**, *23* (40), 4679-4683.
18. Mery, A.; Bernard, P.; Valero, A.; Alper, J. P.; Herlin-Boime, N.; Haon, C.; Duclairoir, F.; Sadki, S., A polyisoidingo derivative as novel n-type conductive binder inside Si@C nanoparticle electrodes for Li-ion battery applications. *J Power Sources* **2019**, *420*, 9-14.
19. Chen, H.; Ling, M.; Hencz, L.; Ling, H. Y.; Li, G.; Lin, Z.; Liu, G.; Zhang, S., Exploring chemical, mechanical, and electrical functionalities of binders for advanced energy-storage devices. *Chemical Reviews* **2018**, *118* (18), 8936-8982.
20. Lepage, D.; Michot, C.; Liang, G.; Gauthier, M.; Schougaard, S. B., A soft chemistry approach to coating of LiFePO<sub>4</sub> with a conducting polymer. *Angewandte Chemie International Edition* **2011**, *50* (30), 6884-6887.
21. Shi, Y.; Yu, G., Designing hierarchically nanostructured conductive polymer gels for electrochemical energy storage and conversion. *Chemistry of Materials* **2016**, *28* (8), 2466-2477.
22. Liu, G.; Xun, S.; Vukmirovic, N.; Song, X.; Olalde-Velasco, P.; Zheng, H.; Battaglia, V. S.; Wang, L.; Yang, W., Polymers with tailored electronic structure for high capacity lithium battery electrodes. *Adv Mater* **2011**, *23* (40), 4679-83.
23. Salem, N.; Lavrisa, M.; Abu-Lebdeh, Y., Ionically-functionalized poly(thiophene) conductive polymers as binders for silicon and graphite anodes for li-ion batteries. *energy technology* **2016**, *4* (2), 331-340.
24. Shi, Y.; Peng, L.; Ding, Y.; Zhao, Y.; Yu, G., Nanostructured conductive polymers for advanced energy storage. *Chemical Society Reviews* **2015**, *44* (19), 6684-6696.
25. Viganò, M.; Ferretti, F.; Caselli, A.; Ragaini, F.; Rossi, M.; Mussini, P.; Macchi, P., Easy entry into reduced Ar-BIANH<sub>2</sub> compounds: a new class of quinone/hydroquinone-type redox-active couples with an easily tunable potential. *Chemistry – A European Journal* **2014**, *20* (44), 14451-14464.
26. Patnaik, S. G.; Vedarajan, R.; Matsumi, N., BIAN based electroactive polymer with defined active centers as metal-free electrocatalysts for oxygen reduction reaction (orr) in aqueous and nonaqueous media. *ACS Applied Energy Materials* **2018**, *1* (3), 1183-1190.
27. Choi, N.-S.; Ha, S.-Y.; Lee, Y.; Jang, J. Y.; Jeong, M.-H.; Shin, W. C.; Ue, M., Recent progress on polymeric binders for silicon anodes in lithium-ion batteries. *J. Electrochem. Sci. Technol* **2015**, *6* (2), 35-49.

28. Villa, M.; Miesel, D.; Hildebrandt, A.; Ragaini, F.; Schaarschmidt, D.; Jacobi von Wangelin, A., Synthesis and catalysis of redox-active bis(imino)acenaphthene (bian) iron complexes. *ChemCatChem* **2017**, *9* (16), 3203-3209.
29. Huang, J.; Ge, H.; Li, Z.; Zhang, J., Dynamic electrochemical impedance spectroscopy of a three-electrode lithium-ion battery during pulse charge and discharge. *Electrochimica Acta* **2015**, *176*, 311-320.
30. Agubra, V. A.; Fergus, J. W., The formation and stability of the solid electrolyte interface on the graphite anode. *J Power Sources* **2014**, *268*, 153-162.
31. Hu, Y.; Kong, W.; Li, H.; Huang, X.; Chen, L., Experimental and theoretical studies on reduction mechanism of vinyl ethylene carbonate on graphite anode for lithium ion batteries. *Electrochemistry Communications* **2004**, *6* (2), 126-131.
32. Li, J.; Armstrong, B. L.; Kiggans, J.; Daniel, C.; Wood, D. L., Lithium ion cell performance enhancement using aqueous LiFePO<sub>4</sub> cathode dispersions and polyethyleneimine dispersant. *Journal of The Electrochemical Society* **2012**, *160* (2), A201-A206.
33. Yu, D. Y. W.; Fietzek, C.; Weydanz, W.; Donoue, K.; Inoue, T.; Kurokawa, H.; Fujitani, S., Study of LiFePO<sub>4</sub> by cyclic voltammetry. *Journal of The Electrochemical Society* **2007**, *154* (4), A253.
34. Levi, M. D.; Aurbach, D., The mechanism of lithium intercalation in graphite film electrodes in aprotic media. Part 1. High resolution slow scan rate cyclic voltammetric studies and modeling. *Journal of Electroanalytical Chemistry* **1997**, *421* (1), 79-88.
35. Leftheriotis, G.; Papaefthimiou, S.; Yianoulis, P., Dependence of the estimated diffusion coefficient of Li<sub>x</sub>WO<sub>3</sub> films on the scan rate of cyclic voltammetry experiments. *Solid State Ionics* **2007**, *178* (3), 259-263.
36. Padhi, A. K., Phospho-olivines as Positive-electrode materials for rechargeable lithium batteries. *Journal of The Electrochemical Society* **1997**, *144* (4), 1188.
37. Fulcher, G. S., Analysis of recent measurements of the viscosity of glasses. *Journal of the American Ceramic Society* **1925**, *8* (6), 339-355.
38. Huang, J.; Li, Z.; Zhang, J., Dynamic electrochemical impedance spectroscopy reconstructed from continuous impedance measurement of single frequency during charging/discharging. *J Power Sources* **2015**, *273*, 1098-1102.
39. Smaran, K. S.; Joshi, P.; Vedarajan, R.; Matsumi, N., Optimisation of potential boundaries with dynamic electrochemical impedance spectroscopy for an anodic half-cell based on organic-inorganic hybrid electrolytes. *ChemElectroChem* **2015**, *2* (12), 1913-1916.

40. Dementjev, A. P.; de Graaf, A.; van de Sanden, M. C. M.; Maslakov, K. I.; Naumkin, A. V.; Serov, A. A., X-Ray photoelectron spectroscopy reference data for identification of the  $C_3N_4$  phase in carbon–nitrogen films. *Diamond and Related Materials* **2000**, *9* (11), 1904-1907.
41. Collins, J.; Gourdin, G.; Foster, M.; Qu, D., Carbon surface functionalities and SEI formation during Li intercalation. *Carbon* **2015**, *92*, 193-244.
42. Bleda-Martínez, M. J.; Lozano-Castelló, D.; Morallón, E.; Cazorla-Amorós, D.; Linares-Solano, A., Chemical and electrochemical characterization of porous carbon materials. *Carbon* **2006**, *44* (13), 2642-2651.
43. Tan, K. L.; Tan, B. T. G.; Kang, E. T.; Neoh, K. G., X-ray photoelectron spectroscopy studies of the chemical structure of polyaniline. *Physical Review B* **1989**, *39* (11), 8070-8073.
44. Wang, H.; Zhang, C.; Liu, Z.; Wang, L.; Han, P.; Xu, H.; Zhang, K.; Dong, S.; Yao, J.; Cui, G., Nitrogen-doped graphene nanosheets with excellent lithium storage properties. *Journal of Materials Chemistry* **2011**, *21* (14), 5430-5434.
45. Lu, M.; Cheng, H.; Yang, Y., A comparison of solid electrolyte interphase (SEI) on the artificial graphite anode of the aged and cycled commercial lithium ion cells. *Electrochimica Acta* **2008**, *53* (9), 3539-3546.
46. Leroy, S.; Blanchard, F.; Dedryvère, R.; Martinez, H.; Carré, B.; Lemordant, D.; Gonbeau, D., Surface film formation on a graphite electrode in Li-ion batteries: AFM and XPS study. *Surface and Interface Analysis* **2005**, *37* (10), 773-781.
47. Ning, G.; Haran, B.; Popov, B. N., Capacity fade study of lithium-ion batteries cycled at high discharge rates. *J Power Sources* **2003**, *117* (1), 160-169.
48. Jayakumar, T. P.; Badam, R.; Matsumi, N., Allylimidazolium-based poly(ionic liquid) anodic binder for lithium-ion batteries with enhanced cyclability. *ACS Applied Energy Materials* **2020**, *3* (4), 3337-3346.
49. Courtel, F. M.; Niketic, S.; Duguay, D.; Abu-Lebdeh, Y.; Davidson, I. J., Water-soluble binders for MCMB carbon anodes for lithium-ion batteries. *J Power Sources* **2011**, *196* (4), 2128-2134.
50. Pohjalainen, E.; Sorsa, O.; Juurikivi, J.; Kallio, T., Water-Soluble Acrylate Binder for Graphite Electrodes in Lithium-Ion Batteries. *Energy Technology* **2016**, *4* (4), 470-472.
51. Buqa, H.; Holzappel, M.; Krumeich, F.; Veit, C.; Novák, P., Study of styrene butadiene rubber and sodium methyl cellulose as binder for negative electrodes in lithium-ion batteries. *J Power Sources* **2006**, *161* (1), 617-622.

52. Wang, L.; Fu, Y.; Battaglia, V. S.; Liu, G., SBR–PVDF based binder for the application of SLMP in graphite anodes. *RSC Advances* **2013**, 3 (35), 15022-15027.

## Chapter 3

# Poly(BIAN)/Poly(acrylic acid) Based Self-Healing Composite Binder for High Capacity Silicon Anodes in Lithium-Ion Secondary Batteries

### 3.1 Abstract

Natural abundance and high theoretical capacity make silicon a promising anode material in Li-ion batteries (LIBs). However, repeated alloying/dealloying with lithium ions results in the pulverization of Si anodes due to the large volume expansion. This leads to its poor performance in terms of cyclability, reversible capacity, and capacity retention. Polymer binders have been recognized with the potential to stabilize the silicon anodes. Here, the design, synthesis, and application of an n-type self-healing polymer composite poly(bisiminoacenaphthenequinone)/poly(acrylic acid) (P-BIAN/PAA) is reported as a binder for the Si anode. Computational and electrochemical studies reveal that the low lying LUMO of P-BIAN/PAA inspires its n-doping which facilitates the formation of a thin solid-electrolyte interface (SEI) with reduced impedance and ion-conducting pathways through the polymer matrices. As a result, the charge and discharge studies show a very stable long cycling behavior up to 600 cycles with a high reversible capacity of about  $2100 \text{ mAhg}^{-1}_{\text{Si}}$  and ~95% capacity retention. P-BIAN/PAA polymer composite has provided a new perspective towards designing robust binder composites with n-type intrinsic conductivity and self-healing properties for the next-generation high-capacity LIBs.

## 3.2 Introduction

Recent progress made in electrochemical energy storage devices demands lithium-ion batteries (LIBs) with high energy density and long cycle life for their emerging applications in hybrid and electric vehicles (EVs), consumer electronics, and renewable energy storage devices<sup>1-2</sup>. As an alternative to the conventionally used graphite anode, Si has emerged as a potential anode material because of its high theoretical capacity of 3579 mAhg<sup>-1</sup> (Li<sub>15</sub>Si<sub>4</sub>), low discharge potential (<0.5 V vs Li/Li<sup>+</sup>), natural abundance, and nontoxicity<sup>3</sup>. However, on repeated de-/alloying, drastic volume expansion (>300%) followed by pulverization of Si particles results in the loss of interparticle electrical contact, formation of a thick solid-electrolyte interface (SEI) hindering lithium-ion diffusion, and fractured electrode laminate<sup>4</sup>. Hence the cyclability, reversible capacity, and coulombic efficiency get significantly compromised<sup>5</sup>. This inherent failure mechanism of Si anodes to some extent has been overcome by the processing of the naturally available Si to nanostructures like nanoparticles, yolk-shell nanoparticles, nanotubes, nanowires, core-shell nanowires, nanoporous structures, and nanocomposites<sup>6-9</sup>. But their complex and costly production is unsustainable for the ever-growing demands of high energy density devices.

Alternatively, the addition of multi-functional polymeric binders in small proportions enhances the sustainable performance of Si anodes<sup>10</sup>. In this regard, two classes of polymers have shown promising results: (a) conducting polymers (CPs), and (b) self-healing polymers (SHPs)<sup>11</sup>. Liu et al. first reported a polyfluorene-based novel conducting polymer as a binder for Si anodes with improved cyclability and discharge capacity<sup>12</sup>. In succession, a plethora of conducting binders were explored with different functionalities like poly(fluorene-methylbenzoic ester) (PFFOMB)<sup>12</sup>, poly(3,4-ethylenedioxythiophene) PEDOT<sup>13-14</sup>, polyaniline (PANI)<sup>15-16</sup>, poly(phenanthrenequinone) (PPQ)<sup>17</sup>, poly(2,7-9,9-dioctylfluorene-2,7-9,9-(di(oxy-,2,5,8-trioxadecane))fluorene-co-2,7-fluorenone-co-2,5-1-methylbenzoate ester) (PEFM)<sup>18</sup>, and PEDOT:PSS (where PSS is poly(styrenesulfonate))<sup>19-20</sup>. Though the enhanced conductivity could improve the performance of Si anodes, the lack of mechanical robustness has been a pertaining problem with conductive binders thereby acting as a hurdle in the wholesome performance of Si anodes.

Therefore, as a strategy to achieve the desired physical robustness without compromising the electronic conductivity, recently, polymer composites combining CPs like polyaniline (PANI), polypyrrole (PPy), and polythiophene (Pth) with carboxylate-containing polymers like

(poly(acrylic acid) (PAA), carboxymethyl cellulose (CMC), sodium carboxymethyl chitosan (CCTS), and sodium alginate (SA) have been employed as binders to silicon anodes<sup>21-22</sup>. In CP/carboxyl-containing polymer composite structures, the CP offers a uniform conductive matrix that facilitates ionic and electronic transport, while the carboxylate-containing polymer acts as a dopant for the CP and provides mechanical robustness because of its self-healing property<sup>21</sup>. However, the problem of the formation of a thick SEI upon repeated exposure of newly pulverized Si surfaces which impedes the free diffusion of lithium-ions by increasing the battery's internal impedance has not been convincingly addressed. Therefore, the design and application of versatile binders which are not only conducting and self-healing in nature but also have an ability to tailor a thin SEI with enhanced lithium-ion diffusion will potentially stabilize the silicon anodes. In this regard, the combination of an n-type CP/carboxylate-containing polymer can be one novel combination to tailor a thin SEI. The n-doping ability of the CP in the anodic environment can limit the extent of electrolytic decomposition on the electrode surface and tentatively stabilize the interface for prolonged cyclability of the battery.

Compounds of the family bisiminoacenaphthenequinone (Ar-BIAN) were brought to general attention by Elsevier and his group as essential ligands for transition metals owing to their rich electrochemical and redox properties<sup>23-24</sup>. Recently, our group reported BIAN-fluorene copolymer as a binder for graphite anode wherein the low-lying lowest unoccupied molecular orbital (LUMO) of BIAN led to the n-doping of the polymer in the anodic environment which influenced the formation of a thin SEI with decreased interfacial impedance and resulted in stable performance of the graphite anode<sup>25</sup>. This inspired us to design a composite binder for silicon anodes utilizing P-BIAN as the conducting link with an ability to tailor a thin SEI in combination with a protic polymer to attain the self-healing property through hydrogen bond network formation. Hence, herein is reported P-BIAN/PAA, an n-type conducting multifunctional self-healing polymer composite comprising of P-BIAN in dynamic electrostatic hydrogen bonding with PAA as a binder for silicon anodes. Figure 1a shows P-BIAN - belonging to the class of CPs and PAA - a carboxylate containing polymer. The electrostatic hydrogen bonding between the nitrogen atoms in the diimine backbone of P-BIAN and the carboxyl moiety of the PAA forms a self-healing polymer composite (P-BIAN/PAA). The structural scheme of P-BIAN/PAA composite is shown in Figure 1b. The composite framework is capable of (a) providing structural flexibility to accommodate large volume change of silicon anodes (Figure 1c), (b) controlling the electrolytic reduction via n-doping of binder to form an effective and thin SEI having lowered impedance with enhanced lithium-ion



diffusion, (c) maintaining electronic conductivity throughout the electrode laminate and good adherence to the copper current collector, and (e) consequentially, improve the reversible capacity, cyclability, and capacity retention of Si anodes

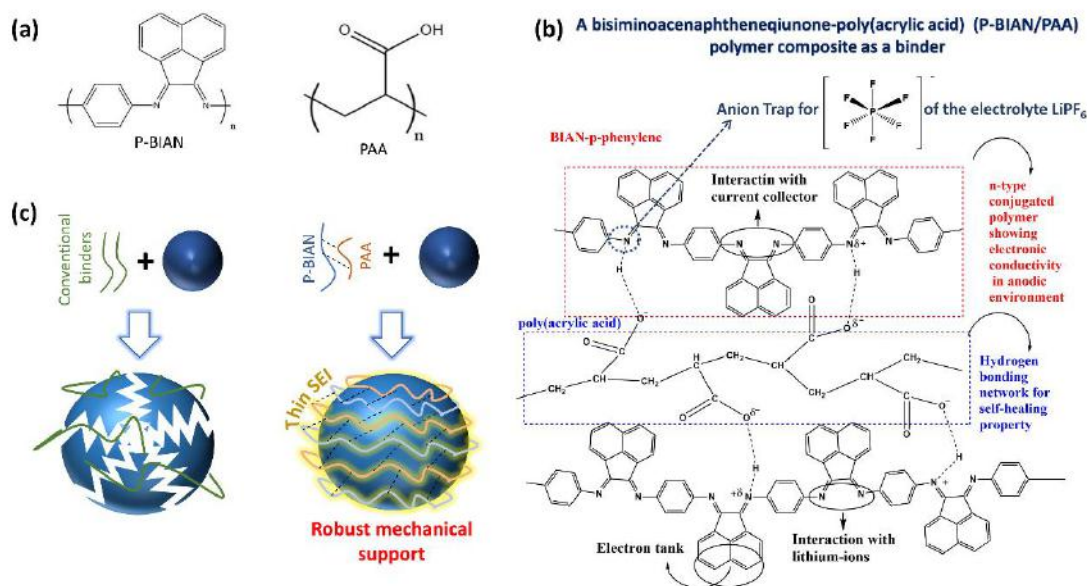


**Figure 1:** (a) Chemical structures of the precursor polymers P-BIAN and PAA, (b) Schematic of the P-BIAN/PAA composite showing its design strategy, and (c) Schematic comparing the improved mechanical robustness in case of P-BIAN/PAA composite that can prevent Si-anodes from getting pulverized prematurely with that of the conventional binders and repair the cracks by filling owing to its self-healing property.

### 3.3 Experimental Section

#### 3.3.1 Materials

Acenaphthenequinone, 1,4-phenylenediamine, *N*-methylpyrrolidone (NMP), and acetic acid were purchased from Tokyo Chemical Industry Co., Ltd. Super dehydrated acetonitrile was purchased from Wako Pure Chemical Industries, Ltd. Poly(acrylic acid) was purchased from Sigma-Aldrich. 1.0 M  $LiPF_6$  (50/50) EC/DEC electrolyte was purchased from Sigma-Aldrich. Silicon nanoparticles (SiNPs) of size <100 nm was purchased from Aldrich, Graphite superfine powder (<50  $\mu\text{m}$ ) was procured from Merck to be used as an active material. Battery-grade acetylene black was purchased from Denka Japan Private Co., Ltd., to be used as a conductive additive. Copper foil of a thickness of 20  $\mu\text{m}$  was purchased from the Nilaco corporation. All the chemicals were used without any further purification.

### 3.3.2 Electrode preparation

The P-BIAN copolymer was synthesized by following the procedure reported by our group<sup>26</sup>. The synthetic scheme is shown in Figure 2. The P-BIAN/PAA synthesis and electrode preparation followed a one-pot synthetic scheme. The P-BIAN and PAA polymers (20:5 wt. %) were heated at 80 °C with stirring for 3 hours in a polar aprotic solvent *N*-methyl-2-pyrrolidone (NMP). To the above reaction mixture, 25 wt % silicon nanoparticles (SiNPs) were then added, and the reaction mixture was refluxed at 180 °C for 3 hours with slow stirring and intermittent ultra-sonication for 30 minutes at room temperature. After 3 hours of reflux, 30 wt % graphite super fine powder and 15 wt % acetylene black (AB) were added, and the resultant reaction mixture was refluxed at 180 °C for 6 hours to obtain a slurry of good uniformity. The obtained slurry was coated on a copper foil of a thickness of ~20 μm. The coated electrode was vacuum dried and calendered at 50 μm thickness at 80 °C. The Si/C composite electrode was prepared with constituents Si/C/P-BIAN/PAA/AB in the ratio 25 wt% : 30 wt% : 25 wt% : 20 wt%, respectively with P-BIAN and PAA in 1.5:1 molar ratio. The electrode for the control study was prepared with the conventional PAA binder having constituents (Si/C/PAA/AB) in the ratio 25 wt% : 30 wt% : 25 wt% : 20 wt%, respectively.

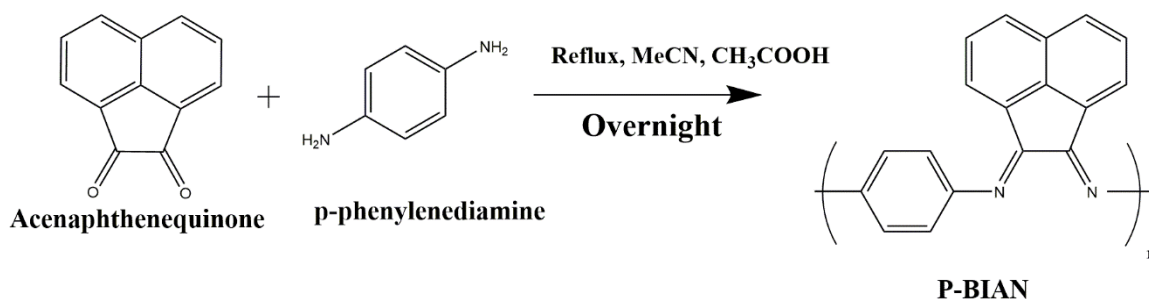


**Figure 2:** Synthetic scheme of the P-BIAN

### 3.3.3 Characterization of electrodes

The FT-IR spectrum was recorded using Perkin Elmer 100 FT-IR spectrometer. The spectrum was averaged over 100 scans with a resolution of 2 cm<sup>-1</sup> in the ATR mode. The morphology and composition of the samples were determined by FESEM (Hitachi S-4500 instrument at 1.0 kV voltage) and X-ray photoelectron spectroscopy (XPS) measurements were conducted on Fisons instruments S-probe TM 2803.

### 3.3.4 Coin-cell fabrication and electrochemical characterization

2025-type coin cells were fabricated configuring Si/C as an anode, polypropylene separator (25  $\mu\text{m}$ , Celgard 2500), 1.0M LiPF<sub>6</sub> in (50/50) EC/DEC electrolyte, and Li metal as the counter as well as the reference electrode. The molar ratio between the EC of the electrolyte and P-BIAN present in the electrode was 1:1.8. The anodic half-cells were fabricated in an argon-filled glovebox (UNICO UN-650, H<sub>2</sub>O, and O<sub>2</sub> level <0.1 ppm). Electrofield-EFT-001 was used for the charge and discharge tests at 25 °C. A VSP potentiostat (BioLogic) electrochemical analyzer/workstation was used for the electrochemical characterization of the fabricated half-cells by cyclic voltammetry (CV) measurements between OCP and 0.01 V vs Li/Li<sup>+</sup> at 25 °C at a scan rate of 0.1 mVs<sup>-1</sup>. Electrochemical impedance spectroscopy (EIS) and dynamic electrochemical impedance spectroscopy (DEIS) studies were conducted on a VSP potentiostat (Biologic) within a frequency range of 10 mHz to 0.1 Hz with a sinus amplitude of 10 mV.

## 3.4 Results and Discussion

### 3.4.1 Theoretical studies

For the rational design of binders for Si anodes, it is essential to calculate their highest occupied molecular orbital (HOMO) and lowest unoccupied molecular orbital (LUMO) energy levels<sup>27</sup>. Compounds with a high lying HOMO are susceptible to gradual oxidation. Those with a low lying LUMO tend to undergo reduction in the cathodic and anodic environments, respectively<sup>28-29</sup>. In comparison with the electrolyte components, the conjugated compounds of the BIAN family have a low lying LUMO owing to their diimine backbone<sup>25</sup>. But for the strategic application of BIAN-based polymers to tailor the formation of a thin SEI on the anode surface, it was important to engineer the LUMO energy level of P-BIAN through combination with external dopant polymer (PAA) for further reduction of the LUMO level. In this regard, the dynamic crosslinking of the BIAN moiety with PAA as a dopant was computationally mimicked and evaluated by the DFT-based geometry and energy optimization calculations were executed on the Materials Studio (Dmol3). The computational parameters were as follows: DND basis set, gga (pW91) density functional, and unrestricted spin polarization. The DFT optimized structure highlighting the electrostatic hydrogen bonding between the diimine of P-BIAN and the carboxyl group of PAA is shown in Figure 3a. The comparison between the HOMO-LUMO energy levels of the electrolyte components (ethylene carbonate (EC) and

diethyl carbonate (DEC)), P-BIAN, and P-BIAN/PAA is shown in Figure 3b. The carbonate components of the electrolyte EC/DEC were found to have high-lying LUMOs ( $E_{\text{LUMO}} = -0.28$  eV for EC &  $-0.06$  eV for DEC) whereas the P-BIAN/PAA composite binder was evaluated to be having  $E_{\text{LUMO}} = -3.4$  eV. Also, as listed in Table 1, the LUMO of P-BIAN/PAA binder was substantially low in comparison with the conventional binders like CMC, SBR, poly(vinyl chloride), etc<sup>27</sup>. Unlike conventional binders, because of the presence of low lying LUMO in the reducing anodic environment, the n-dopable P-BIAN/PAA composite binder is expected to have the potential to influence the formation of a thin SEI that can promote an enhanced lithium-diffusion and reduce the interfacial impedance by restricting the excessive electrolyte decomposition on the anode surface.

**Table 1:** A list of the HOMO-LUMO energy level values of various kinds of binders.

Binders	HOMO (eV)	LUMO (eV)	Reference
PEO	-11.2	7.1	27
SBR	-8.9	5.1	
PMA	-12.2	4.95	
CMC	-12.1	4.8	
PVC	-12.2	4.78	
PVDF	-12.47	1.46	25
PAA	-6.1	-1.3	Our work
P-BIAN	-4.58	-3.17	
P-BIAN/PAA	-4.4	-3.4	Our work

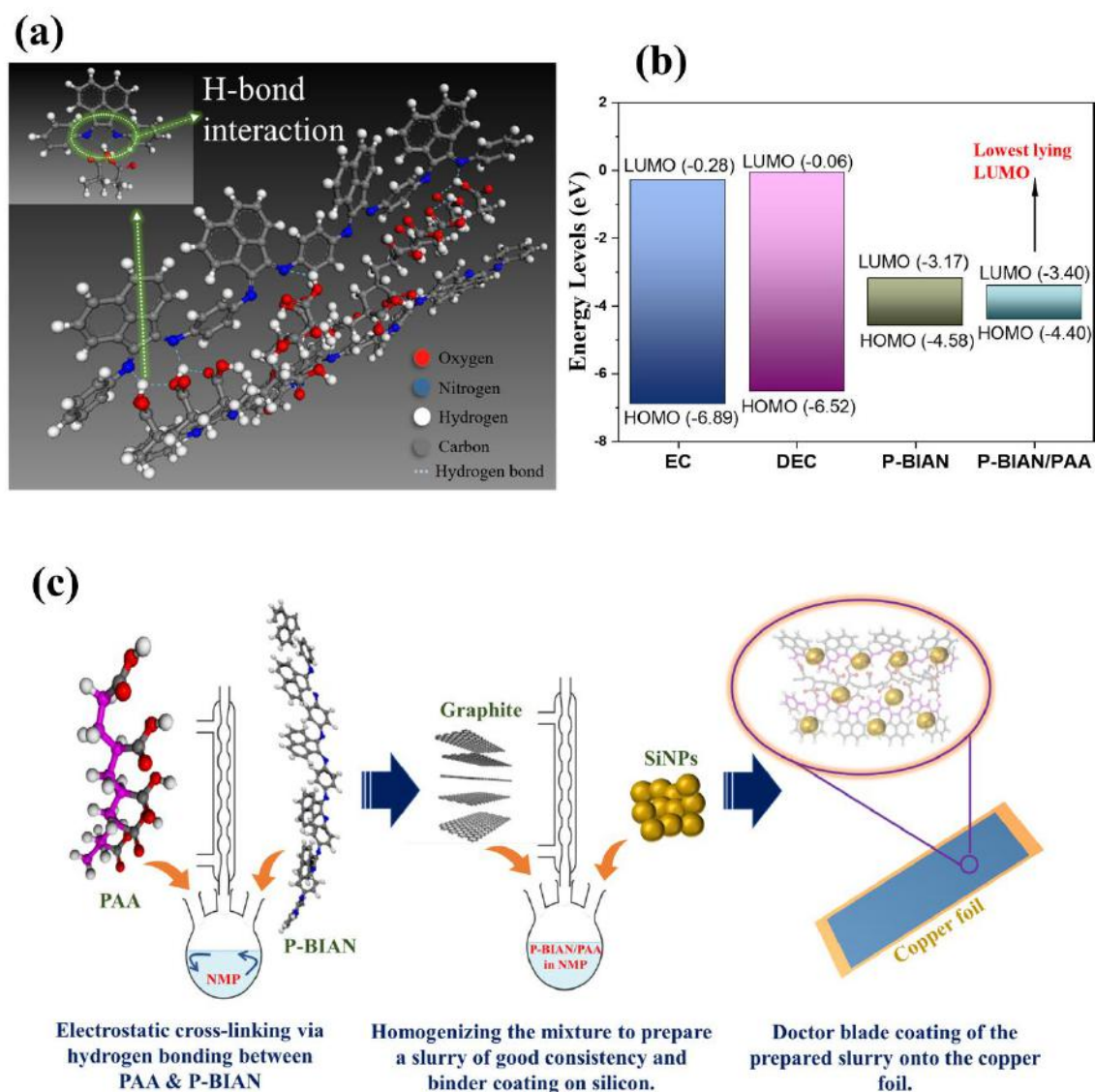


**Figure 3:** (a) Optimized structure P-BIAN/PAA polymer composite, (b) HOMO-LUMO energy level comparison between the electrolyte components, P-BIAN, and P-BIAN/PAA binder, and (c) schematic of the preparation procedure of Si/C/P-BIAN/PAA/AB electrode.

### 3.4.2 Pristine electrode characterization

We have studied the properties of LIB anode with P-BIAN/PAA as a self-healing conducting binder, SiNPs/graphite (Si/C) composite as the active materials, and acetylene black (AB) as conductive additive. The Si/C/P-BIAN/PAA/AB composite electrode was prepared by casting and coating the slurry on the copper foil prepared in one-pot reflux set-up as outlined in the schematic shown in Figure 3c. The prepared Si/C/P-BIAN/PAA/AB pristine electrode was characterized by XPS and FT-IR techniques. Since all the nitrogen atoms in the diimine (C=N) backbone of the BIAN framework are  $-sp^2$  hybridized, the XPS N 1s spectrum

(Figure 4a) of the BP-copolymer showed only one characteristic  $-sp^2$ -type nitrogen peak at 399.5 eV<sup>30</sup>. However, on mixing of P-BIAN with PAA via hydrogen bonding followed by the interaction of the P-BIAN/PAA composite binder with SiNPs during the slurry preparation, the XPS N 1s spectrum of the pristine Si/C/P-BIAN/PAA/AB anode showed two distinct peaks (Figure 4b). The peak at 399.5 eV was attributed to the typical diimine (C=N) nitrogen of the BIAN and the peak at 401.0 eV was attributed to the quaternary diimine nitrogen atoms reflecting their cumulative participation in the electrostatic hydrogen bonding with PAA and the surface hydroxyl groups on SiNPs (Figure 5)<sup>31-32</sup>. To support the XPS studies in establishing the successful electrostatic networking of P-BIAN and PAA via hydrogen bonding during the electrode preparation, FT-IR spectra of the Si/C/P-BIAN/PAA/AB pristine electrode, commercial SiNPs, P-BIAN, and PAA were recorded as shown in Figure 4c. In the spectral profile of the P-BIAN, bands at 1659  $\text{cm}^{-1}$  and 772  $\text{cm}^{-1}$  were attributed to the stretching vibrations of (C=N) and wagging vibrations of (C-N) of the diimine framework in the P-BIAN, respectively<sup>33-34</sup>. The spectral profile of PAA showed characteristic bands at 3550-2450  $\text{cm}^{-1}$ , 1700  $\text{cm}^{-1}$ , 1458  $\text{cm}^{-1}$ , 1465  $\text{cm}^{-1}$ , and 1165  $\text{cm}^{-1}$  attributed to stretching vibrations of (OH): carboxylic acid, (C=O): carboxylic acid, bending vibration of (OH): carboxylic acid, methylene (C-H) backbone, and (C-O), respectively<sup>35-36</sup>. The commercially obtained SiNPs showed bands at 2900-3400  $\text{cm}^{-1}$  and 1190-1076  $\text{cm}^{-1}$  attributed to the stretching vibrations of Si-OH and asymmetric stretching vibrations of Si-O-Si<sup>37</sup>. In the spectral profile of the Si/C/P-BIAN/PAA/AB pristine electrode, particularly, our attention was focused on regions characteristic to the P-BIAN/PAA composite binder with the presence of bands (i) in the region 2750-3000  $\text{cm}^{-1}$ : attributed to quaternary N-H vibrational stretch of H-bonded nitrogen atoms<sup>38-39</sup> in P-BIAN/PAA connected via electrostatic hydrogen bonding between the P-BIAN moiety and PAA as well as in the region 2650-3300  $\text{cm}^{-1}$ : attributed to intermolecular bonded (-OH-- ) of PAA<sup>40</sup>, (ii) at 1700  $\text{cm}^{-1}$ : attributed to (C=O) vibrational stretch of PAA<sup>35-36</sup>, and (iii) at 1585  $\text{cm}^{-1}$ : attributed to (C=N) vibrational stretch of the diimine nitrogen in the P-BIAN moiety<sup>33-34</sup>. The comprehensive band assignments of the respective spectral profiles are listed in Table 2. Therefore, the XPS studies supported by the FT-IR analysis confirmed significant interaction of P-BIAN with PAA along with SiNPs by dynamic electrostatic hydrogen bonding interaction during the electrode preparation.

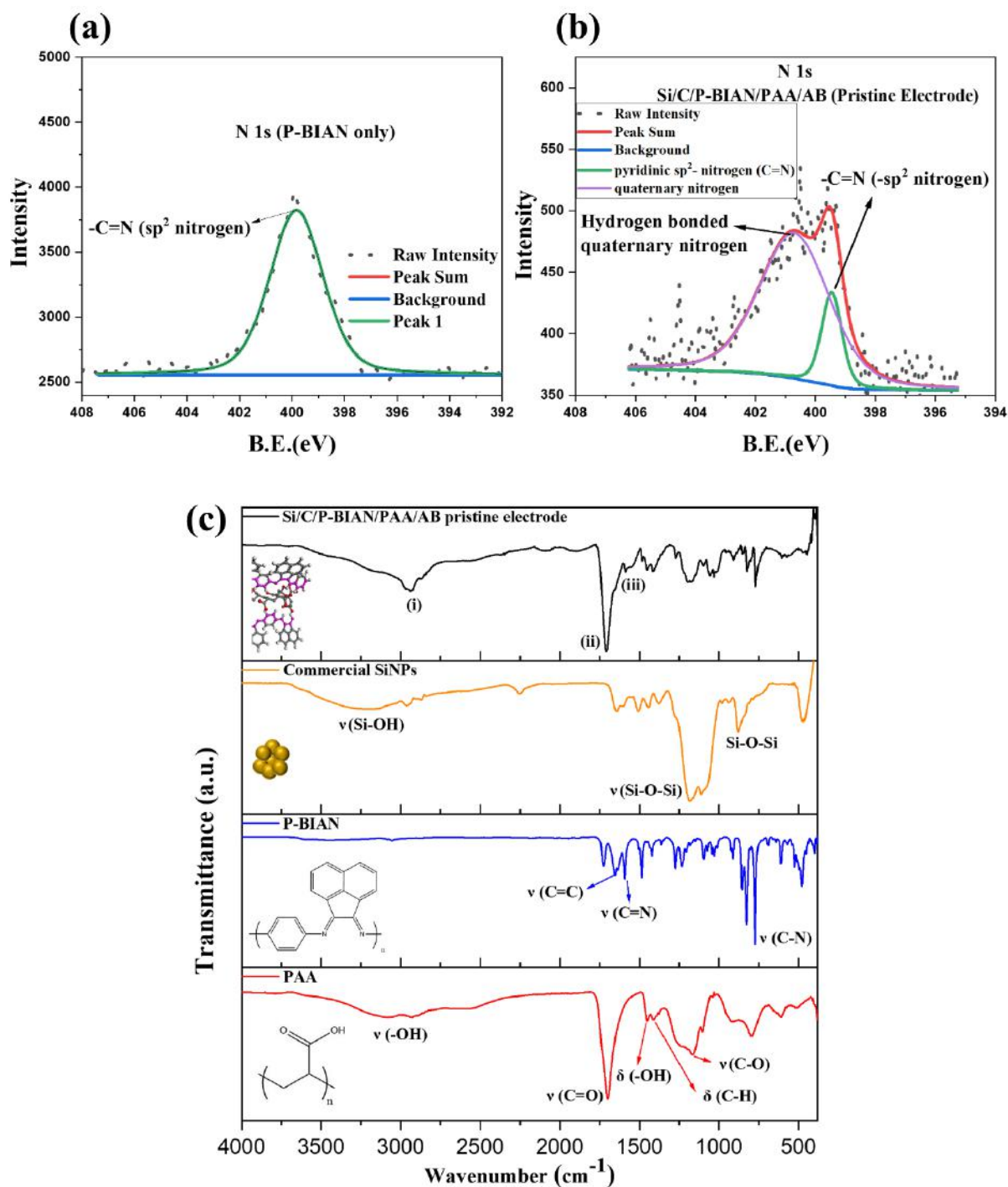


**Figure 4:** XPS N 1s spectrum of (a) the pristine P-BIAN and (b) pristine Si/C/P-BIAN/PAA/AB electrode. (c) FT-IR spectra of the pristine Si/C/P-BIAN/PAA/AB electrode, commercial SiNPs, P-BIAN, and PAA, respectively

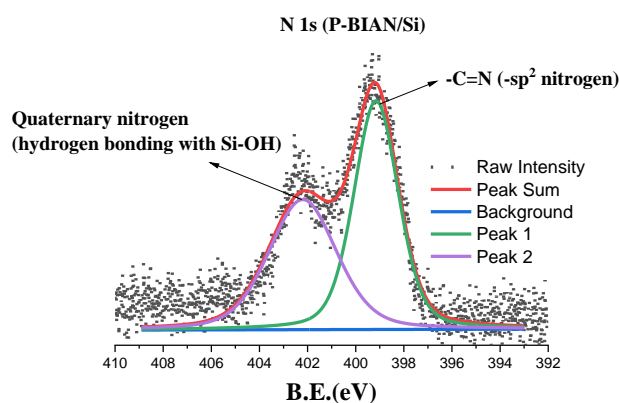


**Figure 5:** XPS N 1s spectrum of P-BIAN copolymer/SiNPs composite.

**Table 2:** FT-IR assignments of the following systems: P-BIAN, PAA, commercial SiNPs, and pristine Si/C/P-BIAN/PAA/AB anode.

Species	Observed Bands (cm <sup>-1</sup> )	Expected Region (cm <sup>-1</sup> )	Assignment	Reference
<b>P-BIAN</b>	1659 (m) 1592 (m) 772 (s)	1650-1600 1640-1570 1120-700	$\nu$ (C=C) aromatic $\nu$ (C=N) imine $\omega$ (C-N) aromatic amine	41 33-34 33-34
<b>PAA</b>	3550-2450 (s, broad) 1700 (vs) 1458 (m) 1465 (m) 1165 (s)	3500-2500 1760-1670 1440-1395 1450-1500 1000-1300	$\nu^s$ (OH) carboxylic acid $\nu$ (C=O) carboxylic acid $\delta$ (OH) carboxylic acid $\delta$ (C-H) methylene $\nu^s$ (C-O)	35-36
<b>SiNPs (commercial)</b>	2900-3400 (s, broad) 1190-1076 (s, broad)	2700-3350 1000-1250	$\nu^s$ (Si-OH) $\nu^a$ (Si-O-Si)	37



<b>Si/C/P- BIAN/PAA/AB pristine electrode</b>	2750-3000 (s, broad)	2800-3000	$\nu^s$ (N-H) amine salt	38-39
	2650-3300 (s, broad)	2700-3300	$\nu^s$ (OH) intermolecular bonded	40
	1700 (s)	1760-1670	$\nu$ (C=O) carboxylic	35-36
	1585 (m)	1640-1570	acid	35-36
	1396 (m)	1440-1395	$\nu$ (C=N) imine	35-36
	1457 (m)	1450-1500	$\delta$ (OH) carboxylic acid	35-36
	1032 (s, broad)	1000-1250	$\delta$ (C-H) methylene $\nu^a$ (Si-O-Si)	37

<sup>a</sup>Relative intensities are shown in parentheses:  $\nu^s$  – very strong, s – strong, and m – medium.

<sup>b</sup> $\nu$ : stretching,  $\omega$  wagging, and  $\delta$ : bending; a: asymmetric mode, s: symmetric mode.

### 3.4.3 Electrochemical characterization

For the electrochemical characterization, anodic half-cells with three different configurations were fabricated: (i) with P-BIAN/PAA binder-based anode (Si/C/P-BIAN/PAA/AB anode = 25/30/25/20 by wt % ) with the electrode thickness  $\sim 27 \mu\text{m}$  and active material (Si/C) loading of  $\sim 0.87 \text{ mg cm}^{-2}$ , (ii) control system with the conventional PAA binder-based anode (Si/C/PAA/AB anode = 25/30/25/20 by wt % ) with the electrode thickness  $\sim 25 \mu\text{m}$  and active material (Si/C) loading of  $\sim 0.83 \text{ mg cm}^{-2}$ , and (iii) only P-BIAN binder-based anode (Si/C/P-BIAN/AB anode = 25/30/25/20 by wt%) with electrode thickness  $\sim 25 \mu\text{m}$  and active material (Si/C) loading of  $\sim 0.84 \text{ mg cm}^{-2}$ .

#### Cyclic voltammetry studies

The fabricated anodic half-cells were subjected to cyclic voltammetry (CV) studies. Figure 6a shows the cyclic voltammogram of Si/C/P-BIAN/PAA/AB-based anodic half-cell recorded at 0.66 V was characteristic to the electrolytic decomposition at the anode surface<sup>42</sup> forming SEI and the initial alloying of the crystalline Si ( $\text{Li}_{15}\text{Si}_4$ ) was observed at 0.0047 V<sup>43</sup>. However, from the second reverse scan onwards, the peak corresponding to the formation of amorphous lithiated Si phase ( $\text{Li}_{12}\text{Si}_7$ ) was observed at 0.17 V<sup>43</sup>. In the forward scan, the two anodic peaks characteristic to the transformation of amorphous  $\text{Li}_x\text{Si}$  to Si phase were observed at 0.32 V and 0.53 V, respectively.<sup>19-20, 43</sup> Similar characteristic peaks were observed in the CV

profile of the control system as shown in Figure 6b. These characteristic peaks were consistent with the previous reports on silicon anodes<sup>43-45</sup>. To compare the extent of electrolyte decomposition between both the systems, the area under the curve in the electrolytic decomposition potential range for respective first reverse scans was calculated. For Si/C/P-BIAN/PAA/AB anodic half-cell, the mathematical area under the curve in the potential range 0.53 V - 0.73 V was calculated to be -1.96 (Figure 6c). Whereas for the control system, the mathematical area under the curve in the potential range 0.47 V – 0.76 V was calculated to be -7.91 which is approximately 4 times larger than the Si/C/P-BIAN/PAA/AB anodic half-cell (Figure 6d). Thus, due to the low lying LUMO of the P-BIAN/PAA binder, its n-doping in the reducing anodic environment restricted the extent of electrolyte decomposition on the surface of Si/C/P-BIAN/PAA/AB anode against the control system. As a result, in the case of Si/C/P-BIAN/PAA/AB anodic half-cell, the anodic currents of 3<sup>rd</sup> and 4<sup>th</sup> cycles superimposed with distinctive Si dealloying peaks with higher intensity are showing better cyclic stability unlike the control system (Figure 6e).

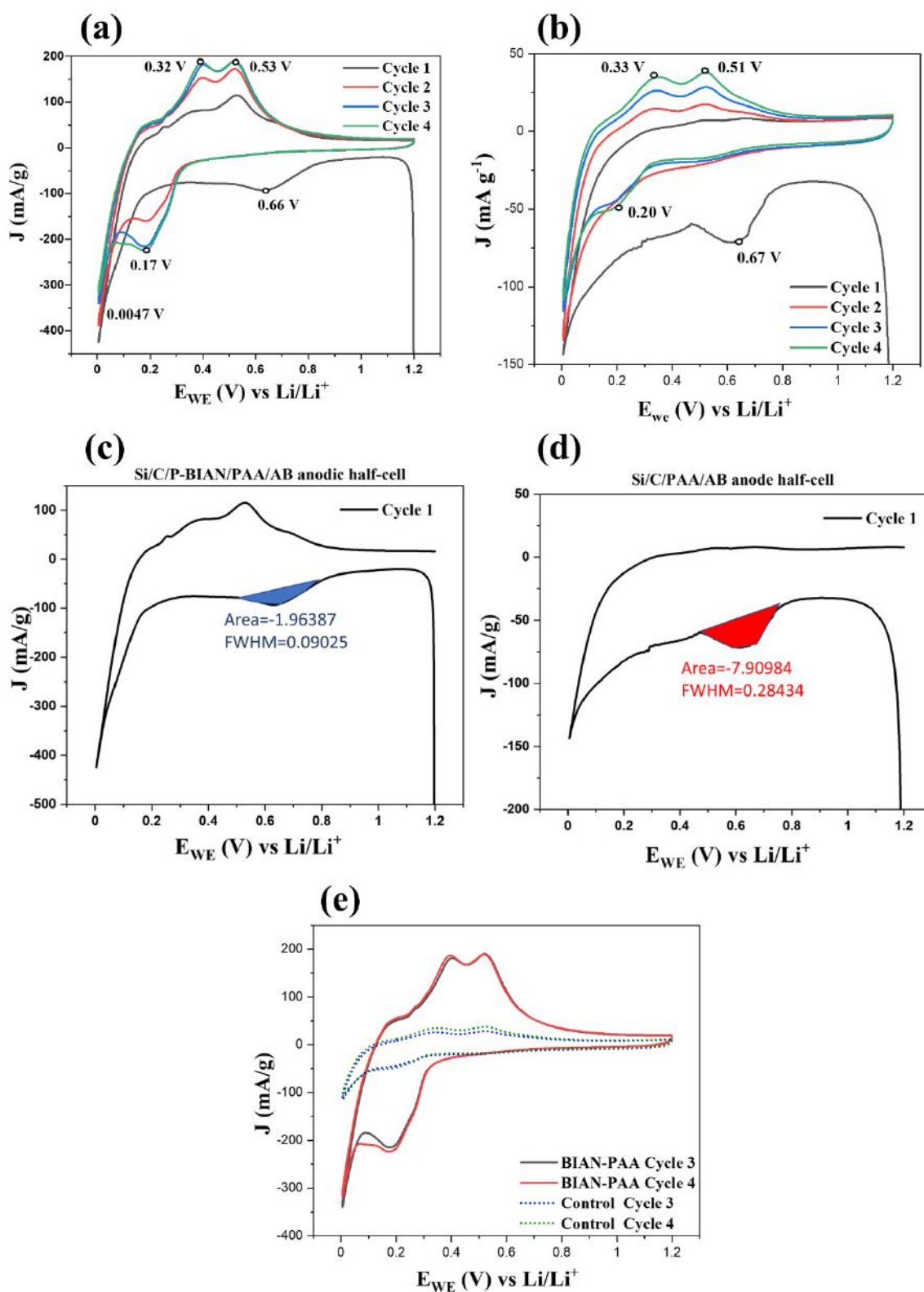


**Figure 6:** Electrochemical performance comparison between Si/C/P-BIAN/PAA/AB anode and control system. (a) Cyclic voltammograms of the Si/C/P-BIAN/PAA/AB anodic half-cell and (b) Cyclic voltammogram of the control system (PAA binder-based anodic half-cell). Mathematical area under the curve for the first reverse scan profile of (c) Si/C/P-

BIAN/PAA/AB anodic half-cell, (d) control system, and (e) comparison of the 3<sup>rd</sup> and 4<sup>th</sup> cycles cyclic voltammograms of Si/C/P-BIAN/PAA/AB anodic half-cell and control system, respectively.

### Charge-discharge studies

Figure 7a demonstrates the long-term cycling profiles the Si/C/P-BIAN/PAA/AB anode and control system recorded at a current density of 500 mA g<sup>-1</sup>. The Si/C/P-BIAN/PAA/AB anode shows the first cycle reversible capacity of 3202 mAh g<sup>-1</sup><sub>Si</sub> with an initial coulombic efficiency (ICE) of 87.54% against the control system showing a reversible capacity of 1893 mAh g<sup>-1</sup><sub>Si</sub> with an ICE of 82.36%. Further, in the case of Si/C/P-BIAN/PAA/AB anode, the reversible capacity stabilizes to ~2100 mAh g<sup>-1</sup><sub>Si</sub> within 18 cycles against the control system which takes 50 cycles of de-/alloying to stabilize at ~1500 mAh g<sup>-1</sup><sub>Si</sub>. Notably, the P-BIAN/PAA composite binder stabilized the performance of Si anodes up to over 600 cycles with the reversible capacity of ~2100 mAh g<sup>-1</sup><sub>Si</sub> against the control system with the reversible capacity of 900 mAh g<sup>-1</sup><sub>Si</sub> after only 320 cycles. Figure 7b shows the galvanostatic de-/alloying profiles of the 1<sup>st</sup>, 10<sup>th</sup>, 100<sup>th</sup>, 300<sup>th</sup> and 600<sup>th</sup> cycles of Si anodes with P-BIAN/PAA composite binder at a current density of 500 mA g<sup>-1</sup>. In the alloying half-cycle, the plateau in the potential region 0.12 V – 0.23 V vs Li/Li<sup>+</sup> corresponds to the lithium alloying of amorphous silicon ( $\alpha$ -Li<sub>x</sub>Si). In the dealloying half-cycle, plateaus in potential regions 0.52 V – 0.35 V vs Li/Li<sup>+</sup> and 0.32 V – 0.19 V vs Li/Li<sup>+</sup> correspond to the dealloying of amorphous Li<sub>x</sub>Si phase to Si which were consistent with the representative peaks observed in cyclic voltammograms (Figure 6a). The CEs corresponding to the first 20 cycles of de-/alloying for Si/C/P-BIAN/PAA/AB anodic half-cell and control system were compared and analysed as shown in Figure 7c. The initial coulombic efficiency (ICE) for Si/C/P-BIAN/PAA/AB anode was recorded to be 87.54% against the control system with 82.36%. This reflected the lower extent of irreversible capacity loss in case of Si/C/P-BIAN/PAA/AB anode in comparison to the control system because of the restricted electrolyte decomposition. Also, the CE corresponding to the Si/C/P-BIAN/PAA/AB anode averaged to ~98.9% within first 20 cycles in comparison to the control system with an average of ~95.0%. This indicated that the electrolyte decomposition on the anode surface in case of the control system was spanning over 20 cycles of de-/alloying owing to the exposure of new Si surfaces because of poor binding ability. This could lead to a potentially thick SEI in case of the control system. Whereas, in the case of Si/C/P-BIAN/PAA/AB anodic half-cell, the quick stabilization of the coulombic efficiency to 98.9% within first 5 cycles showed that the excellent binding ability of P-

BIAN/PAA binder which restricted the pulverization of SiNPs and their exposure to the electrolyte. Therefore, it could potentially have an optimally thin SEI. Figure 7d compares the reversible capacity retention between the control system and Si/C/P-BIAN/PAA/AB anode. The average capacity retention in the case of Si/C/P-BIAN/PAA/AB-based anode was determined to be  $\sim 95.0\%$  after 600 cycles whereas in the case of the control system the average capacity retention dropped to  $\sim 54.0\%$  after 320 cycles of de-/alloying. Hence, the Si/C/P-BIAN/PAA/AB anode outperformed the control system in terms of specific reversible capacity, cyclability, and capacity retention.

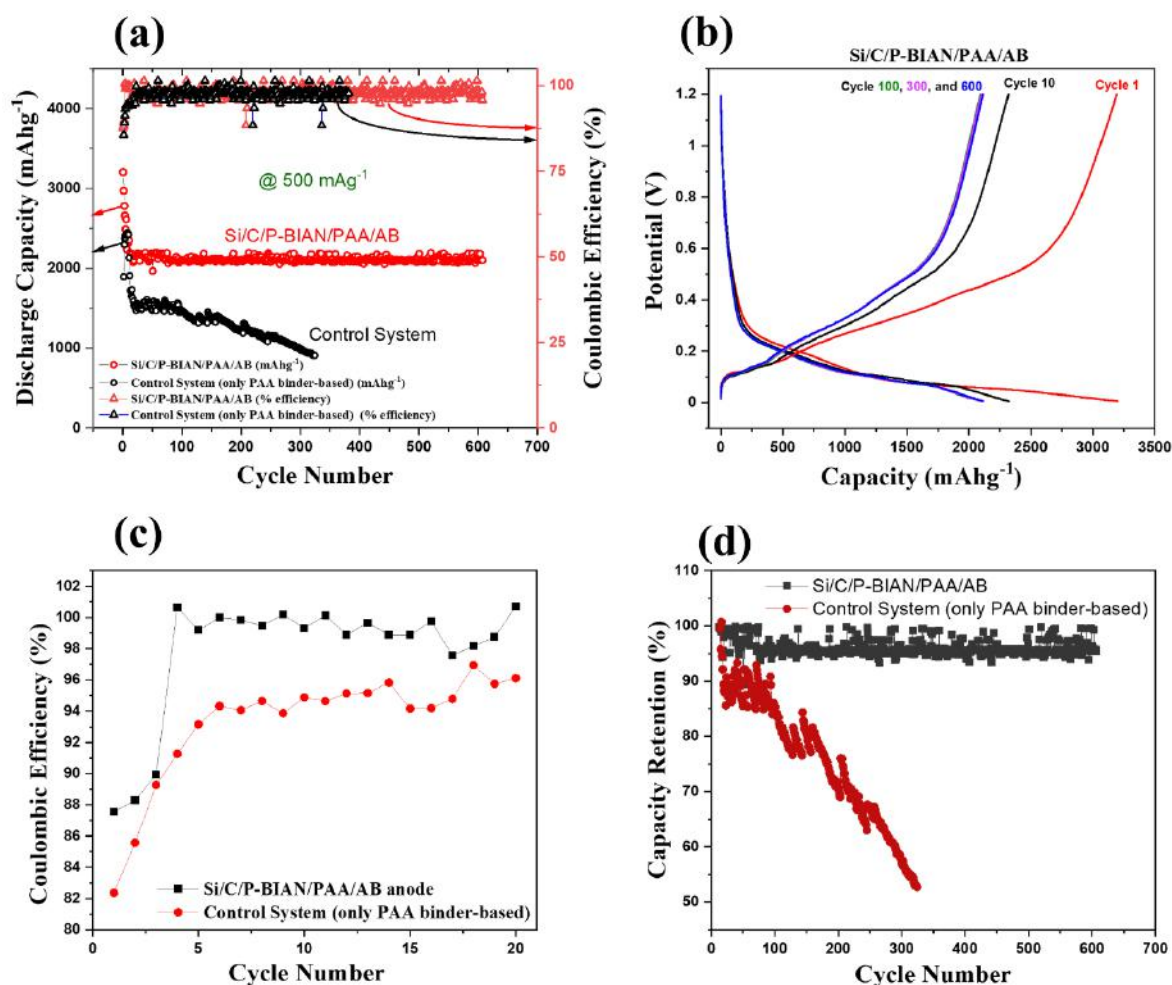


**Figure 7:** Charge-discharge studies of Si/C/P-BIAN/PAA/AB anode-based cell and control system (only PAA binder-based). (a) long-term cycling stability comparison of Si anodes with P-BIAN/PAA binder and control system (only PAA binder-based) at 500 mA g<sup>-1</sup>, (b) charge and discharge profiles of Si/C/P-BIAN/PAA/AB anode at 500 mA g<sup>-1</sup>, (c) coulombic efficiency comparison plot for the first 20 cycles of de-/alloying between the control system (only PAA binder-based) and Si/C/P-BIAN/PAA/AB anodic half-cell, and (d) comparison of capacity retention between the control system and Si/C/P-BIAN/PAA/AB anode.

retention of Si/C/P-BIAN/PAA/AB anode with the control system (only PAA binder-based), respectively.

#### **(Dynamic) electrochemical impedance spectroscopy studies**

To determine the internal impedance in Si/C/P-BIAN/PAA/AB anodic half-cell, electrochemical impedance spectroscopy (EIS) studies were carried out. The EIS measurements were recorded at open circuit potential (OCP) without direct current (DC). Figures 8a and 8b show the Nyquist comparison profiles between Si/C/P-BIAN/PAA/AB anodic-half-cell and control system recorded after fabrication and after CV, respectively. The internal impedance of the Si/C/P-BIAN/PAA/AB anode after fabrication was 620  $\Omega$  against the control system with 1100  $\Omega$ . After CV studies, for Si/C/P-BIAN/PAA/AB anode, the internal impedance reduced to 360  $\Omega$  ( $R_{SEI}+R_{CT}$ ) against the control system with 800  $\Omega$  ( $R_{SEI}+R_{CT}$ ). To understand the improvement in the interfacial properties during the cycling, Nyquist plots after 15, 30, and 50 cycles of de-/alloying were recorded at the state of discharge as shown in Figures 8c and 8d. With increasing number of cycles, as the SEI matured, the internal impedance of the Si/C/P-BIAN/PAA/AB anodic half-cell decreased. Whereas, in the case of the control system, though the internal impedance decreased with increasing cycle number, it was always higher than the Si/C/P-BIAN/PAA/AB anodic half-cell. This is indicative of the impact of the extent of electrolyte decomposition on the internal impedance of the cell as well as its long-term cycling performance.

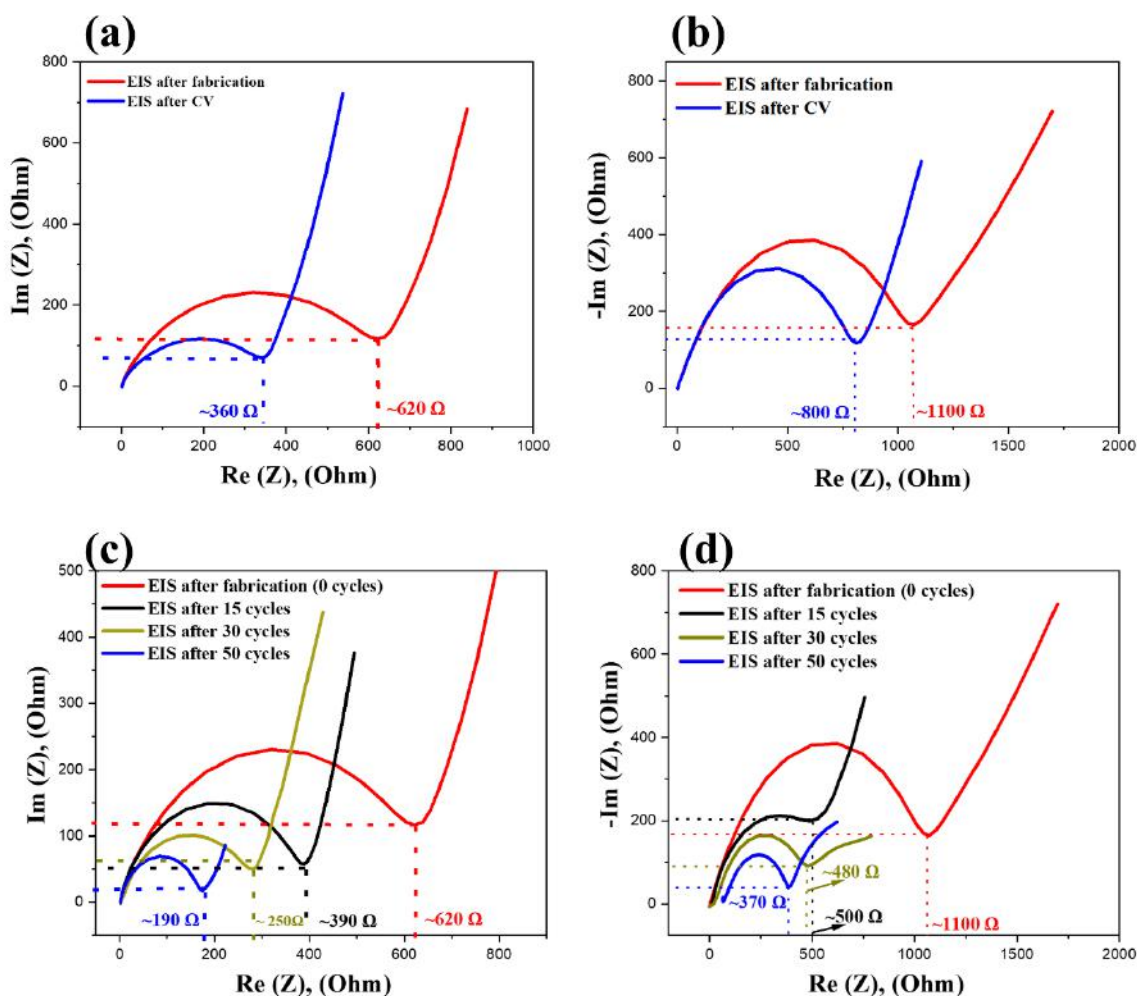


**Figure 8:** Nyquist impedance profiles recorded after fabrication and CV of (a) Si/C/P-BIAN/PAA/AB anodic half-cell, and (b) the control system. Nyquist impedance profiles recorded after fabrication, 15 cycles, 30 cycles, and 50 cycles of charge & discharge of (c) Si/C/P-BIAN/PAA/AB anodic half-cell, and (d) the control system.

Therefore, to analyze the types of interfaces present and their contribution to the overall cell impedance, dynamic electrochemical impedance spectroscopy (DEIS) studies were carried out. In DEIS, the impedance profiles were recorded at various potentials during the charge & discharge which helped in reflecting various interfacial processes happening during the real time cycling of the battery. The frequency response of anodic half-cells was recorded corresponding to an AC signal in the potential window of 0.005 V – 1.2 V vs Li/Li<sup>+</sup>. The DEIS 3-D Nyquist profile during the alloying half-cycle for Si/C/P-BIAN/PAA/AB anodic half-cell and the control system are shown in Figures 9a and 9b, respectively. Similarly, the DEIS 3-D Nyquist profile during the dealloying half-cycle are shown in Figure 9c and 9d. To understand the types of interfaces, various probable Equivalent Electric Circuit Models (EECMs) were

tried to fit the DEIS Nyquist profiles. The best fit EECM was (RL(QR)(CR)(QR)(CW)) is shown in Figure 9e. The elements corresponding to the EECM were sequentially classified as follows: Ohmic electrolytic resistance ( $R_e$ ), intrinsic resistance of the silicon anode comprising of the particle to particle and particle to current collector ( $R_{PC}$ ), solid-electrolyte interface ( $R_{SEI}$ ), charge transfer resistance ( $R_{CT}$ ), and Warburg infinite diffusion element ( $Z_{GFW}$ ). Table 3 & 4 tabulate the resistance values corresponding to each of the interface elements as classified by EECM for the Si/C/P-BIAN/PAA/AB and control systems, respectively. The SEI resistance ( $R_{SEI}$ ) comparison between the control system and Si/C/P-BIAN/PAA/AB anodic half-cell during lithiation is shown in Figure 9f. In the case of Si/C/P-BIAN/PAA/AB anodic half-cell, the interfacial impedance ( $R_{SEI}$ ) was substantially lower than the control system owing to the restricted electrolytic decomposition as well as stabilized long-term de-/alloying of SiNPs without exposure of new Si surfaces due to their pulverization. The representative Nyquist plot fit with the EECM (Figure 10) shows the corresponding attributed interfaces. Hence, the DEIS studies provided a comprehensive understanding on the types of interfaces and their corresponding impedance values for Si/C/P-BIAN/PAA/AB anode and the control system, respectively.



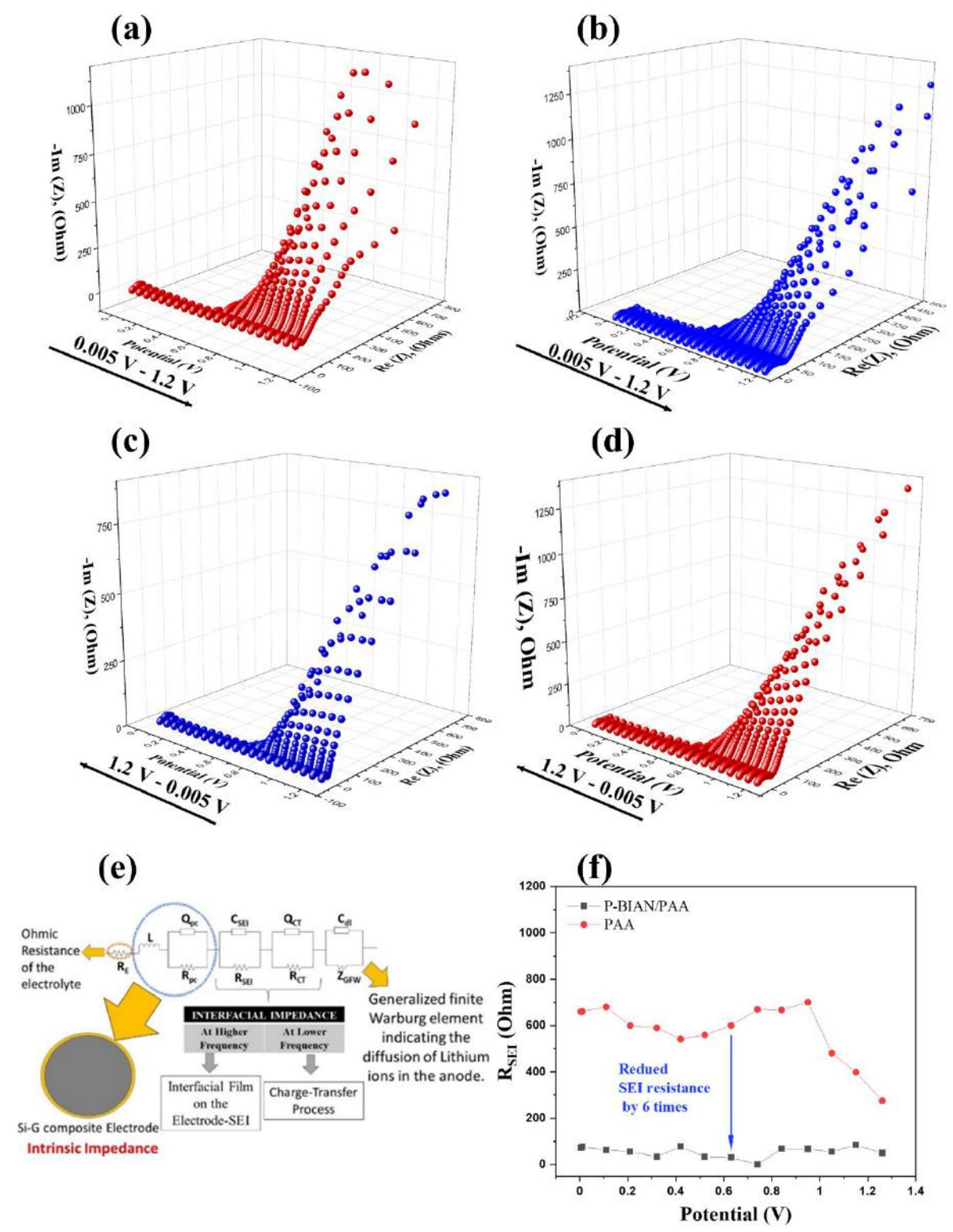


**Figure 9:** DEIS profiles during the alloying process after 100 cycles for (a) Si/C/P-BIAN/PAA/AB anodic half-cell, and (b) the control system. DEIS profiles during dealloying after 100 cycles for (c) Si/C/P-BIAN/PAA/AB anodic half-cell, and (d) control system (only PAA binder). (e) Equivalent circuit model (EECM) used to fit the DEIS data and (f) a

comparison plot of SEI impedance ( $R_{SEI}$ ) vs potential (V) during lithiation for Si/C/P-BIAN/PAA/AB anodic half-cell and the control system.

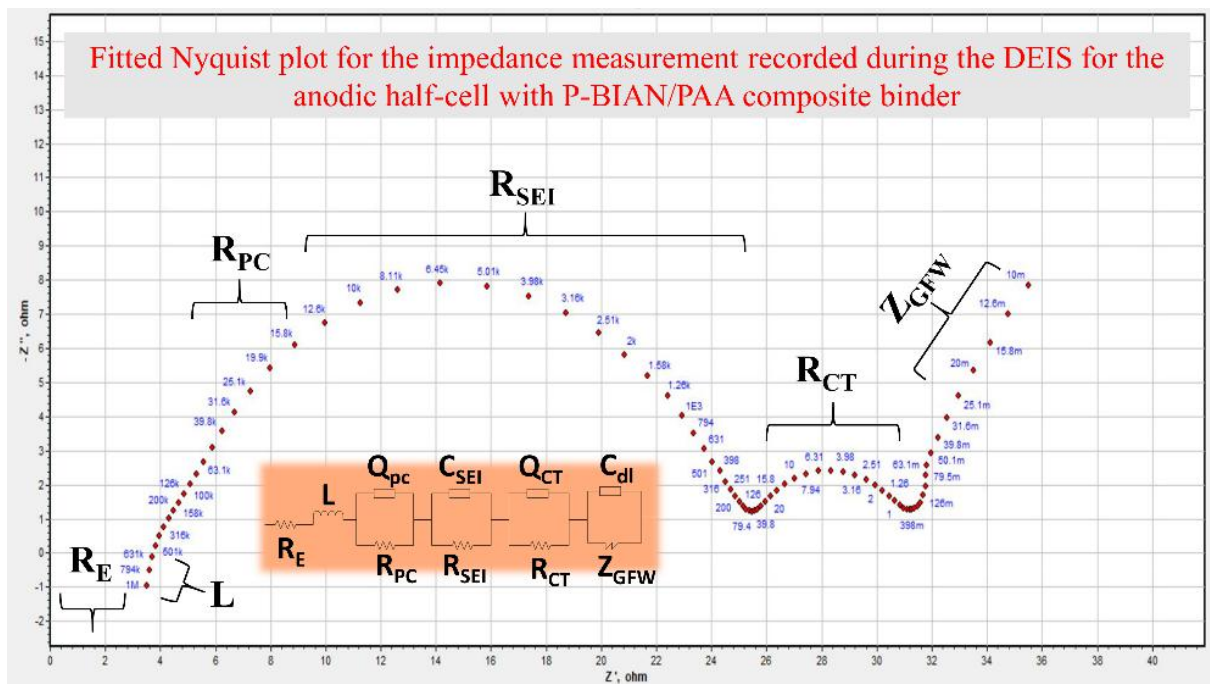


**Figure 10:** An EECM fit representative Nyquist plot during lithiation in the case of the Si/C/P-BIAN/PAA/AB anodic half-cell showing various interfaces.

**Table 3:** DEIS circuit fitting parameters during charging for Si/C/P-BIAN/PAA/AB anodic half-cell

$R_s$	$R_{PC}$	$R_{SEI}$	$R_{CT}$	$\chi^2$	Circuit	Potential (V)
1.549	10.45	50.25	36.63	0.000667	R(L)(QR)(CR)(QR)(CW)	1.20
1.435	22.52	84.32	60.31	9.9E-05	R(L)(QR)(CR)(QR)(RW)	1.14
2.0	2.88	19.67	52.21	2.30E-05	R(L)(QR)(CR)(QR)(CW)	1.08
1.62	1.19	55.32	15.48	5.51E-05	R(L)(QR)(CR)(QR)(CW)	1.02
1.74	119	66.97	49.93	4.46E-05	R(L)(QR)(CR)(QR)(CW)	0.96
4.85	20.42	49.35	86.19	1.52E-05	R(L)(QR)(CR)(QR)(CW)	0.90
4.81	3.50	68.21	54.39	2.29E-05	R(L)(QR)(CR)(QR)(CW)	0.84
5.93	5.55	13.90	33.54	5.21E-05	R(L)(QR)(CR)(QR)(CW)	0.78
1.95	10.39	0.1	1.45	6.42E-05	R(L)(QR)(CR)(QR)(CW)	0.72
1.52	1.59	63.9	9.65E+02	9.44E-05	R(L)(QR)(CR)(QR)(CW)	0.66
2.58	6.41	30.15	3.61E+01	8.19E-05	R(L)(QR)(CR)(QR)(CW)	0.60
1.66	7.31	33.49	2.49E+01	8.99E-05	R(L)(QR)(CR)(QR)(CW)	0.54
2.58	2.89	59.18	21.44	1.46E-05	R(L)(QR)(CR)(QR)(CW)	0.48
2.51	2.84	77.42	6.43	1.52E-05	R(L)(QR)(CR)(QR)(CW)	0.42
3.50	44.45	43.19	3.53	1.53E-05	R(L)(QR)(CR)(QR)(CW)	0.36
4.50	43.21	34.21	7.86	1.43E-05	R(L)(QR)(CR)(QR)(CW)	0.30
6.41	22.29	56.31	94.18	1.99E-05	R(L)(QR)(CR)(QR)(CW)	0.24
33.51	30.45	2.529	74.29	2.15E-05	R(L)(QR)(CR)(QR)(CW)	0.18
2.99	0.002	63.48	91.4E+01	2.15E-05	R(L)(QR)(CR)(QR)(CW)	0.12
10.36	22.49	75.9	3.22	2.16E-05	R(L)(QR)(CR)(QR)(CW)	0.06
1.1	39.48	62.53	0.65	5.55E-05	R(L)(QR)(CR)(QR)(CW)	0.005

**Table 4:** DEIS circuit fitting parameters during charging with the control system (only PAA as the binder).

$R_s$	$R_{PC}$	$R_{SEI}$	$R_{CT}$	$\chi^2$	Circuit	Potential (V)
44.32	1.25	275.43	55.51	0.0005	R(L)(QR)(CR)(QR)(CW)	1.20
22.45	44.61	399.28	64.45	5.9×10 <sup>-5</sup>	R(L)(QR)(CR)(QR)(CW)	1.14
1.09	3.90E+04	401	43.41	1.50E-05	R(L)(QR)(CR)(QR)(CW)	1.08
2.54	2.85E+11	480.98	48.15	4.61E-05	R(L)(QR)(CR)(QR)(CW)	1.02

### CHAPTER 3

2.99	20.73	700.42	47.87	6.66E-05	R(L)(QR)(CR)(QR)(CW)	0.96
2.31	54.51	689.90	52.54	0.32E-05	R(L)(QR)(CR)(QR)(CW)	0.90
1.85	6.51E+02	667.41	31.76	4.69E-05	R(L)(QR)(CR)(QR)(CW)	0.84
2.4	5.55	644.71	89.41	3.71E-05	R(L)(QR)(CR)(QR)(CW)	0.78
1.98	3.68	669.32	0.52	5.82E-05	R(L)(QR)(CR)(QR)(CW)	0.72
0.84	1.86	600.32	6.42E+02	1.74E-05	R(L)(QR)(CR)(QR)(CW)	0.66
0.984	8.54	622.43	2.51E+01	7.51E-05	R(L)(QR)(CR)(QR)(CW)	0.60
0.95	9.85	559.21	5.43E+01	0.90E-05	R(L)(QR)(CR)(QR)(CW)	0.54
0.85	1.01	550.42	32.36	0.66E-05	R(L)(QR)(CR)(QR)(CW)	0.48
0.92	19.43	541.49	5.63	7.65E-05	R(L)(QR)(CR)(QR)(CW)	0.42
0.86	53.67	650.33	4.67	6.66E-05	R(L)(QR)(CR)(QR)(CW)	0.36
1.94	100	590.1	1.43	4.78E-05	R(L)(QR)(CR)(QR)(CW)	0.30
1.84	66.31	600	65.41	2.69E-05	R(L)(QR)(CR)(QR)(CW)	0.24
1.74	67.15	680	99.54	5.05E-05	R(L)(QR)(CR)(QR)(CW)	0.18
1.54	98.39	659.31	2.36E+01	1.53E-05	R(L)(QR)(CR)(QR)(CW)	0.12
1.68	12.85	661.34	1.23	1.62E-05	R(L)(QR)(CR)(QR)(CW)	0.06
19.4	33.89	660.21	0.41	4.57E-05	R(L)(QR)(CR)(QR)(CW)	0.005

The electronic conductivity calculations of the P-BIAN/PAA binder and PAA were carried out by recording the Nyquist profiles of anodic half-cells having electrodes with respective binder coatings (without active material and conductive additive). Figure 11 shows the Nyquist profiles of the electrodes coated with P-BIAN/PAA and PAA binders vs Li/Li<sup>+</sup> at OCP, respectively. As shown in the Table 5, the conductivity of P-BIAN/PAA binder was calculated to be  $6.90 \times 10^{-3} \Omega^{-1} \text{ m}^{-1}$  which was one order magnitude higher than its counterpart PAA ( $6.82 \times 10^{-4} \Omega^{-1} \text{ m}^{-1}$ ).

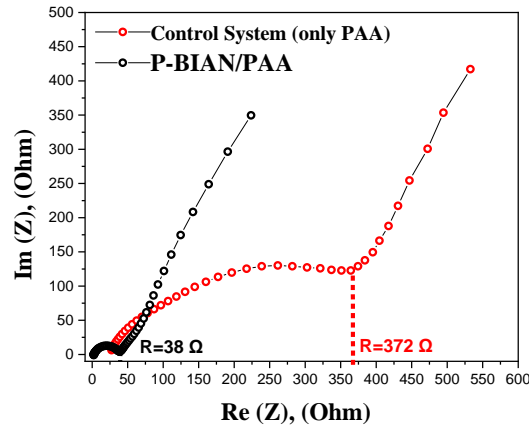


**Figure 11:** Nyquist spectrum of anodic half-cells having electrodes with pure binder coating (without active material and conductive additive)

$$R = \rho \frac{l}{A} \quad (1)$$

In equation 1, R is the resistance in ohm ( $\Omega$ ), l is the length in meter (m) of the specimen, A is the cross-sectional area ( $m^2$ ) of the specimen, and  $\rho$  the resistivity ( $\Omega m$ ). The conductivity  $\sigma$  ( $\Omega^{-1} m^{-1}$ ) of a material is the inverse of its resistivity as shown in equation 2.

$$\sigma = \frac{1}{\rho} \quad (2)$$

**Table 5:** Parameters associated with the conductivity measurement of P-BIAN/PAA and PAA binders.

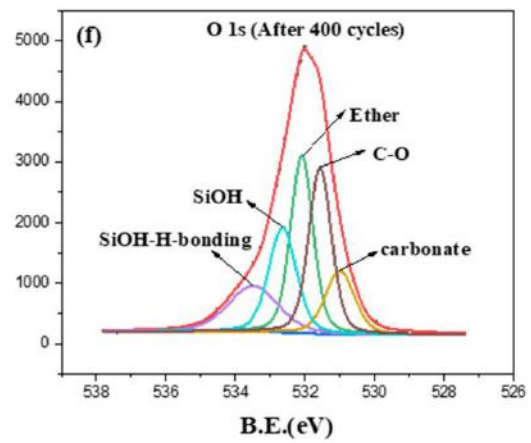
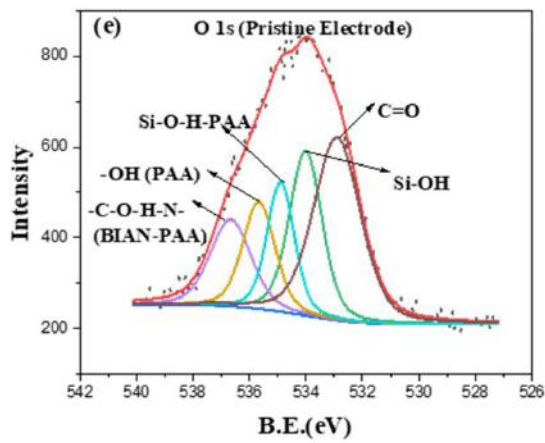
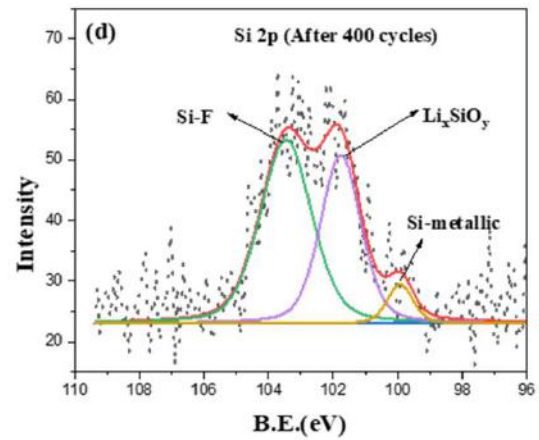
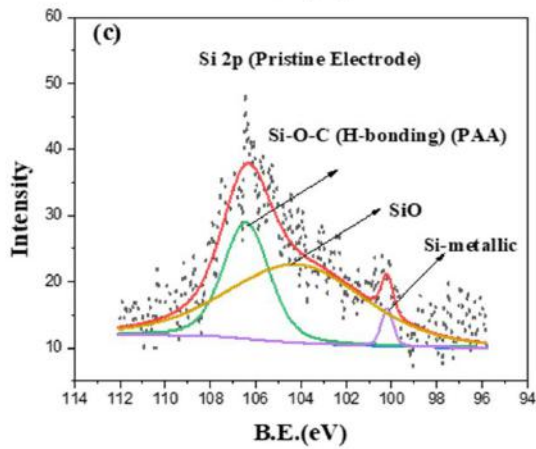
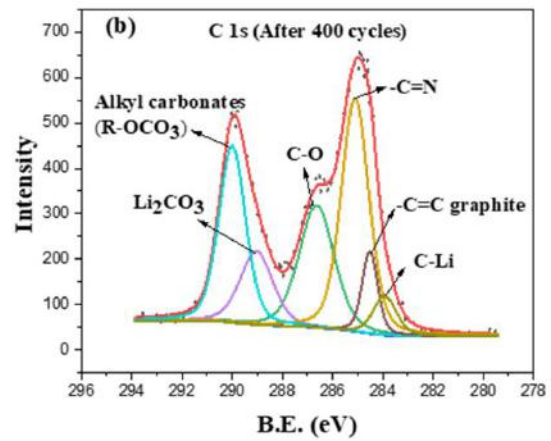
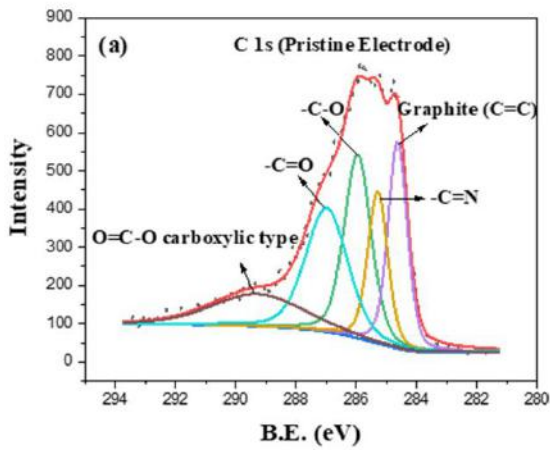
Material	Area of the electrode ( $A$ )	Thickness of the electrode ( $L$ )	Resistance	Conductivity
P-BIAN/PAA	$1.77 \times 10^{-4} m^2$	$47 \pm 0.5 \mu m$	$38 \Omega$	$6.90 \times 10^{-3} \Omega^{-1} m^{-1}$
Control System	$1.77 \times 10^{-4} m^2$	$45 \pm 0.5 \mu m$	$372 \Omega$	$6.82 \times 10^{-4} \Omega^{-1} m^{-1}$

### 3.4.4 Post-mortem characterization of anodes

#### X-ray photoelectron spectroscopy (XPS) studies

To understand the influence P-BIAN/PAA composite binder on the SEI and its composition, X-ray photoelectron spectroscopy (XPS) measurements of the pristine Si/C/P-BIAN/PAA/AB anode and the anode after 400 cycles of charge & discharge were carried out. The half-cell was disassembled in an Argon filled glove box at OCP. The electrode was separated from the redundant cell components and washed with the dehydrated DEC solvent

multiple times without much agitation to minimize the removal of the organic SEI from the electrode before left for drying under high vacuum for 16 hours. The obtained XPS spectra were calibrated to the graphite carbon (C=C) at 284.6 eV<sup>46</sup>. The deconvolution and curves fitting were performed keeping 70% Gaussian 30% Voigt peak shape. Figure 12 shows the comparison between the spectra corresponding to various elements detected in the Pristine Si/C/P-BIAN/PAA/AB electrode and the electrode after 400 cycles of de-/alloying. The binding energy values of relevant peaks for the pristine electrode and electrode after 400 cycles and their corresponding % area under the curve for (a) C 1s, (b) Si 2p, and (c) N 1s are tabulated in Table 6. The XPS measurements demonstrated that the SEI was comprising of electrolyte decomposition products like LiF, Li<sub>x</sub>PF<sub>y</sub>, Li<sub>2</sub>CO<sub>3</sub>, ether carbonates, and R-COOLi. Since the detection depth of XPS technique is 5-10 nm into the surface of the sample, the detection of (i) graphitic peak (C=C) at 284.6 eV<sup>30, 46</sup> and sp<sup>2</sup> carbon of the diimine (C=N)<sup>30</sup> in P-BIAN/PAA at 285.1 eV in C 1s, (ii) Si-metallic peak at 100.1 eV and Li<sub>x</sub>SiO<sub>y</sub> at 101.8 eV in Si 2p<sup>47</sup> and (iii) pyridine type-sp<sup>2</sup> (C=N)<sup>30</sup> nitrogen at 399.9 eV and hydrogen bonded quaternary nitrogen of P-BIAN/PAA composite at 403 eV in N 1s<sup>31-32</sup> spectra means that the SEI formed in the case of Si/C/P-BIAN/PAA/AB anode was thinner than 5-10 nm.



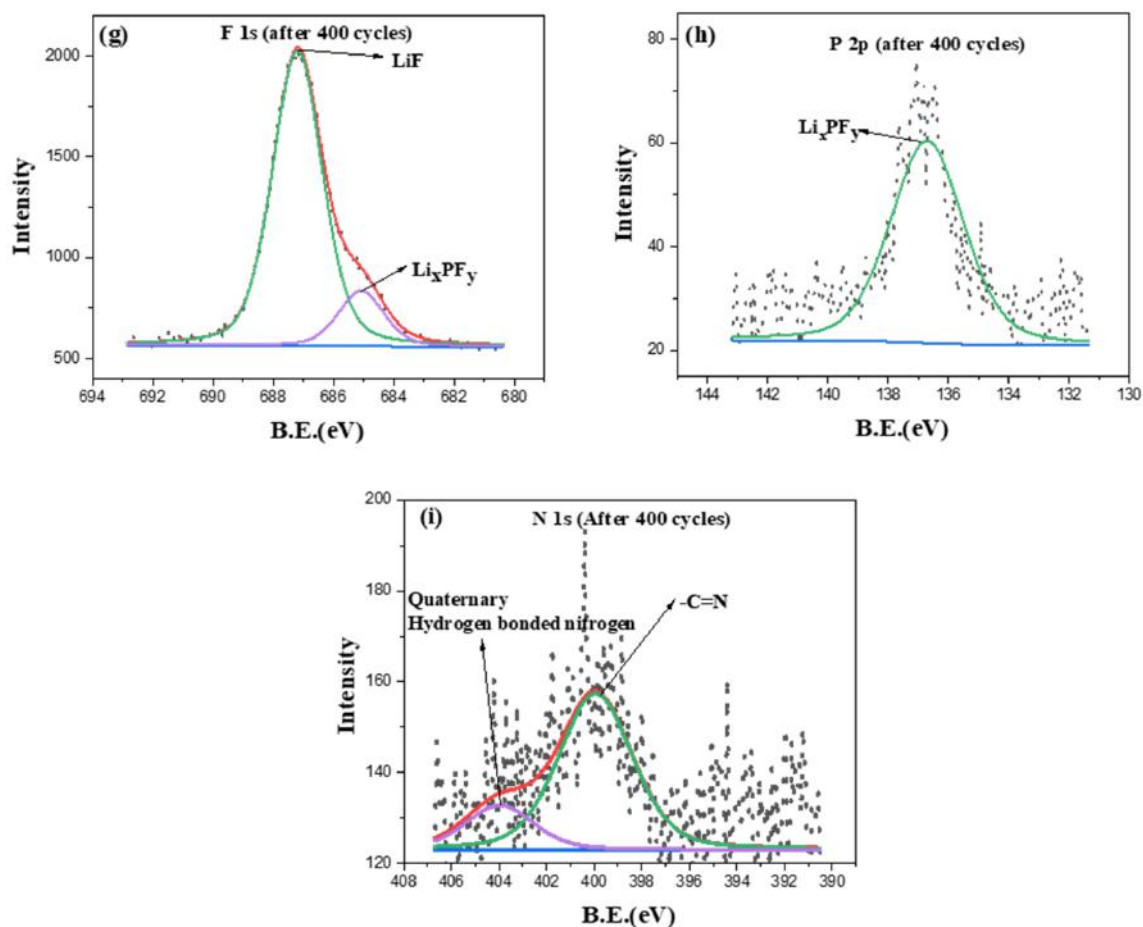


**Figure 12:** The XPS spectra for the Si/C/P-BIAN/PAA/AB electrode are as follows: (a) & (b) showing the attributed peaks to the C 1s spectra of the pristine electrode and the electrode after 400 cycles, (c) & (d) showing the attributed peaks to the Si 2p spectra of the pristine electrode and the electrode after 400 cycles, (e) & (f) showing the attributed peaks to the O 1s spectra of the pristine electrode and the electrode after 400 cycles, and (g), (f), & (i) showing the attributed peaks to the F 1s, P 2p and N 1s spectra of the electrode after 400 cycles, respectively.



**Table 6:** Tabulated binding energy values of relevant elemental peaks for the pristine electrode and electrode after 400 cycles explaining the SEI thickness and their corresponding % area under the curve for (a) C 1s, (b) Si 2p, and N 1s.

(a) C 1s (Pristine electrode and after 400 cycles)

Component	Pristine (eV)	% area under the curve	After 400 cycles (eV)	% area under the curve
C-Li	-	-	283.8	4.8
Graphite	284.6	19.9	284.6	17.2
-C=N (P-BIAN/PAA)	285.2	15.03	285.1	20.5
C-O	-	-	286.5	21.5
O=C-O carboxylic type (PAA)	289.3	14.5	-	-
Lithium carbonates (Li <sub>2</sub> CO <sub>3</sub> )	-	-	289.2	12.6
Alkyl carbonates (R-OCO <sub>2</sub> -Li)	-	-	290.0	23.1

(b) Si 2p (Pristine electrode and after 400 cycles)

Component	Pristine (eV)	% area under the curve	After 400 cycles (eV)	% area under the curve
Si-metallic	100.2	16.2	100.1	5.7
SiO	104.1	64.5	101.8 (Li <sub>x</sub> SiO <sub>y</sub> )	39.3
Si-O-C (H-bonding PAA)	106.3	32.7	-	-
SiF	-	-	103.4	55

(c) N 1s (Pristine electrode and after 400 cycles)

Component	Pristine (eV)	% area under the curve	After 400 cycles (eV)	% area under the curve
Pyridinic Type (C=N)	399.7	15.6	399.9	76.5
H-bonded quaternized diimine	400.7	84.3	403	23.4

### Scanning electron microscope (SEM) measurements (Morphology studies)

The FESEM micrographs of Si/C/P-BIAN/PAA/AB pristine electrode, control study pristine electrode, disassembled Si/C/P-BIAN/PAA/AB electrode after 400 cycles, and disassembled control study electrode after 320 cycles are shown in Figure 13. The Si/C/P-BIAN/PAA/AB pristine electrode showed a smooth and robust morphology throughout the laminate. After 400 cycles of de-/alloying, the distinct features of electrode were not observed

due to the presence of SEI. The uniform contrast over the surface of electrode showed a uniform SEI layer over the surface with microcracks because of repeated de-/alloying for 400 long cycles. However, the electrode laminate was stable and did not peel off even after 400 cycles owing to the adherence of the electrode laminate offered by the P-BIAN moiety of P-BIAN/PAA binder. In contrast, the control study pristine electrode with only PAA binder showed microcracks ( $<1\ \mu\text{m}$ ). And after 320 cycles of de-alloying, the control study electrode showed the emergence of long microcracks ( $>20\ \mu\text{m}$ ) with poor adherence to the current collector.

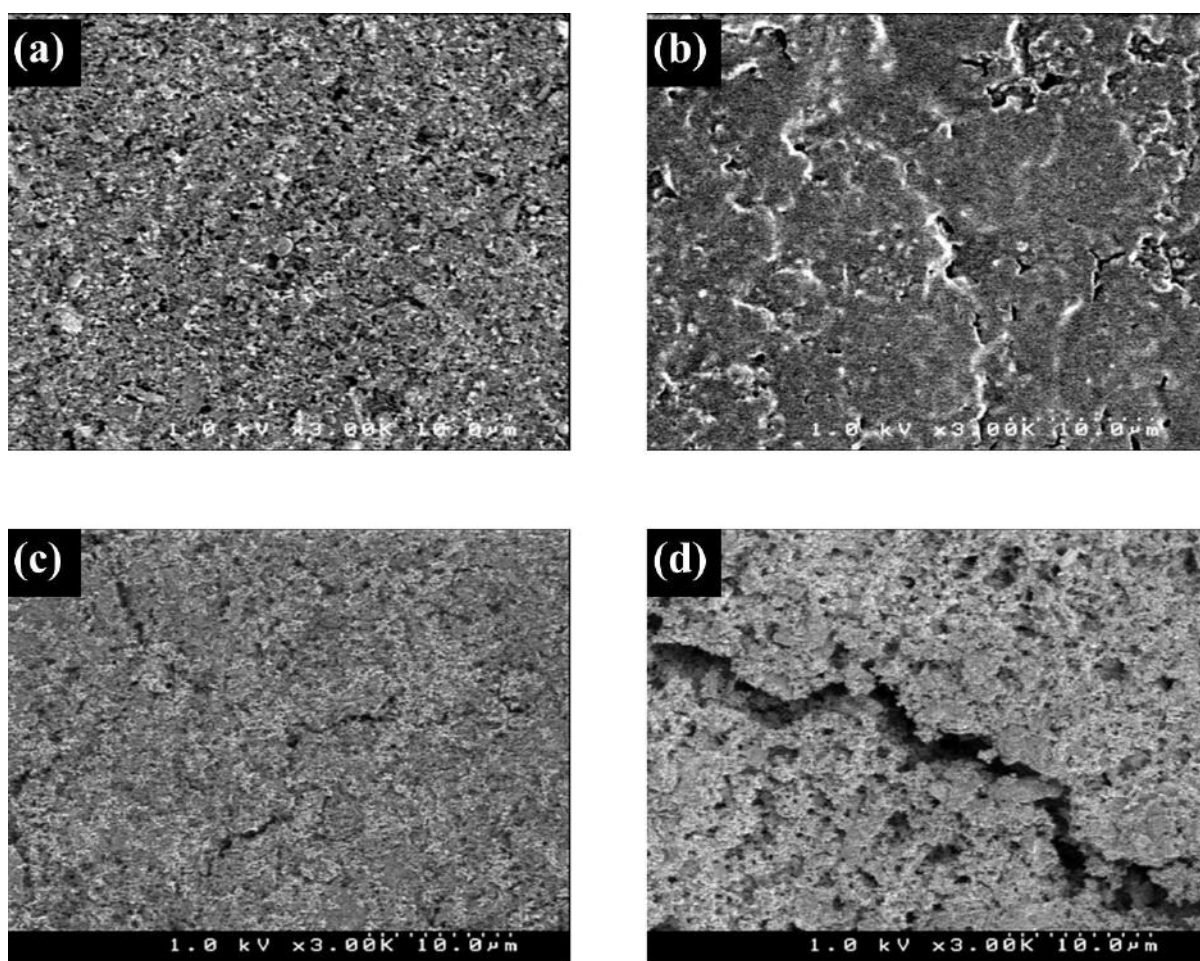


**Figure 13:** The FESEM micrographs of the Si/C/P-BIAN/PAA/AB electrode (a) Pristine electrode and (b) after 400 cycles of charge & discharge at position-a. The control study electrode (c) pristine electrode and (d) after 320 cycles of charge & discharge.

### 3.5 Conclusion

The robust n-type self-healing polymer composite P-BIAN/PAA stabilized the Si anodes in terms of rate capability, specific capacity, cyclability, capacity retention, and coulombic efficiency on its application as a binder. Because of its low-lying LUMO, the cathodic doping of the P-BIAN/PAA binder in the anodic environment restricted the excessive decomposition of the electrolyte on the anode surface and enhanced the lithium-ion diffusion through the SEI which was confirmed by cyclic voltammetry studies. The impedance spectroscopy studies showed that the restricted electrolytic decomposition on the Si/C/P-BIAN/PAA/AB anode resulted in its low interfacial ( $R_{SEI}$ ) and charge transfer ( $R_{CT}$ ) impedances. Therefore, the formation of a tailored thin SEI and the dynamic self-healing electrostatic hydrogen bonding in BIAN-PAA provided a robust mechanical support to the silicon anodes during the de-/alloying and avoided its premature pulverization. As a result, the Si/C/P-BIAN/PAA/AB anode showed an excellent cyclability up to 600 cycles, specific capacity of  $\sim 2100 \text{ mAhg}^{-1}_{Si}$ ,  $\sim 98.9\%$  average coulombic efficiency, and 95% capacity retention after 600 cycles. After the electrochemical evaluation of the Si/C/P-BIAN/PAA/AB anode, the post-mortem analysis by XPS and SEM studies confirmed that the SEI formed in case of P-BIAN/PAA composite-based anode was thin, and the electrode morphology well retained with good adherence to the current collector. Hence the design and application of novel polymer composites comprising of n-type conducting polymers (CPs) cross-linked via electrostatic interaction with carboxylate-containing polymers like P-BIAN/PAA hold a promising future in high-capacity electrode materials.

### References

1. Kim, T.; Song, W.; Son, D.-Y.; Ono, L. K.; Qi, Y., Lithium-ion batteries: outlook on present, future, and hybridized technologies. *Journal of Materials Chemistry A* **2019**, 7 (7), 2942-2964.
2. Wang, M.; Tang, Y., A review on the features and progress of dual-ion batteries. *Advanced Energy Materials* **2018**, 8 (19), 1703320.
3. Jin, Y.; Zhu, B.; Lu, Z.; Liu, N.; Zhu, J., Challenges and recent progress in the development of Si anodes for lithium-ion battery. *Advanced Energy Materials* **2017**, 7 (23), 1700715.
4. Chae, S.; Ko, M.; Kim, K.; Ahn, K.; Cho, J., Confronting issues of the practical implementation of Si anode in high-energy lithium-ion batteries. *Joule* **2017**, 1 (1), 47-60.

5. McDowell, M. T.; Lee, S. W.; Nix, W. D.; Cui, Y., 25th Anniversary Article: Understanding the Lithiation of silicon and other alloying anodes for lithium-ion batteries. *Advanced Materials* **2013**, *25* (36), 4966-4985.
6. Wu, H.; Cui, Y., Designing nanostructured Si anodes for high energy lithium ion batteries. *Nano Today* **2012**, *7* (5), 414-429.
7. Lv, X.; Wei, W.; Huang, B.; Dai, Y., Achieving high energy density for lithium-ion battery anodes by Si/C nanostructure design. *Journal of Materials Chemistry A* **2019**, *7* (5), 2165-2171.
8. Luo, W.; Chen, X.; Xia, Y.; Chen, M.; Wang, L.; Wang, Q.; Li, W.; Yang, J., Surface and interface engineering of silicon-based anode materials for lithium-ion batteries. *Advanced Energy Materials* **2017**, *7* (24), 1701083.
9. Su, X.; Wu, Q.; Li, J.; Xiao, X.; Lott, A.; Lu, W.; Sheldon, B. W.; Wu, J., Silicon-based nanomaterials for lithium-ion batteries: A Review. *Advanced Energy Materials* **2014**, *4* (1), 1300882.
10. Chen, H.; Ling, M.; Hencz, L.; Ling, H. Y.; Li, G.; Lin, Z.; Liu, G.; Zhang, S., Exploring chemical, mechanical, and electrical functionalities of binders for advanced energy-storage devices. *Chemical Reviews* **2018**, *118* (18), 8936-8982.
11. Kwon, T.-w.; Choi, J. W.; Coskun, A., The emerging era of supramolecular polymeric binders in silicon anodes. *Chemical Society Reviews* **2018**, *47* (6), 2145-2164.
12. Liu, G.; Xun, S.; Vukmirovic, N.; Song, X.; Olalde-Velasco, P.; Zheng, H.; Battaglia, V. S.; Wang, L.; Yang, W., Polymers with tailored electronic structure for high capacity lithium battery electrodes. *Advanced Materials* **2011**, *23* (40), 4679-4683.
13. Yao, Y.; Liu, N.; McDowell, M. T.; Pasta, M.; Cui, Y., Improving the cycling stability of silicon nanowire anodes with conducting polymer coatings. *Energy & Environmental Science* **2012**, *5* (7), 7927-7930.
14. McGraw, M.; Kolla, P.; Yao, B.; Cook, R.; Quiao, Q.; Wu, J.; Smirnova, A., One-step solid-state in-situ thermal polymerization of silicon-PEDOT nanocomposites for the application in lithium-ion battery anodes. *Polymer* **2016**, *99*, 488-495.
15. Zhang, C.; Chen, Q.; Ai, X.; Li, X.; Xie, Q.; Cheng, Y.; Kong, H.; Xu, W.; Wang, L.; Wang, M.-S.; Yang, H.; Peng, D.-L., Conductive polyaniline doped with phytic acid as a binder and conductive additive for a commercial silicon anode with enhanced lithium storage properties. *Journal of Materials Chemistry A* **2020**, *8* (32), 16323-16331.

16. Tong, J.; Han, C.; Hao, X.; Qin, X.; Li, B., Conductive polyacrylic acid-polyaniline as a multifunctional binder for stable organic quinone electrodes of lithium-ion batteries. *ACS Applied Materials & Interfaces* **2020**, *12* (35), 39630-39638.
17. Kim, S.-M.; Kim, M. H.; Choi, S. Y.; Lee, J. G.; Jang, J.; Lee, J. B.; Ryu, J. H.; Hwang, S. S.; Park, J.-H.; Shin, K.; Kim, Y. G.; Oh, S. M., Poly(phenanthrenequinone) as a conductive binder for nano-sized silicon negative electrodes. *Energy & Environmental Science* **2015**, *8* (5), 1538-1543.
18. Wu, M.; Song, X.; Liu, X.; Battaglia, V.; Yang, W.; Liu, G., Manipulating the polarity of conductive polymer binders for Si-based anodes in lithium-ion batteries. *Journal of Materials Chemistry A* **2015**, *3* (7), 3651-3658.
19. Zeng, W.; Wang, L.; Peng, X.; Liu, T.; Jiang, Y.; Qin, F.; Hu, L.; Chu, P. K.; Huo, K.; Zhou, Y., Enhanced ion conductivity in conducting polymer binder for high-performance silicon anodes in advanced lithium-ion batteries. *Advanced Energy Materials* **2018**, *8* (11), 1702314.
20. Wang, L.; Liu, T.; Peng, X.; Zeng, W.; Jin, Z.; Tian, W.; Gao, B.; Zhou, Y.; Chu, P. K.; Huo, K., Highly stretchable conductive glue for high-performance silicon anodes in advanced lithium-ion batteries. *Advanced Functional Materials* **2018**, *28* (3), 1704858.
21. Nguyen, V. A.; Kuss, C., Review—Conducting polymer-based binders for lithium-ion batteries and beyond. *Journal of The Electrochemical Society* **2020**, *167* (6), 065501.
22. Bresser, D.; Buchholz, D.; Moretti, A.; Varzi, A.; Passerini, S., Alternative binders for sustainable electrochemical energy storage – the transition to aqueous electrode processing and bio-derived polymers. *Energy & Environmental Science* **2018**, *11* (11), 3096-3127.
23. van Asselt, R.; Elsevier, C. J.; Smeets, W. J. J.; Spek, A. L.; Benedix, R., Synthesis and characterization of rigid bidentate nitrogen ligands and some examples of coordination to divalent palladium. X-ray crystal structures of bis (p-tolylimino) acenaphthene and methylchloro [bis(o,o'-diisopropylphenyl-imino) acenaphthene] palladium (II). *Recueil des Travaux Chimiques des Pays-Bas* **1994**, *113* (2), 88-98.
24. Gasperini, M.; Ragaini, F.; Cenini, S., Synthesis of Ar-BIAN ligands (Ar-BIAN = bis(aryl)acenaphthenequinonediimine) having strong electron-withdrawing substituents on the aryl rings and their relative coordination strength toward palladium(0) and -(II) complexes. *Organometallics* **2002**, *21* (14), 2950-2957.

25. Patnaik, S. G.; Vedarajan, R.; Matsumi, N., BIAN based functional diimine polymer binder for high performance Li ion batteries. *Journal of Materials Chemistry A* **2017**, *5* (34), 17909-17919.
26. Patnaik, S. G.; Vedarajan, R.; Matsumi, N., BIAN based electroactive polymer with defined active centers as metal-free electrocatalysts for oxygen reduction reaction (ORR) in aqueous and nonaqueous media. *ACS Applied Energy Materials* **2018**, *1* (3), 1183-1190.
27. Choi, N.-S.; Ha, S.-Y.; Lee, Y.; Jang, J. Y.; Jeong, M.-H.; Shin, W. C.; Ue, M., Recent progress on polymeric binders for silicon anodes in lithium-ion batteries. *J. Electrochem. Sci. Technol* **2015**, *6* (2), 35-49.
28. Villa, M.; Miesel, D.; Hildebrandt, A.; Ragaini, F.; Schaarschmidt, D.; Jacobi von Wangelin, A., Synthesis and catalysis of redox-active bis(imino)acenaphthene (BIAN) iron complexes. *ChemCatChem* **2017**, *9* (16), 3203-3209.
29. Huang, J.; Li, Z.; Zhang, J., Dynamic electrochemical impedance spectroscopy reconstructed from continuous impedance measurement of single frequency during charging/discharging. *J Power Sources* **2015**, *273*, 1098-1102.
30. Golczak, S.; Kanciurzevska, A.; Fahlman, M.; Langer, K.; Langer, J. J., Comparative XPS surface study of polyaniline thin films. *Solid State Ionics* **2008**, *179* (39), 2234-2239.
31. Collins, J.; Gourdin, G.; Foster, M.; Qu, D., Carbon surface functionalities and SEI formation during Li intercalation. *Carbon* **2015**, *92*, 193-244.
32. Wang, H.; Zhang, C.; Liu, Z.; Wang, L.; Han, P.; Xu, H.; Zhang, K.; Dong, S.; Yao, J.; Cui, G., Nitrogen-doped graphene nanosheets with excellent lithium storage properties. *Journal of Materials Chemistry* **2011**, *21* (14), 5430-5434.
33. Gillan, E. G., Synthesis of nitrogen-rich carbon nitride networks from an energetic molecular azide precursor. *Chemistry of Materials* **2000**, *12* (12), 3906-3912.
34. Zimmerman, J. L.; Williams, R.; Khabashesku, V. N.; Margrave, J. L., Synthesis of spherical carbon nitride nanostructures. *Nano Letters* **2001**, *1* (12), 731-734.
35. Velasco-Barraza, R. D.; Vera-Graziano, R.; López-Maldonado, E. A.; Oropeza-Guzmán, M. T.; Dastager, S. G.; Álvarez-Andrade, A.; Iglesias, A. L.; Villarreal-Gómez, L. J., Study of nanofiber scaffolds of PAA, PAA/CS, and PAA/ALG for its potential use in biotechnological applications. *International Journal of Polymeric Materials and Polymeric Biomaterials* **2018**, *67* (13), 800-807.
36. Yi, X.; Xu, Z.; Liu, Y.; Guo, X.; Ou, M.; Xu, X., Highly efficient removal of uranium(vi) from wastewater by polyacrylic acid hydrogels. *RSC Advances* **2017**, *7* (11), 6278-6287.

37. Jiang, S.; Hu, B.; Sahore, R.; Zhang, L.; Liu, H.; Zhang, L.; Lu, W.; Zhao, B.; Zhang, Z., Surface-functionalized silicon nanoparticles as anode material for lithium-ion battery. *ACS Applied Materials & Interfaces* **2018**, *10* (51), 44924-44931.
38. Martinez-Felipe, A.; Brebner, F.; Zaton, D.; Concellon, A.; Ahmadi, S.; Piñol, M.; Oriol, L., Molecular recognition via hydrogen bonding in supramolecular complexes: a fourier transform infrared spectroscopy study. *Molecules* **2018**, *23* (9), 2278.
39. Cao, H.; Qi, F.; Liu, R.; Wang, F.; Zhang, C.; Zhang, X.; Chai, Y.; Zhai, L., The influence of hydrogen bonding on N-methyldiethanolamine-extended polyurethane solid–solid phase change materials for energy storage. *RSC Advances* **2017**, *7* (19), 11244-11252.
40. Hishikawa, Y.; Togawa, E.; Kondo, T., Characterization of individual hydrogen bonds in crystalline regenerated cellulose using resolved polarized FTIR spectra. *ACS Omega* **2017**, *2* (4), 1469-1476.
41. Faniyi, I. O.; Fasakin, O.; Olofinjana, B.; Adekunle, A. S.; Oluwasusi, T. V.; Eleruja, M. A.; Ajayi, E. O. B., The comparative analyses of reduced graphene oxide (RGO) prepared via green, mild and chemical approaches. *SN Applied Sciences* **2019**, *1* (10), 1181.
42. Agubra, V. A.; Fergus, J. W., The formation and stability of the solid electrolyte interface on the graphite anode. *J Power Sources* **2014**, *268*, 153-162.
43. Tian, M.; Wu, P., Nature plant polyphenol coating silicon submicroparticle conjugated with polyacrylic acid for achieving a high-performance anode of lithium-ion battery. *ACS Applied Energy Materials* **2019**, *2* (7), 5066-5073.
44. Li, X.; Yan, C.; Wang, J.; Graff, A.; Schweizer, S. L.; Sprafke, A.; Schmidt, O. G.; Wehrspohn, R. B., Stable silicon anodes for lithium-ion batteries using mesoporous metallurgical silicon. *Advanced Energy Materials* **2015**, *5* (4), 1401556.
45. Zhang, J.; Zhang, K.; Yang, J.; Lee, G.-H.; Shin, J.; Wing-hei Lau, V.; Kang, Y.-M., Bifunctional conducting polymer coated CoP core–shell nanowires on carbon paper as a free-standing anode for sodium ion batteries. *Advanced Energy Materials* **2018**, *8* (20), 1800283.
46. Dementjev, A. P.; de Graaf, A.; van de Sanden, M. C. M.; Maslakov, K. I.; Naumkin, A. V.; Serov, A. A., X-Ray photoelectron spectroscopy reference data for identification of the C<sub>3</sub>N<sub>4</sub> phase in carbon–nitrogen films. *Diamond and Related Materials* **2000**, *9* (11), 1904-1907.
47. Philippe, B.; Dedryvère, R.; Allouche, J.; Lindgren, F.; Gorgoi, M.; Rensmo, H.; Gonbeau, D.; Edström, K., Nanosilicon electrodes for lithium-ion batteries: interfacial mechanisms

studied by hard and soft X-ray photoelectron spectroscopy. *Chemistry of Materials* **2012**, *24* (6), 1107-1115.



## Chapter 4

# Crosslinked Polymer BIAN Matrices to Stabilize Silicon Anode in Lithium-Ion Secondary Batteries

### 4.1 Abstract

For the substantial production of electric vehicles, portable electronic devices, and (hybrid)-electric vehicles, high-energy density rechargeable lithium-ion batteries are the need of the hour. The current state-of-the-art anode active material (graphite) cannot suffice for the need of high energy due to its limited specific capacity ( $372 \text{ mAhg}^{-1}$ ). In this regard, Si has emerged as a sustainable alternative because of its natural abundance as well as high theoretical gravimetric capacity ( $4200 \text{ mAhg}^{-1}$ ). However, inherent failure mechanism of Si anodes is the biggest roadblock on their way towards potential commercialization. Therefore, as means to stabilize Si anodes, this work describes the design, synthesis, and adoption of novel conducting/crosslinked polymer matrices of poly(BIAN) (P-BIAN) as binder for Si anodes. Crosslinked P-BIAN matrices as binder exhibits its versatility by (a) providing mechanical robustness to Si anodes upon volume expansion and restrict their pulverization, (b) undergoing n-doping in the reducing anodic environment to restrict the electrolyte decomposition on the anode surface to tailor SEI with low impedance, and (c) maintaining electrical conductivity within the electrode laminate. The fabricated anodic half-cell with crosslinked P-BIAN matrices as binder exhibits excellent cyclic stability for over 1000 cycles with a high reversible capacity of  $\sim 2500 \text{ mAhg}^{-1}$  at a high current-rate  $500 \text{ mA}g^{-1}$  with 99.1% capacity retention. Theoretical evaluation of the binder and electrochemical characterization of anodic half-cells support the excellent performance of Si anodes with crosslinked P-BIAN polymer as binder.

## 4.2 Introduction

For the development of next-generation high-energy density lithium-ion batteries (LIBs) with excellent cyclic stability and high reversible specific capacity, silicon (Si) has attracted the attention of researchers and industries across the globe as a potential anode material choice<sup>1-2</sup>. Unlike conventional graphite anode material that has theoretical gravimetric capacity of 372 mAhg<sup>-1</sup>, Si is potent with 3579 mAhg<sup>-1</sup> ascribed to Li<sub>15</sub>Si<sub>14</sub> phase<sup>3</sup>. In addition, its abundance in the Earth's crust (cost-effectiveness), non-toxicity, and appropriate de/alloying potential (0.5 V vs Li/Li<sup>+</sup>) has inspired tremendous efforts towards aiming its commercialization<sup>4-5</sup>. However, some major drawbacks as mentioned below have kept its full-fledged commercialization at bay. The rapid volume expansion (~300%) within a few de/alloying cycles leads to pulverization of Si particles. As a result, the electrolyte within the battery gets continuous exposure to new Si surfaces and keeps on getting decomposed on the electrode surface making the solid-electrolyte interface (SEI) thick with high internal impedance, low lithium-ion diffusivity, and adding to irreversible capacity loss. Also, Si particles lose interparticle electrical contact with the conductive additive and electrical contact with the current collector leading to the fractured electrode laminate<sup>6</sup>. Therefore, Si anodes suffer drastic capacity fade showing poor cyclability and low coulombic efficiency<sup>6</sup>. To mitigate these drawbacks, the processing of Si wafers to various nanostructured Si like nanoparticles<sup>7-9</sup>, nanospheres<sup>9</sup>, yolk-shell-type nanoparticle morphology<sup>10</sup>, nanowires<sup>11</sup>, porous nanospheres<sup>8</sup>, and pomegranate structures<sup>12</sup> has been a famous strategy. However, this strategy significantly increases the cost of production and hence been recognized as unsustainable to meet the ever-increasing demand of LIBs.

Though polymer binders do not contribute to the energy density of anodes, their ability to stabilize and enhance the performance of active materials is indisputable. Also, they fare better in terms of being sustainable and cheaper choice in comparison to processing of Si to various nanostructures. To stabilize Si anodes, various types of polymer binders have been explored till date. Erstwhile attempts involved the use of synthetic polymers (individually or in combination) like poly(acrylic acid)<sup>13</sup>, PR-PAA<sup>14-15</sup>, polyimide<sup>16</sup>, and biopolymer like carboxymethyl cellulose (CMC)<sup>17</sup>, sodium alginate<sup>18</sup>, PAA/CMC<sup>19</sup>, cyclodextrin<sup>20</sup>, guar gum<sup>21</sup>, and chitosan<sup>22</sup>. Unfortunately, their non-conducting nature required the use of large quantity of conductive additive (carbon black) which caused decrease in the derivable capacity of Si anodes. Hence, upon comprehensive analysis of failure mechanism (pulverization upon volume

expansion and thick-unstable SEI) of Si anodes, the design and synthesis of advanced polymer (as reported in the literature) to stabilize Si anodes has been dedicated to following categories of binders:

- (i) **Conducting** (polyaniline (PANI)<sup>23</sup>, poly(3,4-ethylenedioxythiophene) (PEDOT)<sup>24</sup>, PEDOT:PSS (where PSS is poly(styrenesulfonate)<sup>25-26</sup>, poly(2,7-9,9-dioctylfluorene-2,7-9,9-(di(oxy-,2,5,8-trioxadecane))fluorene-co-2,7-fluorene-co-2,5-1-mehtylbenzoate ester) (PEFM), etc.)<sup>27-28</sup>
- (ii) **Self-healing** (Alginate (Alg-C) –  $\beta$ - D-mannuromic acid (M)/poly(acrylic acid) (PAA)<sup>29</sup>, KSMC (5-methyl-5-(4-vinylbenzyl) Meldrum's acid<sup>30</sup>, styrene<sup>31</sup>, methyl methacrylate<sup>31</sup>, lithium 2-methyl-2-(4-vinyl benzyl)malonate<sup>32</sup>, millipede-inspired combination of Na-CMC<sup>33</sup>, alginate<sup>22</sup>, and native XG<sup>22</sup>, etc.)<sup>34</sup>
- (iii) **Crosslinked** (chitosan (CS)- $\beta$ -(1-4)-linked D-glucosamine (deacetylated unit) and N-acetyl- D-glucosamine (acetylated unit)<sup>35</sup>, sodium alginate-PAA (SA-PAA), crosslinked dextrin<sup>36</sup>, poly(vinyltriethoxysilane)(PVTES)-Na(poly acrylic acid) (NaPAA)-(PVTES-NaPAA), c-PAA-CMC<sup>37</sup>, etc.)<sup>16</sup>
- (iv) **Strategic combinations** like **conducting/self-healing** (silicon nanoparticles-polyaniline (SiNP-PANI) hydrogel<sup>38</sup>, poly(1-pyrenemehtyl methacrylate-co-methacrylic acid) (PPyMAA)<sup>39</sup>, etc.) and **conducting/crosslinked** (glycerol-crosslinked PEDOT:PSS)<sup>40</sup>.

The stabilization of silicon anodes requires a binder system to be multifaceted/versatile in ways like (a) administer robust mechanical support to prevent pulverization upon volume expansion, (b) provide intrinsic electrical conductivity in the electrode laminate to prevent energy loss and increase the efficiency, and (c) influence the architecture of SEI formed on the electrode surface with low impedance and thinner dimension for better lithium-ion diffusion. Out of all the binder categories mentioned above, binders belonging to the category (iv) the strategic combination (conducting/self-healing and conducting/crosslinked) have been most potent and successful on their application. They were mainly designed to stabilize Si anodes by administering the mechanical support and provide electrical conductivity. But the ability to tune the SEI formed on the anode surface was beyond their scope. Further, between conducting/self-healing-type and conducting/crosslinked-type binders, good progress has been made in the design and application of the former-type. However, though the latter-type is more potent, only a few reports have been published on it. Hence, the design and synthesis of **conducting/crosslinked-type** wholesome binder systems that can not only administer the

mechanical robustness and electrical conductivity but also tailor the architecture of SEI by virtue of their tunable electronic properties is a prime topic of research to meet all the challenges encountered while working with Si anodes.

In this regard, compounds of the family aryl-bisiminoacenaphthenequinone (Ar-BIAN) have shown promising character. This class of compounds are rich with wide spectrum of electrochemical and redox properties because they have been recognized as essential ligands for transition metals for a long time (explored by Elsevier and his group for the first time)<sup>41-42</sup>. Exploiting their redox, structural, and electrochemical chemistry, our group reported two different types of BIAN-based binders (a) BIAN-fluorene copolymer<sup>43</sup> and (b) BIAN-paraphenylene (BP)-copolymer<sup>44</sup> for stabilizing graphite anode in LIBs. Three most salient features that led to their exceptional performance as binders for graphite anodes are (a) ability to establish  $\pi$ - $\pi$  interaction with graphite to give mechanical support during de-/lithiation, (b) ability to maintain electrical conductivity in the electrode laminate, and (b) low-lying lowest unoccupied molecular orbital (LUMO) led n-doping in the anodic environment that positively restricted the reductive decomposition of electrolyte on the anode surface to form a thin and low-impedance SEI. We further advanced their application towards developing conducting/self-healing multi-functional P-BIAN/PAA composite binder to stabilize silicon anodes as reported in the previous chapter of this dissertation. P-BIAN/PAA composite binder showed its versatility in administering mechanical stability by its self-healing nature due to the presence of dynamic electrostatic hydrogen bonding between BIAN and PAA polymers, maintaining the electrical conductivity owing to BIAN moiety, and most importantly tailoring the SEI formation on Si anodes by manipulating the amount of electrolyte decomposition to an optimal amount for better lithium-ion diffusion and lowered cell impedance.

As discussed earlier, the combination of conducting/crosslinked-system has a better scope of stabilizing Si anodes than conducting/self-healing-system because crosslinked matrices have been proven to be more robust in restricting the volume expansion and pulverization of Si anodes. Therefore, aiming to design a BIAN-based binder system to further enhance the stability of Si anodes, in this chapter, crosslinked P-BIAN matrices as a binder for Si anodes is reported. P-BIAN crosslinked matrices were synthesized by stitching BP-copolymer units via 1,6-dibromohexane as linkers wherein the electron rich diimine in the BIAN backbone were the crosslinking host sites. The synthesized P-BIAN crosslinked matrices were potent with 3-fold advanced significance like (a) highly robust to provide mechanical support to Si anodes for prolonged cycling at higher current-rates, (b) maintain the electrical

conductivity within the electrode laminate, and (c) tailor the SEI on silicon particles by undergoing n-doping by virtue of engineered low-lying LUMO upon crosslinking. The Si anodes with P-BIAN crosslinked matrices exhibited excellent stability with high reversible capacity. The structural significance of P-BIAN crosslinked matrices is shown in Figure 1.

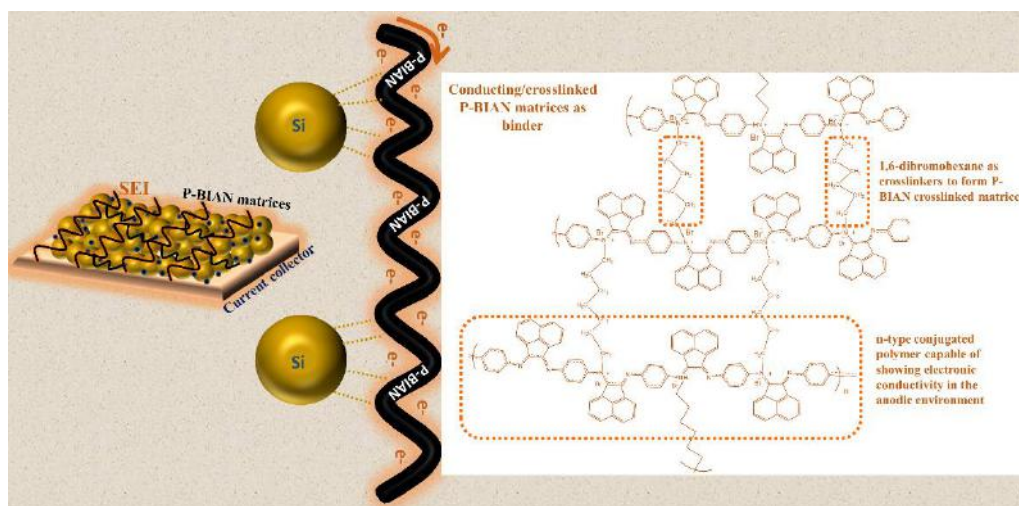


**Figure 1:** Schematic depicting the structural significance of P-BIAN crosslinked matrices to stabilize Si anodes in LIBs.

## 4.3 Experimental Section

### 4.3.1 Materials

1,6-dibromohexane, 1,4-phenylenediamine, *N*-methylpyrrolidone (NMP), acetic acid, and acenaphthenequinone were purchased from Tokyo Chemical Industry Co., Ltd. (TCI). Super dehydrated acetonitrile was purchased from Wako Pure Chemical Industries, Ltd. 1.0 M LiPF<sub>6</sub> (50/50) EC/DEC electrolyte was purchased from Sigma-Aldrich. Silicon nanoparticles (SiNPs) of size <100 nm was purchased from Aldrich, Graphite superfine powder (<50 μm) was purchased from Merck. Battery-grade acetylene black was purchased from Denka Japan Private Co., Ltd., to be used as a conductive additive. Copper foil of a thickness 20 μm was purchased from the Nilaco corporation. All the chemicals were used without any further purification for the synthesis of polymer and electrode fabrication, respectively.

### 4.3.2 Instrumentation

$^1\text{H}$  NMR spectrum was recorded with Bruker Avance II 400 Mhz spectrometer. Chemical shifts were labelled in ppm according to the protons of the deuterated solvent used as an internal standard. The FT-IR spectra were recorded using Perkin Elmer 100 FT-IR spectrometer. The spectra were averaged over 100 scans with a resolution of  $2\text{ cm}^{-1}$  in the ATR mode. Hitachi S-4500 FESEM instrument was used to obtain SEM images of respective anodes before and after fabrication at 1.0 kV voltage. X-ray photoelectron spectroscopy (XPS) measurements were conducted on Fisons instruments S-probe TM 2803.

### 4.3.3 P-BIAN crosslinked polymer matrices synthesis

The P-BIAN copolymer was synthesized as per the procedure reported by our group<sup>45</sup>. Figure 2a shows the synthetic scheme of P-BIAN. It was characterized by  $^1\text{H}$ -NMR and FT-IR as shown in Figure 2b and Figure 2c, respectively. Further for the synthesis of crosslinked P-BIAN matrices, a solution of P-BIAN copolymer (1.497 g, 10 mmol) in *N*-methylpyrrolidone (NMP) (150 ml) was set-up to stir under reflux in nitrogen atmosphere. To this, 1,6-dibromohexane (5 mmol, 0.77 ml) was added dropwise. The resultant reaction mixture was stirred and refluxed at  $150\text{ }^\circ\text{C}$  for 24 hours followed by refrigeration for 3 hours. The product was obtained by evaporating the NMP solvent under reduced pressure and drying under vacuum at  $120\text{ }^\circ\text{C}$  for 12 hours. The obtained product was a black colored sticky compound. Figure 3 shows the synthetic scheme of the crosslinked P-BIAN polymer matrices. It was characterized by  $^1\text{H}$ -NMR, XPS, and FT-IR techniques. Figure 4a shows the  $^1\text{H}$ -NMR spectrum of the synthesized crosslinked P-BIAN polymer [( $\delta$ , ppm) 1.95 (-CH<sub>2</sub>, m, 4H), 2.31 (-CH<sub>2</sub>, m, 4H), 3.32 (-CH<sub>2</sub>, t, 4H), and 7.79 – 8.21 (aromatic protons)] and the peaks corresponding to NMP solvent are [( $\delta$ , ppm) 3.43 (-CH<sub>2</sub>, t, 2H), 2.78 (-CH<sub>3</sub>, s, 3H), 2.02 (-CH<sub>2</sub>, m, 2H), and 1.78 (-CH<sub>2</sub>, t, 2H)]. Figure 4b and 4c show the XPS N 1s spectrum of the P-BIAN copolymer and crosslinked P-BIAN polymer, respectively. In N 1s spectrum of P-BIAN copolymer, only single peak at 400.1 eV corresponding to diimine (C=N) backbone of the P-BIAN framework that are  $\text{-sp}^2$  hybridized (pyridinic-type) was observed. Whereas, in the N 1s spectrum of crosslinked P-BIAN, the detection of a signature second peak at 403.5 eV corresponding to quaternary diimine nitrogen after crosslinking confirmed the successful crosslinking of P-BIAN polymeric units to form crosslinked matrices. The XPS results were supported by FT-IR characterization of crosslinked P-BIAN polymer. As shown in Figure 4d, the presence of quaternary nitrogen  $\nu$ -stretch bands ( $2850 - 3100\text{ cm}^{-1}$ ) and aliphatic C-H  $\nu$ -

stretch bands ( $2750\text{-}2890\text{ cm}^{-1}$ ) were characteristic of P-BIAN and linker hexane unit in the crosslinked P-BIAN polymer. Table 1 lists all the characteristic infrared spectroscopic bands corresponding to P-BIAN and crosslinked P-BIAN polymer matrices, respectively.

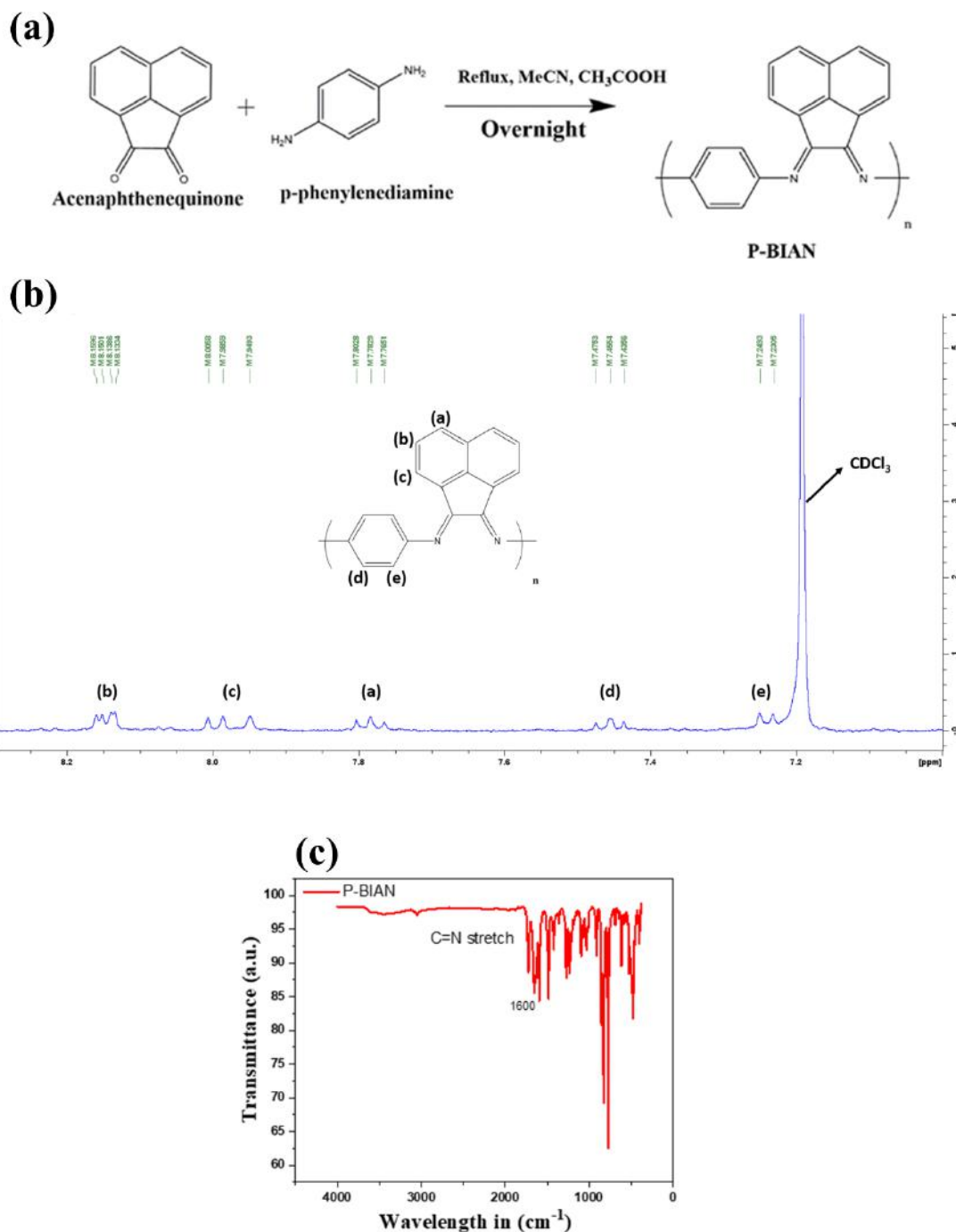


**Figure 2:** (a) Synthetic scheme of P-BIAN, (b)  $^1\text{H-NMR}$ , and (c) FT-IR spectra of P-BIAN

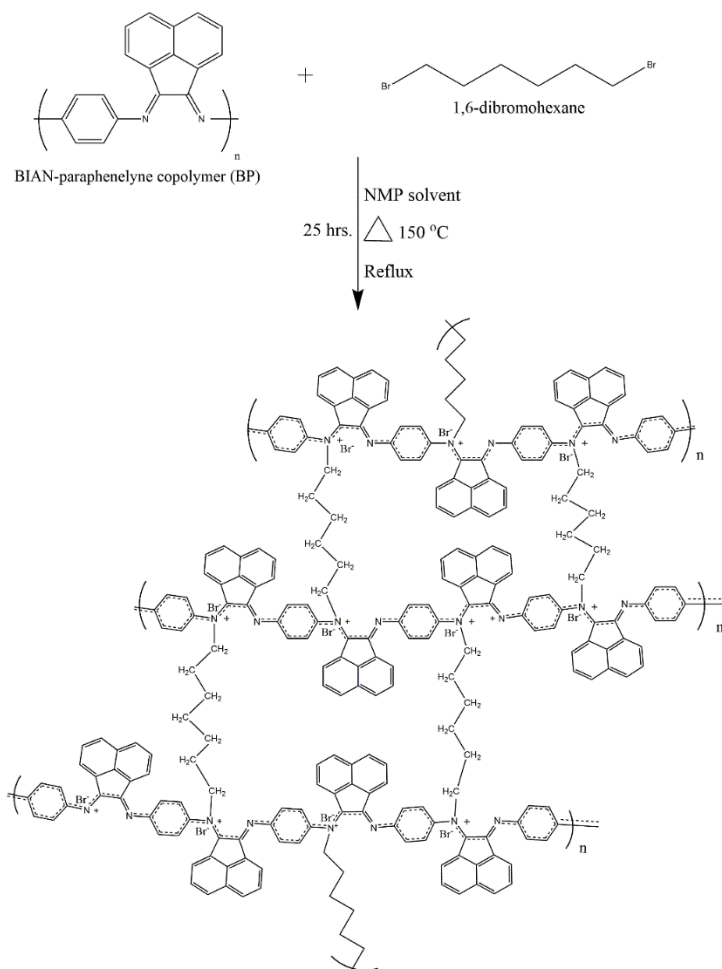


**Figure 3:** Synthetic scheme of the crosslinked P-BIAN polymer matrices

**Table 1:** FT-IR assignments of the following systems: P-BIAN and crosslinked P-BIAN

Species	Observed Bands (cm <sup>-1</sup> )	Assignment
<b>P-BIAN</b>	1659 (m)	$\nu$ (C=C) aromatic <sup>46</sup>
	1592 (m)	$\nu$ (C=N) imine <sup>47-48</sup>
	772 (m)	$\omega$ (C-N) aromatic amine <sup>47-48</sup>
<b>Crosslinked P-BIAN binder</b>	2850-3100 (m)	$\nu$ (Quaternary nitrogen) <sup>49</sup>
	2750-2890 (m)	Aliphatic C-H <sup>46</sup>
	1644 (s)	$\nu$ (C=C) aromatic <sup>46</sup>
	1507 (m)	$\nu$ (C=N) imine <sup>47-48</sup>
	761 (s)	$\omega$ (C-N) aromatic amine <sup>47</sup>

<sup>a</sup>Relative intensities are shown in parantheses: vs – very strong, s – strong, and m – medium.

<sup>b</sup> $\nu$ : stretching,  $\omega$  wagging, and  $\delta$ : bending; a: asymmetric mode, s: symmetric mode.



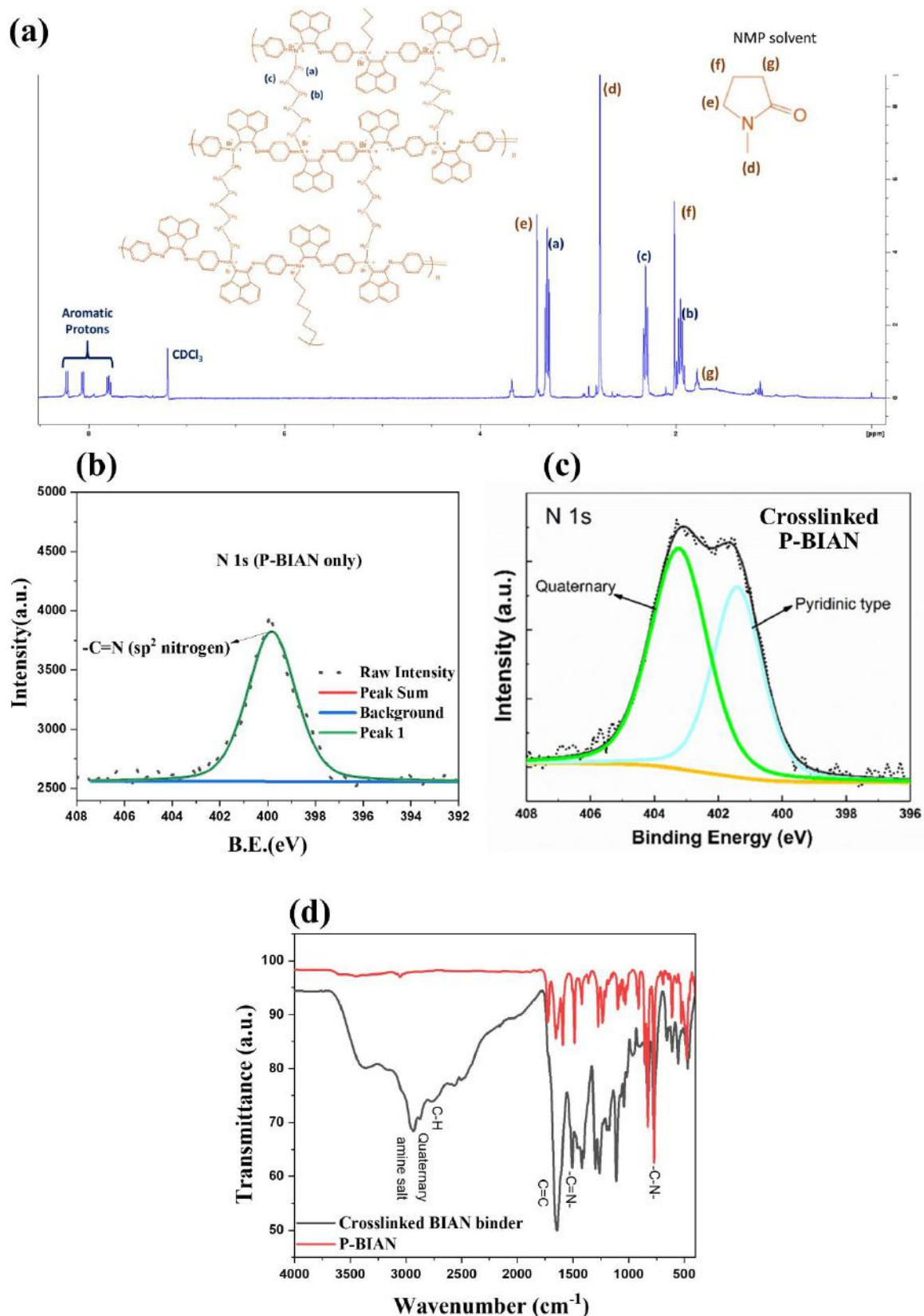


**Figure 4:** (a)  $^1\text{H}$ -NMR spectrum of the crosslinked P-BIAN polymer. XPS N 1s spectra of (b) P-BIAN copolymer and (c) crosslinked P-BIAN binder. (d) FT-IR spectrum of the crosslinked P-BIAN binder.

### 4.3.4 Electrode preparation

Anodes were prepared by casting the slurry comprising of 35 wt % silicon nanoparticles (SiNPs) (particle size <100 nm), 25 wt % graphite, 20 wt % crosslinked P-BIAN binder, and 20 wt % acetylene black (conductive additive) in NMP solvent onto a copper foil by doctor blade method. The obtained electrodes were dried at 90 °C in vacuum for 12 hours to completely remove the solvent. After drying, the electrodes were roll-pressed (calendered) at 80 °C with thickness 60 µm. Finally, the electrodes were punched into disc-electrodes to assemble coin cells for electrochemical evaluation. Similarly, two types of anodes for control studies were prepared based on two conventional binders PAA (20 wt %) and CMC-Na (20 wt %) reported in the literature while maintaining similar proportions of active materials – 35 wt % SiNPs and 25 wt % graphite, and conductive additive - acetylene black 20 wt %. Table 2 lists the composition of respective electrode constituents used in this study and Table 3 details the electrode thickness and laminate loading for each type of electrode, respectively.

**Table 2:** Composition of respective electrode constituents

<b>Crosslinked P-BIAN binder-based anode (Si/C/P-BIAN-crosslinked/AB)</b>	
<b>Constituents</b>	<b>Composition (wt %)</b>
Silicon nanoparticles (SiNPs)	35
Graphite	25
Crosslinked P-BIAN binder	20
Acetylene black	20
<b>Control Study (Electrode 1: Si/C/PAA/AB) and (Electrode 2: Si/C/CMC/AB)</b>	
<b>Constituents</b>	<b>Composition (wt %)</b>
Silicon nanoparticles (SiNPs)	35 (same for electrode 1 and 2)
Graphite	25 (same for electrode 1 and 2)
PAA	20 (Electrode 1)
CMC-Na	20 (Electrode 2)
Acetylene black	20 (same for electrode 1 and 2)

**Table 3:** Details of electrode thickness and laminate loading for each type of electrode, respectively.

Type of electrode	Total electrode thickness	Only copper disc thickness	Thickness of the laminate loading
Si/C/PAA/AB (control)	45 ± 0.5 μm	20 μm	25 ± 0.5 μm
Si/C/CMC/AB (control)	47 ± 0.5 μm	20 μm	27 ± μm
Si/C/P-BIAN-crosslink/AB	46 ± 0.5 μm	20 μm	26 ± 0.5 μm

### 4.3.5 Electrochemical measurements

CR-2025-type coin cells were fabricated configuring Li metal as the counter-reference electrode, polypropylene separator (25 μm, Celgard 2500), 1.0M LiPF<sub>6</sub> in (50/50) EC/DEC electrolyte, and Si/C anode. The anodic half-cells were prepared in a glovebox filled with argon (UNICO UN-650, H<sub>2</sub>O, and O<sub>2</sub> level <0.1 ppm). Charge-discharge studies were carried at 25 °C on Electrofield-EFT-001. A VSP potentiostat (BioLogic) electrochemical analyzer/workstation was used for the electrochemical characterization of the fabricated half-cells by cyclic voltammetry (CV) measurements between OCP and 1.2 V vs Li/Li<sup>+</sup> at a scan rate of 0.1 mVs<sup>-1</sup> at 25 °C. Electrochemical impedance spectroscopy (EIS) and dynamic electrochemical impedance spectroscopy (DEIS) studies were conducted on a VSP potentiostat (Biologic) within a frequency range of 10 mHz to 0.1 Hz with a sinus amplitude of 10 mV.

## 4.4 Results and Discussion

### 4.4.1 Theoretical studies

As the compounds with a high-lying highest occupied molecular orbital (HOMO) are prone to gradual oxidation in the cathodic environment, the compounds with a low-lying lowest unoccupied molecular orbital (LUMO) are susceptible to reduction in the anodic environment<sup>50-52</sup>. Being one of the constituents in the anode, binders get exposure to the electrolyte via the surface of the anode. Therefore, by virtue of their band energies (LUMO in the case of binder for anodes), a binder system has a great potential to determine the quality of SEI formation via optimizing the reductive decomposition of the electrolyte on the anode surface. The stability and performance of Si anodes is dependent of the quality of SEI to a large

extent<sup>3</sup>. So, to tailor an effective/robust SEI, the binder system must have tunable electronic properties. In this regard, the conjugated compounds of the BIAN family have proven their worth owing to their low-lying LUMO<sup>43-44</sup>. Their electronic properties are highly tunable because of the presence of electron rich diimine nitrogen atoms. By undergoing crosslinking through diimine backbone (quaternization of nitrogen atoms), the LUMO energy level of the crosslinked P-BIAN polymer would have lowered prospectively. Hence, the crosslinked P-BIAN polymer was computationally evaluated by the DFT-based geometry and energy optimization calculations on Materials Studio via Dmol3. The optimization parameters were: gga (pW91) density functional, DND basis set, and unrestricted spin polarization. The DFT optimized structure of the crosslinked P-BIAN is shown in Figure 5a. The calculated HOMO-LUMO band energies of crosslinked P-BIAN were compared with electrolyte components (ethylene carbonate (EC) and diethyl carbonate (DEC)), precursor polymer P-BIAN, and our earlier reported P-BIAN/PAA binder for Si anodes as shown in Figure 5b. Electrolyte components EC and DEC were calculated to show high-lying LUMOs ( $E_{\text{LUMO}} = -0.28$  eV for EC and  $-0.06$  eV for DEC), respectively. Table 4 lists the comparison table based on HOMO-LUMO band energies among various binders reported in the literature (SBR, PAA, CMC, etc.) and crosslinked P-BIAN binder. The crosslinked P-BIAN binder was evaluated to be having the lowest-lying LUMO among all with  $E_{\text{LUMO}} = 3.67$  eV. The low-lying LUMO of the crosslinked P-BIAN binder has the potential to undergo n-doping in reducing anodic environment which would restrict the excessive reductive decomposition of electrolyte on the surface of the anode. Therefore, the n-doping of the crosslinked P-BIAN can be instrumental in tailoring the architecture of the SEI as well as lower the irreversible capacity loss that happens by uncontrolled electrolyte decomposition.

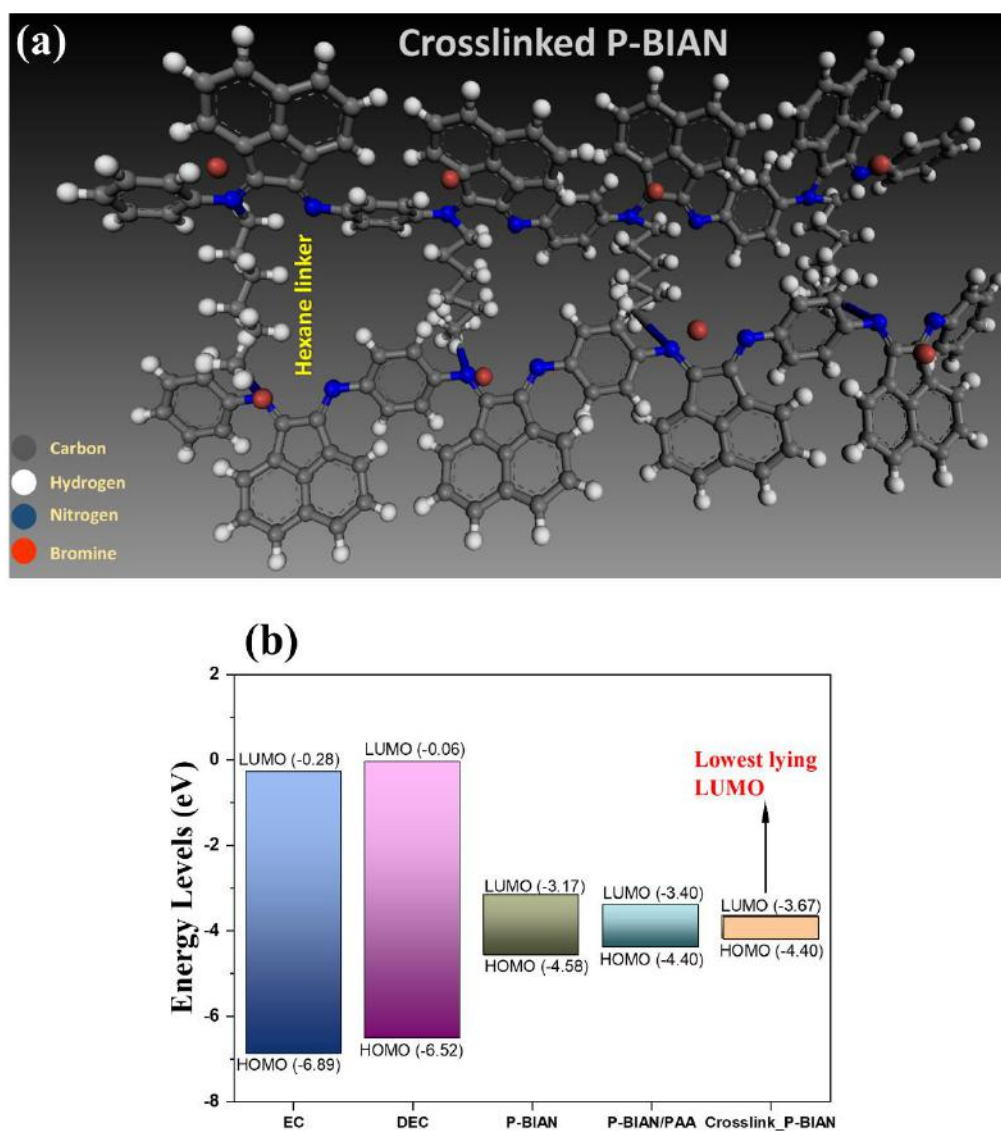


**Figure 5:** (a) DFT optimized structure of crosslinked P-BIAN binder and (b) HOMO-LUMO energy level comparison among electrolyte components, P-BIAN, P-BIAN/PAA, and crosslinked P-BIAN binders, respectively.

**Table 4:** A comparison list of crosslinked P-BIAN with different binders reported in the literature based on their HOMO-LUMO energy levels

Binders	HOMO (eV)	LUMO (eV)	Reference
PEO	-11.2	7.1	50
SBR	-8.9	5.1	
PMA	-12.2	4.95	
CMC	-12.1	4.8	
PVC	-12.2	4.78	

PVDF	-12.47	1.46	43
PAA	-6.1	-1.3	44
P-BIAN	-4.58	-3.17	
P-BIAN/PAA	-4.4	-3.4	Chapter-3
Crosslinked P-BIAN	-4.19	-3.67	This work

## 4.4.2 Electrochemical characterization

### Cyclic voltammetry studies

The anodic half-cells fabricated with anode comprising of P-BIAN crosslinked binder and control study binders (PAA and CMC) were subjected to cyclic voltammetry (CV) studies. Figure 6a shows the cyclic voltammogram of Si/C/P-BIAN-crosslink/AB anode-based half-cell recorded within the operating potential window 0.005 and 1.2 V (vs Li/Li<sup>+</sup>) at a scan rate of 0.1 mVs<sup>-1</sup>. In the first reverse scan, the characteristic peak at 0.67 V was attributed to electrolyte decomposition at Si/C/P-BIAN-crosslink/AB anode<sup>53</sup> and the peak at 0.0045 V was attributed to the initial alloying of the crystalline Si phase (Li<sub>15</sub>Si<sub>4</sub>)<sup>54</sup>. After the alloying of crystalline Si phase in the first reverse scan, from second cycle onwards, the peak corresponding to the alloying of amorphous Si phase (Li<sub>12</sub>Si<sub>7</sub>) was observed at 0.19 V<sup>54</sup>. In the forward scan, the two anodic peaks observed at 0.33 V and 0.54 V were characteristic to the transformation of amorphous Li<sub>x</sub>Si phase formed during alloying to Si phase back again<sup>26, 54-55</sup>. Similar characteristic peaks attributed to electrolyte decomposition, alloying of crystalline Si phase in the first reverse scan, alloying of amorphous Si phase from second reverse onwards, and dealloying of lithiated amorphous Si phase to Si were observed in control studies-based anodic half-cells with PAA (Figure 6b) and CMC-Na (Figure 6c) binders, respectively. Further, cyclic voltammograms corresponding to 3<sup>rd</sup> and 4<sup>th</sup> cycles for the respective anodes were compared as shown in Figure 6d. The anodic peaks of Si/C/P-BIAN-crosslink/AB anodic half-cell were distinctive with high intensity exhibiting two phase dealloying of amorphous silicon phase with good cyclability. However, in the case of Si/C/PAA/AB anode though the peaks were distinct, the sharpness and intensity were poor which could be attributed to volume expansion driven partial dealloying. And in the case of Si/C/CMC/AB anode, two distinctive peaks corresponding to two-step dealloying of amorphous Si were not observed exhibiting rapid phase transformation that could lead to poor

cyclability at higher currents. Hence, Si/C/P-BIAN-crosslink/AB anodic half-cell showed superior performance with all distinctive characteristic Si alloying and dealloying peaks with promising cyclability upon repeated charge-discharge in comparison to control binders'-based anodic half-cells.

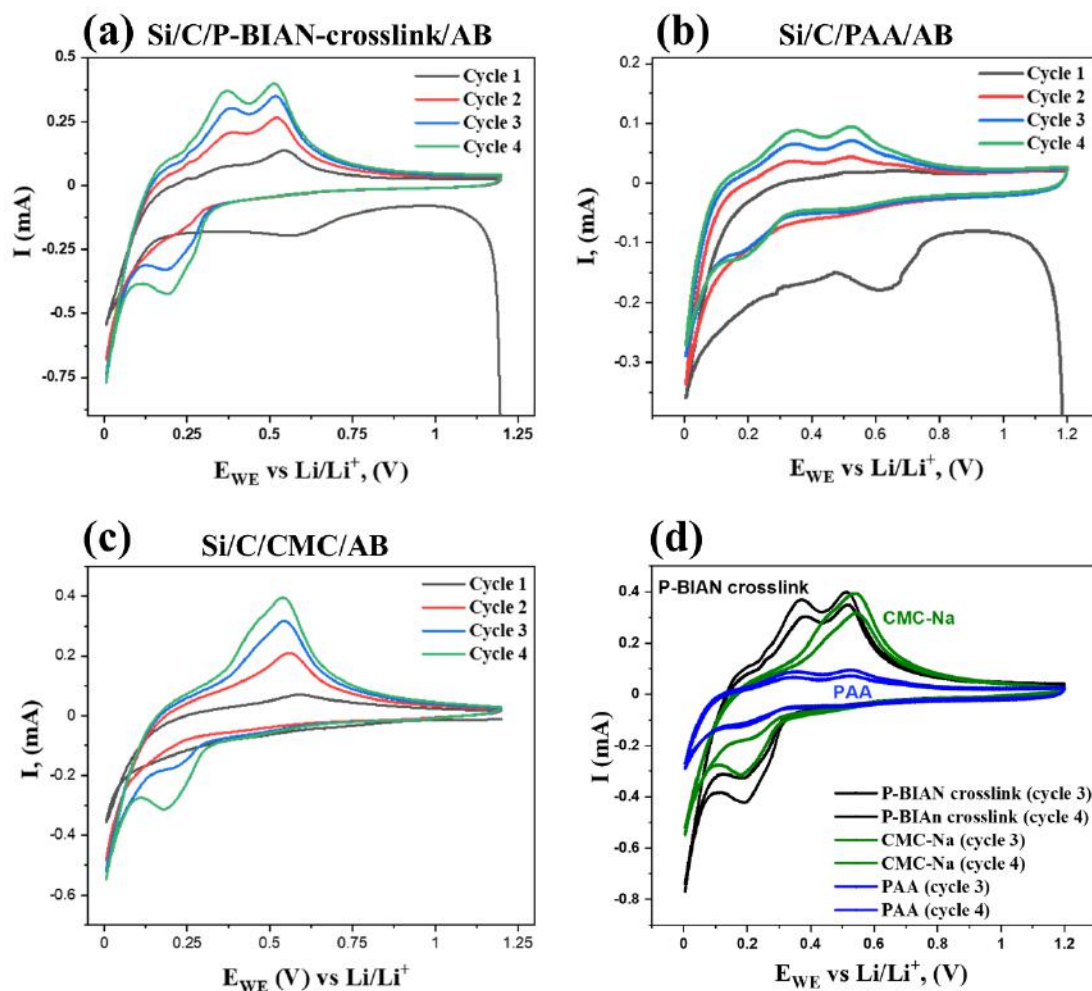


**Figure 6:** Cyclic voltammograms of (a) Si/C/P-BIAN-crosslink/AB anode-based half-cell vs  $Li/Li^+$ , (b) control (Si/C/PAA/AB) anode-based half-cell vs  $Li/Li^+$ , (c) control (Si/C/CMC/AB) anode-based anodic half-cell vs  $Li/Li^+$ , and (d) comparison of the 3<sup>rd</sup> and 4<sup>th</sup> cycles from the cyclic voltammograms of Si/C/P-BIAN-crosslink/AB, Si/C/PAA/AB, and Si/C/CMC/AB anodes, respectively.

### Charge-discharge studies

The long-term cycling performance comparison between Si/C/P-BIAN-crosslinked/AB anodic half-cell and control systems (Si/C/PAA/AB and Si/C/CMC/AB) is shown in Figure 7a. The first 10 cycles of de-/alloying were carried out at  $150 \text{ mA g}^{-1}$  for better interface formation which was followed by long-term cycling at a high current of  $500 \text{ mA g}^{-1}$ . The first cycle

reversible capacities for Si/C/P-BIAN-crosslinked/AB anodic half-cell was recorded to be 2512 mAhg<sup>-1</sup> and control (Si/C/PAA/AB and Si/C/CMC/AB) anodic half-cells were recorded to be 1893 mAhg<sup>-1</sup> and 2600 mAhg<sup>-1</sup>, respectively. However, the corresponding initial coulombic efficiencies (ICEs) for Si/C/P-BIAN-crosslinked/AB anodic half-cell was 88.2% which was significantly higher than control systems (Si/C/PAA/AB and Si/C/CMC/AB) with 85.0% and 81.0%, respectively. The higher ICE in the case of Si/C/P-BIAN-crosslinked/AB anodic half-cell meant lower irreversible capacity loss that is a direct result of restricted decomposition of the electrolyte on the Si/C/P-BIAN-crosslinked/AB anode governed by n-doping of crosslinked P-BIAN binder. Therefore, due to excellent mechanical robustness induced by crosslinked P-BIAN binder and tailored conductive SEI, the Si/C/P-BIAN-crosslinked/AB anode showed excellent cyclability for over 1000 cycles with a high reversible capacity ~2500 mAhg<sup>-1</sup>, 99.03% capacity retention, and >99% coulombic efficiency after initial pre-cycling. Whereas control systems (Si/C/PAA/AB and Si/C/CMC/AB) stood no match with poor cyclability and fading capacity after 400 cycles of de-/alloying. Figure 7b compares the reversible capacity retention between Si/C/P-BIAN-crosslinked/AB anodic half-cell and control systems (Si/C/PAA/AB and Si/C/CMC/AB), respectively. Si/C/P-BIAN-crosslinked/AB anodic half-cell showed an excellent reversible capacity retention of 99.01% after 1000 cycles of de-/alloying in comparison to control systems (Si/C/PAA/AB and Si/C/CMC/AB) with 51.3% after 300 cycles and 42.5% after 400 cycles, respectively. Figure 7c shows the comparison profiles of coulombic efficiencies (CEs) of respective anodes after 40 cycles of de-/alloying at 500 mAhg<sup>-1</sup>. The Si/C/P-BIAN-crosslinked/AB anodic half-cell achieved >99% CE after 16 cycles of de-/alloying from 88.2% first cycle ICE. On the other hand, control systems (Si/C/PAA/AB and Si/C/CMC/AB) showed poor ICEs owing to excessive electrolytic decomposition and showed lower maximum CEs after 40 cycles (97.8% and 98.5%) in comparison to Si/C/P-BIAN-crosslinked/AB anodic half-cell. Hence, the Si/C/P-BIAN-crosslinked/AB anodic half-cell outperformed the conventional binders-based anodic half-cells (Si/C/PAA/AB and Si/C/CMC/AB) in terms of specific capacity at a high current rate of 500 mA g<sup>-1</sup>, cyclability, and capacity retention.



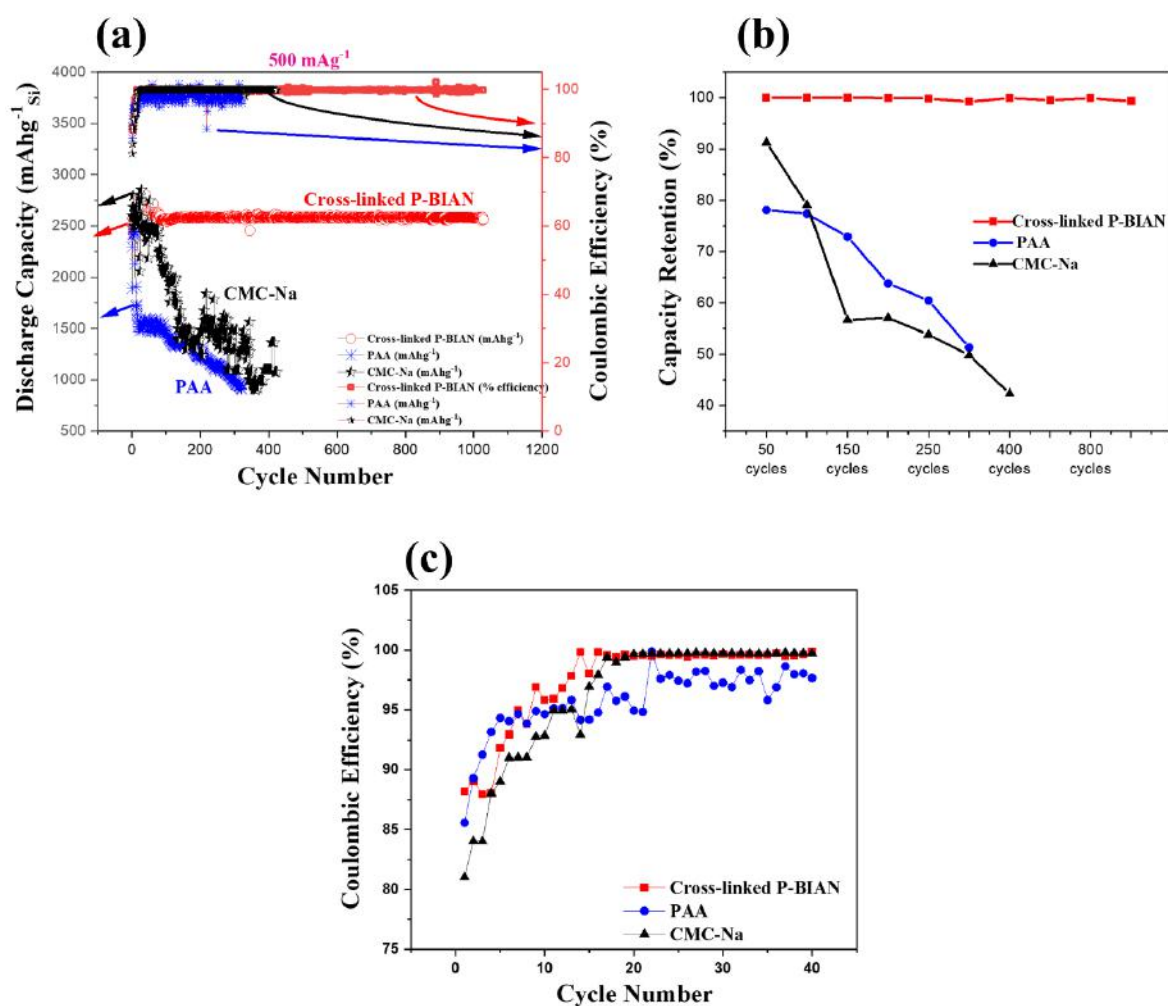


**Figure 7:** Charge-discharge studies of Si/C/P-BIAN-crosslink/AB anodic half-cell and control systems (Si/C/PAA/AB and Si/C/CMC/AB). (a) long-term cyclic stability comparison of respective anodic half-cells at 500 mA g<sup>-1</sup> current, (b) comparison of capacity retention in Si/C/P-BIAN-crosslink/AB anodic half-cell and control systems, and (c) coulombic efficiency comparison after 40 cycles of de-/alloying between Si/C/P-BIAN-crosslink/AB anodic half-cells and control systems, respectively.

#### (Dynamic) electrochemical impedance spectroscopy studies

To determine the internal impedance in Si/C/P-BIAN-crosslink/AB anodic half-cell and control systems (Si/C/PAA/AB and Si/C/CMC/AB), electrochemical impedance spectroscopy (EIS) measurements were carried out. The EIS profiles were recorded at an open circuit potential (OCP) without direct current (DC). Figure 8a, 8b, and 8c show the Nyquist impedance profiles of Si/C/P-BIAN-crosslink/AB, control system (Si/C/PAA/AB), and control system (Si/C/CMC/AB)-based anodic half-cells immediately after fabrication and after 15 cycles of de-/alloying. In the case of Si/C/P-BIAN-crosslink/AB anodic half-cell, the internal

impedance immediately after fabrication was recorded to be 415  $\Omega$  in comparison to control systems (Si/C/PAA/AB and Si/C/CMC/AB) with 620  $\Omega$  and 1875  $\Omega$ , respectively. After 15 cycles of de-/alloying, in the case of Si/C/P-BIAN-crosslink/AB anodic half-cell internal impedance reduced to mere 110  $\Omega$  constituting of impedance contribution by SEI and charge-transfer (CT) ( $R_{SEI}+R_{CT}$ ) in comparison to control systems (Si/C/PAA/AB and Si/C/CMC/AB) with 360  $\Omega$  and 250  $\Omega$  ( $R_{SEI}+R_{CT}$ ), respectively. Therefore, owing to the excellent interface formed because of n-doping of crosslinked P-BIAN binder, the electrolytic decomposition on the anode surface and the internal impedance in the case of Si/C/P-BIAN-crosslink/AB anodic half-cell were significantly lowered both pre-cycling and post-cycling.

Further, to determine the electronic conductivity of crosslinked P-BIAN binder as well as conventional PAA and CMC binders, Nyquist impedance profiles of anodic half-cells with copper electrodes coated with respective binders (without active material and conductive additive) were recorded. Figure 8d and 8e shows the Nyquist profiles of copper foil electrode coated with crosslinked P-BIAN binder and conventional binders (PAA and CMC) vs Li/Li<sup>+</sup> at OCP, respectively. Table 5 lists that the electronic conductivity of crosslinked P-BIAN binder was calculated to be  $2.16 \times 10^{-3} \Omega^{-1}m^{-1}$  which was higher than the conventional binders PAA ( $6.82 \times 10^{-4} \Omega^{-1}m^{-1}$ ) and CMC ( $1.32 \times 10^{-4} \Omega^{-1}m^{-1}$ ).

$$R = \rho \frac{l}{A} \quad (1)$$

In equation 1, R is the resistance in ohm ( $\Omega$ ), l is the length in meter (m) of the specimen, A is the cross-sectional area ( $m^2$ ) of the specimen, and  $\rho$  the resistivity ( $\Omega m$ ). The conductivity  $\sigma$  ( $\Omega^{-1} m^{-1}$ ) of a material is the inverse of its resistivity as shown in equation 2.

$$\sigma = \frac{1}{\rho} \quad (2)$$

**Table 5:** Parameters associated with electronic conductivity measurements for respective binder systems.

Material	Area of the electrode (A)	Thickness of the electrode (L)	Resistance	Conductivity
P-BIAN/PAA	$1.77 \times 10^{-4} m^2$	$46 \pm 0.5 \mu m$	120 $\Omega$	$2.16 \times 10^{-3} \Omega^{-1} m^{-1}$
Control System (PAA binder)	$1.77 \times 10^{-4} m^2$	$45 \pm 0.5 \mu m$	476 $\Omega$	$6.82 \times 10^{-4} \Omega^{-1} m^{-1}$
Control System (CMC binder)	$1.77 \times 10^{-4} m^2$	$47 \pm 0.5 \mu m$	2010 $\Omega$	$1.32 \times 10^{-4} \Omega^{-1} m^{-1}$

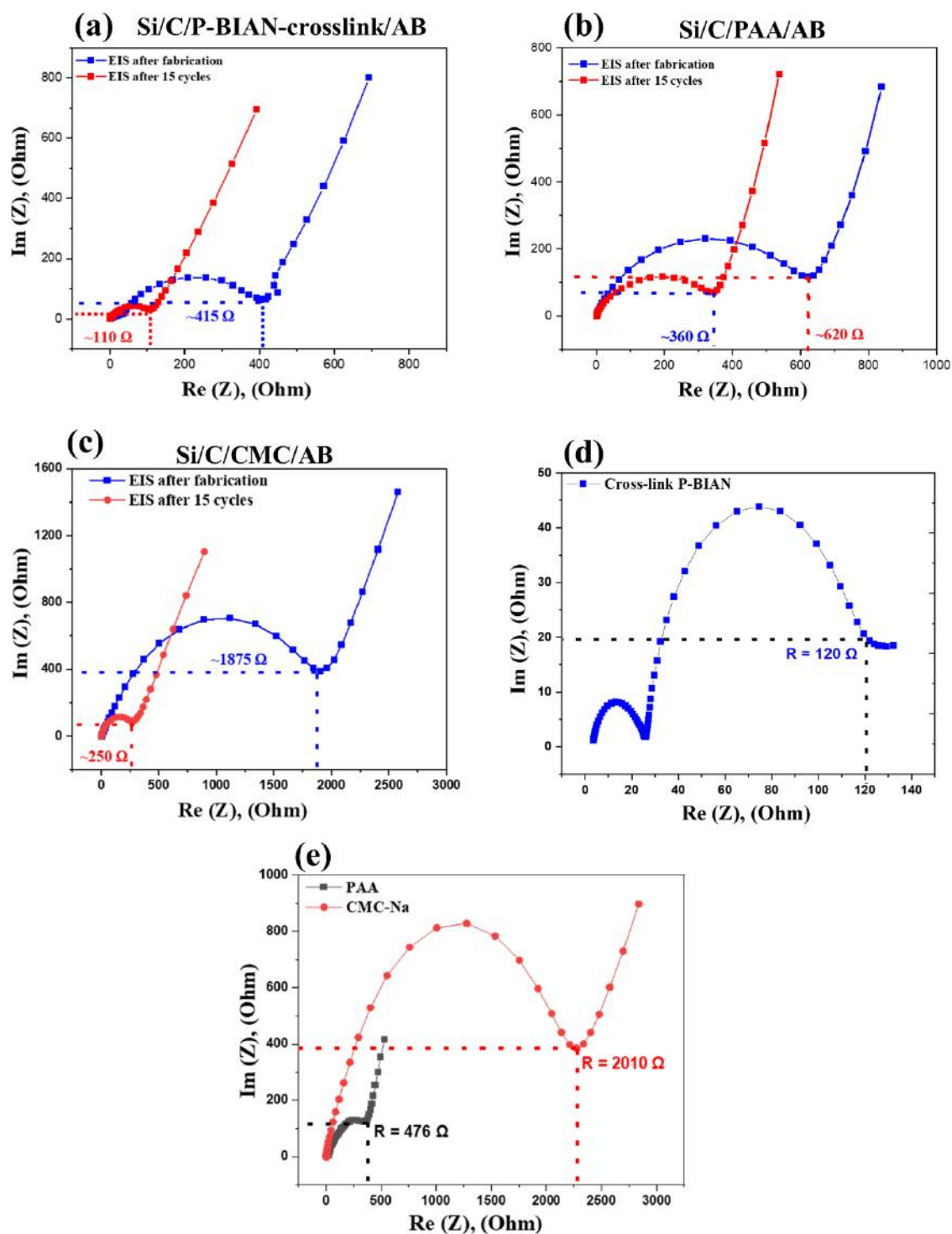


**Figure 8:** Nyquist Impedance profiles recorded after fabrication and 15 cycles of de-/alloying of (a) Si/C/P-BIAN-crosslink/AB anodic half-cell, (b) control system – Si/C/PAA/AB, and (c) control system – Si/C/CMC/AB, respectively. Nyquist profile of anodic half-cells having electrodes with pure binder coating (without active material and conductive additive) (a) crosslinked P-BIAN binder and (b) conventional binders (PAA and CMC), respectively.

For thorough understanding of the types of interfaces and their contribution to the overall cell impedance, dynamic electrochemical impedance spectroscopy (DEIS) studies were carried out. In this, the impedance profiles of the cell at various potential steps during the respective charge and discharge cycles are recorded. This phenomenon helps to understand various interfacial processes that happen during the real time charge-discharge of the battery. The frequency response of anodic half-cells under study were recorded corresponding to an AC signal in the operating potential window of the battery i.e., 0.005 V – 1.2 V vs Li/Li<sup>+</sup>. The DEIS 3D-Nyquist impedance profiles during alloying and dealloying half-cycles for Si/C/P-BIAN-crosslinked/AB anodic half-cell after 1000 cycles and control systems (Si/C/PAA/AB after 300 cycles and Si/C/CMC/AB after 400 cycles) are shown in Figure 9. To get comprehensive understanding on the types of interfaces that are present, various tentative Equivalent Electrical Circuit Models (EECMs) were tried to computationally fit each of the Nyquist profiles at each potential step for all anodic half-cells during the DEIS study. The best fit EECM was (RL(QR)(CR)(QR)(CW)) (Figure 10a). Each element in the electrical circuit model is classified as follows: Ohmic electrolytic resistance ( $R_e$ ), intrinsic resistance of the silicon anode comprising of the particle to particle and particle to current collector ( $R_{PC}$ ), solid-electrolyte interface ( $R_{SEI}$ ), charge transfer resistance ( $R_{CT}$ ), and Warburg infinite diffusion element ( $Z_{GFW}$ ). Table 6,7, and 8 list the circuit fitting parameters (resistance corresponding to each of the interfaces involved) as per the EECM for anodes with respective binder systems. SEI is one of the most important constituents that determine the performance of a LIBs. Therefore, the SEI resistance ( $R_{SEI}$ ) values for each of the binder system-based anodic half-cells was plotted against corresponding potential (V) steps as shown in Figure 10b. It was evidently seen that the  $R_{SEI}$  in the case of Si/C/P-BIAN-crosslinked/AB anodic half-cell was substantially lower than control systems (Si/C/PAA/AB and Si/C/CMC/AB), respectively. Therefore, the n-doping of the crosslinked P-BIAN binder in the anodic environment tailored the architecture of SEI with lowered interfacial impedance. This enhanced the performance of Si anodes manifold in comparison to conventional binder systems. The DEIS study effectively elaborated on the interfacial impedance which determine the cell's performance to a great extent.

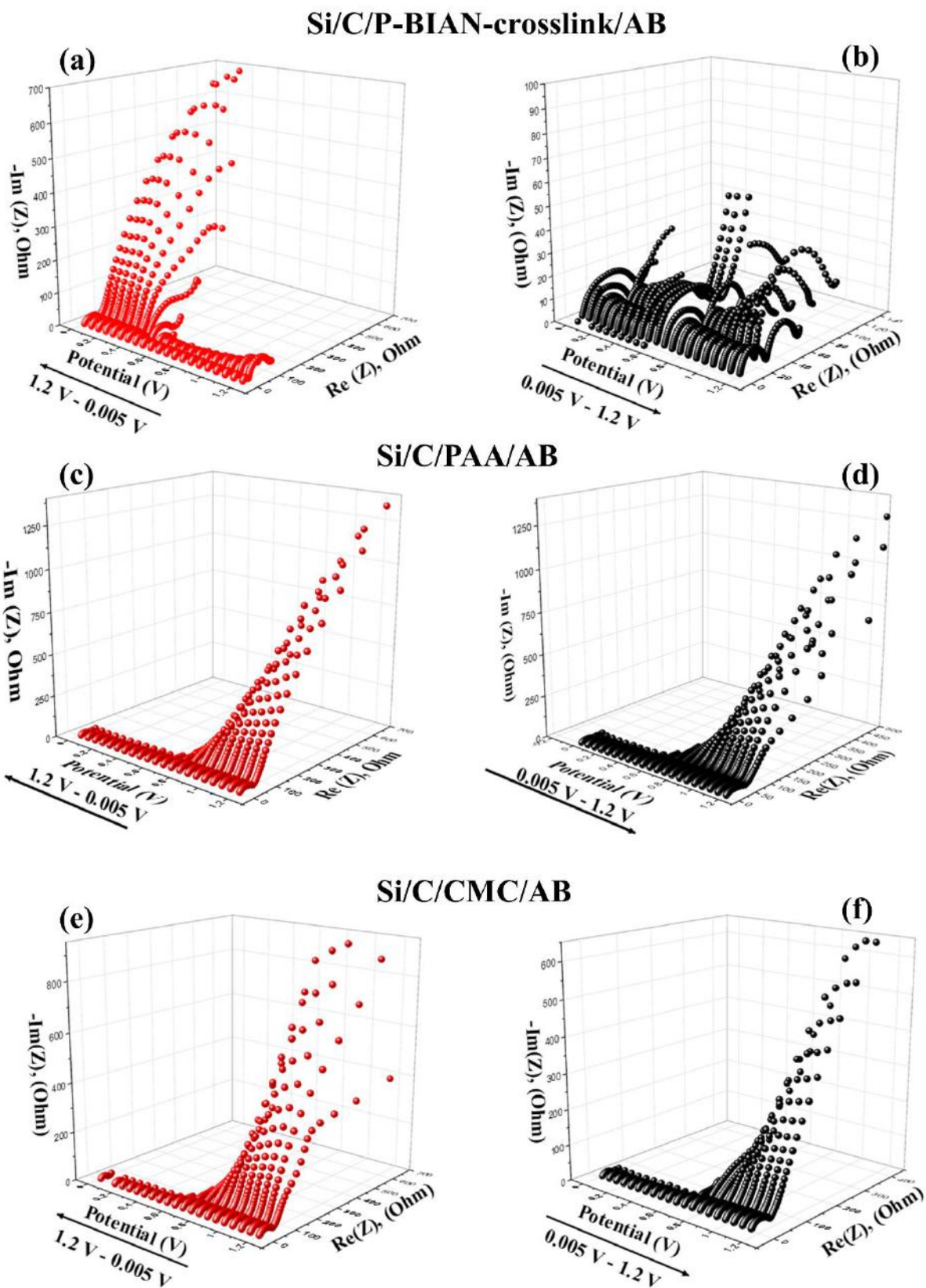


**Figure 9:** DEIS 3-D Nyquist profiles recorded after 1000 cycles for Si/C/P-BIAN-crosslinked/AB anodic half-cell (a) during alloying half-cycle and (b) during dealloying half-

cycle, after 300 cycles for control system Si/C/PAA/AB anodic half-cell (c) during alloying half-cycle and (d) during dealloying half-cycle, and after 400 cycles for control system Si/C/CMC/AB anodic half-cycle (e) during alloying half-cycle and (f) during dealloying half-cycle, respectively.

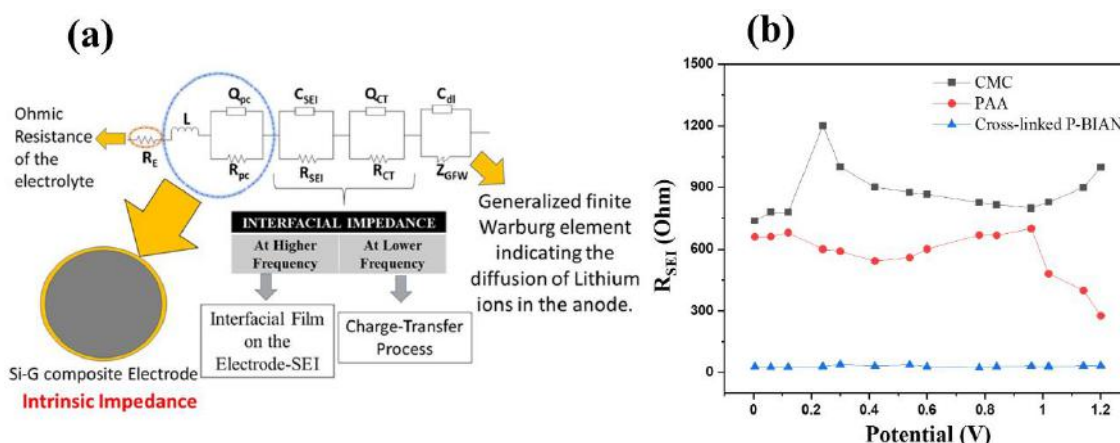


**Figure 10:** (a) The best fit Equivalent Electrical Circuit Model (EECM) for Nyquist impedance profiles and (b) a comparison plot depicting the SEI impedance ( $R_{SEI}$ ) vs potential (V) during alloying half-cycle for Si/C/P-BIAN-crosslinked/AB and control system (Si/C/PAA/AB and Si/C/CMC/AB) anodic half-cells, respectively.

**Table 6:** DEIS circuit fitting parameters during alloying for Si/C/P-BIAN-crosslink/AB anodic half-cell

$R_s$	$R_{pc}$	$R_{SEI}$	$R_{CT}$	$\chi^2$	Circuit	Potential (V)
1.549	10.45	33.18	36.63	0.000667	R(L)(QR)(CR)(QR)(CW)	1.20
1.435	22.52	31.84	60.31	9.9E-05	R(L)(QR)(CR)(QR)(RW)	1.14
2.0	2.88	29.46	52.21	2.30E-05	R(L)(QR)(CR)(QR)(CW)	1.08
1.62	1.19	29.04	15.48	5.51E-05	R(L)(QR)(CR)(QR)(CW)	1.02
1.74	119	31.84	49.93	4.46E-05	R(L)(QR)(CR)(QR)(CW)	0.96
4.85	20.42	35.84	86.19	1.52E-05	R(L)(QR)(CR)(QR)(CW)	0.90
4.81	3.50	28.79	54.39	2.29E-05	R(L)(QR)(CR)(QR)(CW)	0.84
5.93	5.55	22.8	33.54	5.21E-05	R(L)(QR)(CR)(QR)(CW)	0.78
1.95	10.39	37.6	1.45	6.42E-05	R(L)(QR)(CR)(QR)(CW)	0.72

## CHAPTER 4

1.52	1.59	22.95	9.65E+02	9.44E-05	R(L)(QR)(CR)(QR)(CW)	0.66
2.58	6.41	28.05	3.61E+01	8.19E-05	R(L)(QR)(CR)(QR)(CW)	0.60
1.66	7.31	37.51	2.49E+01	8.99E-05	R(L)(QR)(CR)(QR)(CW)	0.54
2.58	2.89	36.04	21.44	1.46E-05	R(L)(QR)(CR)(QR)(CW)	0.48
2.51	2.84	30.98	6.43	1.52E-05	R(L)(QR)(CR)(QR)(CW)	0.42
3.50	44.45	31.75	3.53	1.53E-05	R(L)(QR)(CR)(QR)(CW)	0.36
4.50	43.21	38.9	7.86	1.43E-05	R(L)(QR)(CR)(QR)(CW)	0.30
6.41	22.29	29.06	94.18	1.99E-05	R(L)(QR)(CR)(QR)(CW)	0.24
33.51	30.45	28.10	74.29	2.15E-05	R(L)(QR)(CR)(QR)(CW)	0.18
2.99	0.002	26.45	91.4E+01	2.15E-05	R(L)(QR)(CR)(QR)(CW)	0.12
10.36	22.49	25.84	3.22	2.16E-05	R(L)(QR)(CR)(QR)(CW)	0.06
1.1	39.48	29.07	0.65	5.55E-05	R(L)(QR)(CR)(QR)(CW)	0.005

**Table 7:** DEIS circuit fitting parameters during alloying for Si/C/PAA/AB anodic half-cell

$R_s$	$R_{PC}$	$R_{SEI}$	$R_{CT}$	$\chi^2$	Circuit	Potential (V)
44.32	1.25	275.43	55.51	0.0005	R(L)(QR)(CR)(QR)(CW)	1.20
22.45	44.61	399.28	64.45	$5.9 \times 10^{-5}$	R(L)(QR)(CR)(QR)(CW)	1.14
1.09	3.90E+04	401	43.41	1.50E-05	R(L)(QR)(CR)(QR)(CW)	1.08
2.54	2.85E+11	480.98	48.15	4.61E-05	R(L)(QR)(CR)(QR)(CW)	1.02
2.99	20.73	700.42	47.87	6.66E-05	R(L)(QR)(CR)(QR)(CW)	0.96
2.31	54.51	689.90	52.54	0.32E-05	R(L)(QR)(CR)(QR)(CW)	0.90
1.85	6.51E+02	667.41	31.76	4.69E-05	R(L)(QR)(CR)(QR)(CW)	0.84
2.4	5.55	644.71	89.41	3.71E-05	R(L)(QR)(CR)(QR)(CW)	0.78
1.98	3.68	669.32	0.52	5.82E-05	R(L)(QR)(CR)(QR)(CW)	0.72
0.84	1.86	600.32	6.42E+02	1.74E-05	R(L)(QR)(CR)(QR)(CW)	0.66
0.984	8.54	622.43	2.51E+01	7.51E-05	R(L)(QR)(CR)(QR)(CW)	0.60
0.95	9.85	559.21	5.43E+01	0.90E-05	R(L)(QR)(CR)(QR)(CW)	0.54
0.85	1.01	550.42	32.36	0.66E-05	R(L)(QR)(CR)(QR)(CW)	0.48
0.92	19.43	541.49	5.63	7.65E-05	R(L)(QR)(CR)(QR)(CW)	0.42
0.86	53.67	650.33	4.67	6.66E-05	R(L)(QR)(CR)(QR)(CW)	0.36
1.94	100	590.1	1.43	4.78E-05	R(L)(QR)(CR)(QR)(CW)	0.30
1.84	66.31	600	65.41	2.69E-05	R(L)(QR)(CR)(QR)(CW)	0.24

## CHAPTER 4

1.74	67.15	680	99.54	5.05E-05	R(L)(QR)(CR)(QR)(CW)	0.18
1.54	98.39	659.31	2.36E+01	1.53E-05	R(L)(QR)(CR)(QR)(CW)	0.12
1.68	12.85	661.34	1.23	1.62E-05	R(L)(QR)(CR)(QR)(CW)	0.06
19.4	33.89	660.21	0.41	4.57E-05	R(L)(QR)(CR)(QR)(CW)	0.005

**Table 8:** DEIS circuit fitting parameters during alloying for Si/C/CMC/AB anodic half-cell

$R_s$	$R_{PC}$	$R_{SEI}$	$R_{CT}$	$\chi^2$	Circuit	Potential (V)
44.32	1.25	998.1	55.51	0.0005	R(L)(QR)(CR)(QR)(CW)	1.20
22.45	44.61	900.17	64.45	$5.9 \times 10^{-5}$	R(L)(QR)(CR)(QR)(CW)	1.14
1.09	3.90E+04	859.47	43.41	1.50E-05	R(L)(QR)(CR)(QR)(CW)	1.08
2.54	2.85E+11	828.85	48.15	4.61E-05	R(L)(QR)(CR)(QR)(CW)	1.02
2.99	20.73	800.73	47.87	6.66E-05	R(L)(QR)(CR)(QR)(CW)	0.96
2.31	54.51	846.73	52.54	0.32E-05	R(L)(QR)(CR)(QR)(CW)	0.90
1.85	6.51E+02	816.84	31.76	4.69E-05	R(L)(QR)(CR)(QR)(CW)	0.84
2.4	5.55	826.86	89.41	3.71E-05	R(L)(QR)(CR)(QR)(CW)	0.78
1.98	3.68	800.83	0.52	5.82E-05	R(L)(QR)(CR)(QR)(CW)	0.72
0.84	1.86	817.37	6.42E+02	1.74E-05	R(L)(QR)(CR)(QR)(CW)	0.66
0.984	8.54	867.05	2.51E+01	7.51E-05	R(L)(QR)(CR)(QR)(CW)	0.60
0.95	9.85	876.93	5.43E+01	0.90E-05	R(L)(QR)(CR)(QR)(CW)	0.54
0.85	1.01	800.95	32.36	0.66E-05	R(L)(QR)(CR)(QR)(CW)	0.48
0.92	19.43	900.93	5.63	7.65E-05	R(L)(QR)(CR)(QR)(CW)	0.42
0.86	53.67	967.04	4.67	6.66E-05	R(L)(QR)(CR)(QR)(CW)	0.36
1.94	100	999.78	1.43	4.78E-05	R(L)(QR)(CR)(QR)(CW)	0.30
1.84	66.31	1200.38	65.41	2.69E-05	R(L)(QR)(CR)(QR)(CW)	0.24
1.74	67.15	1067.94	99.54	5.05E-05	R(L)(QR)(CR)(QR)(CW)	0.18
1.54	98.39	779.17	2.36E+01	1.53E-05	R(L)(QR)(CR)(QR)(CW)	0.12
1.68	12.85	780.16	1.23	1.62E-05	R(L)(QR)(CR)(QR)(CW)	0.06
19.4	33.89	736.74	0.41	4.57E-05	R(L)(QR)(CR)(QR)(CW)	0.005



### 4.4.3 Post-mortem characterization of anodes

#### Scanning electron microscope (SEM) measurements (Morphology studies)

After electrochemical evaluation of the anodes comprising of the crosslinked P-BIAN binder and control system (PAA and CMC) binders, the anodes were retrieved by disassembling anodic half-cells after 1000 cycles for Si/C/P-BIAN-crosslinked/AB and control systems (Si/C/PAA/AB – 300 cycles and Si/C/CMC/AB – 400 cycles), respectively. In the case of Si/C/P-BIAN-crosslinked/AB, the pristine electrode showed excellent adherence to the copper current collector and FESEM micrograph showed uniform morphology (Figure 11a). Even after 1000 cycles of de-/alloying, the Si/C/P-BIAN-crosslink/AB anode maintained its adherence to the copper current collector, however, due to long cycling at a high current rate, the anode morphology constituted of micro cracks due to the pulverization of SiNPs (Figure 11b). Also, the electrode laminate did not peel off while handling though it had undergone 1000 cycles of rapid charge-discharge. In the case of anode with PAA binder (control system: (i) Si/C/PAA/AB), there was a contrasting difference between the morphology of the pristine (Figure 11c) and anode after 400 cycles of charge-discharge (Figure 11d) with electrode laminate peeling-off while handling. Similarly, the anode with CMC binder (control system: (ii) Si/C/CMC/AB) underwent a drastic morphological change from its pristine morphology to that after 400 cycles of charge-discharge. Large cracks were developed due to the volume expansion and pulverization of SiNPs (Figure 11e and 11f). The FESEM morphological studies highlighted the mechanical robustness provided by crosslinked P-BIAN binder matrices to Si anodes. This was responsible for their excellent cyclic stability for over 1000 cycles of de-/alloying in comparison to conventional binders (PAA and CMC-Na). The average particle size of silicon nanoparticles (SiNPs) is 100 nm as described by the seller (Sigma-Aldrich). Therefore, the diameter of the SiNP being 100 nm, the area would be  $125.6 \mu\text{m}^2$ . Hence, the established interaction between one SiNP and a polymeric chain would have crosslinked P-BIAN matrices with chain diameter of 100 nm or more. Therefore, the length of a single polymer unit was calculated to be 18.5  $\mu\text{m}$  based on the length of a single repeating unit (10.9Å) with  $M_w$  being 17000. Therefore, comparable size of SiNP and polymer chain length is reasonable to explain efficient interaction between them to form self-healing matrices.

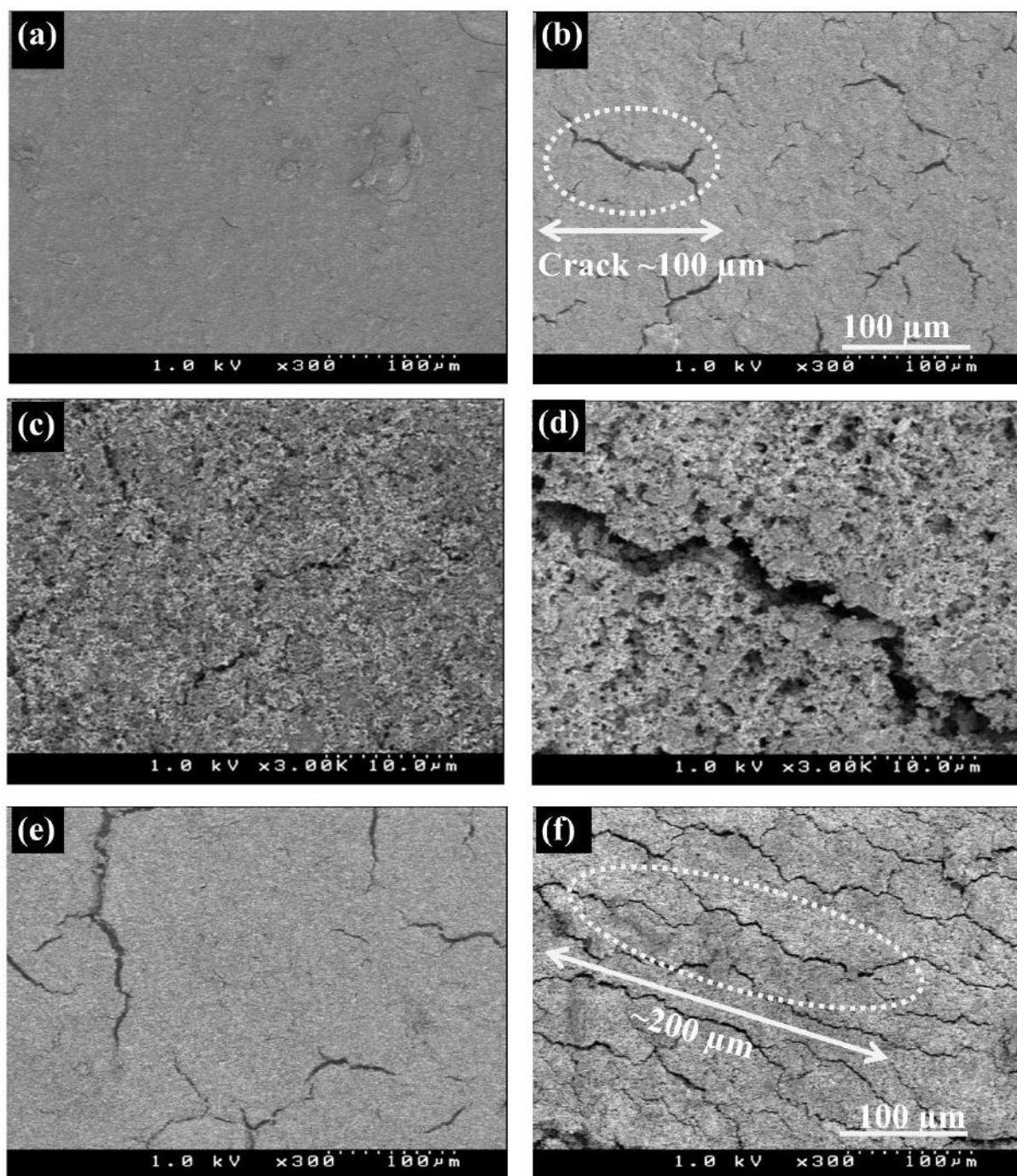


**Figure 11:** The FESEM micrographs of the Si/C/P-BIAN-crosslinked/AB electrode (a) Pristine and (b) after 1000 cycles of de-/alloying. The control study electrode (i) (Si/C/PAA/AB) - (c) Pristine and (d) after 300 cycles and (ii) (Si/C/CMC/AB) - (e) Pristine and (f) after 400 cycles.

## 4.5 Conclusion

The application of crosslinked P-BIAN polymer matrices as a binder for Si anodes, resulted in their excellent stabilization and performance in terms of reversible capacity, cyclability, capacity retention, and coulombic efficiency, respectively. The crosslinked P-BIAN binder provided mechanical support because of the presence of robust P-BIAN crosslinked matrices that restricted the pulverization of SiNPs even on cycling at a high current-rate. The electron rich diimine nitrogen backbone in the BIAN moiety induced necessary electrical conductivity throughout the electrode laminate. The low-lying LUMO of P-BIAN crosslinked matrices (determined from theoretical evaluation of the binder) was tailored on crosslinking with an alkane linker (1,6-dibromohexane). As a result, the binder could undergo n-doping in the reducing anodic environment to restrict the electrolytic decomposition on the anode surface to tune the SEI formation. Cyclic voltammetry studies of Si/C/P-BIAN-crosslinked/AB anodic half-cell showed characteristic electrolytic decomposition, alloying of crystalline Si phase, alloying of Si amorphous phase, and two-step Si dealloying peaks with promising cyclability unlike the conventional binders'-based (PAA and CMC) anodic half-cells. The charge-discharge studies of Si/C/P-BIAN-crosslinked/AB anodic half-cell showed excellent stability of Si anode even at a high current rate of  $500 \text{ mA g}^{-1}$ . A reversible capacity of  $\sim 2500 \text{ mAh g}^{-1}$  with a capacity retention of 99.1% after 1000 cycles was observed in the case of Si/C/P-BIAN-crosslinked/AB anodic half-cell. Further, dynamic electrochemical impedance spectroscopy (DEIS) studies showed that the SEI resistance ( $R_{\text{SEI}}$ ) in case of Si/C/P-BIAN-crosslinked/AB anodic half-cell was substantially lower when compared with control systems with conventional binders (PAA and CMC). Therefore, the n-doping of the crosslinked P-BIAN binder could lead to the formation of an interface with lowered impedance that provided appreciable stability to Si anodes to be cycled for over 1000 cycles. The post-mortem characterization of the cycled Si anode with the cross-linked P-BIAN binder showed good morphology retention as well as adherence to the copper current collector. Hence, conducting/crosslinked-type binder materials such as crosslinked P-BIAN not only administer cyclic stability but also influence the architecture of the interface which would stabilize Si anodes. This protocol will lead to a promising future in the development of next-generation high energy density LIBs based on Si anodes.

## References

1. Goodenough, J. B.; Park, K.-S., The Li-ion rechargeable battery: A perspective. *Journal of the American Chemical Society* **2013**, *135* (4), 1167-1176.
2. Zuo, X.; Zhu, J.; Müller-Buschbaum, P.; Cheng, Y.-J., Silicon based lithium-ion battery anodes: A chronicle perspective review. *Nano Energy* **2017**, *31*, 113-143.
3. Li, J.-Y.; Xu, Q.; Li, G.; Yin, Y.-X.; Wan, L.-J.; Guo, Y.-G., Research progress regarding Si-based anode materials towards practical application in high energy density Li-ion batteries. *Materials Chemistry Frontiers* **2017**, *1* (9), 1691-1708.
4. Jin, Y.; Zhu, B.; Lu, Z.; Liu, N.; Zhu, J., Challenges and recent progress in the development of Si anodes for lithium-ion battery. *Advanced Energy Materials* **2017**, *7* (23), 1700715.
5. Casimir, A.; Zhang, H.; Ogoke, O.; Amine, J. C.; Lu, J.; Wu, G., Silicon-based anodes for lithium-ion batteries: Effectiveness of materials synthesis and electrode preparation. *Nano Energy* **2016**, *27*, 359-376.
6. Obrovac, M. N.; Chevrier, V. L., Alloy negative electrodes for Li-ion batteries. *Chemical Reviews* **2014**, *114* (23), 11444-11502.
7. Zhao, X.; Lehto, V.-P., Challenges and prospects of nanosized silicon anodes in lithium-ion batteries. *Nanotechnology* **2020**, *32* (4), 042002.
8. Zhu, G.; Zhang, F.; Li, X.; Luo, W.; Li, L.; Zhang, H.; Wang, L.; Wang, Y.; Jiang, W.; Liu, H. K.; Dou, S. X.; Yang, J., Engineering the distribution of carbon in silicon oxide nanospheres at the atomic level for highly stable anodes. *Angewandte Chemie International Edition* **2019**, *58* (20), 6669-6673.
9. Du, F.-H.; Li, B.; Fu, W.; Xiong, Y.-J.; Wang, K.-X.; Chen, J.-S., Surface binding of polypyrrole on porous silicon hollow nanospheres for Li-ion battery anodes with high structure stability. *Advanced Materials* **2014**, *26* (35), 6145-6150.
10. Liu, N.; Wu, H.; McDowell, M. T.; Yao, Y.; Wang, C.; Cui, Y., A yolk-shell design for stabilized and scalable Li-ion battery alloy anodes. *Nano Letters* **2012**, *12* (6), 3315-3321.
11. Zamfir, M. R.; Nguyen, H. T.; Moyen, E.; Lee, Y. H.; Pribat, D., Silicon nanowires for Li-based battery anodes: a review. *Journal of Materials Chemistry A* **2013**, *1* (34), 9566-9586.
12. Chen, D.; Tao, C.; Chen, T.; Liu, X.; Liu, Y.; Xu, G.; Han, G., Pomegranate-like silicon-based anodes self-assembled by hollow-structured Si/void@C nanoparticles for Li-ion batteries with high performances. *Nanotechnology* **2020**, *32* (9), 095402.

13. Lee, K.; Lim, S.; Tron, A.; Mun, J.; Kim, Y.-J.; Yim, T.; Kim, T.-H., Polymeric binder based on PAA and conductive PANI for high performance silicon-based anodes. *RSC Advances* **2016**, *6* (103), 101622-101625.
14. Choi, S.; Kwon, T.-w.; Coskun, A.; Choi, J. W., Highly elastic binders integrating polyrotaxanes for silicon microparticle anodes in lithium ion batteries. *Science* **2017**, *357* (6348), 279-283.
15. Cho, Y.; Kim, J.; Elabd, A.; Choi, S.; Park, K.; Kwon, T.-w.; Lee, J.; Char, K.; Coskun, A.; Choi, J. W., A pyrene–poly(acrylic acid)–polyrotaxane supramolecular binder network for high-performance silicon negative electrodes. *Advanced Materials* **2019**, *31* (51), 1905048.
16. Zhang, L.; Zhang, L.; Chai, L.; Xue, P.; Hao, W.; Zheng, H., A coordinatively cross-linked polymeric network as a functional binder for high-performance silicon submicro-particle anodes in lithium-ion batteries. *Journal of Materials Chemistry A* **2014**, *2* (44), 19036-19045.
17. Kwon, T.-w.; Choi, J. W.; Coskun, A., The emerging era of supramolecular polymeric binders in silicon anodes. *Chemical Society Reviews* **2018**, *47* (6), 2145-2164.
18. Ling, L.; Bai, Y.; Wang, Z.; Ni, Q.; Chen, G.; Zhou, Z.; Wu, C., Remarkable effect of sodium alginate aqueous binder on anatase TiO<sub>2</sub> as high-performance anode in sodium ion batteries. *ACS Applied Materials & Interfaces* **2018**, *10* (6), 5560-5568.
19. Wei, L.; Chen, C.; Hou, Z.; Wei, H., Poly (acrylic acid sodium) grafted carboxymethyl cellulose as a high performance polymer binder for silicon anode in lithium ion batteries. *Scientific Reports* **2016**, *6* (1), 19583.
20. Jeong, Y. K.; Kwon, T.-w.; Lee, I.; Kim, T.-S.; Coskun, A.; Choi, J. W., Hyperbranched  $\beta$ -cyclodextrin polymer as an effective multidimensional binder for silicon anodes in lithium rechargeable batteries. *Nano Letters* **2014**, *14* (2), 864-870.
21. Li, J.-T.; Wu, Z.-Y.; Lu, Y.-Q.; Zhou, Y.; Huang, Q.-S.; Huang, L.; Sun, S.-G., Water soluble binder, an electrochemical performance booster for electrode materials with high energy density. *Advanced Energy Materials* **2017**, *7* (24), 1701185.
22. Chen, H.; Ling, M.; Hencz, L.; Ling, H. Y.; Li, G.; Lin, Z.; Liu, G.; Zhang, S., Exploring chemical, mechanical, and electrical functionalities of binders for advanced energy-storage devices. *Chemical Reviews* **2018**, *118* (18), 8936-8982.
23. Zhang, C.; Chen, Q.; Ai, X.; Li, X.; Xie, Q.; Cheng, Y.; Kong, H.; Xu, W.; Wang, L.; Wang, M.-S.; Yang, H.; Peng, D.-L., Conductive polyaniline doped with phytic acid as a binder and conductive additive for a commercial silicon anode with enhanced lithium storage properties. *Journal of Materials Chemistry A* **2020**, *8* (32), 16323-16331.

24. Yao, Y.; Liu, N.; McDowell, M. T.; Pasta, M.; Cui, Y., Improving the cycling stability of silicon nanowire anodes with conducting polymer coatings. *Energy & Environmental Science* **2012**, *5* (7), 7927-7930.
25. Han, Y.; Qi, P.; Zhou, J.; Feng, X.; Li, S.; Fu, X.; Zhao, J.; Yu, D.; Wang, B., Metal-organic frameworks (MOFs) as sandwich coating cushion for silicon anode in lithium ion batteries. *ACS Applied Materials & Interfaces* **2015**, *7* (48), 26608-26613.
26. Zeng, W.; Wang, L.; Peng, X.; Liu, T.; Jiang, Y.; Qin, F.; Hu, L.; Chu, P. K.; Huo, K.; Zhou, Y., Enhanced ion conductivity in conducting polymer binder for high-performance silicon anodes in advanced lithium-ion batteries. *Advanced Energy Materials* **2018**, *8* (11), 1702314.
27. Wu, M.; Song, X.; Liu, X.; Battaglia, V.; Yang, W.; Liu, G., Manipulating the polarity of conductive polymer binders for Si-based anodes in lithium-ion batteries. *Journal of Materials Chemistry A* **2015**, *3* (7), 3651-3658.
28. Zhao, Y.; Yang, L.; Zuo, Y.; Song, Z.; Liu, F.; Li, K.; Pan, F., Conductive binder for Si anode with boosted charge transfer capability via n-type doping. *ACS Applied Materials & Interfaces* **2018**, *10* (33), 27795-27800.
29. Ryou, M.-H.; Kim, J.; Lee, I.; Kim, S.; Jeong, Y. K.; Hong, S.; Ryu, J. H.; Kim, T.-S.; Park, J.-K.; Lee, H.; Choi, J. W., Mussel-inspired adhesive binders for high-performance silicon nanoparticle anodes in lithium-ion batteries. *Advanced Materials* **2013**, *25* (11), 1571-1576.
30. Kwon, T.-w.; Jeong, Y. K.; Lee, I.; Kim, T.-S.; Choi, J. W.; Coskun, A., Systematic molecular-level design of binders incorporating meltdrum's acid for silicon anodes in lithium rechargeable batteries. *Advanced Materials* **2014**, *26* (47), 7979-7985.
31. Jang, S.-Y.; Han, S.-H., Fabrication of Si negative electrodes for Li-ion batteries (LIBs) using cross-linked polymer binders. *Scientific Reports* **2016**, *6* (1), 38050.
32. Gao, S.; Sun, F.; Brady, A.; Pan, Y.; Erwin, A.; Yang, D.; Tsukruk, V.; Stack, A. G.; Saito, T.; Yang, H.; Cao, P.-F., Ultra-efficient polymer binder for silicon anode in high-capacity lithium-ion batteries. *Nano Energy* **2020**, *73*, 104804.
33. Jeong, Y. K.; Kwon, T.-w.; Lee, I.; Kim, T.-S.; Coskun, A.; Choi, J. W., Millipede-inspired structural design principle for high performance polysaccharide binders in silicon anodes. *Energy & Environmental Science* **2015**, *8* (4), 1224-1230.
34. Wang, C.; Wu, H.; Chen, Z.; McDowell, M. T.; Cui, Y.; Bao, Z., Self-healing chemistry enables the stable operation of silicon microparticle anodes for high-energy lithium-ion batteries. *Nature Chemistry* **2013**, *5* (12), 1042-1048.

35. Chen, C.; Lee, S. H.; Cho, M.; Kim, J.; Lee, Y., Cross-linked chitosan as an efficient binder for si anode of li-ion batteries. *ACS Applied Materials & Interfaces* **2016**, 8 (4), 2658-2665.
36. Chen, S.; Ling, H. Y.; Chen, H.; Zhang, S.; Du, A.; Yan, C., Development of cross-linked dextrin as aqueous binders for silicon based anodes. *J Power Sources* **2020**, 450, 227671.
37. Koo, B.; Kim, H.; Cho, Y.; Lee, K. T.; Choi, N.-S.; Cho, J., A highly cross-linked polymeric binder for high-performance silicon negative electrodes in lithium ion batteries. *Angewandte Chemie International Edition* **2012**, 51 (35), 8762-8767.
38. Wu, H.; Yu, G.; Pan, L.; Liu, N.; McDowell, M. T.; Bao, Z.; Cui, Y., Stable Li-ion battery anodes by in-situ polymerization of conducting hydrogel to conformally coat silicon nanoparticles. *Nature Communications* **2013**, 4 (1), 1943.
39. Zhao, H.; Wei, Y.; Qiao, R.; Zhu, C.; Zheng, Z.; Ling, M.; Jia, Z.; Bai, Y.; Fu, Y.; Lei, J.; Song, X.; Battaglia, V. S.; Yang, W.; Messersmith, P. B.; Liu, G., Conductive polymer binder for high-tap-density nanosilicon material for lithium-ion battery negative electrode application. *Nano Letters* **2015**, 15 (12), 7927-7932.
40. Liu, X.; Zai, J.; Iqbal, A.; Chen, M.; Ali, N.; Qi, R.; Qian, X., Glycerol-crosslinked PEDOT:PSS as bifunctional binder for Si anodes: Improved interfacial compatibility and conductivity. *Journal of Colloid and Interface Science* **2020**, 565, 270-277.
41. van Asselt, R.; Elsevier, C. J.; Smeets, W. J. J.; Spek, A. L.; Benedix, R., Synthesis and characterization of rigid bidentate nitrogen ligands and some examples of coordination to divalent palladium. X-ray crystal structures of bis (p-tolylimino) acenaphthene and methylchloro [bis(o,o'-diisopropylphenyl-imino) acenaphthene] palladium (II). *Recueil des Travaux Chimiques des Pays-Bas* **1994**, 113 (2), 88-98.
42. Gasperini, M.; Ragaini, F.; Cenini, S., Synthesis of Ar-BIAN ligands (Ar-BIAN = bis(aryl)acenaphthenequinonediiimine) having strong electron-withdrawing substituents on the aryl rings and their relative coordination strength toward palladium(0) and -(II) complexes. *Organometallics* **2002**, 21 (14), 2950-2957.
43. Patnaik, S. G.; Vedarajan, R.; Matsumi, N., BIAN based functional diimine polymer binder for high performance Li ion batteries. *Journal of Materials Chemistry A* **2017**, 5 (34), 17909-17919.
44. Gupta, A.; Badam, R.; Nag, A.; Kaneko, T.; Matsumi, N., Bis-imino-acenaphthenequinone-paraphenylene-type condensation copolymer binder for ultralong cyclable lithium-ion rechargeable batteries. *ACS Applied Energy Materials* **2021**, 4 (3), 2231-2240.

45. Patnaik, S. G.; Vedarajan, R.; Matsumi, N., BIAN based electroactive polymer with defined active centers as metal-free electrocatalysts for oxygen reduction reaction (ORR) in aqueous and nonaqueous media. *ACS Applied Energy Materials* **2018**, *1* (3), 1183-1190.
46. Faniyi, I. O.; Fasakin, O.; Olofinjana, B.; Adekunle, A. S.; Oluwasusi, T. V.; Eleruja, M. A.; Ajayi, E. O. B., The comparative analyses of reduced graphene oxide (RGO) prepared via green, mild and chemical approaches. *SN Applied Sciences* **2019**, *1* (10), 1181.
47. Gillan, E. G., Synthesis of nitrogen-rich carbon nitride networks from an energetic molecular azide precursor. *Chemistry of Materials* **2000**, *12* (12), 3906-3912.
48. Zimmerman, J. L.; Williams, R.; Khabashesku, V. N.; Margrave, J. L., Synthesis of spherical carbon nitride nanostructures. *Nano Letters* **2001**, *1* (12), 731-734.
49. Martinez-Felipe, A.; Brebner, F.; Zaton, D.; Concellon, A.; Ahmadi, S.; Piñol, M.; Oriol, L., Molecular recognition via hydrogen bonding in supramolecular complexes: A fourier transform infrared spectroscopy study. *Molecules* **2018**, *23* (9), 2278.
50. Choi, N.-S.; Ha, S.-Y.; Lee, Y.; Jang, J. Y.; Jeong, M.-H.; Shin, W. C.; Ue, M., Recent progress on polymeric binders for silicon anodes in lithium-ion batteries. *J. Electrochem. Sci. Technol* **2015**, *6* (2), 35-49.
51. Villa, M.; Miesel, D.; Hildebrandt, A.; Ragaini, F.; Schaarschmidt, D.; Jacobi von Wangelin, A., Synthesis and catalysis of redox-active bis(imino)acenaphthene (BIAN) iron complexes. *ChemCatChem* **2017**, *9* (16), 3203-3209.
52. Huang, J.; Ge, H.; Li, Z.; Zhang, J., Dynamic electrochemical impedance spectroscopy of a three-electrode lithium-ion battery during pulse charge and discharge. *Electrochimica Acta* **2015**, *176*, 311-320.
53. Agubra, V. A.; Fergus, J. W., The formation and stability of the solid electrolyte interface on the graphite anode. *J Power Sources* **2014**, *268*, 153-162.
54. Tian, M.; Wu, P., Nature plant polyphenol coating silicon submicroparticle conjugated with polyacrylic acid for achieving a high-performance anode of lithium-ion battery. *ACS Applied Energy Materials* **2019**, *2* (7), 5066-5073.
55. Wang, L.; Liu, T.; Peng, X.; Zeng, W.; Jin, Z.; Tian, W.; Gao, B.; Zhou, Y.; Chu, P. K.; Huo, K., Highly stretchable conductive glue for high-performance silicon anodes in advanced lithium-ion batteries. *Advanced Functional Materials* **2018**, *28* (3), 1704858.



## Chapter 5

### General Conclusions

#### 5.1 Conclusions

##### Chapter 1

This chapter provided a linear overview of the past, present, and future of non-renewable sources of energy, their drawbacks, and electrochemical power sources as their potential alternatives. A deductive significance was provided as to why LIBs have an edge over other electrochemical energy storage technologies to take us into a sustainable, eco-friendly, and cost-effective future while meeting the ever-growing high energy density requirements at various fronts. The current trend in LIB electrodes (cathodes and anodes) based on latest literature survey was reported with graphite as current commercial choice and Si being recognized as the next-generation anode active material. Further, the drawbacks associated with each of these electrodes were detailed by recognizing that in both the types of electrodes, the solid-electrolyte interface (SEI) is a critical factor that determines their stability. Hence, a short overview to SEI was provided to comprehend its importance, factors influencing its formation, and ways to develop possible strategies to tailor its formation on electrodes. Going further by narrowing down to the focus of this research work, an importance to the need of polymer binders as add-ons that can not only mitigate other drawbacks associated with graphite and Si anodes but also lead to the formation of an interface that stabilizes these electrodes was provided. In this regard, the success story of the polymeric binders belonging to the compounds of the family bisiminoacenaphthene (BIAN) in stabilizing graphite was provided with their historic structural, chemical, and electrochemical significance. Finally, the chapter was closed by providing an objective and scope of this thesis. As a part of objective and scope section, salient structural, chemical, and electrochemical features of BIAN-based compounds were provided with highlights being their tunable electronic properties (low-lying LUMO). This provided the scope of designing BIAN-based composite and crosslinked polymers to stabilize not only graphite but also the next generation silicon anodes that not only administer mechanical support and electrical conductivity but also tailor the SEI formation on the electrode surface with lowered impedance for better cyclability of anodes. The chapter provided a complete perspective of the aims and objectives of this work.

## Chapter-2

This chapter narrated the success story of BIAN-p-phenylene (BP)-copolymer as an alternate binder choice for graphite anode over conventionally used PVDF binder. The BP-copolymer binder exhibited better interfacial properties, reversible capacity, capacity retention, lithium-ion diffusion, and morphology retention in comparison to the conventional PVDF binder. The structural benefits like  $\pi$ - $\pi$  stacking with graphite, n-type characteristics with intrinsic electronic conductivity, and diimine nitrogen atoms to interact with copper current collector empowered the BP binder to provide robust mechanical support to the active material (graphite). The theoretical evaluation of the BP-copolymer and CV studies indicated that its low-lying LUMO inspired the binder doping which prevented the electrolyte decomposition on the anode surface unlike the conventional PVDF binder. The suppressed electrolyte decomposition led to the formation of a thinner solid-electrolyte interface (SEI) which was confirmed by the XPS analysis of the cycled anode. The impedance spectroscopy studies showed a reduced interfacial impedance ( $R_{SEI}$ ) for BP binder-based anode. As a result, the BP based anodic half-cell showed improved charge and discharge performance (1735 cycles) at a high current rate 1C with 95% capacity retention. Though alternate anode material choices to graphite are being pursued, graphite is still a commercial choice. Therefore, further stabilizing graphite anode with an alternate binder choice to design an effective SEI and mitigate the problems encountered while working with the conventional binder PVDF is crucial.

## Chapter-3

This chapter detailed the design rationale, synthesis, and performance of a novel n-type self-healing polymer composite P-BIAN/PAA as a binder to stabilize Si anodes. P-BIAN/PAA stabilized the Si anodes in terms of rate capability, specific capacity, cyclability, capacity retention, and coulombic efficiency on its application as a binder. Due to its low-lying LUMO, it could undergo cathodic doping in the anodic environment and restrict the excessive decomposition of the electrolyte on the anode surface. The impedance spectroscopy studies showed that the restricted electrolytic decomposition on the P-BIAN/PAA-based anode resulted in its low interfacial ( $R_{SEI}$ ) and charge transfer ( $R_{CT}$ ) impedances. Therefore, the formation of a tailored thin SEI and the dynamic self-healing electrostatic hydrogen bonding in BIAN-PAA provided a robust mechanical support to the silicon anodes during the de-/alloying and avoided its premature pulverization. The P-BIAN/PAA-based anode showed an excellent cyclability up to 600 cycles, specific capacity of  $\sim 2100 \text{ mAhg}^{-1}_{Si}$ ,  $\sim 98.9\%$  average

coulombic efficiency, and 95% capacity retention after 600 cycles. Therefore, this provided insights on the importance of designing strategized novel polymer composites that are n-type conducting polymers (CPs) linked via electrostatic interaction with carboxylate-type polymer to provide mechanical robustness and tune the interface formation on Si anode.

## Chapter-4

This chapter elaborated another strategy of conducting/crosslinked class of polymers in stabilizing Si anodes over conducting/self-healing class. The design, synthesis, and electrochemical evaluation of crosslinked P-BIAN were discussed in comparison to conventional binder systems (PAA and CMC). Crosslinked P-BIAN polymer matrices stabilized the performance of Si anodes in terms of reversible capacity, cyclability, capacity retention, and coulombic efficiency, respectively. Excellent mechanical support by virtue of its robust crosslinked matrices even at high current rate, intrinsic electronic conductivity due to the presence of diimine backbone, and low-lying LUMO driven n-doping in anodic environment to tailor an effective SEI were the highlighting features of this polymer. The charge-discharge studies of the crosslinked P-BIAN-based anodic half-cell showed excellent stability of Si anode even at a high current rate of  $500 \text{ mA g}^{-1}$  with reversible capacity of  $2500 \text{ mAh g}^{-1}$  and capacity retention of 99.1% after 1000 cycles. This chapter streamlined the class of binders that are effective in stabilizing Si anodes by their versatility to synergize their application on the electrode surface as well as the interface between the electrode and electrolyte.

## 5.2 Future Prospects

In this dissertation work, the author has explored the application of novel BIAN-based functional polymers as binders by exploring their rich redox chemistry, electrochemical significance, and structure-property relationship to stabilize high-performance LIB anodes. The author has hierarchically tried to stabilize graphite and Si anodes in a LIB by designing BIAN-based polymers that can mitigate major drawbacks associated with these electrodes and most importantly tailor the formation of SEI on the electrode surface. The highlighting features of BIAN family of compounds are electron reservoir property, n-doping ability in reducing anodic environment, rich redox chemistry, intrinsic electronic conductivity, tunable electronic properties, and coordinating ability because of electron rich nitrogen atoms. Also, the compounds of this family have been utilized as ligands for transition metals for their catalytic

utility. Therefore, their exceptional coordinating capability via the imine moiety has potential to form variety of composite polymers and monomers with an external dopant to diimine framework. This creates a wider scope of opportunity to explore a plethora of conducting/crosslinked, conducting/self-healing, and self-healing type BIAN-based polymers with varying electronic property to tune the interface as needed for stabilizing not only Si anodes but also other high-capacity materials like phosphorous, boron, MoS<sub>2</sub>, etc. in next-generation LIBs that suffer drastic volume expansion/contraction on charge-discharge. This class of compounds can find its versatile application in future energy storage technologies like Na, K, and Mg-ion batteries. Also, their utility as potential molecular connects to metallic/semi-conducting electrodes for memory devices in M-m-M (Metal-molecule-Metal) junctions can be of great significance. Finally, the author believes that this thesis can serve as a platform for the thoughtful design of future composite binder materials to stabilize high-capacity anode materials in Li-ion, Na-ion, K-ion, and Mg-ion batteries.

## Publications and Conferences

### Patents:

#### 1. JP2020-83527

Date of Submission: May 11, 2020

“Novel polymer binder system composites for secondary batteries.”

Submitted by Japan Advanced Institute of Science and Technology (JAIST)

Authors: Noriyoshi Matsumi, Rajashekar Badam, and **Agman Gupta**

#### 2. JP2020-83526

Date of Submission: May 11, 2020

“Stabilizer for secondary battery cathode, its preparation, method for stabilization and electrolytes containing the compound.”

Submitted by Japan Advanced Institute of Science and Technology (JAIST)

Authors: Noriyoshi Matsumi, Rajahsekar Badam, **Agman Gupta**, Naoki Takaya, Shunsuk Masuo, and Hajime Minagawa

#### 3. Japanese Patent Filing in Progress (May 2021)

“Crosslinked Polymer BIAN Matrices to Stabilize Silicon Anodes in Lithium-Ion Secondary Batteries.”

To be submitted by Japan Advanced Institute of Science and Technology (JAIST)

Authors: Noriyoshi Matsumi, Rajashekar Badam, and **Agman Gupta**

### Publications:

1. “Bis-imino-acenaphthenequinone-Paraphenylene-Type Condensation Copolymer Binder for Ultralong Cyclable Lithium-Ion Rechargeable Batteries.”

**Agman Gupta**, Rajashekar Badam, Aniruddha Nag, Tatsuo Kaneko, and Noriyoshi Matsumi  
ACS Appl. Energy Mater. **2021**, 4(3), 2231-2240.

2. “Optimization of Cation-doped Nano-hydroxyapatite in Combination with Amorphous Aluminium Hydroxide for Defluoridation.”

**Agman Gupta**, Chelli Sai Manohar and Belliraj Siva Kumar  
Water Supply 2019, 19 (6), 1686-1694.

**Article In the Pipeline:**

1. “Poly(BIAN)/Poly(acrylic acid) Based Self-Healing Composite Binder for High Capacity Silicon Anodes in Lithium-Ion Secondary Batteries.” (*Japanese Patent*)

Agman Gupta, Rajashekar Badam, and Noriyoshi Matsumi

(Submitted to “*Advanced Energy Materials*”)

**Articles Under Preparation:**

1. “Crosslinked Polymer BIAN Matrices to Stabilize Silicon Anodes in Lithium-Ion Secondary Batteries.” (*Japanese patent filing in progress*)

Agman Gupta, Rajashekar Badam, and Noriyoshi Matsumi

2. “Stabilization of Li-Ion Battery Cathode Using Microbially Synthesized Aromatic Diamine.” (*Japanese Patent*)

Agman Gupta, Rajashekar Badam, Hajime Minagawa, Shunsuke Masuo, Naoki Takaya, and Noriyoshi Matsumi.

**Oral Presentations:**

1. “BIAN-paraphenylene Type Polymer Binder for Ultra-long Cyclable Lithium Rechargeable Battery”.

Agman Gupta, Rajashekar Badam and Noriyoshi Matsumi

**The 60<sup>th</sup> Battery Symposium in Japan, Kyoto International Conference Centre, November 13-15, 2019**

2. “Lithium-Ion Secondary Battery with Silicon Based Anode Highly Stabilized with Self-healing Polymer Binder Matrices”.

Agman Gupta, Rajashekar Badam, and Noriyoshi Matsumi

**69<sup>th</sup> Symposium on Macromolecules, SPSJ (Society for Polymer Science Japan), Presentation Number 2ESB02, Ueda Campus-Iwate University, Japan, September 16-18, 2020**

3. “Polymerized BIAN/Poly(acrylic acid) Based Composite Binder for High Capacity Silicon Anodes in Lithium Ion Secondary Batteries”

Agman Gupta, Rajashekar Badam, and Noriyoshi Matsumi

**The 61<sup>st</sup> Battery Symposium, WEB conference (online), Japan, November 18-20, 2020**

4. “BIAN/Poly(acrylic acid) Based n-Type Self-Healing Composite Binder for High Capacity Silicon Anodes in Lithium Ion Batteries”.

**Agman Gupta**, Rajashekar Badam, and Noriyoshi Matsumi

**The 101<sup>st</sup> CSJ Annual Meeting, Online Meeting, Japan, March 19-22, 2021**

### **Poster Presentations:**

1. “BIAN-paraphenylene Type Condensation Polymer Binder for High Performance Li-ion Battery Anode”

**Agman Gupta**, Rajashekar Badam and Noriyoshi Matsumi

**68<sup>th</sup> Symposium in Macromolecules, SPSJ (Society for Polymer Science Japan), September 25-27, 2019, Bunkyo Campus, Fukui University.**

2. “Lithium Ion Secondary Batteries Utilizing Polymerized BIAN/Poly(acrylic acid) Composite Binder for Silicon Anode”

**Agman Gupta**, Rajashekar Badam, and Noriyoshi Matsumi

**69<sup>th</sup> SPSJ Annual Meeting, Presentation Number 2b076, Fukuoka International Congress Centre & Fukuoka Kokusai Centre, Japan, May 27-29, 2020**

3. “Stabilization of Lithium-Ion Secondary Battery Cathode Using Microbially Synthesized Dianiline Type Compound as Additive”.

**Agman Gupta**, Rajashekar Badam, Hajime Minagawa, Syunsuke Masuo, Naoki Takaya, and Noriyoshi Matsumi

**69<sup>th</sup> SPSJ Annual Meeting, Presentation Number 2Pa077, Fukuoka International Congress Centre & Fukuoka Kokusai Centre, Japan, May 27-29, 2020**

4. “Stabilization of Lithium-Ion Battery Cathode Using Microbially Synthesized Aromatic Diamine”.

**Agman Gupta**, Rajashekar Badam, Hajime Minagawa, Syunsuke Masuo, Naoki Takaya, and Noriyoshi Matsumi

**69<sup>th</sup> Symposium on Macromolecules, SPSJ (Society for Polymer Science Japan), Presentation Number PC0315, Ueda Campus-Iwate University, Japan, September 16-18, 2020**

5. “Lithium-Ion Secondary Batteries with Silicon Based Anode Highly Stabilized with Self-Healing Polymer Binder Matrices.”

**Agman Gupta**, Rajashekar Badam, and Noriyoshi Matsumi

**International Symposium for Innovative Sustainable Materials & The 7<sup>th</sup> International Symposium for Green Innovation Polymers (GRIP 2020), Presentation Number P08, Japan Advanced Institute of Science and Technology (JAIST), Japan, November 9-11, 2020**

6. “Crosslinked BIAN Polymer Matrices to Stabilize Silicon Anode in Lithium-Ion Secondary Battery.”

**Agman Gupta**, Rajashekar Badam, and Noriyoshi Matsumi

**70<sup>th</sup> SPSJ Annual Meeting, SPSJ (Society for Polymer Science Japan),  
Presentation Number 3Pc063, Online Annual Meeting, Japan, May 26-28, 2021**

### **Awards:**

**1. Recipient of Japanese Government (Monbukagakusho: MEXT) Scholarship (2018-2021)** to pursue doctoral studies (PhD) under the guidance of Prof. Noriyoshi Matsumi at Japan Advanced Institute of Science and Technology (JAIST).

**2. Best Presentation Award of JAIST World Conference (JWC) 2020** - International Symposium for Innovative Sustainable Materials & The 7<sup>th</sup> International Symposium for Green Innovation Polymers (GRIP2020)

**Presentation Title:** “*Lithium-Ion Secondary Batteries with Silicon Based Anode Highly Stabilized with Self-Healing Polymer Binder Matrices*”

**3. Excellent Poster Award** at the 70<sup>th</sup> Annual Meeting of the Society of Polymer Science, Japan (May 26-28, 2021). **Poster Number:** 3Pc063

**Poster Title:** “*Crosslinked BIAN Polymer Matrices to Stabilize Silicon Anode in Lithium Ion Secondary Batteries*”

## **Curriculum Vitae**

### **Personal Data**

Name: Agman Gupta

Date of Birth: 18<sup>th</sup> October 1995

### **Education:**

2018-2021 (Present): PhD student in the Graduate School of Advanced Science and Technology, Japan Advanced Institute of Science and Technology (JAIST), Ishikawa, Japan (Under MEXT Scholarship)

2016-2018: Master of Science (MSc. in Chemistry), Sri Sathya Sai Institute of Higher Learning (SSSIHL), India. (CGPA: 7.9 A)

2013-2016: Bachelor of Science (BSc. in Chemistry), Sri Sathya Sai Institute of Higher Learning (SSSIHL), India. (CGPA: 7.5)